Diss. ETH No 20602

NOVEL PROBES FOR SCANNING NEAR-FIELD OPTICAL MICROSCOPY

DISSERTATION

Submitted to

ETH ZURICH

for the degree of

DOCTOR OF SCIENCES

by

VALERIA LOTITO

Laurea Specialistica in Ingegneria Elettronica (M.Sc.),

Politecnico di Bari (Italy)

born on 30/09/1983

citizen of

Italy

accepted on the recommendation of

Prof. Dr. Gian-Luca Bona, examiner

Prof. Dr. Christian Hafner, co-examiner

Dr. Urs Sennhauser, co-examiner

2012

Index

Abstract

Scanning near-field optical microscopy (SNOM) is a tool of primary importance for nanostructure investigation because it allows extraction of topographic and optical information about the specimen under test. The technique, based on the near-field interaction between a sharp probe and the sample, enables to overcome the diffraction limit of conventional optical microscopy.

Of course, the probe itself plays a major role. Unfortunately, the most widespread probe configuration, the so-called aperture probe based on a metal-coated dielectric with an aperture left at the end, is inadequate for high resolution applications. On the contrary, an alternative structure consisting in a fully metal-coated dielectric probe allows the achievement of high resolution at the cost of a complication in the experimental set-up due to the need for a radially polarized excitation.

In this thesis, we propose and investigate novel probe structures based on the introduction of an asymmetry in order to get high resolution under linearly polarized excitation. A finite element based model has been developed to study the behaviour of the novel configurations, compare their performance to those of a fully metal-coated probe and assess the influence of structural parameters on the performance of the novel probe.

All the structures break the original rotational symmetry of the probe. However two of them still exhibit reflection symmetry (probe with an oblique cut and probe based on azimuthal corrugations limited to just one half of the structure) and, hence, still require some alignment of the input linear polarization with respect to the asymmetry; the other two (probe with a single spiral corrugation and probe with azimuthal corrugations arranged in a spiral-like fashion) do not possess such a symmetry, thereby allowing superfocusing for any arbitrary direction of the input linear polarization. On the grounds of these characteristics we grouped the asymmetric structures into two categories, which we called “directional” and “adirectional”. Nonetheless, independently of the specific features, it is noteworthy that all configurations allow obviating the need for a radially polarized excitation with a significant simplification in the experimental set-up.

The practical feasibility of the proposed novel probes, both directional and adirectional, has been experimentally demonstrated. In fact, the desired structural modifications can be easily introduced by focused ion beam nanostructuring in an originally axisymmetric fully metal-coated probe using either a head-on drilling or a slicing approach properly adapted to our case. In the first approach the ion beam is aligned along the tip axis, while in the second case it is incident at an angle between 0° and 90° with respect to the probe axis according to the desired structure. The overall fabrication procedure is simple and much less demanding and time-consuming than the one required for other

modified probe configurations suggested by other groups for superfocusing under linearly polarized excitation.

A SNOM set-up working in illumination mode has been built with the aim to characterize the probe behaviour. For the optical characterization, single fluorescent molecules were chosen for a two-fold reason: first, they represent a means to get purely optical information about the probe behaviour without the risk of topographic artifacts likely to occur in samples with topographic variations due to the coupling between optical and topographic signals; second, they can be interpreted as point-like detectors providing a vectorial picture of the field distribution at the probe apex. Measurements carried out on single fluorescent molecules with an asymmetric probe based on an oblique cut have revealed optical resolution better than 20 nm and a near-field distribution at the probe apex with a mainly longitudinal component. Comparison with a numerical model developed to investigate probe-molecule interactions has shown a good agreement between theoretical predictions and experimental data.

In the light of the theoretical and experimental results, we are confident that the novel probes suggested in this thesis could be promising candidates for high resolution SNOM applications.

In chapter 1 the general principles of SNOM are discussed together with the properties of aperture probes; in chapter 2 the properties of alternative probe structures, in particular those of fully metal-coated probes, are introduced and the numerical approach adopted to model the novel probes is presented; in chapter 3 and 4 the developed model is used to investigate in detail the properties of the novel asymmetric structures based on directional and adirectional asymmetries, while in chapter 5 the interaction of the asymmetric probes with single fluorescent molecules is theoretically modelled and analyzed; in chapter 6, the procedures for the fabrication of the novel asymmetric probes are outlined; in chapter 7, the construction of the SNOM set-up used to carry out probe characterization is described; chapter 8 reports the results of probe characterization based especially on optical measurements using single fluorescent molecules. Finally, overall conclusions are drawn and possible future perspectives are discussed in chapter 9.

Sommario

La microscopia ottica a scansione a campo prossimo (meglio nota con l'acronimo inglese SNOM) rappresenta uno strumento fondamentale per l'analisi di nanostrutture perché consente di studiare simultaneamente la topografia e le proprietà ottiche del campione in esame. La tecnica, basata sull'interazione in campo prossimo tra una sonda appuntita ed un campione, permette il superamento del limite di diffrazione della microscopia ottica convenzionale.

La sonda stessa riveste ovviamente un ruolo di primaria importanza. Purtroppo la configurazione più comune, la cosiddetta sonda ad apertura, basata su di un dielettrico rivestito di metallo con un'apertura all'apice, si rivela inadeguata per applicazioni ad alta risoluzione. Al contrario, una struttura alternativa, costituita da una sonda dielettrica interamente rivestita di metallo, consente il raggiungimento di elevata risoluzione a scapito di una complicazione nel set-up sperimentale a causa della necessità di una eccitazione a polarizzazione radiale.

In questa tesi vengono proposte nuove strutture per la sonda, basate sull'introduzione di una asimmetria, al fine di raggiungere elevata risoluzione con eccitazione a polarizzazione lineare. Un modello basato sul metodo degli elementi finiti è stato sviluppato per analizzare il comportamento delle nuove configurazioni, confrontarlo con quello di sonde interamente rivestite di metallo e valutare l'effetto di diversi parametri strutturali sulle prestazioni.

Tutte le strutture sono prive di simmetria rotazionale. Tuttavia due di esse (sonda con taglio obliquo e sonda con corrugazioni azimutali limitate solo ad una metà della struttura) presentano simmetria di riflessione e pertanto richiedono allineamento della polarizzazione lineare in ingresso rispetto all'asimmetria; le altre due (sonda a singola corrugazione a spirale e sonda con corrugazioni azimutali organizzate a spirale) non hanno tale simmetria e, conseguentemente, permettono di ottenere elevata risoluzione per qualsiasi direzione della polarizzazione lineare in ingresso. Sulla base di tali caratteristiche le asimmetrie sono state suddivise in due classi indicate come "direzionali" e "adirezionali". Ciononostante, indipendentemente dalle proprietà precipue, è da osservare come tutte le strutture permettano di evitare l'uso della polarizzazione radiale con una conseguente semplificazione dell'assetto sperimentale.

Inoltre è stata anche dimostrata sperimentalmente la fattibilità delle nuove strutture proposte, sia direzionali che adirezionali. Infatti le modifiche strutturali desiderate possono essere facilmente introdotte con nanostrutturazione mediante un fascio ionico focalizzato in una sonda assisimmetrica interamente rivestita di metallo, utilizzando due approcci denominati "head-on drilling" e "slicing" adeguatamente adattati alle strutture da realizzare. Nel primo caso il fascio ionico è allineato lungo l'asse della sonda, nel secondo caso è incidente ad un angolo tra 0° e 90° rispetto all'asse della sonda

in base alla struttura desiderata. La procedura di fabbricazione complessiva è semplice, meno laboriosa e più rapida di quella richiesta per la fabbricazione di strutture modificate sviluppate da altri gruppi al fine di ottenere alta risoluzione con polarizzazione lineare.

Allo scopo di caratterizzare il comportamento delle sonde è stato costruito un set-up SNOM in modalità di illuminazione. Per la caratterizzazione ottica sono state scelte singole molecole fluorescenti per una duplice ragione: in primo luogo, perché rappresentano il mezzo per ottenere informazione puramente ottica senza rischio di artefatti topografici riscontrabili in campioni con variazioni topografiche e dovuti all'accoppiamento tra segnale ottico e topografico; in secondo luogo, perché sono in grado di fornire un'immagine vettoriale della distribuzione di campo all'apice della sonda. Le misure effettuate su singole molecole fluorescenti con una sonda asimmetrica basata su un taglio obliquo hanno rivelato una risoluzione ottica migliore di 20 nm ed una distribuzione del campo prossimo all'apice della sonda dominata dalla componente longitudinale. Il confronto con il modello numerico sviluppato per lo studio dell'interazione sonda-molecola ha mostrato un buon accordo tra previsioni teoriche e risultati sperimentali.

Alla luce dei risultati teorici e sperimentali, siamo fiduciosi che le nuove sonde proposte in questa tesi possano costituire una soluzione ideale per applicazioni SNOM ad alta risoluzione.

Nel capitolo 1 sono discussi i principi generali della SNOM e le proprietà delle sonde ad apertura; nel capitolo 2 sono introdotte le proprietà di strutture alternative, in particolare quelle di sonde interamente rivestite di metallo, e viene presentato il modello numerico adottato per modellizzare le sonde; nei capitoli 3 e 4 il modello sviluppato è adoperato per l'analisi dettagliata delle proprietà delle nuove sonde asimmetriche direzionali ed adirezionali, mentre nel capitolo 5 l'interazione di tali strutture asimmetriche con singole molecole fluorescenti è analizzata a livello teorico; nel capitolo 6, sono illustrate le procedure per la fabbricazione delle nuove sonde asimmetriche; nel capitolo 7 si riporta la costruzione del set-up sperimentale per la caratterizzazione delle sonde; nel capitolo 8 sono discussi i risultati della caratterizzazione delle sonde basata, in particolare, su misure ottiche su singole molecole fluorescenti. Infine, nel capitolo 9 sono riportate le conclusioni del lavoro e le possibili prospettive future.

Zusammenfassung

Die optische Rasternahfeldmikroskopie, oft mit dem englischen Akronym als SNOM bezeichnet, stellt ein wichtiges Verfahren für die Untersuchung der Nanostrukturen dar, weil sie die Möglichkeit bietet, die Oberflächetopographie einer Probe simultan mit den optischen Eigenschaften zu vermessen. Dieses Verfahren, das auf der Wechselwirkung zwischen einer spitzen Sonde und einer Probe beruht, erlaubt es, die Beugungsgrenze der konventionellen optischen Mikroskopie zu durchbrechen.

Die Sonde spielt für die Leistungsfähigkeit eines Nahfeldmikroskops eine zentrale Rolle. Leider ist die weit verbreitete Apertursonde, die aus einem spitzen metallbeschichteten Dielektrikum mit einer kleinen Öffnung am vordersten Ende besteht, für hochauflösende Anwendungen nicht geeignet. Dagegen kann eine aus einem vollständig mit Metall beschichteten Dielektrikum bestehende aperturlose Sonde hohe Auflösung gewährleisten, aber nur mit einem komplizierten experimentellen Aufbau, da das Licht in der Spitze radial polarisiert sein muss.

In dieser Dissertation werden neuartige asymmetrische SNOM Sonden vorgeschlagen und analysiert, um eine hohe Auflösung auch mit der Einkopplung von linear polarisiertem Licht zu erreichen. Mit Hilfe der Finite-Elemente-Methode wurde ein theoretisches Modell entwickelt, um die Feldverteilung in der Nähe der Spitze der neuen Sonden zu berechnen, ihre Leistungsfähigkeit mit denen einer vollständig mit Metall beschichteten Sonde zu vergleichen und die Auswirkungen struktureller Eigenschaften abzuschätzen.

Alle in dieser Arbeit hergestellten Strukturen haben deshalb keine Rotationssymmetrie. Jedoch haben zwei Sonden (Sonde mit schrägem Schnitt und Sonde mit Azimutalkorrugationen) noch eine Spiegelsymmetrie, weshalb sie eine Justage der Ausrichtung der linear polarisierten Beleuchtung zur Asymmetrierichtung benötigen. Dagegen haben die andere Strukturen (Sonde mit einziger spiralförmiger Korrugation und Sonde mit Azimutalkorrugationen, die spiralförmig gegliedert sind) keine Spiegelsymmetrie. Damit erlauben sie eine hohe Auflösung für beliebige Richtungen der linear polarisierten Beleuchtung. Auf Grund der verschiedenen Eigenschaften wurden die asymmetrische Strukturen in zwei Kategorien gruppiert, die als “directional” und “adirectional” benannt wurden. Unabhängig von spezifischen Charakteristiken ist mit allen diesen Strukturen die radiale Polarisation nicht mehr notwendig.

Die Funktionalität der neuen Sonden (“directional” und “adirectional”) wurde experimentell nachgewiesen. Die strukturellen Modifizierungen einer vollständig metallbeschichteten Sonde können einfach mit einem fokussierten Ionenstrahles ausgeführt werden. Zwei verschiedene Methode, als “head-on drilling” und “slicing” bekannt, wurden angewandt und unseren Strukturen

angepasst. In der ersten Methode ist der Ionenstrahl parallel zur Sondenachse ausgerichtet; in der zweiten ist der Einfallswinkel zur Sondenachse zwischen 0° und 90°. Das Fabrikationverfahren ist einfach und schnell im Vergleich zu den von anderen Gruppen vorgeschlagenen Strukturen zur Erreichung hoher Auflösungen mit linear polarisierter Beleuchtung.

Um die neuen Sonden zu charakterisieren wurde ein experimenteller SNOM Aufbau konzipiert und entwickelt, der im Beleuchtungsmodus funktioniert. Für die optische Charakterisierung wurden aus zwei Gründen meist Einzelmolekülproben benutzt: erstens erlauben sie selektiv optische Eigenschaften zu messen, ohne Risiko von Topographie-Artefakten, die in Proben mit topographischen Änderungen aus der Kopplung zwischen topographischen and optischen Signalen stammen können; zweitens liefern die Moleküle, die als punktförmige Detektoren interpretiert werden können, eine Vektor-Beschreibung der Feldverteilung in der Nähe der Spitze der neuen Sonden. Messungen an Einzelmolekülproben sind mit einer asymmetrischen Sonde ausgeführt worden, die einen schrägen Schnitt an der Spitze aufweisen: Ergebnisse haben eine Auflösung unter 20 nm und eine meist longitudinale Feldverteilung demonstriert. Der Vergleich mit unserem numerischen Modell der Wechselwirkung zwischen der Sonde und den Molekülen zeigt, dass die experimentellen Daten gut mit theoretischen Voraussagen übereinstimmen.

Anhand der theoretischen und experimentellen Ergebnissen stellen die neue Sonden eine hervorragende Alternative für hochauflösende SNOM Anwendungen dar.

Im Kapitel 1 werden die allgemeinen Prinzipien der Rasternahfeldmikroskopie beschrieben und die Eigenschaften der Apertursonde diskutiert; im Kapitel 2 werden die Eigenschaften anderen Sondenstrukturen, insbesondere die einer vollständig mit Metall beschichteten Sonde, eingeführt und das numerische Modell für die Berechnung der Feldverteilung in der Nähe der Spitze unserer neuartigen Sonden vorgestellt; in Kapiteln 3 und 4 wird das Modell für die Analyse der neuartigen asymmetrischen Sonden (“directional” und “adirectional”) benutzt; im Kapitel 5 wird die Wechselwirkung zwischen asymmetrischen Sonden und Einzelmolekülproben theoretisch analysiert; im Kapitel 6 werden die Verfahren für die Fabrikation der neuartigen Sonden beschrieben; im Kapitel 7 wird die Konstruktion des experimentellen Aufbaus für die Charakterisierung der Sonden illustriert; im Kapitel 8 werden die experimentellen Ergebnisse der Charakterisierung der Sonden diskutiert, insbesondere optische Messungen an Einzelmolekülproben; schlieβlich werden im Kapitel 9 die allgemeinen Resultate dieser Dissertation zusammengefasst und ein Ausblick zur Weiterentwicklung gegeben.

List of abbreviations

AFM = atomic force microscopy

APD = avalanche photodiode

BOR-FDTD = body of revolution FDTD

DPPC = *L*-*α*-dipalmitoylphosphatidylcholine

FEM = finite element method

FIB = focused ion beam

FDTD = finite difference time domain

FIT = finite integration technique

FWHM = full width at half maximum

GIS = gas injection system

HV = high voltage

LMIS = liquid metal ion source

MMP = multiple multipole

PCB = printed circuit board

PI = proportional/integral

PLL = phase locked loop

PMMA = polymethylmethacrylate

PS = polystyrene

PSTM = photon scanning tunnelling microscopy

PVA = polyvinyl alcohol

QY = quantum yield

SEM = scanning electron microscopy

SNOM = scanning near-field optical microscopy

SPPs = surface plasmon polaritons

STOM = scanning tunnelling optical microscopy

STM = scanning tunnelling microscopy

TEAA = triethylamine alane

TEM = transmission electron microscopy

TiBA = triisobutylaluminium

TMA = trimethylaluminium

TMAA = trimethylamine alane

TRITC-DHPE = *N*-(6-tetramethylrhodaminethiocarbamoyl)-1,2-dihexadecanoyl-*sn*-glycero-3-phosphoethanolamine, triethylammonium salt

TTL = transistor-transistor logic

WKB = Wentzel-Kramers-Brillouin

1. Introduction

High resolution microscopy is essential in both life and material science. Scanning near-field optical microscopy (SNOM) has emerged over the past years as a fundamental tool to get nanoscale insight into a specimen casting light on both topography and optical properties of a sample. Such a technique is based on the near-field interaction between a sample and a probe: a key role in the achievable sample imaging is of course played by the characteristics of the probe itself, independently of whether it is used to illuminate and/or collect light from the sample. In this chapter, the fundamental principles of near-field microscopy are presented and the characteristics of the most commonly used probe configuration, the aperture probe, are illustrated.

1.1. SNOM vs conventional optical microscopy and scanning probe techniques

The need to explore the properties of samples in the nanoscopic scale has become increasingly important over the past decades due to the tremendous boom of nanotechnology and has fostered the development of different microscopy techniques (Girard and Dereux, 1996; Novotny and Hecht, 2006; Sandoghdar, 2001).

For such small features, conventional optical microscopy fails to be applied as the ultimate attainable spatial resolution is dictated by the insurmountable diffraction limit, which, as explained more extensively later in this chapter, amounts to approximately half the wavelength of the light source used (corresponding to about 200-300 nm for visible radiation) (Dunn, 1999). Non-optical microscopic methods have proliferated to meet the growing demand for high resolution. Scanning electron microscopes (SEM), transmission electron microscopes (TEM) and scanning probe techniques (in which a sharp probe is scanned over the region of interest of a sample and probe-sample distance is controlled using a short-range interaction between the probe and the sample, like tunnelling current in scanning tunnelling microscopy, STM, or van der Waals force in atomic force microscopy, AFM) have allowed the achievement of strong gain in spatial resolution going easily beyond 10 nm and even to the level of single atoms (Dunn, 1999; Hecht et al., 2000; Sangoghdar, 2001). However, such a dramatic improvement in resolution has come at the expense of the optical contrast mechanisms and several other advantages of conventional optical microscopy (Dunn, 1999; Hecht et al., 2000). In fact, optical microscopy is a universal technique that can be used for a wide variety of samples from material to life science and is characterized by lower invasiveness (allowing the sample to be observed in its native environment), ease of operation and relatively low cost (as it

requires no or little sample preparation compared for example to SEM, for which samples need to be vacuum-compatible and, in most of the cases, conductive, imposing restrictions especially in biological applications where samples often need to be studied in their native environment) (Dunn, 1999). Moreover, it offers various contrast mechanisms like polarization, absorption or fluorescence and excels in real time observations (Dunn, 1999). On the contrary, while AFM offers strong insight into sample morphology, it provides little information on chemical properties (Dunn, 1999). Therefore, while non-optical techniques have provided precious information about the topography of samples, *in vitro* and real time dynamic observations have often been hampered by complicated sample manipulation (Dunn, 1999).

In addition to the main parameters interesting for nanostructure analysis such as shape and size, also chemical composition, molecular structure as well as dynamic properties are of utmost importance: this imposes the need for microscopes with high spatial resolution together with high spectral and temporal resolving power (Hecht et al., 2000). By exploiting the evanescent waves (inhomogeneous non-propagating fields) and their interaction with matter, scanning near-field optical microscopy (SNOM) allows the attainment of spatial resolution beyond the classical diffraction limit (Dunn, 1999; Hecht et al., 2000; Novotny and Hecht, 2006; Novotny, 2007). This technique combines the potential advantages of scanning probe technology and optical microscopy and merges the outstanding spectroscopic and temporal selectivity of classical optical microscopy with a sub-100nm lateral resolution (Hecht et al., 2000). High resolution is reached via the detection of non-propagating evanescent waves in the near-field zone, in order to obtain the high spatial frequency information of the object (Novotny and Hecht, 2006). In the rest of the chapter, the basic principles of SNOM are illustrated.

1.2. From classical optical microscopy to SNOM

The lateral resolution of an optical microscope is defined as the shortest distance between two points in an image of a specimen that can still be distinguished as separate entities: as illustrated in Fig. 1.1, two point sources in the object plane generate a combined image pattern in the image plane and they are optically resolved if their distance Δr is such that they can still be discerned (Novotny and Hecht, 2006).

The light from each point can be described with a point-spread function, which defines the spread of a single point source (Novotny and Hecht, 2006). The distance Δr in the object plane is mapped onto a distance $M\Delta r$ in the image plane, where M is the magnification of the optical system: in Abbe's definition of resolution, the minimum distance $M\Delta r$ for two point sources to be resolved is such that the minimum of one point-spread function coincides with the first maximum of the second

point-spread function (Novotny and Hecht, 2006). The point-spread function f of a dipole oriented orthogonally to the optical axis is given by an Airy pattern of the form:

$$f \propto \left[\frac{2J_1(\rho)}{\rho} \right]^2 \tag{1.1}$$

where J_1 is the first order Bessel function of the first kind and $\rho = \frac{k_0 rn}{M} \sin\alpha$, with $r = \sqrt{x^2 + y^2}$ (supposing that the optical axis lies along z), α the angle of observation (semiangle of the light acceptance cone of the system), n the index of refraction of the medium between the object plane and the imaging system, k_0 the wavenumber in free space ($k_0 = \frac{2\pi}{\lambda}$ with λ being the wavelength) (Novotny and Hecht, 2006). We remind that the numerical aperture NA of the system is defined as $NA = n\sin\alpha$. Therefore, the minimum distance Δr for two points to be resolved in the image plane can be calculated by imposing $\rho \cong 3.832$, yielding:

$$\Delta r \cong \frac{3.832}{2\pi} \frac{\lambda}{NA} \cong 0.61 \frac{\lambda}{NA} \tag{1.2}$$

Such limit, valid for incoherently illuminated or incoherently radiating objects, coincides with the Rayleigh criterion of resolution (Zhu, 2005).

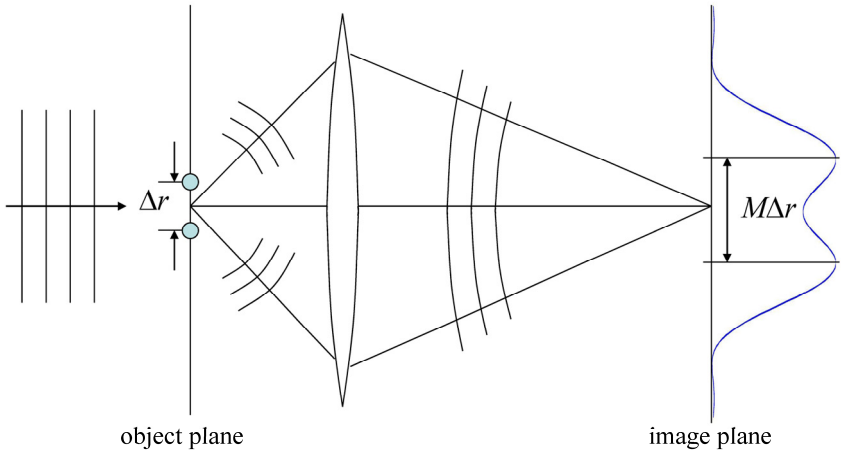

Fig. 1.1 – Schematic of an imaging system (adapted from Novotny and Hecht, 2006)

Other alternative definitions of lateral resolution can be provided: on the grounds of Sparrow's definition, the ultimate resolution limit is reached when the dip in the combined point-spread function from the two objects disappears, i.e. it has a zero second order derivative in the center. If

$f(r)$ is the point-spread function of a point source located in r = 0, then the combined image $F(r)$ of two identical $f(r)$ located in r_0 and - r_0 is such that $F''(0) = 2f''(r_0)$ if $f(r)$ is symmetric. Therefore, the minimum distance Δr between two points must be twice as much as the distance of the first inflection point from the center of the image. In case of an Airy function, this condition is met for $\rho \cong 1.4877$. Hence, the minimum resolution is given by:

$$\Delta r \cong 0.47 \frac{\lambda}{NA} \qquad \textbf{(1.3)}$$

A graphical illustration of the criteria of resolution is reported in Fig. 1.2.

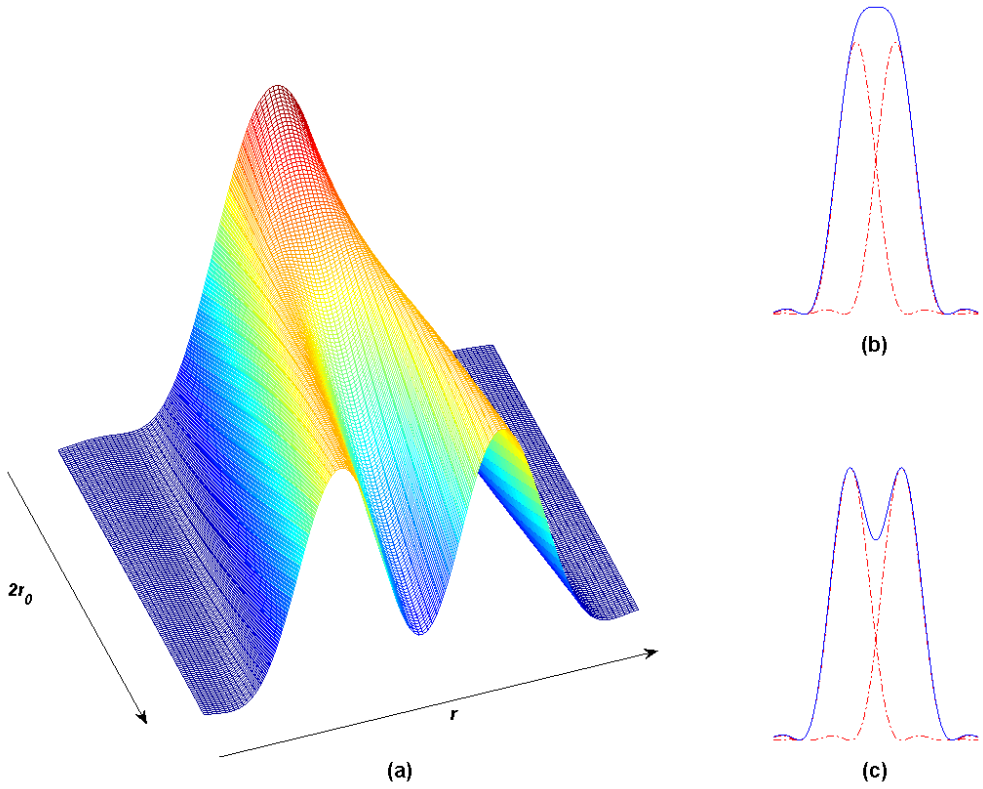

Fig. 1.2 – Resolution in conventional optical microscopy: (a) combined image *F(r)* of two identical *f(r)* located in r_0 and $-r_0$ as a function of increasing distance between the two point sources $2r_0$ (the arrow indicates the direction of increase in the distance); (b) Sparrow criterion of resolution; (c) Rayleigh criterion of resolution. In (b) and (c) the red lines indicate $f(r + r_0)$ and $f(r - r_0)$, while the blue line is the combined function *F(r)* (adapted from Sandoghdar, 2001).

More in general, the resolution can be approximated as (Pohl, 2004):

$$\Delta r \cong c_1 \frac{\lambda}{NA} \qquad \textbf{(1.4)}$$

with c_1 being a factor dependent on illumination and detection conditions. For example, if a ring-shaped illumination is used, then $c_1 = 0.36$; furthermore, in a confocal set-up using identical components for excitation and detection, the point-spread function is the square of the expression (1.1), resulting in $c_1 = \frac{0.61}{\sqrt{2}}$.

Independently of the specific formulation, even with modern objectives working in high index media such as water or oil, the numerical aperture can be as high as 1.3-1.4, thereby giving rise to a maximum resolution approximately equal to half the wavelength of the radiation used, which, for visible light applications, results in 250-300 nm (Dunn, 1999). The ultimate resolution limit of traditional microscopy can also be explained in the light of the Heisenberg uncertainty principle, according to which (Novotny and Hecht, 2006):

$$\Delta k_{\|} \cdot \left|\Delta r\right| \geq 1 \qquad \textbf{(1.5)}$$

where $k_{\|} = \sqrt{k_x^2 + k_y^2} = \sqrt{\left|\vec{k}\right|^2 - k_z^2}$ and $\left|\vec{k}\right| = \frac{2\pi n}{\lambda}$. It follows that the ultimate limit for resolution is:

$$\Delta r \geq \frac{\lambda}{2\pi n} \qquad \textbf{(1.6)}$$

The limit (1.6) overestimates the achievable resolution compared to (1.2)-(1.4) because it does not take into account the limits of a real imaging system.

More insight into the limitations of classical optical microscopy and a basic understanding of the principles of SNOM can be gained by adopting a Fourier optics approach or angular spectrum representation (Novotny and Hecht, 2006). A time-harmonic monochromatic electric field propagating in the half space $z \geq 0$ with all the sources located in $z < 0$ must satisfy the vector Helmotz equation:

$$\nabla^2 \vec{E}(x,y,z) + k^2 \vec{E}(x,y,z) = 0 \qquad \textbf{(1.7)}$$

where $\vec{E}(x,y,z) = (E_x, E_y, E_z)$ and $\vec{E}(x,y,z,t) = \mathrm{Re}\left\{\vec{E}(x,y,z)\, e^{-i\omega t}\right\}$. The two-dimensional Fourier representation of $\vec{E}(x,y,z)$ for $z = const > 0$ is:

$$\tilde{\vec{E}}(k_x, k_y; z) = \frac{1}{4\pi^2} \int\int_{-\infty}^{\infty} \vec{E}(x,y,z)\, e^{-i(k_x x + k_y y)}\, dxdy \qquad \textbf{(1.8)}$$

In its turn, the inverse Fourier transform can be written as:

$$\vec{E}(x,y,z) = \int\int_{-\infty}^{\infty} \tilde{\vec{E}}(k_x, k_y; z)\, e^{i(k_x x + k_y y)}\, dk_x dk_y \qquad \textbf{(1.9)}$$

Inserting (1.9) into (1.7), one gets that the Fourier spectrum $\vec{\hat{E}}$ evolves along $z > 0$ as:

$$\vec{\hat{E}}(k_x, k_y; z) = \vec{\hat{E}}(k_x, k_y; 0)\, e^{ik_z z} \qquad \textbf{(1.10)}$$

Replacing (1.10) in (1.9) one gets for $z \geq 0$:

$$\vec{E}(x, y, z) = \int\int_{-\infty}^{\infty} \vec{\hat{E}}(k_x, k_y; 0)\, e^{i(k_x x + k_y y + k_z z)} dk_x dk_y \qquad \textbf{(1.11)}$$

known as angular spectrum representation.

According to equation (1.11), supposing that $z = 0$ coincides with the sample plane, the Fourier components at the position of the detector $z = d$ can be calculated from the known Fourier components at the sample plane $z = 0$ by simply multiplying by the factor $e^{ik_z d}$; one can distinguish two cases (Hecht, 1996):

1. $k_{\|}^2 = k_x^2 + k_y^2 \leq k^2$ and hence real k_z; the relevant Fourier components are propagating homogeneous plane waves corresponding to features in the field distribution larger than $\frac{\lambda}{2\pi n} = \frac{1}{k}$; they will always reach the detector and contribute to the image and represent the far-field;

2. $k_{\|}^2 = k_x^2 + k_y^2 > k^2$ and hence imaginary k_z; the relevant Fourier components are exponentially decaying inhomogeneous nonpropagating evanescent waves corresponding to fine features in the field distribution smaller than $\frac{\lambda}{2\pi n} = \frac{1}{k}$; these represent the so-called near-field and if $d >> \frac{1}{k_z}$ they do not contribute to the formation of the image, which is the case for classical optical microscopy. Therefore, propagation in the *z* direction results in low pass filtering of the field.

Scanning near-field optical microscopy allows the attainment of high resolution by recovering the evanescent components. In order to retrieve these components one should use a probe located close to the sample such that $d << \frac{1}{k_z}$. More specifically, the necessary distance can be shown to be $d << \frac{\lambda}{2\pi\sqrt{2(\lambda\nu_{\|} - 1)}}$ with $\nu_{\|}^2 = \left(\frac{k_x}{2\pi}\right)^2 + \left(\frac{k_y}{2\pi}\right)^2$ for the signal to remain of considerable size: for example, spatial frequencies of the order $\nu_{\|} = \frac{100}{\lambda}$ decay at about $d \approx \frac{\lambda}{90}$ (Sandoghdar, 2001).

In brief, the key idea behind SNOM lies in preserving the spatial frequencies associated with evanescent waves that are lost during propagation from the source to the detector, thereby increasing the bandwidth of spatial frequencies (Novotny and Hecht, 2006). For the sake of simplicity, we can first illustrate the basic theory behind Synge's original idea for the microscope: in his proposal, the backside of an aperture in an opaque screen should be illuminated, thereby confining the light passing through the aperture to the dimensions of the hole (Fig. 1.3(a)); the light emerging from the aperture located in the near-field of the sample should be used to image the specimen (Dunn, 1999; Synge, 1928).

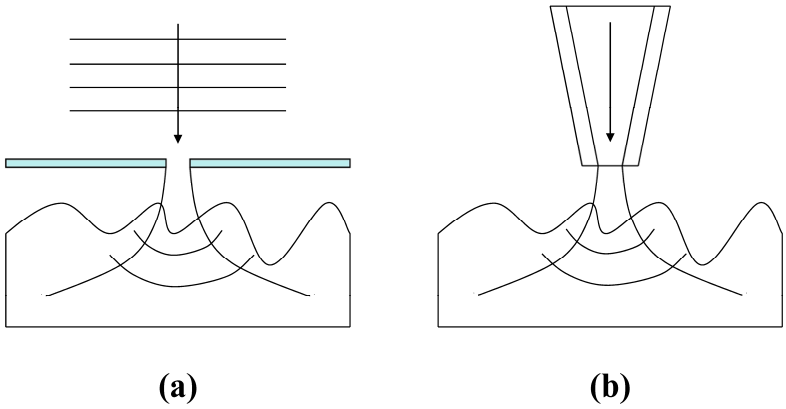

Fig. 1.3 – Schematic of an aperture probe: (a) sketch of the idea proposed by Synge; (b) practical implementation based on a metal-coated tapered fiber with an aperture left at the end.

As the aperture acts as a filter, in addition to the already observed filtering effect of wave propagation, the object is filtered also by the Fourier transform of the aperture. Therefore, additional constraints have to be imposed on the size of the probe: in fact, in order for the image to include the wished spatial frequencies, the width of the filter should be larger than $2k$, which means that the characteristic size s of the aperture should be less than $\frac{\lambda}{2}$. The smaller the aperture, the higher the spatial frequencies that can be detected (Sandoghdar, 2001). However, the smaller the aperture size (i.e., the stronger the field is laterally confined), the faster the field decays along z and hence the closer the aperture probe should be brought to the sample and the stronger the coupling between the probe and the sample is (Novotny et al., 1998). Such remarks can be easily inferred by the fact that the transverse wavenumber for an aperture of characteristic size s is given approximately by $j\frac{n\pi}{s}$ with j = 1,2,3…; a certain j field mode is evanescent if $s << j\frac{n\lambda}{2}$; in particular if $s << \frac{n\lambda}{2}$, all the field modes are evanescent (Novotny et al., 1998).

1.3. Aperture SNOM probes

A more accurate description of the field distribution close to an aperture is given by the theory of diffraction by a small hole, namely by the Bethe-Bouwkamp theory that treats the passage of light through a subwavelength diameter hole in an infinitely thin perfectly conductive screen (Bethe, 1944; Bouwkamp, 1950; 1954; Dunn, 1999). Such model replaces conventional diffraction methods focusing on diffraction through holes of radius a large compared to the wavelength of radiation ($a >> \lambda$) and failing to accurately satisfy the boundary conditions at the aperture (i.e. no tangential component of the electric field on the screen) (Dunn, 1999). This work confirms the feasibility of Synge's idea and provides a portray of the radiation emerging from a near-field probe, although calculations assume perfect conductivity and disregard the finite thickness of the screen (Dunn, 1999).

The most remarkable features of the field distributions computed according to this model are the existence of substantial z-components in the electric field (with significant field enhancement near the edges of the hole in the screen) as well as the rapidly changing character of the intensity profile as a function of the distance from the aperture (Dunn, 1999). Furthermore, the theory highlights a fundamental limit of aperture probes, i.e. the need of a trade-off between resolution and throughput. In fact, the transmission coefficient through the aperture is proportional to $(a/\lambda)^4$ (Bouwkamp, 1954). As a consequence, a decrease in the size of the aperture entails a slump in the light passing through the aperture in spite of better confinement.

Although Synge laid down the foundation for aperture SNOM probes and even proposed a way to precisely scan the aperture close to the surface using piezo-electric actuators, the first practical implementation dates back to Ash and Nicholls (1972) who used 3 cm microwave radiation, aperture size of 1.5 mm and aperture-sample distance of 0.5 mm (Ash and Nicholls, 1972; Dunn, 1999; Novotny, 2007; Synge, 1932).

Scaling the idea down to visible wavelengths allows of course the attainment of better resolution, but imposes stronger technological difficulties to be overcome, which postponed the actual realization in this spectral regime by two decades (Lewis et al., 1984; Pohl et al., 1984). Moreover, in order to scan samples while avoiding the risk of contact, the aperture must lie at the end of a tapered probe (Novotny and Hecht, 2006). This can be done for example by polishing a quartz rod to a sharp tip, subsequently evaporating a thin metal layer on it and finally creating an aperture by pressing the tip against a flat surface.

Metal-coated tapered dielectric probes (typically fiber probes) with an aperture left at the end are still today the most commonly employed SNOM probe structure (Fig. 1.3(b)). Such probes can be

viewed as a tapered hollow metal waveguide filled with a dielectric, in which the mode structure changes as a function of the characteristic dimension of the dielectric core (Novotny and Hafner 1994; Novotny and Hecht, 2006). Guided modes run into cut-off one after the other with decreasing diameter, until, at a well-defined diameter, even the last guided mode, the fundamental HE_{11} mode, runs into cut-off; for smaller diameters of the dielectric core, the energy in the core decays exponentially because of the purely imaginary propagation constant of all the modes; a rough estimate of the power transmission through aperture probes can be done by using a mode matching analysis and subdividing the tapered part of the probe into small cylindrical waveguide slices as carried out by Novotny and Hecht (2006). According to this analysis (valid as long as the cone semi-angle δ of the taper is not too large, i.e., $10° < \delta < 50°$), the power loss in the n^{th} waveguide section is:

$$P_{loss}(ndz) = P(ndz)(1 - e^{-2\alpha_{11}(ndz)dz}) \quad \textbf{(1.12)}$$

where $\alpha_{11}(ndz)$ is the attenuation constant of the fundamental HE_{11} mode in the n^{th} waveguide section, depending on the diameter of the waveguide section, on the wavelength and on the material properties (the propagation constant k_z of any mode in a lossy waveguide can be written as $k_z=\beta+i\alpha$) (Novotny and Hecht, 2006). Therefore:

$$P([n+1]dz) = P(ndz) - P_{loss}(ndz) \quad \textbf{(1.13)}$$

and, taking the limit $dz \to 0$, the power distribution in a section z computed starting from the power in z_0 becomes (Novotny and Hecht, 2006):

$$P(z) = P(z_0)e^{-2\int_{z_0}^{z}\alpha_{11}(z)dz} \quad \textbf{(1.14)}$$

Approximate expressions derived for α_{11} have shown that power transmission is higher for larger δ because the transmitted power can be formulated as:

$$\frac{P_{out}}{P_{in}} \propto e^{-B\cot(\delta)} \quad \textbf{(1.15)}$$

with B being a constant; increasing the taper angle from 10° to 45° increases the power throughput by nine orders of magnitude, the spot size remaining almost unaffected (Novotny and Hecht, 2006).

Differently from the case of an aperture in a perfectly conducting screen, resolution is affected not only by the aperture size but also by the finite conductivity of the real metal (in fact, at optical frequencies, the best metals have skin depths of 6-10 nm, which enlarges the effective aperture size) (Novotny and Hecht, 2006).

Another problem affecting real metal-coated dielectric probes is the partial dissipation of energy in the metal layer due to multiple back-reflections from the taper and metal absorption, resulting in significant heating of the metal coating and in its possible destruction. The heating effects have been analyzed both experimentally and theoretically as they can lead to thermal damage of the probe (which can reach temperatures of several hundred Celsius) and even to its destruction: variations in throughput and resolution occur as a result of aperture expansion and tip contraction and elongation; strong mechanical stresses arising from the different thermal expansion coefficients of the fiber and the metal coating can exceed the adhesion between the metal and the fiber causing partial detachment and even breakdown of the metal layer either by straightforward melting or by fracture and subsequent rolling up of the metal sheets due to internal stress; thermal expansion of the tip also makes it difficult to control the probe-sample distance; light leakage from cracks due to thermal fatigue can cause sample illumination from regions other than the aperture causing degradation of probe performance (Ambrosio et al., 2005; 2006; Biehler and La Rosa, 2002; Dickenson et al., 2007; Finot et al., 2004; Gucciardi et al., 1999; La Rosa et al., 1995; La Rosa and Hallen, 2002). Probe to sample heat transfer can also take place, which, even though useful if the probe is used in lithography and optical recording, can be detrimental for sensitive samples like fluorescent molecules (Erickson and Dunn, 2005; Gucciardi et al., 2005; Kazantsev et al., 1998; Latini et al., 2004; 2005; Stähelin et al., 1996). Although the use of additional adhesion layers or multilayer coatings and the choice of proper fabrication techniques can improve the thermal damage threshold (Stähelin et al., 1996), yet thermal effects pose limits to the maximum power that can be sent down such a probe, which means that a decrease in the probe throughput cannot be compensated by an increase in the injected power in order to avoid thermal damage (Novotny and Hecht, 2006).

In brief, the performance of aperture probes is influenced mainly by two factors: the taper cone angle and the size of the aperture. The tapered structure of the probe, in fact, imposes limits on the amount of light that can reach the aperture (Sandoghdar, 2001). The efficiency of guiding light to the aperture depends on the distribution of the propagating modes in the tapered waveguide; the mode structure in a metallic waveguide is related to the core diameter: when the fundamental HE_{11} mode runs into cut-off, it becomes an evanescent wave and its mode field decays exponentially; the amount of light reaching the probe aperture depends on the distance separating the aperture and the HE_{11} cut-off diameter (Hecht et al., 2000). The larger the opening angle of the tapered structure and the higher the refractive index of the dielectric core, the better the light transmission of the probe is, as the final cut-off diameter approaches the probe apex (Novotny and Hecht, 2006).

1.4. Hints about aperture SNOM probe fabrication

The fabrication of fiber-based aperture SNOM probes is articulated in two steps: (1) creation of a taper; (2) formation of a metal coating with the exception of an aperture left at the apex. The first task is usually performed using one of the following approaches:

1. *Heating and pulling method*: it consists in locally heating of the fiber using a CO_2 laser and subsequent pulling apart the two parts; the tip shape thus obtained depends on several process parameters (e.g. temperature and duration of the heating, size of the heated area, etc.); the main advantage of this technique is the smoothness of the achieved taper; the fundamental drawback is the difficulty to get large taper angles (Hecht et al., 2000).
2. *Chemical etching*: the so-called Turner technique consists in dipping the fiber into an HF solution covered with an overlayer of organic solvent; tip formation occurs at the meniscus created at the fiber at the interface between HF and the solvent; the main advantage is the high reproducibility in large quantities in just one step and the control on the taper angle by varying the organic solvent used as overlayer; the main disadvantage is the roughness of the glass surface, which can be avoided using the so-called tube etching method (Hecht et al., 2000). In the latter approach, the fiber is not stripped before being dipped into HF; hence, tip formation occurs inside the small volume defined by the polymer coating due to the convective flow of HF; the method is less amenable to roughness, while guaranteeing the possibility to produce large taper angles (Hecht et al., 2000). Selective chemical etching allows the fabrication of probes with much shorter tapers, as only the core is tapered, by exploiting the difference in etching rates between core and cladding; usually in this case a two-step etching procedure is used in which first the cladding diameter is reduced to avoid collision with the sample surface and then the fiber end is sharpened to create the taper (Pangaribuan et al., 1994).

It is noteworthy that, in general, tapers created by heating and pulling and etching are not completely identical (Novotny and Hecht, 2006). In fact, for pulled tips the refractive index profile in the taper is changed because both the fiber core and the cladding are affected (tapered core structure), while for etched tips the fiber core is unaffected as long as the diameter of the taper is larger than the core diameter (tapered cladding structure) (Barnard and Lit, 1993: Novotny and Hecht, 2006). In pulled fibers, differently from etched fibers, time-dependent polarization behaviour is observed; moreover the thinning of the core can lead to unfavourable mode distortions during propagation of light towards the tip apex (Novotny and Hecht, 2006). For pulled fibers, the initial effect of the taper is a spreading of the guided mode due to the thinning of the core: when the mode starts to perceive the metal coating, the waveguide turns its character from a dielectric to a metallic hollow one filled with a dielectric (Hecht et al., 2000). In the case of a taper produced by etching,

there is no mode spreading effect because the core diameter is not affected by the chemical etching and, consequently, the influence of the metal coating starts to be important for smaller waveguide diameters closer to the aperture (Hecht et al., 2000). Tapers created by etching perform better than those created by heating and pulling with respect to thermal damage (Dickenson et al., 2007), especially those created by selective etching (Ambrosio et al., 2006). SEM inspection of fiber tips reveals that pulled tips tend to exhibit a flat plateau at the apex (whose diameter depends on the pulling parameters) and probably due to brittle rupture when the diameter of the glass filament becomes very small (Novotny and Hecht, 2006).

As said, the second step of fabrication consists in metallization. For example, coating of dielectric tips with aluminium (one of the most commonly used metal coatings) can be carried out by thermal evaporation, electron-beam assisted evaporation or sputtering: thermal and e-beam evaporation are directional processes and allow certain areas to be excluded from being coated by exploiting shadowing effects; on the contrary, sputtering is an isotropic process (Novotny and Hecht, 2006). Apertures at the apex of fiber tips can be formed by exploiting the shadowing effects of the first two methods: the tips are oriented at a certain angle, to avoid exposure of the very end of the tip to the metal; tips are rotated during deposition to get a uniform coating; the deposition rate of metal at the tip apex is much smaller than on the sides, with the consequent self-aligned formation of an aperture at the apex (Hecht et al., 2000; Novotny and Hecht, 2006). However, evaporation and sputtering suffer from the possible formation of rather large grains with a typical size of about 100 nm, an unfavourable phenomenon because of the potential light leakage at grain boundaries and related imperfections (interfering with the weak wanted emission at the apex) and of the creation of not well-defined apertures (since the aperture size is usually smaller than the average grain size); moreover, grains prevent the actual optical aperture from approaching close to the sample because of protruding particles, limiting contrast, intensity and resolution; aluminium coatings produced by e-beam evaporation are often smoother than those created by thermal evaporation (Novotny and Hecht, 2006). Moreover, novel coatings like Al-Yb alloys can be used to reduce grain formation (Liang and Grütter, 2002). The smoothness of gold-coated probes can be improved by mercury treatment (Aiyer et al., 2001).

As an alternative to aperture punching (used by the pioneers of SNOM probes) and to the exploitation of shadowing effects, another method can be used for the creation of an aperture, relying on focused ion beam milling (FIB): the conventional aluminium coated probes are cut by slicing them perpendicularly to the fiber axis (Novotny and Hecht, 2006; Veerman et al., 1998). FIB milling can be used either to smooth an existing aperture by removing protruding grains or to open a closed tip to any desired aperture radius; FIB treated probes show superior performance because no grains prevent approach of the probe very close to the sample (Novotny and Hecht, 2006).

Chalcogenide glasses, fluoride glasses, zinc selenide or silver halide can be used as supporting tapered structures instead of optical fibers according to the spectral range of interest (Unger et al., 1998). Moreover, microfabrication techniques have been employed to create aperture metal-coated silicon dioxide probes integrated on silicon AFM cantilevers (Heinzelmann et al., 1999; Mitsuoka et al., 2000) or aperture metal-coated hybrid silicon nitride probes (Noell et al., 1997) obtained by gluing a microfabricated probe on top of an optical fiber. Microfabrication techniques have been used for the fabrication of aperture probes not only with conical shape but also with pyramidal profile, which can be either cantilevered probes or hybrid probes based, for example, on silicon dioxide, silicon nitride, photoplastic materials and sometimes with a hollow structure (Biagioni et al., 2005; 2005a; Celebrano et al., 2009; Genolet et al., 2001; Jin and Xu, 2006; 2008; Kim et al., 2000; Minh et al., 2001; 2001a; Oesterschulze et al., 1998).

Further details about probe structures and technological processes will be given in Chapter 6. In the following paragraphs the basic criteria of classification of SNOM are reported.

1.5. SNOM scanning control modes

There exist basically three different mechanisms to scan a near-field probe over the sample (Greffet and Carminati, 1997; Novotny and Hecht, 2006):

1. *Constant height mode* (Fig. 1.4(a)): it consists in keeping the probe at a fixed height above the mean plane of the sample; this approach can be applied only to samples with small topographic variations in order to avoid crashing the probe against the specimen. The tip is moved in the plane $z = z_0$ and optical signal $S(\vec{r}_{\parallel}, z_0)$ is recorded, with $\vec{r}_{\parallel} = (x, y)$.

2. *Constant intensity mode* (Fig. 1.4(b)): the optical signal S is kept constant with a feedback system, forcing the tip to follow a surface $z = h(\vec{r}_{\parallel})$, which, in general, does not reproduce the topography of the sample; the image is formed by recording the motion of the tip z.

3. *Constant distance mode* (Fig. 1.4(c)): the probe is kept at constant distance from the sample. The tip is forced to follow a surface $z = f(\vec{r}_{\parallel})$ by an auxiliary non-optical distance control mechanism. The optical signal that is recorded is $S[\vec{r}_{\parallel}, f(\vec{r}_{\parallel})]$. Independently of the specific distance control mechanism, it is assumed that the tip follows the topography of the sample and $f(\vec{r}_{\parallel})$ is the convolution of the sample profile by a function that describes the probe geometry. Beside the methods employed in AFM and STM (Novotny and Hecht, 2006), the most remarkable development, especially for fiber probes, in probe-sample distance control using the same probe to record simultaneously optical and topographical signal has been the introduction

of the *shear-force detection* mechanism by two different American groups (Betzig and Finn 1992; Toledo-Crow et al., 1992). In this case, the probe vibrates parallel to the sample surface, typically at the resonance frequency of its mechanical support; amplitude, phase and/or frequency of the oscillation are influenced by the proximity of the sample; the range of interaction of shear force goes from 1 to 100 nm, depending on the type of the probe and on the specific practical implementation (Novotny and Hecht, 2006). In order to detect the probe oscillation, the use of piezoelectric devices attached to the fiber itself has prevailed against optical detection methods that could interfere with the detection of the weak near-field signal: among them, the piezoelectric tuning fork has received the greatest attention (Karrai and Grober, 1995; Novotny and Hecht, 2006). The probe is glued on one of the prongs of a commercially available tuning fork, which is oscillated at a resonance frequency of typically 32.768 kHz (Fig. 1.5). During the final approach, due to the action of shear forces, the resonance frequency is detuned with respect to the driving oscillator, with a decrease in amplitude and a phase shift; although the origin of such forces is still not entirely understood, several possible interaction mechanisms have been proposed as an explanation, e.g. capillary forces, viscous damping in thin water films, van der Waals forces, electrostatic image forces and actual intermittent contact between fiber and sample (Gregor et al., 1996; Hecht et al., 2000, Toledo-Crow et al., 1992). Different variants of the shear-force detection employing a tuning fork have been used, including glue-free systems based on pure mechanical contact between the fiber probe and the tuning fork, in order to circumvent the tedious gluing procedure and the inconvenience inherent in the use of the glue (time required for gluing, degradation of the quality factor of the resonance due to migration of the glue along the arms of the tuning fork, difficulty to readjust a poorly glued fiber) (Morville et al., 2005; Mühlschlegel et al., 2006; Salvi et al., 1998).

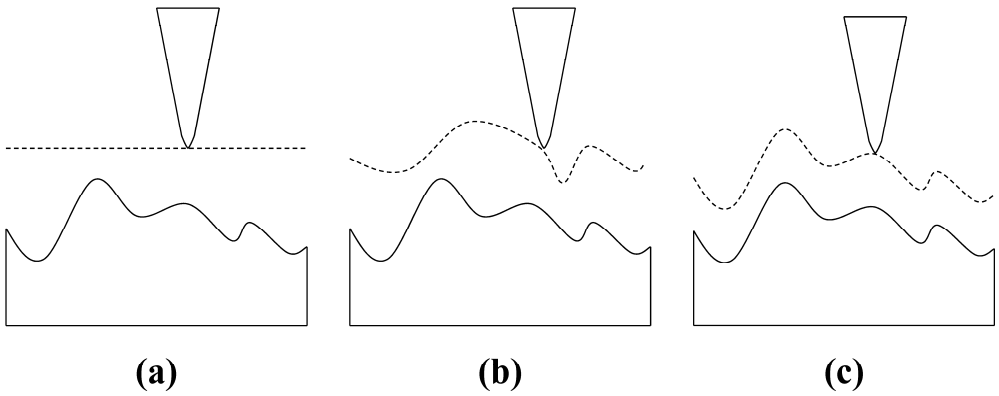

Fig. 1.4 – SNOM scanning control modes: (a) constant height mode; (b) constant intensity mode; (c) constant distance mode.

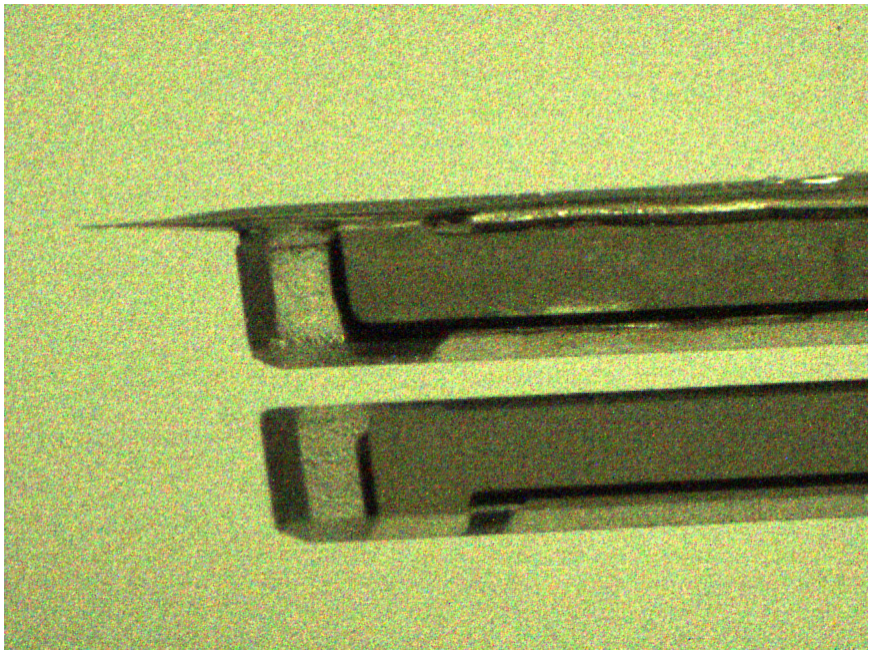

Fig. 1.5 – Photograph of a fiber SNOM probe glued on one of the two prongs of a quartz tuning fork with resonance frequency equal to 2^{15} Hz = 32768 Hz.

The most widespread scanning control mode is the constant distance mode as it allows a very close approach to the sample, although more prone to artifacts (i.e. a wrong interpretation of the image) originated by the coupling between the *z*-motion of the probe induced by a non-optical distance regulation mechanism and the purely optical information of the image (Greffet and Carminati, 1997; Hecht et al., 1997). Although the other two control modes have been demonstrated to be theoretically equivalent and more likely to produce images with purely optical contrast, they have found less favour among experimentalists as they are more susceptible to probe crashing: in fact, in constant height mode, a precise knowledge of the mean plane of the sample structure is essential to avoid crashing, whereas, in constant intensity mode, complex scattering from the surface topography results in an intensity distribution that, in general, does not decrease monotonically away from the surface (Carminati and Greffet, 1996; Greffet and Carminati, 1997; Hecht et al., 1997; Sandoghdar, 2001).

1.6. SNOM operating modes

SNOM instruments can also be classified on the grounds of the method employed to excite the sample and to collect the signal coming from the sample. Using this criterion, we can describe three main different configurations (Bouhelier et al., 2005; Bouhelier, 2006; Cefalì et al., 2008; Hartschuh, 2008; Hecht, 1996; Hecht et al., 1998; Novotny and Hecht, 2006; Novotny, 2007; Rasmussen and Deckert, 2005):

1. *transmission mode*;
2. *reflection mode*;
3. *scattering type*.

1.6.1. Transmission mode

It can be distinguished into two main subcategories:

- *Illumination mode* (Fig. 1.6(a)): it is based on the near-field excitation of the structure to be analyzed and on the far-field detection of the propagating waves resulting from an interaction between the near-field and the sample. In a typical set-up, the sample is mounted on a glass slide and is illuminated by laser light coupled into the fibre probe (Betzig and Trautmann, 1992). Light emitted by the probe locally interacts with the sample and, according to the sample and the contrast mechanism of interest, can be absorbed, phase-shifted, or locally excite fluorescence (Dunn, 1999; Hecht et al., 2000). Light emerging from the interaction zone is collected from beneath the transparent sample using a microscope objective with high *NA* or mirror systems and focused onto a photo-detector; polarization and spectral control can be added in both illumination and detection paths using, e.g., wave plates, polarizers and filters (Hecht et al., 2000). Collection, redistribution and filtering of light in the detection path can be carried out with an inverted microscope (on the top of which the SNOM head is built), that can also be suitably used to locate and study the sample before performing SNOM experiments (Dunn, 1999; Hecht et al., 2000). An alternative configuration, called forbidden light SNOM, allows recovering also light normally undergoing total internal reflection (above the critical angle θ_c corresponding to $k_{||} = k$) and thus failing to reach the detector; in order to discriminate forbidden light ($\theta > \theta_c$) from allowed light ($\theta < \theta_c$), special angularly resolved detection or combination of elliptical mirrors and lenses can be used (Hecht, 1996; Hecht et al., 1998; 2000; Heinzelmann et al., 1995).
- *Collection mode* (Fig. 1.6(b)): it is just the reverse situation of the previous mode, that is the sample is broadly irradiated with a far-field excitation and the near-field response at the sample surface is detected using a sub-wavelength optical probe (Betzig et al., 1987; Bouhelier et al., 2005; Novotny and Hecth, 2006). In an alternative configuration, named either scanning tunnelling optical microscope (STOM) or photon scanning tunnelling microscope (PSTM), the sample is illuminated with a sort of dark field illumination using an evanescent wave arising from a laser light beam totally internally reflected within a prism or a hemisphere that serves also as sample support: more specifically, the probe illuminates the sample through the substrate at a single well-defined angle $\theta > \theta_c$ (corresponding to $k_{||} > k$) such that total internal reflection

occurs at the probe side of the sample; the tip converts a portion of the local light intensity into a waveguide mode propagating to the photo-detector at its far end (Bouhelier et al., 2005; Courjon et al., 1989; Hecht, 1996; Novotny and Hecht, 2006; Reddick et al., 1990).

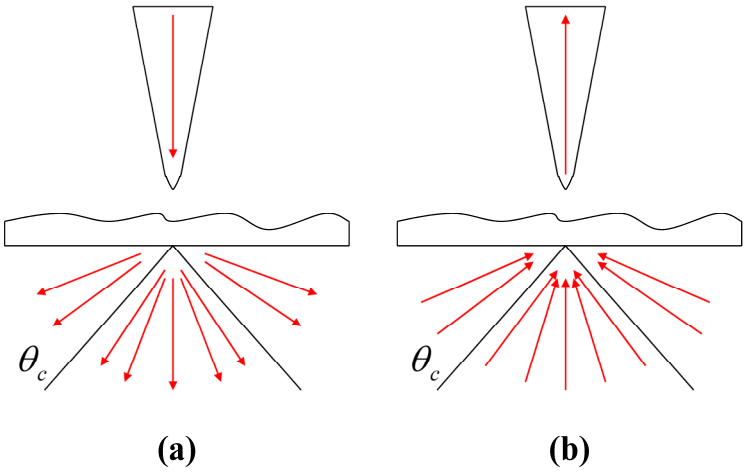

Fig. 1.6 – Transmission modes: (a) illumination mode; (b) collection mode (adapted from Hecht, 1996).

Image formation in transmission mode has been thoroughly investigated in several studies (Bozhevolnyi et al., 1999; Greffet and Carminati, 1997; Hecht et al., 1998; Méndez et al., 1997; van Lebeke and Barchiesi, 1992; van Lebeke et al., 1995): in particular, the equivalence between illumination and collection modes has been demonstrated.

1.6.2. Reflection mode

The interaction between the sample and the probe is measured in reflection. This configuration is particularly attractive because of several potential applications to non-transparent samples including data storage and studies on semiconductors (Novotny and Hecht, 2006). One can distinguish three different variants: *illumination mode reflection*, *collection mode reflection* and *illumination/collection mode* (Fig. 1.7). In the first approach, the incident illumination is sent down the probe and the reflected light is collected in the far-field (Cline and Isaacson, 1995), for example using an objective lens (Saiki et al., 1995) or an elliptical mirror coaxial with the fiber tip (Durkan and Shvets, 1998) or using multiple fibers to steer the signal onto the detectors (Guttroff et al., 1996). In the second case, an external light beam is focused on the sample and the reflected light is collected through the probe (Cline et al., 1991; Cline and Isaacson, 1995). In both the previous modes some specific features that distinguish reflection from transmission mode can be pointed out. Collection of the near-field light on the same side of the sample as the probe requires the use of a long working distance objective and some of the collection or illumination solid angle may be

obstructed by the probe and probe holder assembly; such problems represent major disadvantages compared to transmission mode together with the lower signal-to-noise ratio and the difficulty to decouple topography from true optical contrast (Cline and Isaacson, 1995; Weston and Buratto, 1997). Illumination/collection mode allows circumventing the need for additional far-field optics close to the probe and makes it easier to decouple topographic from optical signal (Weston and Buratto, 1997): in this case, near-field interactions are exploited for both excitation and detection because the light is both emitted and collected by the probe. A beam-splitter or a directional coupler or a dichroic mirror is typically used to separate incident from reflected light (Fukura et al., 2009; Grosjean et al., 2010; Pilevar et al., 1995; Sakai et al., 2006; Suzuki and Saiki, 2009).

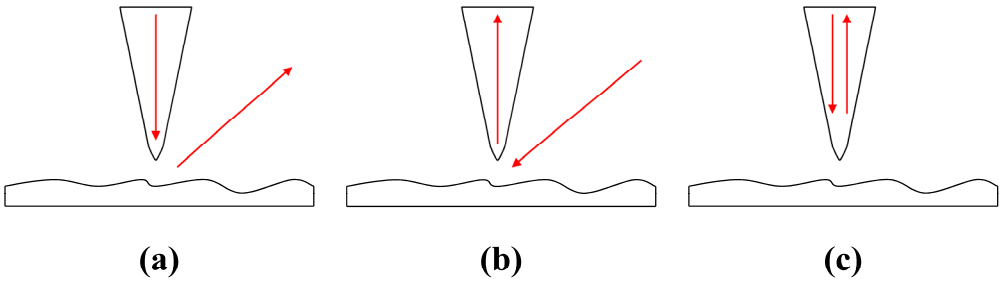

Fig. 1.7 – Reflection modes: (a) illumination mode reflection; (b) collection mode reflection; (c) illumination/collection mode.

1.6.3. Scattering type

This mode stems from an idea of Synge alternative to the aperture and consisting in the use of a small particle as a light source which, if brought close to the sample surface, scatters not only the incident field but also the field scattered from the surface, giving rise to an infinite number of scattering iterations between the sample and the particle: only one or few terms in this series are relevant depending on the properties of the particle and the sample and on the excitation conditions (Novotny, 2007).

One can distinguish two different cases: in the *weak scattering* or *local scattering* approach, the interaction between the exciting field and the sample is dominant over the interaction between the external field and the probe and hence the probe acts as a local perturbation; in the *strong scattering* or *local excitation* approach, the interaction between the probe and the exciting field is prevalent and the enhanced field generated by the probe can be considered as an independent light source exciting the sample at a short distance (Novotny and Stranick, 2006; Novotny, 2007). Therefore, the probe can perform two functions, scattering and/or enhancing a near-field signal, depending on tip material

and illumination conditions (Bouhelier and Bachelot, 2007; Novotny and Stranick, 2006). The probe structure used in both cases is typically a pointed probe, such as a metal or dielectric tip or a metal particle attached to a dielectric probe or a fully metal-coated dielectric probe (Ashino and Ohtsu, 1998; Deutsch et al., 2010; Eghlidi et al., 2009; Höppener and Novotny, 2008; Höppener et al., 2009; Inouye, 2001; Kalkbrenner et al., 2001; Keilmann, 2004; 2009; Novotny, 2007; Protasenko et al., 2004; Sqalli et al., 2000).

In weak scattering approach, such a pointed probe locally perturbs the field at the sample surface and the response to this perturbation is detected in the far-field at the same frequency of the incident light; as the field close to any laser-irradiated object is made up of both propagating and evanescent waves, the latter can be partially converted into propagating waves using a pointed probe as a local scatterer (Novotny and Stranick, 2006). In the strong scattering approach, the pointed probe is used as a local light source: the field near the apex of such probes, under proper polarization and excitation conditions and appropriate probe material and geometry, can become strongly enhanced over the field of the illuminating laser light, thus representing a nanoscopic light source (Novotny and Stranick, 2006). The field enhancement can be used to increase the response of spectroscopic interactions, such as fluorescence or Raman scattering, and for second harmonic generation (Bouhelier et al., 2003; 2004; Bouhelier, 2006; Bouhlier and Bachelot, 2007; Bouhelier and Novotny, 2007; Bulgarevich and Futamata, 2004; Hartschuh et al., 2003; 2004; 2006; Hartschuh, 2008; Novotny, 2007; Protasenko et al., 2004). The two different approaches are often referred to as scattering SNOM and tip enhanced near-field optical microscopy or field-enhanced SNOM, respectively (Bouhelier et al., 2003; 2004; 2005; Bouhelier, 2006; Bouhelier and Bachelot, 2007; Bouhelier and Novotny, 2007; Hartschuh et al., 2004; Hartschuh, 2008; Novotny and Stranick, 2006). Fig. 1.8 reports a comparison between schemes for illumination and detection for the case of weak scattering and for the one of strong scattering. In Fig. 1.8(a) a tip scatters the near-field of an object illuminated in the far-field from the bottom; the locally scattered field is detected with conventional far-field optics; the illumination from the bottom can be replaced by side illumination, with the choice between one illumination scheme and the other depending mostly on sample requirements (Bouhelier et al., 2005). In Fig. 1.8(b) under favourable illumination conditions field enhancement can be created at the tip that acts as a local light source and the increased sample response is usually collected with the same optics used for tip illumination (Bouhelier et al., 2005).

Field enhancement can originate from different effects, which can also occur in combination, depending on tip geometries, tip materials and experimental conditions: surface plasmon oscillations (i.e. collective oscillations of the conduction electrons), the electrostatic lightning rod effect (due to the geometric singularities of sharply pointed objects leading to highly localized surface-charge densities) and the antenna effect (if the tip length is an odd integer multiple of half of the

wavelength) (Bouhelier et al., 2005; Bouhelier, 2006; Bouhelier and Bachelot, 2007; Hartschuh et al., 2004; Hartschuh, 2008). Antenna and plasmon resonances have distinct wavelength-dependence, resulting in maximum field enhancement tunable in the visible spectrum; the lightning rod effect, depending on metal conductivity at different frequencies, typically increases in the infrared range (Hartschuh, 2008).

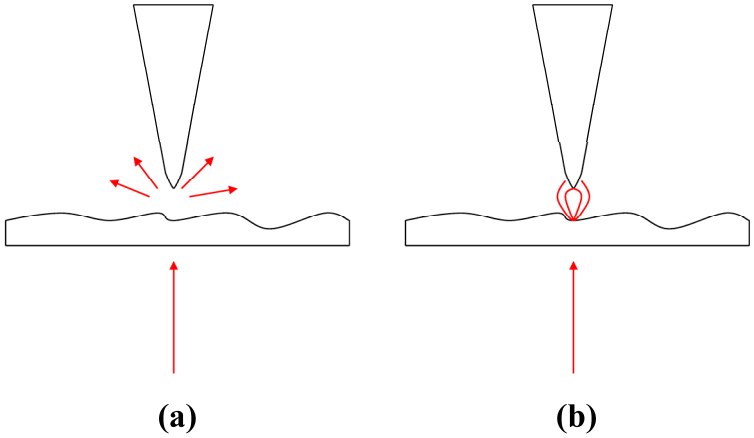

Fig. 1.8 – Scattering type SNOM: (a) weak scattering; (b) strong scattering (adapted from Bouhelier et al., 2005).

In a pointed metal probe, the incident light drives the free electrons in the metal along the polarization direction; the charge density inside a metal probe is zero ($\nabla \cdot \vec{E} = 0$); charges accumulate on the metal surface; for incident field polarization perpendicular to the tip axis, diametrically opposite points on the tip surface have opposite charges and therefore the tip apex remains uncharged; for incident polarization parallel to the tip axis, the induced surface charge is almost rotationally symmetric and has its maximum at the apex leading to field enhancement (Bouhelier and Bachelot, 2007; Bouhelier and Novotny, 2007; Hartschuh et al., 2004). From an experimental point of view different options can be adopted to provide the necessary polarization for field enhancement (Bouhelier, 2006; Bouhelier and Bachelot, 2007; Hartschuh, 2008). Fig. 1.9(a) reports the case of laser excitation illuminating the tip from the side; the polarization of light is oriented in such a way that a strong component of the electric field is along the probe axis; the advantage of side illumination is that it can be applied to opaque samples, but a main drawback is represented by a large excitation area, resulting in a strong background (Bouhelier, 2006). In Fig. 1.9(b) the probe is excited by an evanescent field created by total internal reflection inside a hemispherical lens or a prism, with a strong reduction in the scattered background: only *p* polarized light generates field enhancement at the probe apex; as a variant, one can use a high *NA* oil

immersion objective, which increases the electric field perpendicular to the interface (Bouhelier, 2006). In Fig. 1.9(c) tightly focused laser beams are used: for focal regions approaching the theoretical size limit imposed by diffraction, the electric field is made up of two transverse components and longitudinal components oriented along the direction of propagation, which do not propagate and exist only in the focal region; for a fundamental Gaussian beam, such longitudinal components are very weak (Bouhelier and Bachelot, 2007). However, diffraction-limited focal spots of higher order laser modes, like Hermite-Gaussian beams and radially polarized excitation, possess strong longitudinal field components that, if exactly aligned along the tip axis, can give rise to strong field enhancement (Bouhelier and Bachelot, 2007; Höppener and Novotny, 2008). As shown in Fig. 1.9(d), nontransparent samples can be investigated at high *NA* using parabolic mirror objectives, instead of glass objectives, and radially polarized excitation (Hartschuh, 2008).

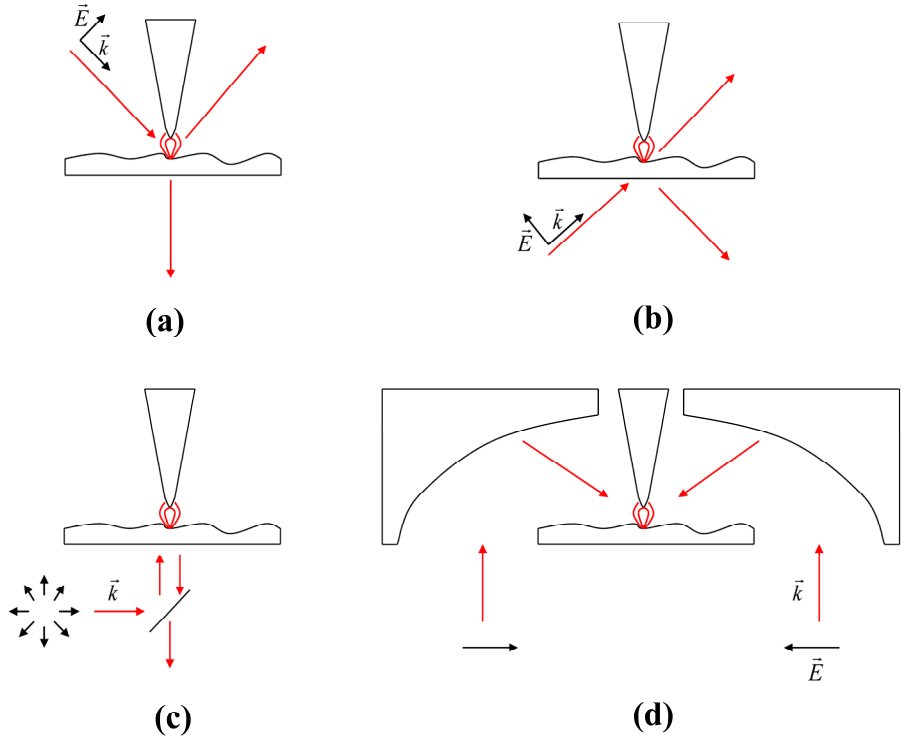

Fig. 1.9 – Strong scattering schemes: (a) side illumination with a strong polarization component aligned along the tip axis; (b) evanescent excitation through total internal excitation with *p* polarized light; (c) excitation by longitudinal fields created by radially polarized excitation; (d) scheme alternative to (c) for non-transparent samples using a parabolic mirror (adapted from Bouhelier, 2006; Bouhelier and Bachelot, 2007; Hartschuh, 2008).

Apart from polarization, field enhancement is also influenced by the material: a good electrical conductor like aluminium, tungsten, iridium, silver or gold is required for charges to move freely on

the structure from an electrostatic point of view, even if the presence of surface plasmon waves suggests that an electrodynamic description taking into account the wavelength dependence of the dielectric function $\varepsilon = \varepsilon' + i\varepsilon''$ and size effect (retardation) is necessary; according to such an analysis, aluminium, silver and gold are advisable in the visible range due to the low absorption loss ($\varepsilon'' << \varepsilon'$) (Bouhelier, 2006; Bouhelier and Bachelot, 2007). Shape effects like tip radius and shape (sphere, ellipsoid, prolate spheroid, etc.) and cone angle have shown to play a role in the enhancement as well as the excitation wavelength (Bouhelier, 2006; Bouhelier and Bachelot, 2007). The antenna effect is exploited in dielectric tips such as silicon probes or in those based on metal particles (Bouhelier, 2006; Eghlidi et al. 2009; Höppener and Novotny 2008; Höppener et al., 2009). Instead of pointed probes, single particles like individual gold nanoparticles bound to fibers can be used (Sqalli et al., 2000). Due to the common use of pointed probes devoid of aperture, scattering approaches are often globally indicated as apertureless SNOM (Novotny, 2007).

1.7. Final remarks

The basic features of SNOM microscopy have beeen discussed, from the fundamental principles to the actual implementations of probe-sample distance control and excitation/detection schemes. As emerged in the previous paragraphs, the most widespread SNOM probe configuration is the aperture probe, underlying the first idea set out by Synge, but whose performance is severely affected by serious limits on both throughput and resolution. In the next chapter the problem of optimization of probe structure, which represents the core of the thesis, will be discussed together with the approach adopted for the modelling of probe behaviour.

2. Modelling of SNOM probe behaviour

In this chapter, the basic ideas adopted for the optimization of the probe structure are outlined. As aperture probes are affected by fundamental limits on resolution and throughput, the structure chosen as starting point for the development of our novel probe designs is the fully metal-coated dielectric probe that, under properly polarized excitation, allows the attainment of strong field localization. Of course, modelling of probe behaviour is essential for the design of optimized probe structures but poses great challenges due to the need to model nanoscale phenomena. All these issues are discussed in the following paragraphs. At the end, the numerical approach adopted for probe modelling throughout the thesis is presented.

2.1. Optimization of SNOM probe structure: the fully metal-coated dielectric probe

In the previous chapter different experimental approaches used to study the near-field interaction between the probe and the sample have been discussed. Independently of the specific operating mode and set-up, the SNOM probe plays a key role in the performance of a near-field microscope and has been subject to lingering attempts of optimization.

Aperture probes have been at the heart of SNOM since its very beginning and still represent the most common probe structure. However, several attempts have been carried out to overcome their fundamental limitations, i.e. poor throughput and poor resolution, already pointed out in paragraph 1.3. Two main routes have been followed to improve their performance, i.e. optimization of the taper profile and of the aperture shape (Fig. 2.1).

As pointed out in the previous brief introduction on fabrication methods, chemical etching leads to an advantageous reduction of the overall taper length and a better control of the overall taper shape. Using selective chemical etching, which allows etching only the core of the fiber, probes based on multiple tapers like the double taper, the triple taper and the steeple-on-mesa taper profiles have been realized: the goal of these structures was to benefit from the advantages of large taper angles in signal throughput at least for part of the probe because the use of a single taper with a large taper angle would not be convenient during approach to the sample (Antosiewicz et al., 2008; Mononobe et al., 1998; Nakamura et al., 2001; Saiki et al., 1996; Saiki and Matsuda, 1999; Sakai et al., 2006; Yatsui et al., 1998). An asymmetrically edged probe with a sharp edge at the foot of the conical taper has shown to improve the transmission of HE_{11} mode with proper linearly polarized excitation along the direction of the asymmetry (Yatsui et al., 1997). Probes with nanometric

dielectric protrusions out of the aperture have been proposed to improve the resolution of aperture probes (Mononobe et al., 1997). Also the taper profile of probes produced by heating and pulling has been optimized: for this fabrication process the overall probe profile can be varied by controlling some process parameters; parabolic profiles have shown to give rise to higher throughput compared to conical profiles (Garcia-Parajo et al., 1995). Theoretical studies have been carried out to assess the influence of taper profile on probe performance to determine optimal shapes in terms of throughput: for example, structures based on the alternation of conical and cylindrical sections or analytical expressions for improved taper profiles have been proposed as well as corrugations at the interface between the dielectric core and the metal coating or on the external metal coating in both pyramidal and conical probe structures; in the latter two cases, the increase in the throughput is due to the exploitation of surface plasmon polaritons (SPPs) (Antosiewicz and Szoplik, 2007; Antosiewicz et al., 2011; Arslanov, 2006; Bakunov et al., 2004; Wang et al. 2008; Wang et al., 2010).

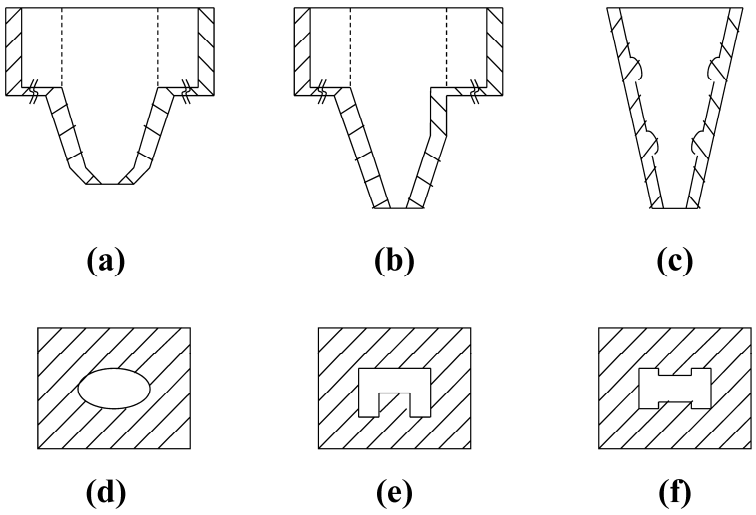

Fig. 2.1 – Examples of optimization of aperture probes by taper shape (upper row) or aperture shape (lower row) modification: (a) probe with double taper; (b) asymmetrically edged probe; (c) probe with corrugations at the interface between inner dielectric and metal coating; (d) elliptic aperture; (e) C-shaped aperture; (f) I-shaped aperture.

Another route followed for the improvement of the performance of aperture probes has been the implementation of aperture shapes different from the typical circular design: rectangular, square, slit, elliptical, C-shaped, I-shaped or dumbbell, H-shaped, bowtie, connected and separated double aperture, triangular, rod hole and tooth hole, gap apertures have been analysed and/or fabricated in fiber and cantilever based probes (Biagioni et al., 2005; Bortchagovsky et al., 2008; Butter and

Hecht, 2006; Colas des Francs et al., 2005; Danzebrink et al., 1999; Jin and Xu, 2004; 2005; 2006; 2008; Li et al., 2010; 2011; Matteo et al., 2004; Minh et al., 2001b; Mivelle et al., 2010; Oesterschulze et al., 1998; Tanaka and Tanaka, 2004). The improved throughput and field localization for some preferential input polarizations is due to the strong asymmetry of such aperture shapes and to the excitation of SPPs.

In order to increase signal throughput, a coaxial design has been investigated and realized on both fiber and cantilever probes: such probes consist of a conical dielectric segment sandwiched between a metallic coating and a metallic cone, which is suitable to transport electromagnetic radiation without exhibiting significant loss even if the structure is much smaller than the wavelength (Demming et al., 2001; Drews et al., 1999; Fischer et al., 1992; Minh et al., 2001; Wang et al., 2007). As an alternative, a bowtie structure based on a pyramidal hollow silicon dioxide probe with square cross section and cladded with metal on only two opposite sides has been proposed (Oesterschulze et al., 2001); other structures based on partial metal claddings in aperture fiber probes, like double-C shaped probes, have also been proposed (Cefalì et al., 2008; Patanè et al., 2008). Input polarization plays a role in these cases as well as for aperture probes based on polarization maintaining fibers (Adiga et al., 2006; Mitsui and Sekiguchi, 2004; Mitsui, 2005).

Despite the efforts in the optimization of the aperture probe to overcome its fundamental limits in throughput and resolution, the current design of aperture probes is not able to sustain routinely ultrahigh resolution imaging because of the limit of the skin depth of the metal coating that increases the effective aperture size, thus making the field distribution at the aperture significantly larger than its physical size (Bouhelier and Novotny, 2007). As observed in chapter 1, better throughput and resolution are expected if an apertureless metal or fully metal-coated probe is used, due to the combination of electrostatic lightning rod effect and surface plasmon excitation for proper illumination conditions. For example, due to the lightning rod effect, strong enhancement is expected at the tip apex, even though a real probe apex does not represent a real singularity (i.e. not defined first and second order derivatives) because of the finite conductivity of real metals and the finite tip radius (Bouhelier an Novotny, 2007). The fundamental problem with such probes is given by the strong background due to far-field illumination, which could be detrimental for some sensitive samples and can be reduced only partially by on-axis illumination (Hartschuh, 2008). In order to reduce such background some groups have envisaged different solutions like far-field excitation of SPPs at the wide end of a tapered metal nanowire by using grating geometry: such SPPs propagate towards the apex of the nanowire leading to nanofocusing, that is delivery and concentration/focusing of the optical energy at the nanoscale, which means a region much smaller than the dimensions allowed by the diffraction limits (Hartschuh, 2008; Stockman, 2004).

Nanofocusing in metal tapered nanorods has been theoretically studied starting from the analysis of the SPP modes of a plasmonic waveguide consisting of a metal nanowire whose axis coincides with the *z* axis and whose dielectric function $\varepsilon_m(\omega)$ is uniform in space with ω being the excitation angular frequency; the wire is surrounded by a dielectric with dielectric function ε_d (Stockman, 2004). By solving the Helmotz equation in cylindrical coordinates (r,φ,z) one gets the dispersion equation in a metallic cylinder (being the relative permeabilities of the metal and the dielectric equal to 1):

$$\left(\frac{n}{R}\right)^2\left(\frac{k_z}{k_0}\right)^2\left(\frac{1}{\kappa_d^2}-\frac{1}{\kappa_m^2}\right)^2=\left[\frac{1}{\kappa_d}\frac{K_n'(\kappa_d R)}{K_n(\kappa_d R)}-\frac{1}{\kappa_m}\frac{I_n'(\kappa_m R)}{I_n(\kappa_m R)}\right]\left[\frac{\varepsilon_d}{\kappa_d}\frac{K_n'(\kappa_d R)}{K_n(\kappa_d R)}-\frac{\varepsilon_m}{\kappa_m}\frac{I_n'(\kappa_m R)}{I_n(\kappa_m R)}\right] \quad \textbf{(2.1)}$$

where I_n and K_n are the modified Bessel functions of the first and second kind, $\kappa_d = k_0\sqrt{n_{eff}^2-\varepsilon_d}$ and $\kappa_m = k_0\sqrt{n_{eff}^2-\varepsilon_m}$, with $n_{eff}=\frac{k_z}{k_0}$ being the effective index of the mode of order *n*; R is the radius of the nanowire.

The three fundamental SPP modes supported by a metal nanowire are the transverse magnetic TM mode and two hybrid modes HE_1 and HE_2, corresponding to $n = 0$, $n = 1$, $n = 2$, respectively (Fig. 2.2).

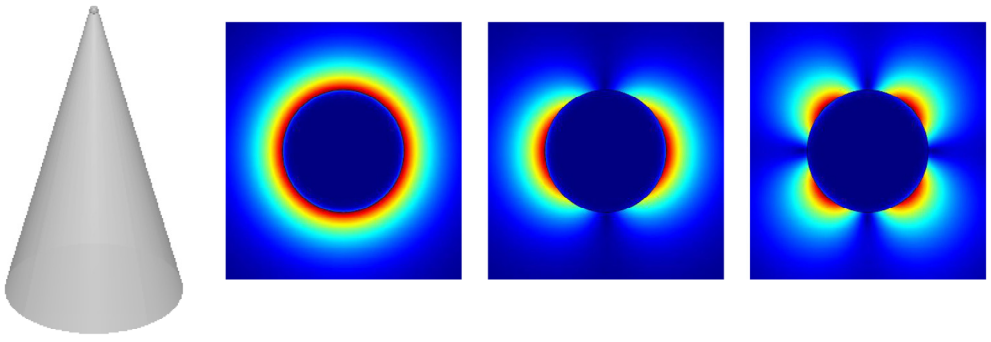

(a) **(b)** **(c)** **(d)**

Fig. 2.2 – Sketch of: (a) metal probe; normalized electric field distributions of (b) TM plasmon mode, (c) HE_1 plasmon mode, (d) HE_2 plasmon mode.

The TM SPP mode can exist for arbitrarily small diameters of the nanowire and, hence, has been shown to be suitable for nanofocusing. Such a mode is axially uniform and is characterized by a magnetic field having only the φ component; both electric and magnetic fields are independent of

φ (Stockman, 2004; Vogel and Gramotnev, 2008). Assuming that the radius $R(z)$ of the nanowire is a smooth function of *z* (which decreases from microscale to nanoscale for *z* going from large negative values to zero), the so-called eikonal or Wentzel-Kramers-Brillouin (WKB) or quasi-classical or geometric optics approximation can be applied to study the SPP modes and back reflections can be neglected (Stockman, 2004). In order to study their propagation in a tapered metal rod, one can use a staircase approximation and interpret the taper as a series of cylindrical nanowires with smoothly decreasing diameters, similarly to what is illustrated in chapter 1 for the analysis of a metal-coated aperture probe. The effective surface index $n_{eff}(R) = n_{eff}(R(z))$ for the TM mode of the plasmonic waveguide at a point *z* can be determined from:

$$\left[\frac{\varepsilon_d}{\kappa_d}\frac{K_1(\kappa_d R)}{K_0(\kappa_d R)} + \frac{\varepsilon_m}{\kappa_m}\frac{I_1(\kappa_m R)}{I_0(\kappa_m R)}\right] = 0 \qquad \textbf{(2.2)}$$

derived from (2.1) with $K_0^{'}(\kappa_d R) = -K_1(\kappa_d R)$ and $I_0^{'}(\kappa_m R) = I_1(\kappa_m R)$. Under the plasmonic condition $\mathrm{Re}\{\varepsilon_m\} < -\varepsilon_d$, one gets the solution for the SPP modes. For a thick wire ($k_0 R >> 1$), the solution is the same as for a flat surface:

$$n_{eff} = \sqrt{\frac{\varepsilon_m \varepsilon_d}{\varepsilon_m + \varepsilon_d}} \qquad \textbf{(2.3)}$$

For a thin, nano-scale radius wire ($k_0 R << 1$) one gets approximately with logarithmic precision (Stockman, 2004):

$$n_{eff}(R) \approx \frac{1}{k_0 R}\sqrt{-\frac{2\varepsilon_d}{\varepsilon_m}}\left[\ln\sqrt{-\frac{4\varepsilon_m}{\varepsilon_d}} - \gamma\right]^{-1} \qquad \textbf{(2.4)}$$

where $\gamma \approx 0.57721$ is the Euler constant. From the previous expression it can be inferred that at the tip ($k_0 R \to 0$), $n_{eff} \to \infty$; therefore, the wave number increases and the SPPs asymptotically stop as both the phase and group velocity tend to zero because they are both proportional to $k_0 R$ (Stockman, 2004). Besides, the study of the propagation of the SPPs through the tapered metal rod carried out with the staircase approximation has revealed an anomalous increase in the SPP field amplitudes, as SPPs approach the tip, because the electric field varies as $\propto R^{-\frac{3}{2}}$ (Babadyanian et al., 2000). As a consequence, the simultaneous wavelength decrease and amplitude increase lead to a concurrent energy localization and, hence, to nanofocusing. Several theoretical studies have shown such a phenomenon (Babadyanian et al., 2000; Kurihara et al., 2007; Ruppin, 2005; Vogel and Gramotnev, 2008), also investigating the effect of taper profiles different from the conical one, like paraboloidal, concave and convex shapes (Kurihara et al., 2009; Vogel and Gramotnev, 2010) and the influence of

dissipation (Vogel and Gramotnev, 2007) and of non-adiabatic conditions (Gramotnev et al., 2008; Issa and Guckenberger 2007). The TM SPP mode can be excited using an axially symmetric grating under radially polarized excitation (Baida and Belkhir, 2009; Maier et al., 2006) or double-sided E-symmetric excitation (Lee et al., 2011) or asymmetric excitation via grating coupling on just one side of the tip (Neacsu et al., 2007; 2010; Ropers et al., 2007; 2008; Sadiq et al., 2011).

An even more promising solution compared to metal probes in terms of simplification of the experimental set-up is the excitation of SPP modes on the metal coating of a fully metal-coated dielectric probe used under internal back excitation (Bouhelier and Novotny, 2007; Ding et al., 2007).

As for metal probes, the adiabatic approximation has been used to evaluate analytically the wave propagation in the fully metal-coated tapered dielectric probe, considering the cone as a succession of cylinders made up of a dielectric core of radius r_1 surrounded by a metal coating of thickness δ located in its turn in a dielectric medium (Janunts et al., 2005): in a first approximation, waveguide modes (WGM) have been calculated as those supported by a dielectric core surrounded by an infinitely thick metallic coating neglecting the external dielectric, while SPP modes have been calculated as those supported by a metallic wire surrounded by a dielectric neglecting the internal dielectric core. Dispersion relations for waveguide modes and for SPP modes have thus been determined (the latter coincides with the dispersion equation for the metal wire). At a certain value of r_1, the wavevector of the WGM can match the one of the SPP mode: in these conditions energy transfer from the WGM into the SPP mode is possible and, as a result, surface plasmons are excited bringing about nanofocusing. The transfer of energy and the field profiles can be determined with this approach using the coupled mode theory (Janunts et al., 2005; Nerkararyan et al., 2006). In this way, the SPPs can be excited using the WGM, thereby overcoming the problem of background inherent in the use of metal probes under external illumination.

The energy transfer from WGM to SPP modes has been thoroughly investigated in several studies, taking into account not only the "outer" SPP modes at the outer metal surface, but also the "inner" SPP modes at the inner metal surface; in some studies, non-conical taper profiles have been scrutinized as well (Abrahamyan and Nerkararyan, 2007; Babayan and Nerkararyan, 2007; Ding et al., 2007; Nerkararyan et al., 2008). The WGM has to present proper characteristics in order for the excited surface plasmons to exhibit axial symmetry, thereby interfering constructively at the tip apex and therefore generating nanofocusing. The three fundamental WGMs are a pair of orthogonal linearly polarized modes followed by a radially polarized one. If the fully metal-coated structure is excited by a linearly polarized HE_{11} mode, then the electric fields of the excited surface plasmons have opposite polarities on the opposite sides of the probe, giving rise to destructive interference at

the very end of the probe; on the contrary, a radially polarized WGM excites SPPs with axial symmetry, which interfere constructively at the tip apex. These mechanisms are responsible for the high field confinement in case of radially polarized excitation compared to the linearly polarized case. The eventual outcome of this process is the creation of an ultrasmall hot spot in the region close to the tip apex in the former situation, as opposed to broader and weaker two-lobed electric field intensity distributions for the latter one. In particular, the size of the achievable hot spot in case of radially polarized excitation (and, hence, the ultimate attainable resolution) is mostly limited by the diameter of the metal apex, which can be decreased at will. Such a behaviour has been confirmed in both theoretical and experimental studies (Bouhelier et al., 2003a; Bouhelier and Novotny, 2007; Chen and Zhan, 2007; 2007a; Descrovi et al., 2005; Ding et al. 2007; Liu and He, 2005; Tortora et al., 2007; Vaccaro et al., 2003) and is sketched in Fig. 2.3.

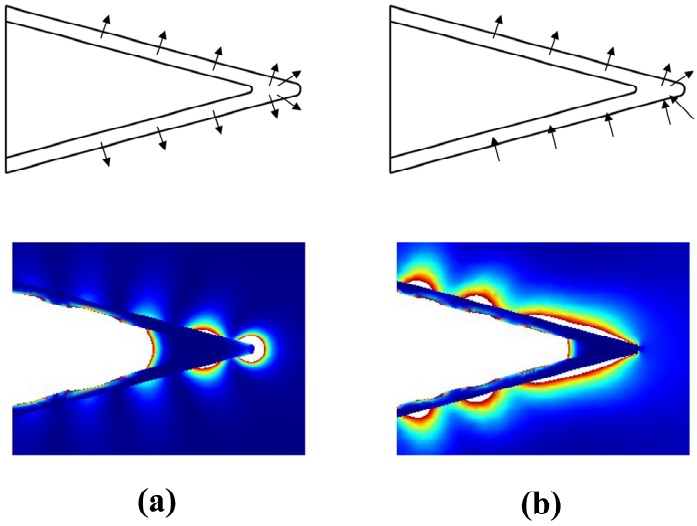

Fig. 2.3 – Sketch of the behaviour of a fully metal-coated dielectric probe under: (a) radially; (b) linearly polarized excitation. Arrows indicate the electric fields associated with the surface plasmons (adapted from Bouhelier et al., 2003a).

It is worth pointing out that, although more exotic probe concepts have been proposed like active probes based on single molecules, quantum dots and nanocrystals glued at the end of bare fiber tips or on metal-coated aperture tips (Chevalier et al., 2005; Drezet et al., 2011; Michaelis et al., 2000; Sandoghdar and Mlynek, 1999; Sandoghdar et al., 2001; Shubeita et al., 2003; Sonnefraud et al., 2006), such probes are still technologically demanding from both material and micro/nanomechanics side and suffer from shifts in resonance lines, which complicates image interpretation. Similar considerations hold for intriguing probes based on the attachment of individual carbon nanotubes and carbon nanotube bundles to silicon tips (Hillenbrand et al., 2003; Mu et al., 2008). On the

contrary, fully metal-coated dielectric probes can benefit from the well-known technologies used for aperture probes pointed out in chapter 1 and treated more in-depth in chapter 6.

Because of its attractive characteristics, the fully metal-coated dielectric probe has been chosen as the starting point for structural optimization in this thesis; as explained in more detail in the next chapter, the goal of the work will be the achievement of field localization (a feature of utmost importance for SNOM applications) under linearly polarized excitation, bringing about a further substantial simplification in experimental set-ups.

2.2. Analysis and optimization of probe structures: the need for numerical tools

The theoretical study of the behaviour of SNOM probes is essential not only to get insight into the characteristics of commonly used probe structures and identify potential problems in imaging, but also to detect possible routes for optimization and predict the implications of the use of novel probe configurations. With such an approach, experimental efforts can be devoted to those probes that theoretically exhibit the most promising features.

As seen in chapter 1, analytical solutions have been determined by Bethe and Bouwkamp for an aperture in an infinitely thin perfectly conducting screen, which laid down the foundation for further theoretical treatments. In the search for a model that could describe more faithfully the aperture probe behaviour, analytical studies that took into account the finite thickness of the metal screen have been carried out (Roberts, 1987; 1989). All of these treatments, however, suffer from neglecting the finite conductivity of the metal cladding used in real SNOM probes and provide little resemblance to the actual tip geometries used in experiments (Dunn, 1999). Ring-like rim charge density distributions have also been used to provide an analytical description of the near- and far-field distribution close to apertures (Antosiewicz and Szoplik, 2007a; Drezet et al., 2004; 2004a; Drezet, 2011). Far-field transmission patterns have been studied by extending Bethe's diffraction model to a conical geometry resembling more closely a real probe structure (Drezet et al., 2001; 2002).

Other semi-analytical approaches have been based on a staircase approximation (Fig. 2.4) in which the longitudinally non-uniform waveguide (the tapered part of the probe) is considered as a succession of cylindrical sections of decreasing radius and the eigenmodes of the uniform waveguides obtained by infinitely stretching along the axis of the probe at each cross section are computed, as illustrated earlier. An analytical evaluation of the power transmitted by an aperture probe based on such an approximation using a mode matching theory has been done, as shown in paragraph 1.3 (Novotny and Hecht, 2006). Starting also from this staircase approximation, different probe profiles like parabolic, exponential and mixed shapes based on the alternation of conical and

cylindrical sections along the taper have been examined using the cross-section method (Arslanov, 2006; Bakunov et al., 2004).

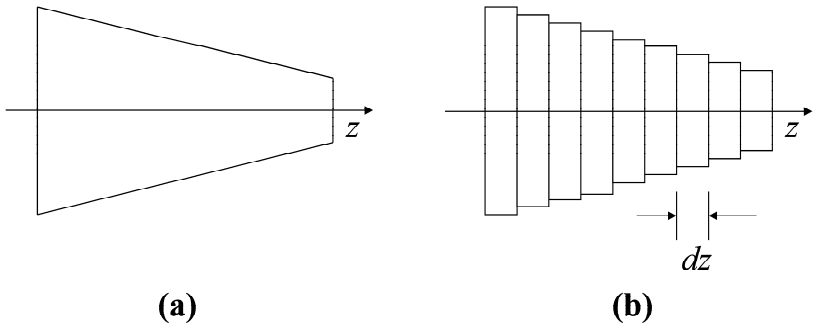

Fig. 2.4 – Staircase approximation: (a) original tapered structure; (b) approximation with cylinders of decreasing radius and thickness *dz* (adapted from Novotny and Hecht, 2006).

As discussed in paragraph 2.1, the staircase approximation has also been used for the analysis of nanofocusing in metal and fully metal-coated dielectric probes using local mode theory in a weakly non-uniform optical waveguide and the eikonal approximation (Babayan and Nerkararyan, 2007; Ding et al., 2007; Nerkararyan et al., 2008; Stockman, 2004; Vogel and Gramotnev, 2007; 2008; 2010).

Although analytical expressions are useful to get an understanding of the probe behaviour, their range of applicability is limited. For example, the eikonal approximation can be applied as long as the adiabatic criterion is satisfied, i.e. for small local taper angles (Babayan and Nerkararyan, 2007; Ding et al., 2007; Gramotnev et al., 2008; Stockman, 2004; Vogel and Gramotnev, 2007; 2008; 2010). In fact, referring to metal probes, such an approximation is valid as long as the eikonal or adiabatic parameter δ is small enough, that is to say if the following condition is satisfied (Stockman, 2004):

$$\delta = \left| R' \frac{d\left(k_0 n_{eff}\right)^{-1}}{dR} \right| << 1 \qquad \textbf{(2.5)}$$

where $R' = \frac{dR}{dz}$ is the wire grading. While this condition, farther away from the tip apex, is satisfied for even large taper angles, because the local rod diameter is larger than the plasmon wavelength, the critical point for adiabaticity is the very end of the tapered wire, for which small R' and, hence, small taper angles become essential (Vogel and Gramotnev, 2008).

On the other hand, the study of probes that do not satisfy this requirement can be of great interest: for example, optimal conditions for nanofocusing on tapered metal rods have been found in nonadiabatic conditions, which fail to be treated analytically (Issa and Guckenberger, 2007). Moreover, analytical methods turn out to be not adequate to model abrupt variations in the tapered profile as they often suppose a weak longitudinal non-uniformity.

Whenever more challenging probe geometries need to be studied, a numerical approach becomes mandatory. For this reason, the development of optimized probe structures has been accompanied and favoured by the flourishing of a vast range of numerical methods giving a glimpse at nanoscale mechanisms (Antosiewicz et al., 2008; Girard and Dereux, 1996; Girard, 2005; Ohtsu, 2005).

Such methods have been extensively used to investigate novel aperture shapes using for example the finite difference time domain method (FDTD) or the field susceptibility technique and in most of the cases considering apertures in thin metal films (Bortchagovsky et al., 2008; Colas des Francs et al., 2005; Jin and Xu, 2004; 2005; Li et al., 2010; 2011; Mivelle et al., 2010). Furthermore, the analysis of wave propagation in tapered structures (either traditional conical tapers or structures modified with corrugations or multiple tapers or partial metal coatings) with an aperture at the end has been carried out using the finite difference beam propagation method (Moar et al., 2006), the FDTD method (Antosiewicz and Szoplik, 2007; Antosiewicz et al., 2008; Christensen, 1995; Nakamura et al., 2001; Patanè et al., 2008; Wang et al., 2008; 2010), the body of revolution FDTD method (BOR-FDTD) (Liu and He, 2005), the finite integration technique (FIT) (Oesterschulze et al., 2001; Pack et al., 2002), the multiple multipole method (MMP) (Novotny et al., 1995). Also coaxial probes and tips with a metal particle attached to the aperture have been numerically investigated (Baida et al., 2003; Demming et al., 2001). Metal probes and fully metal-coated pyramidal probes with different shapes have also been analysed both in case of direct illumination at the metal apex or with far-field excitation farther away from the metal apex as described in paragraph 2.1 (Baida and Belkhir, 2009; Demming et al., 2005; Downes et al., 2006; Gramotnev et al., 2008; Issa and Guckenberger, 2007; Krug et al., 2002; Maier et al., 2006; Wang et al., 2003) using FDTD, BOR-FDTD, FIT, and the finite element method (FEM). The fully metal-coated dielectric structure, which, as anticipated, is the one of interest in this thesis, has been intensively numerically investigated especially under internal back excitation and its polarization-dependent properties have been carefully examined: the need for a radially polarized excitation has been pointed out as essential to get field localization (Bouhelier et al., 2003a; Chen and Zhan, 2007; 2007a; Descrovi et al., 2005; Ding et al., 2007; Kato et al., 2010; Liu and He, 2005; Tanaka et al., 2011; Tortora et al., 2007; Vaccaro et al., 2003).

Even numerical treatment is challenging because near-field probes involve different length scales: while phenomena of major interest for near-field interactions occur in the mesoscopic (sizes

of the order of the incident wavelength) and nanoscopic (structures smaller than 100 nm) regimes (Girard and Dereux, 1996), the overall probe structure, especially for fiber-based probes, can include sections much bigger than the incident wavelength. The computational cost for modelling a probe in its entirety would become prohibitive. Therefore, the overall computational domain is typically restricted to the very end of the probe, often using two-dimensional approximations or exploiting symmetry properties of the structure.

In the light of the previous considerations, we have investigated our novel probes based on appropriate modifications introduced in fully metal-coated dielectric probes adopting a numerical approach and restricting the analysis to the very end of the probe. An overview of the numerical approach adopted for our simulations is provided in paragraph 2.3. In paragraph 2.4, the developed computational model has been used to model the behaviour of the fully metal-coated probe, which represents the reference for comparison for the new probe configurations.

2.3. The finite element method

Among the different numerical methods used in the past to simulate fully metal-coated SNOM probes, ranging from MMP (Bouhelier et al., 2003a; Frey et al., 2006), to FIT (Ding et al., 2007; Nakagawa et al., 2006; 2007; Tortora et al., 2007; Vaccaro et al., 2003), or FDTD (Liu and He, 2005; Quong and Elezabi, 2007), we have preferred FEM, chosen also by Chen and Zhan (2007, 2007a). In fact, MMP and other boundary discretization techniques are efficient for simple, smooth geometries, while time domain methods such as FDTD and FIT are problematic because of the frequency dependence of metal properties and staircasing effects.

FEM is a tool used for the solution of differential equations in many disciplines, ranging from electromagnetics to solid and structural mechanics, from fluid dynamics to acoustics and thermal conduction (Bondeson et al., 2005). A point of strength of FEM is its ability to deal with a complex geometry. Unstructured grids can accommodate for complex geometries in a much more straightforward way than other methods using Cartesian grids like finite difference based methods like FDTD.

The irregular domain is discretized into smaller and regular subdomains, known as finite elements, thereby replacing a domain having an infinite number of degrees of freedom by a system with a finite number of degrees of freedom. The essential principle behind FEM is a piecewise approximation: the solution of a complex problem is obtained by splitting the region of interest into smaller regions and approximating the solution over each subregion by a simple function (Rao 1999).

The procedure consists of the following steps (Rao, 1999):

1. *Structure discretization*: the structure or solution region is divided into subdivisions or elements; the structure needs to be modelled with suitable finite elements. Elements are considered to be interconnected at specified joints called nodes or nodal points and their number, type, size and arrangement need to be properly chosen.
2. *Selection of proper interpolation model*: the field variable inside the finite element is approximated by a simple function. Such approximating functions, called interpolation models, are defined in terms of the values of the field variables at the nodes, which are the new unknowns. The assumed solution must be simple from the computational point of view, but it should also meet some convergence requirements. The solution or the interpolation model is usually a polynomial.
3. *Derivation of element characteristic matrices and vectors*.
4. *Assemblage of element equations to obtain the overall equations*.
5. *Solution for the unknown nodal field variables*.
6. *Computation of element resultants*.

The characteristic matrices and vectors of finite elements can be derived by using a weighted residual approach or a variational approach (Bondeson et al., 2005; Rao, 1999).

A simple description of the weighted residual approach can be stated in the following way (Bondeson et al., 2005). The differential equation to be solved with FEM can be written as:

$$L[f] = s \tag{2.6}$$

where L is an operator, s is the source and f the unknown function to be computed in the region Ω. First the solution domain Ω is subdivided into cells, or elements (for example triangles or quadrilaterals in two-dimensional problems or tertahedra, pyramids, prisms or cubes for three-dimensional problems). Then, the solution is approximated by an expansion in a finite number of basis functions:

$$f(r) \approx \sum_{i=1}^{n} f_i \varphi_i(r) \tag{2.7}$$

where f_i are unknown coefficients multiplying the basis functions $\varphi_i(r)$. The latter are usually low-order polynomials that are non-zero only in a few adjacent elements. Subsequently, the residual:

$$r = L[f] - s \tag{2.8}$$

is formed, which one wants to make as small as possible. Generally, the residual will not be zero pointwise, but it is required to be zero in a weak sense by setting its weighted average to zero. Then,

test or weighting functions w_i, $i = 1, 2, \ldots, n$ (as many as the unknown coefficients) are chosen for weighting the residual r. The Galerkin method is often adopted, according to which the weighting functions are the same as the basis functions ($w_i = \varphi_i$), but different solutions are possible as well, like $w_i = \varphi_i + cL[\varphi_i]$, where the parameter c is optimized (least squares stabilized Galerkin method). More in general, if the weighting functions w_i are different from the basis functions φ_i, one speaks of Petrov-Galerkin method. Finally, one sets the weighted residuals to zero and solves for the unknowns f_i, which means to solve the set of equations:

$$\langle w_i, r \rangle = \int_\Omega w_i r d\Omega = 0 \qquad \textbf{(2.9)}$$

By finite element one indicates an element (for example a triangle) together with a polynomial space defined in this element (e.g., the space of linear functions) and a set of degrees of freedom defined on this space (e.g., the values of the linear functions in the triangle nodes) (Bondeson et al., 2005).

According to the variational approach, the solution f of a self-adjoint ($\langle f, L[\delta f] \rangle = \langle L[f], \delta f \rangle$) linear differential equation is searched for as the stationary point of the quadratic form (Bondeson et al., 2005):

$$I[f] = \frac{1}{2}\langle f, L[f] \rangle - \langle f, s \rangle \qquad \textbf{(2.10)}$$

If δf is a small variation of f, then $I[f]$ is stationary if:

$$\delta I = 0, \forall \delta f \qquad \textbf{(2.11)}$$

The variational formulation leads to the Rayleigh-Ritz method: once f is expanded as in (2.7), one evaluates the quadratic variational form as a function of the expansion coefficients as:

$$I(f_1, f_2, ..., f_N) = I[f] = \frac{1}{2}\sum_i \sum_j L_{ij} f_i f_j - \sum_i s_i f_i \qquad \textbf{(2.12)}$$

where $L_{ij} = \langle \varphi_i, L[\varphi_j] \rangle$, $s_i = \langle \varphi_i, s \rangle$ and $L_{ij} = L_{ji}$ as the operator L is self-adjoint. Finally, the expansion coefficients f_i are determined by imposing I to be stationary with respect to all the coefficients, i.e.:

$$\frac{\partial I}{\partial f_k} = \frac{1}{2}\sum_j L_{kj} f_j + \frac{1}{2}\sum_i L_{ki} f_i - s_k = \sum_i L_{ki} f_i - s_k = 0 \qquad \textbf{(2.13)}$$

The Rayleigh-Ritz and the Galerkin methods are equivalent for self-adjoint differential equations, but the Galerkin method can be used to solve problems that cannot be stated in a variational formulation (Bondeson et al., 2005).

2.4. Computational model and numerical analysis of the behaviour of a fully metal-coated axisymmetric probe

Our three-dimensional (3D) computational model for the simulation of the electromagnetic modes in the investigated probe configurations has been developed with the help of a commercial software (Comsol Multiphysics) based on the finite element method. The computational process is articulated in two steps. First, a two-dimensional (2D) analysis is run to calculate the eigenmodes at the input port. Then, the first three eigenmodes, i.e., the two lowest order linearly polarized modes and the radially polarized mode, are propagated through the probe in a 3D simulation. Second order elements with minimum size of about 0.8 nm have been used. Simulations have been run on a 64 bit workstation with 32 GB of RAM.

The first examined structure is the fully metal-coated dielectric probe under radially and linearly polarized excitation. Although in this case one could benefit from the symmetry properties of the structure, the axisymmetric probe represents only the starting point for the search of optimized configurations, illustrated in the following chapters. As we will see, such structures are characterized by strong asymmetries, which impose the need for full 3D analysis. Therefore, for the sake of a better comparison, a 3D model has been adopted also for the reference axisymmetric structure, without resorting to any of the simplifications used in previous works to handle axially symmetric structures. As the simulations are extremely computationally intensive because of the different scales of the metal layer and the dielectrics, only the very end of the tip is examined. In previous works, simulations involving larger portions have been possible only when the structure was less computationally challenging and one could benefit from the rotational symmetry of the probe to reduce the problem complexity either with the BOR-FDTD method or even with approximate 2D simulations (Antosiewicz and Szoplik, 2007; Liu and He, 2005).

Fig. 2.5 reports the sketch of the simulated axisymmetric probe, consisting of a silica core (n=1.5) surrounded by an aluminium coating (n=0.645+5.029i at the operating wavelength λ=532 nm). The inner silica cone radius is 225 nm, while the metallic hollow cone outer radius is 275 nm. Both cones are rounded: the radius of curvature of the inner cone is 10 nm, the one of the outer cone is 20 nm. The apex angle for both of them is 30°. The overall modelling domain is a 1.6 μm cylinder with radius 1 μm. The probe axis is chosen to lie on the z axis.

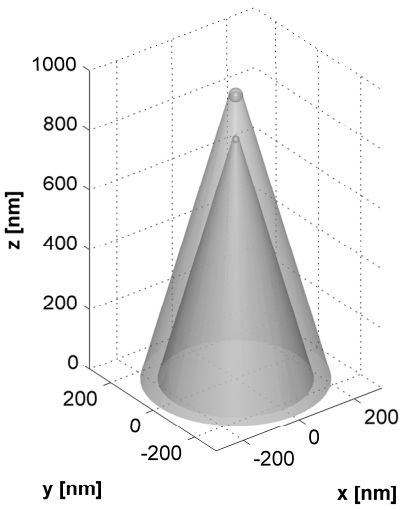

Fig. 2.5 – Sketch of the simulated axisymmetric fully metal-coated dielectric probe.

In Fig. 2.6, the first three eigenmodes, i.e. the two lowest order *x* and *y* linearly polarized modes (H and V) and the radially polarized one (R), are reported together with the corresponding near-field distributions obtained in a transverse plane located at 10 nm from the tip apex. The near-field plots, representing the square of the norm of the electric field, are taken over a 600 nm by 600 nm square area centred around the probe apex and are normalized to the maximum value of the electric field intensity distribution for the radial polarization in order to emphasize the relative field strengths. The same plane will be considered also for the modified asymmetric structures. All the field distributions will be normalized to the R peak value of the standard axisymmetric probe.

Strong localization is observed for the R mode due to the constructive interference of the surface waves along the taper, with an ultrasmall hot spot resulting from the combination of two weaker two-lobed transversely polarized patterns and a stronger single spot *z*-component. The full width at half maximum (FWHM) of the intensity of the electric field was calculated to be 38 nm. Note that this does not represent the ultimate resolution achievable with fully metal-coated probes, because, as shown by Vaccaro et al. (2003), the size of the hot spot is influenced by the final rounding in the metal coating that, in our simulations, was chosen to be 20 nm in radius just for convenience and can be decreased at will. Its value is necessary only as a reference for comparison. On the other hand, destructive interference of surface waves at the tip apex gives rise to two-lobed distributions for the H and V modes, polarized mainly along the *x* and *y* axis, respectively, and extended over an area whose shape is not well defined and whose average size is approximately 400 nm (where the size is measured as the distance over which the field is more than or equal to half of its peak value). The peak value of such distributions is about 50 times smaller than the peak of the R spot.

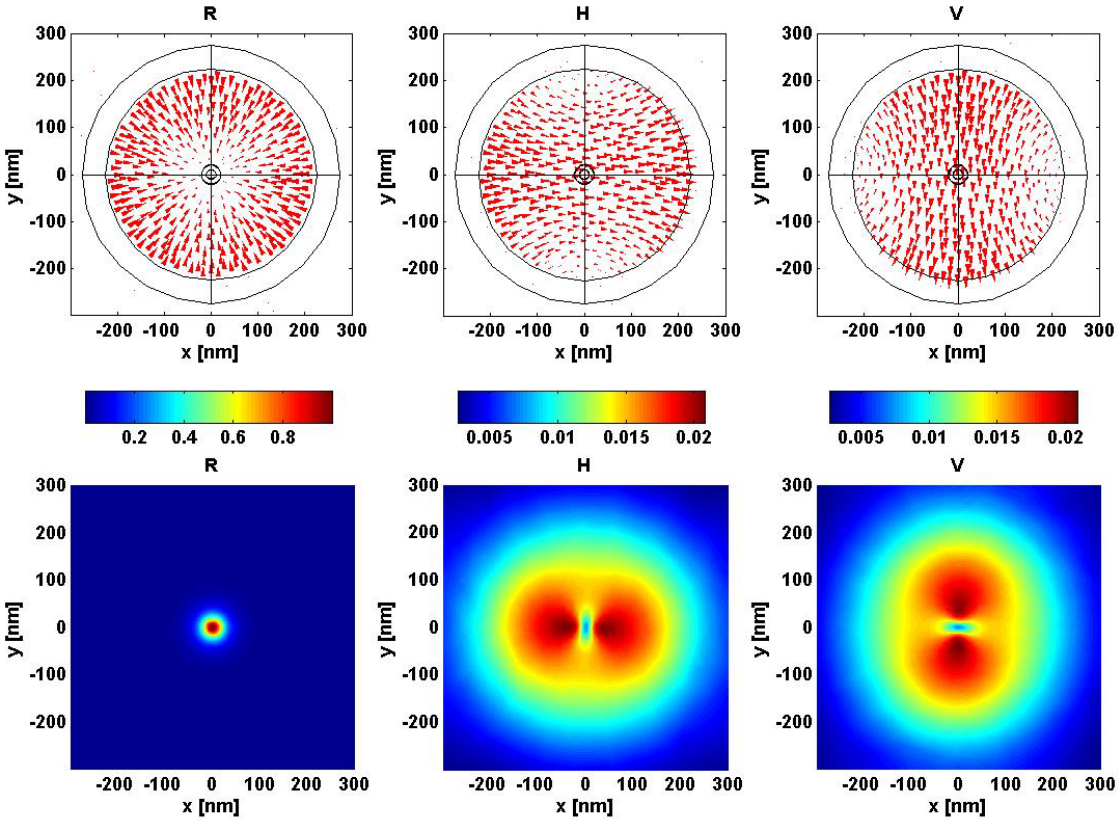

Fig. 2.6 – Input modes (upper row) and corresponding normalized near-field distributions in a plane located at 10 nm from the apex of a standard axisymmetric fully metal-coated probe (lower row).

2.5. Final remarks

The finite element based computational model used in this thesis for the analysis of the behaviour of SNOM probes has been described. As starting point for the design of optimized probes, the fully metal-coated structure has been chosen and numerically investigated. Results reported in this chapter, in agreement with those previously obtained for such a probe, represent the reference for comparison for the novel probe configurations scrutinized in the following chapters. Unless otherwise stated, the same computational model will be used also for the analysis of the new structures.

3. Modelling and simulation of novel asymmetric SNOM probes

The properties of novel probes based on an asymmetric structure are investigated in this chapter; the behaviour of such probes is analysed using finite element based simulations and compared to the one of axisymmetric fully metal-coated probes in order to better highlight the promising features of the new structures. Our results show that the introduction of an asymmetry in an originally axisymmetric structure allows the attainment of strong field localization close to the probe apex under linearly polarized excitation aligned along the direction of the asymmetry, thereby circumventing the need for a cumbersome radially polarized excitation, necessary in the axisymmetric structure for high resolution applications. Hence, the use of the proposed asymmetric structures would entail a significant simplification in experimental procedures. The influence of geometric and material characteristics on the performance of our novel probes is thoroughly scrutinized and amply discussed. The content of this chapter (including text and figures) is mostly published in Lotito et al. (2010, 2010a).

3.1. Asymmetric vs axisymmetric probe design

As anticipated in chapter 2, axisymmetric fully metal-coated probes under internal back excitation hold the promise for high resolution applications, as they can allow the achievement of a strongly localized hot spot, whose size is mostly limited by the diameter of the metal apex which can be decreased at will. However, as already pointed out, the resolution of fully metal-coated tips is highly sensitive to the polarization state of the input field: such desirable field localization properties, of utmost importance for SNOM applications, are affordable only under radially polarized excitation.

The reason for the strongly polarization-dependent behaviour is due to the different characteristics of the surface plasmons excited by the different waveguide modes on the external metal coating. More specifically, the probe input aperture exhibits a pair of orthogonal linearly polarized eigenmodes, followed by a radially polarized one. Our simulations, in agreement with previous numerical and experimental studies, have shown that only the excitation of a radially polarized mode results in a localized hot spot in the near-field zone of the probe apex, with a peak amplitude higher than the one of the linearly polarized modes, a feature of paramount importance for SNOM applications.

Despite its potential attractiveness, the radially polarized excitation exhibits a fundamental drawback, in that it imposes the need for an awkward injection procedure, which is extremely

sensitive to misalignments. For example, referring to the injection method reported by Tortora et al. (2007), the optical axis of the focusing system should be brought as close as possible to the probe axis: in case of lack of fully circular symmetry at injection, the dominant linear field component will couple to other modes in a non-controllable way. As apparent, this would clearly impair the potential benefits stemming from the use of radially polarized modes.

Hence, it would be desirable to find a way to get superfocusing effects similar to those observed for radial polarization injection by using a more easily excitable linearly polarized mode. A possible route that can be followed to pursue this goal consists in breaking the axial symmetry of the fully metal-coated probe so as to avoid the destructive interference between the SPPs excited by a linearly polarized mode on the opposite sides of the axisymmetric structure. If z is the direction of the probe axis and an asymmetry is introduced in the tip structure along x, field confinement under x linearly polarized mode could be expected. The asymmetry can be either present in the probe structure itself or in the probe illumination scheme. As to structural modifications, previous studies showed that even unintentional asymmetries like single and multiple air spherical bubbles or grains in the coating could have a weak field localization effect due to the coupling between the linearly polarized mode along the direction of the asymmetry and the radially polarized one (Nakagawa et al., 2006). As real probes have a large number of random defects and the overall behaviour of the probe is governed by the aggregate behaviour of such defects, a superfocusing based on such a mechanism could not be easily forecast. However, stronger and more easily predictable focusing effects can be achieved by the introduction of intentional modifications like unilateral and bilateral slits (Nakagawa et al., 2007). The behaviour of tip-on-aperture probes and probes based on a monopole antenna can also be explained with similar considerations (Frey et al., 2002; Taminiau et al., 2007). As an alternative, instead of an asymmetric probe structure, an asymmetric illumination scheme has been suggested: in the offset aperture probe, the surface plasmons are excited only on one side of an apertureless probe via an opening close to the probe base (Quong and Ellezabi, 2007), while asymmetric single-sided SPP excitation results in field localization in an axisymmetric apertureless probe (Lee et al., 2011).

In this chapter, two novel asymmetric structures are presented, one based on an oblique cut close to the tip apex stripping off both the metal coating and the inner core, and the other consisting of asymmetric corrugations in the metal coating. As we will see, compared to previously proposed asymmetric structures, the probes we designed are characterized by easier fabrication, higher reproducibility and a richer variety of structural parameters, which can be tailored to tune coupling mechanisms between WGMs and SPPs in order to get superfocusing under a more straightforward linearly polarized excitation. A thorough analysis of the effects of geometric and material parameters has been undertaken, in order to optimize the characteristics of the near-field distributions under

linearly polarized modes. In the following paragraphs, the properties of the probes based on the two different forms of asymmetries will be accurately examined.

3.2. Basic features of the asymmetric structures

The computational model is the same as described in paragraph 2.4.

Fig. 3.1 reports the sketches of the two asymmetric structures discussed in the coming sections, i.e. the tip based on an oblique cut and the one based on asymmetric corrugations.

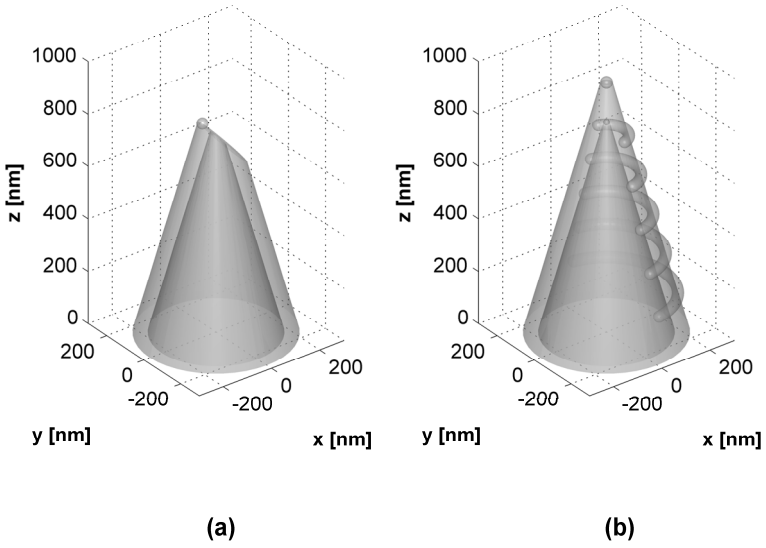

Fig. 3.1 – Sketch of the simulated structures: (a) probe with oblique cut; (b) asymmetrically corrugated fully metal-coated probe.

The tip with an oblique cut (Fig. 3.1(a)) exhibits a cut along a plane which is neither orthogonal nor parallel to the tip axis: the cut angle (defined as the angle between a plane orthogonal to the axis of the tip and the plane of the cut itself) and the cut height (meant as the height of the new tip apex after the cut, measured from the bottom of the computational domain) can be varied.

The structure with asymmetric corrugations (Fig. 3.1(b)) is based on the introduction of semicircular corrugations on the outer metal surface, which could consist in either bumps or grooves. Such surface corrugations are modelled by joining five truncated toroids of radius 20 nm with hemispherical terminations having the same radius: the toroidal sections are filled with air in case of a groove or with metal in case of a bump. As explained later, the case of metal oxide filling will be considered as well. Corrugations are limited to just one half of the tip, hence their angular extension is less than 180°.

More details about the geometric and material parameters of the asymmetric structures are provided in sections 3.3 and 3.4. According to the sketches in Fig. 3.1, for both the asymmetric structures the asymmetry was located along *x*. The near-field distributions obtained in a transverse plane at a given distance (10 nm) from the probe apex under orthogonal *x* and *y* linearly polarized excitations will be considered and compared to the distribution obtained in an axisymmetric probe under radially polarized excitation, studied in paragraph 2.4.

3.3. Asymmetric probe: cut probe

As a first example of asymmetric structure, we considered the one based on an oblique cut: Fig. 3.2 shows the near-field distributions centred around the probe apex obtained for a cut probe with a cut angle of 50° and a cut height of 816 nm under H and V linearly polarized excitation normalized to the peak value obtained in the reference axisymmetric probe under radially polarized excitation.

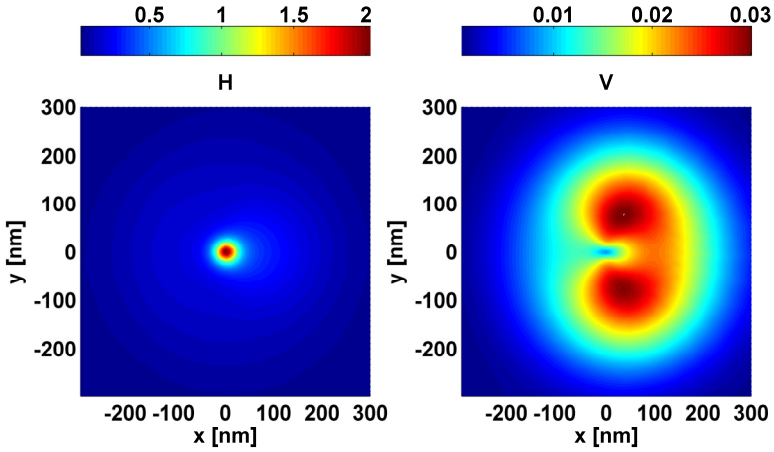

Fig. 3.2 – Normalized near-field intensity distributions over a 600 nm by 600 nm square area in a plane located at 10 nm from the apex of a cut probe with cut angle of 50° and cut height of 816 nm under H (*x*) and V (*y*) linearly polarized excitation; as the probe is asymmetric along *x*, field localization is achieved under H linearly polarized excitation.

As visible, field localization and enhancement with respect to the axisymmetric structure occur for the H linearly polarized mode which is oriented along the direction of the asymmetry (*x* in our case), while, for the orthogonally polarized mode V, no substantial variation with respect to the axisymmetric case is observed. The H distribution appears slightly asymmetric along the *x* axis and shifts preferentially towards the cut area. However, the asymmetry can be reduced by properly tuning some geometric parameters.

In the next subsections, the influence of two different geometric parameters on probe performance will be investigated, more specifically: (i) cut angle; (ii) cut height. Of course, the possibility to get a single-lobed intensity distribution by the injection of a linearly polarized mode is not sufficient alone for SNOM applications. Characteristics like the size of the spot as well as its peak value compared to the one obtained with the injection of a radially polarized mode in an axisymmetric fully metal-coated probe are of primary importance for a thorough and careful comparison of different probe configurations. For this purpose, as figures of merit for a comparison, the FWHM (which is related to the achievable resolution) and peak intensity will be analysed as a function of the geometric parameters of the probe.

3.3.1. Asymmetric cut probe: variation in cut angle

Probe optimization for the cut probe has been carried out by varying the cut angle from 20° to 60° with a step of 10°, while keeping the cut height constant at 816 nm. Fig. 3.3 illustrates the normalized near-field distributions obtained under H and V linearly polarized excitation for variable cut angle.

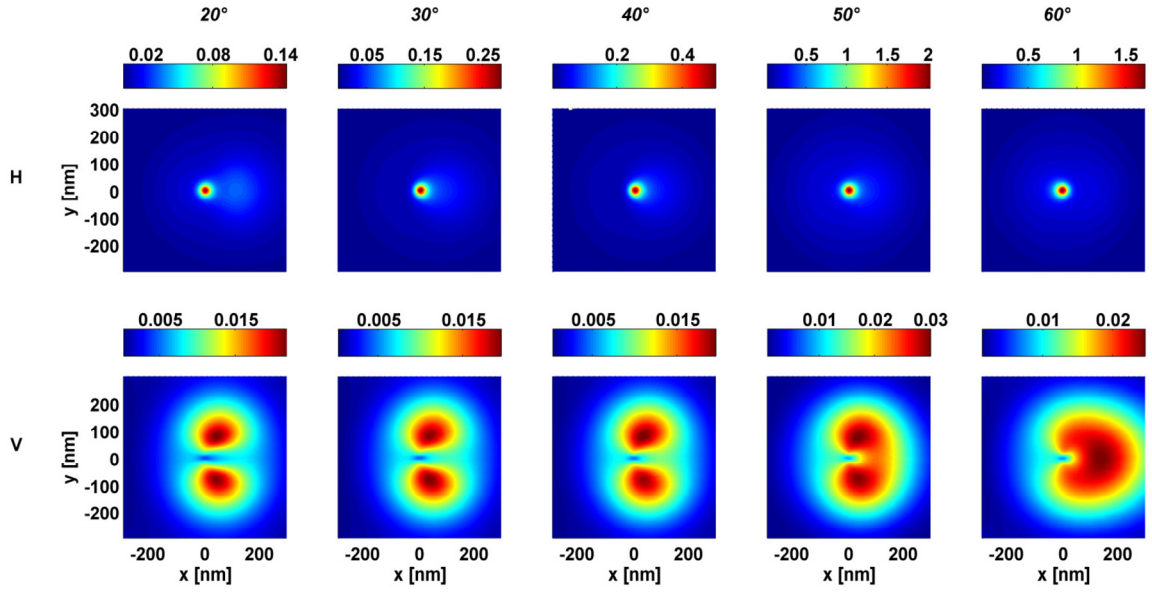

Fig. 3.3 – Normalized near-field intensity distributions over a 600 nm by 600 nm square area in a plane located at 10 nm from the apex of a cut probe with cut height of 816 nm and cut angle variable from 20° to 60° under H (upper row) and V (lower row) excitation.

For all the angles, a localized hot spot is obtained for the H mode, as expected. The two lobes of the V mode, that are initially separated, tend to merge as the angle becomes steeper until getting completely intermingled, resulting in the formation of a strong spread in the field distribution in the

cut area. As to the H spots, the initially asymmetric field distributions become progressively more symmetric about their centre along the x axis as the cut angle increases. However, their FWHM does not change remarkably with the cut angle, as will be shown later.

To get more insight into the obtained field distributions, the line profiles (each normalized to its own maximum, in order to better compare the overall shape and the features of distributions with different magnitudes) for the H mode along x and y directions have been plotted in Fig. 3.4. For each of the two distributions, the profiles are taken along $x=x_{max}$ and $y=y_{max}$ where (x_{max}, y_{max}) are the coordinates of the peak.

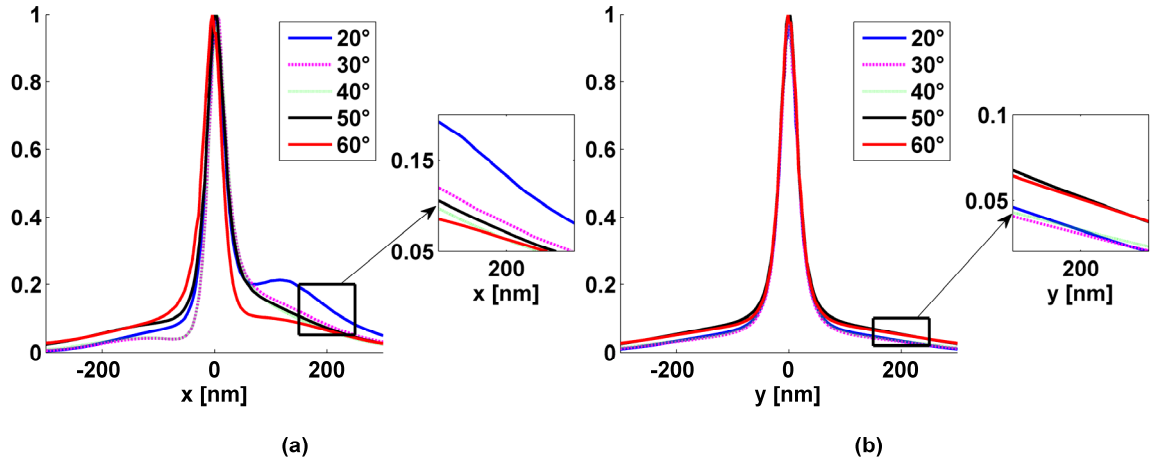

Fig. 3.4 – Normalized near-field intensity distributions under H polarized excitation as a function of the cut angle: (a) profile along *x*; (b) profile along *y*. Each distribution is normalized to its own maximum.

No strong variations occur in the profiles taken along y: the H mode shows good symmetry about the origin; on the contrary, the mode profile along x is quite asymmetric. However, the initial strong asymmetry is significantly reduced as the cut angle increases.

The FWHM and the peak value normalized to the one obtained in an axisymmetric probe under radially polarized excitation are reported in Fig. 3.5 as a function of the cut angle.

As anticipated, no dramatic changes occur in the size of the spots, which is always in the interval between 37 nm and 41 nm. However, steeper cut angles result in an increase in the H peak with respect to the peak one would get using a fully metal-coated axisymmetric tip excited with a radial beam. For very low angles, the intensity of the localized H spot is still very low, but, as the angle increases, it can reach values twice as high as the peak of the hot spot for the radial polarization.

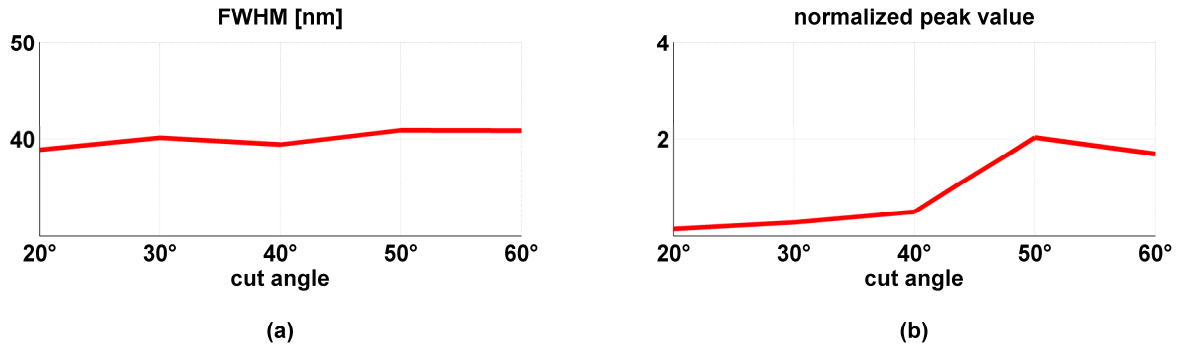

Fig. 3.5 – Characteristics of the near-field intensity distributions in a plane located at 10 nm from the apex of the cut probe under H polarized excitation for variable cut angle: (a) FWHM; (b) peak value normalized to the one achieved in an axisymmetric probe under radially polarized excitation.

3.3.2. Asymmetric cut probe: variation in cut height

The impact of cut height was examined as well: this parameter was increased from 741 nm to 841 nm with a step of 25 nm at a cut angle of 30°. Fig. 3.6 illustrates the corresponding normalized near-field distributions obtained under H and V linearly polarized excitation.

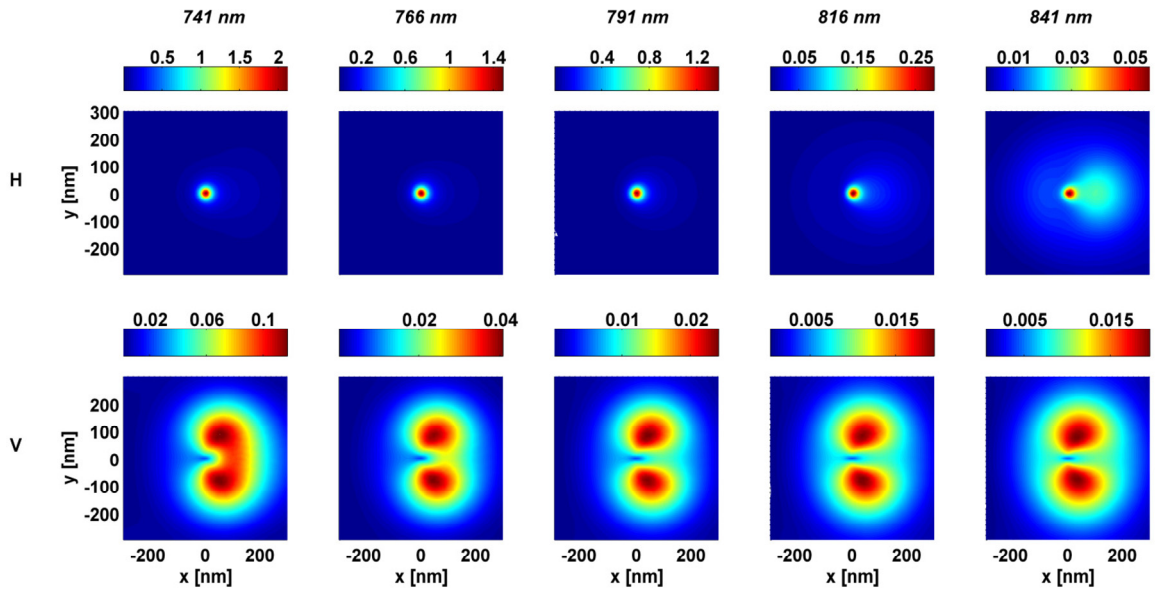

Fig. 3.6 – Normalized near-field intensity distributions over a 600 nm by 600 nm square area in a plane located at 10 nm from the apex of a cut probe with cut angle of 30° and cut height variable from 741 nm to 841 nm under H (upper row) and V (lower row) excitation.

Also in this case, a localized spot is created for the H mode. The lobes of the V distribution tend to separate as the height increases. A study of the profile distributions along the *x* and *y* directions (Fig. 3.7) reveals again a good symmetry along the *y* direction and an asymmetry along the *x* direction, which is particularly striking for the H distribution for higher cuts.

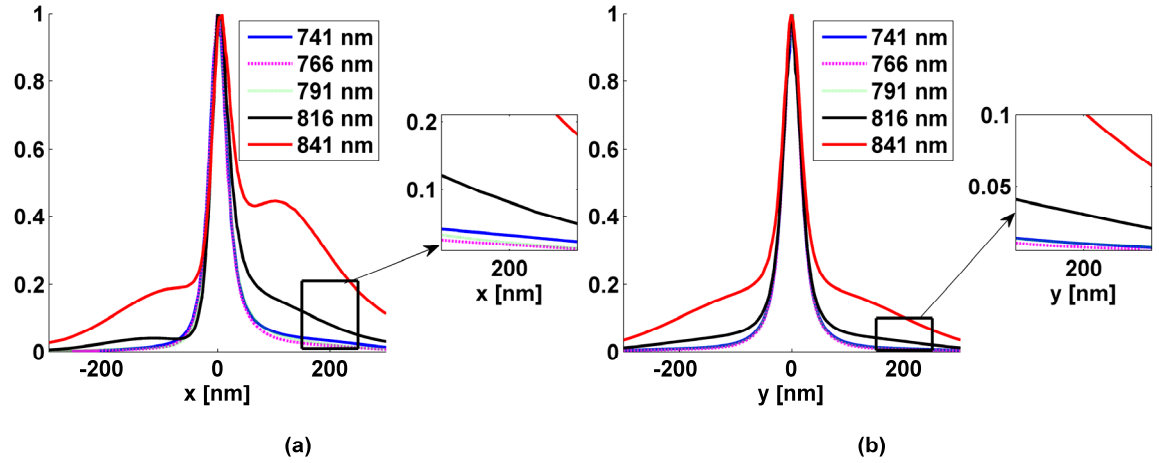

Fig. 3.7 – Normalized near-field intensity distributions under H polarized excitation as a function of the cut height: (a) profile along *x*; (b) profile along *y*. Each distribution is normalized to its own maximum.

The deterioration in the H field distribution is confirmed by the observed values of FWHM (Fig. 3.8(a)). The parameter that undergoes the worst degradation is the peak value of the H distribution that becomes a decreasing fraction of the radial peak value of the standard fully metal-coated tip, as illustrated in Fig. 3.8(b).

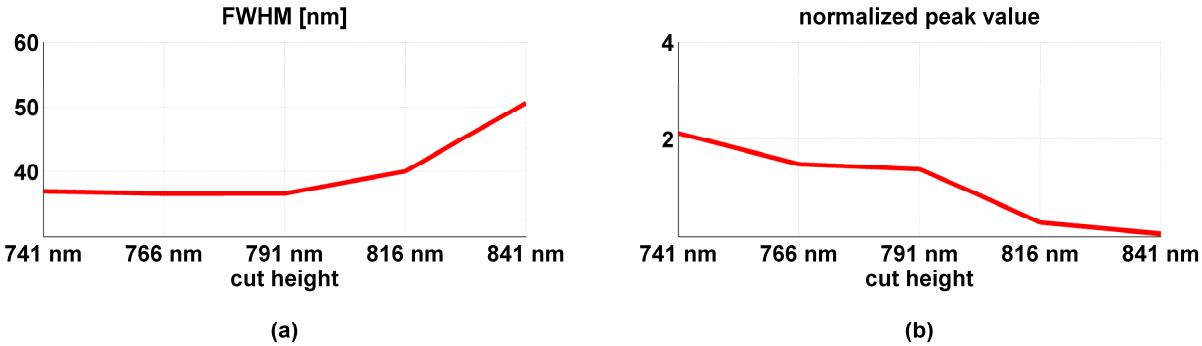

Fig. 3.8 – Characteristics of the near-field intensity distributions in a plane located at 10 nm from the apex of the cut probe under H polarized excitation for variable cut height: (a) FWHM; (b) peak value normalized to the one achieved in an axisymmetric probe under radially polarized excitation.

The results of the simulations with variable cut height suggest the use of cuts involving a larger fraction of the originally axisymmetric probe. As the possible approach to samples with steeper topographic variations would no longer be feasible with cuts at lower heights unless a large cut angle is used at the same time, a trade-off with the quality of the achievable H hot spot is necessary in the choice of the cut height.

The improvement in the peak value of the H hot spot with steeper cut angles and lower cut heights (i.e. cuts farther away from the original apex of the axisymmetric structure) could be explained as the outcome of a better mode coupling occurring when the asymmetry involves a larger region of the original tip. In fact, in both cases, a broader area is stripped off by the cut. Such an analysis agrees with what was previously observed for other modified structures (Nakagawa et al., 2007), for which asymmetries over more extended portions of the original tip gave rise to an increased coupling between one linearly polarized mode and the radially polarized one. Moreover, in the case of steeper cut angles, the transition from the original taper angle to the angle imposed by the cut is smoother, not so abrupt as in case of small cut angles. All these considerations justify the highest peak values achieved in these conditions.

3.4. Asymmetric probe: tip with asymmetric corrugations

The second asymmetric structure we designed is based on asymmetric corrugations involving just one half of the outer metal surface.

Corrugations in SNOM probes have been considered in previous studies for different purposes. The influence of axially symmetric periodic corrugations on the performance of aperture tips has been analysed by Antosiewicz and Szoplik (2007; 2008). SPPs on the internal metal surface were shown to be enhanced by the introduction of either semicircular grooves or rounded rectangular grooves on the core-metal interface. Higher charge density distribution and therefore improved throughput were obtained by varying geometric parameters of the internal corrugation.

The role of corrugations in apertureless probes has been examined experimentally (Ropers et al., 2007; 2008), and numerically (Baida and Belkhir, 2009). In particular, in the experimental studies, linear gratings were written by focused gallium ion beam sputtering on an electrochemically etched gold tip. Gratings were prepared on a number of tips with different distances from the tip end. SPPs were excited in these periodic structures by light impinging on the grating at normal incidence with a wavelength close to the grating period. The optimal choice of the distance between the grating and the tip apex was suggested to be a trade-off between propagation losses increasing with the distance and the desire for an excitation region well separated from the apex to suppress the direct far-field illumination of the apex. In the numerical study, two different cases were investigated: SPP

excitation by light incident first on a single groove and then on a grating of grooves with variable period was examined. In both cases, SPPs were excited giving rise to strong field enhancement at the tip apex, the grating showing greater spectral selectivity than the single groove.

Periodically corrugated metal wires were also proposed for imaging applications in the terahertz regime (Maier et al., 2006; Shen et al., 2008; 2008a) and at microwave frequencies (Wu et al., 2009). In this spectral range, metals resemble a perfect conductor and the negligible penetration of the electromagnetic fields leads to highly delocalized SPPs. However, the dispersion relation of SPPs can be engineered at will by periodically structuring the cylindrical surface with grooves. The geometry-controlled surface waves thus generated were named spoof SPPs because of their mimicking characteristics. Field concentration by tapering the inner radius of the grooves in cylindrical structures (Maier et al., 2006; Shen et al., 2008a) and superfocusing in conical structures (Maier et al., 2006) were reported in numerical simulations.

Differently from the previous studies, in our case, corrugations restricted to one half of the external metal coating are introduced in order to create a structural asymmetry. In the following sections, we analyze the effect of semicircular corrugations on the outer metal surface on the performance of a fully metal-coated tip with internal linearly polarized excitation. Even if the corrugations are located on a regular spatial pattern, they cannot be strictly regarded as a periodic grating. In fact, first, the portion of tip considered is too small to allow a large number of corrugations to be studied and to examine the influence of a change in the period and, second, the alternation of the two materials determining the corrugation (air and metal) will often wipe out the periodicity.

In fact, as anticipated in paragraph 3.2, the corrugations can take on the form of either indentations, that is the metal is carved away from the tip, or bumps, in which case the metal swells. As said, the five sections of rings with an azimuthal extension less than 180° are formed by joining a truncated toroid of 20 nm radius with two hemispheres having the same radius. The radius of the truncated toroids was chosen to create an effective perturbation in the original structure without causing a radical change such as complete metal perforation. The five corrugations are equally spaced in the section of the probe where both the inner core and the metal coating are present. They have a z-spacing amounting to 150 nm (where z is the direction along which the probe axis lies), with the first bottom one centred at 150 nm from the input port. Indentations and bumps in the metal coating are modelled by filling the semirings either with air or with metal. For the sake of simplicity, the different configurations under study will be indicated with the following shorthand notation: each of the semirings will be named after the initial of the filling material, starting from the bottom; for example, a configuration with three lower metal semirings and two upper air semirings will be labelled as *mmmaa*.

The normalized near-field distributions for the structure in Fig. 3.1(b) are reported for the configuration *amama* (Fig. 3.9) for corrugations with an azimuthal extension of 160°.

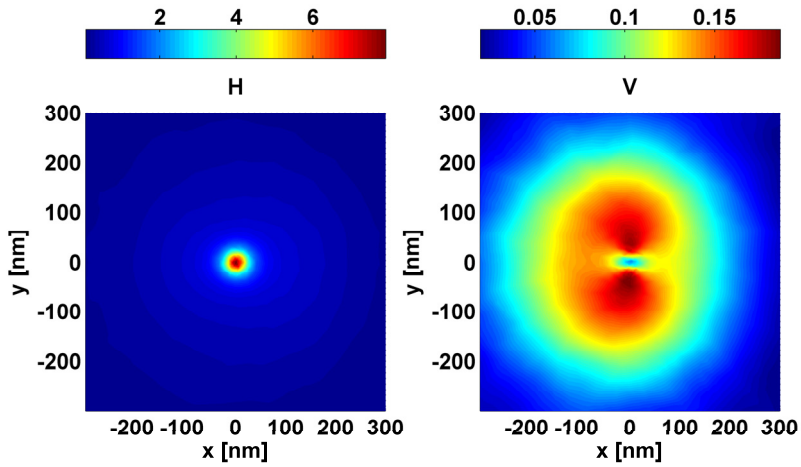

Fig. 3.9 – Normalized near-field intensity distributions over a 600 nm by 600 nm square area in a plane located at 10 nm from the apex of a probe with asymmetric corrugations (*amama* configuration) under H (*x*) and V (*y*) linearly polarized excitation; as the probe is asymmetric along *x*, field localization is achieved under H linearly polarized excitation; *a* stands for air, *m* for metal.

As expected, field localization is achieved under H excitation, while the V distribution does maintain an almost two-lobed pattern: in fact, also in this case, the asymmetry was located along *x*, while the structure is still symmetric along *y*. In the subsequent paragraphs, parametric studies about the suggested configuration are carried out to assess (i) the impact of variations in the sequence of materials (that is, of indentations and bumps), and (ii) the influence of some geometric parameters like the azimuthal extension of the semirings. The effects of the replacement of air with metal oxide will be investigated as well.

3.4.1. Probe with asymmetric corrugations: permutations of grooves and bumps

A systematic analysis of the FWHM and the peak value of the hot spot achieved under H polarized excitation for all the possible permutations of air indentations and metal bumps for the same structure was carried out (Fig. 3.10).

With the exception of only one configuration (*aamaa*), the size of the near-field distribution undergoes a dramatic reduction in all the cases and, for most of the structures, a real ultrasmall spot with a FWHM comparable to that observed for the R mode excitation in the axisymmetric probe is created (Fig. 3.10(a)). The H peak value generally increases compared to the case of the standard axisymmetric probe. However, only few material combinations give rise to values comparable or, in

two cases, even much superior to the radial peak for the axisymmetric probe. Moreover, it can be observed that the presence of the sequence air/metal/air in the upper three semirings brings about higher peak values, with the best results given by the *amama* configuration (Fig. 3.10(b)).

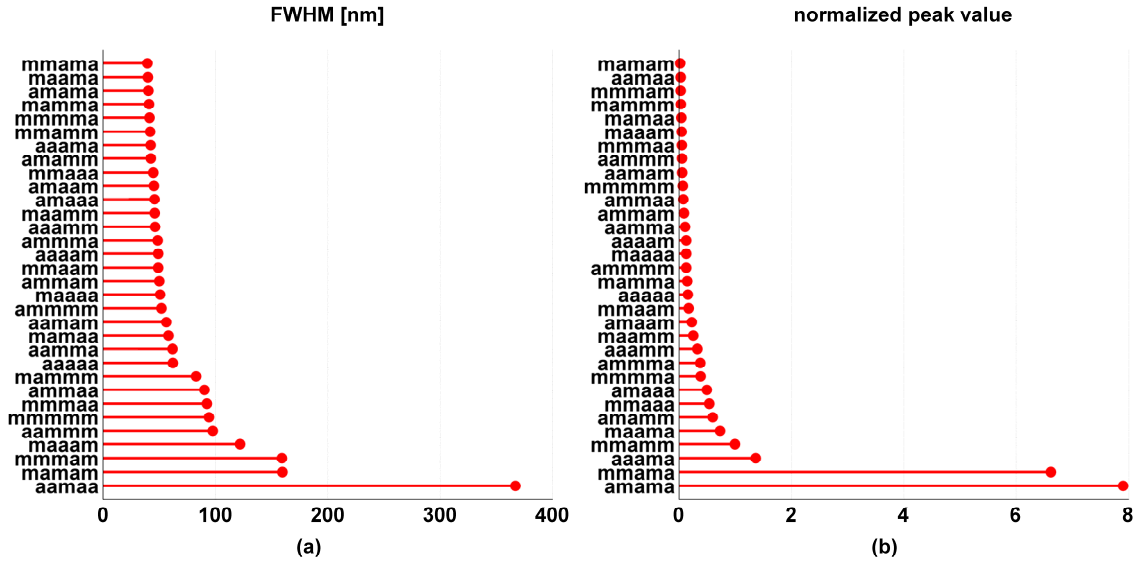

Fig. 3.10 – Characteristics of the near-field intensity distributions in a plane located at 10 nm from the apex of the corrugated probe under H polarized excitation for each of the material permutations in the five semirings: (a) FWHM; (b) peak value normalized to the one achieved in an axisymmetric probe under radially polarized excitation.

An overall analysis of the previous graphs suggests the use of configurations with the air/metal/air combination in the upper three semirings to optimize performances in terms of peak size and strength, with the best results obtained for the *amama* structure. Another conclusion that can be drawn is that, if a certain material combination is effective in achieving field localization for the H distribution, generally the complementary one is not.

All the shown data can be interpreted in the light of the interplay of mode coupling mechanisms and interaction of the external SPPs with the outer surface roughness. In fact, as pointed out previously, in an axisymmetric probe under linearly polarized excitation the SPPs on the opposite sides have opposite polarities and thus their contributions cancel out at the apex. The presence of the corrugation locally tunes the coupling of the inner and outer SPPs and the characteristics of the outer SPPs on one side of the tip. These mechanisms can modify the properties of the SPPs on one side of the tip in such a way that the electric fields associated with SPPs on the opposite sides of the probe do not have opposite phases any longer. Some configurations can result in a net prevalence of the SPPs on one of the two sides and thus in field localization. Moreover, the asymmetry can also

introduce a coupling from one of the linearly polarized modes into the radial one. This means first that, in some cases, even unintentional corrugations stemming from defects could have a beneficial effect on the tip behaviour. Second, intentional corrugations can be introduced on purpose to get a localized hot spot with a linearly polarized excitation, which can be obtained in an easier way than the radial one.

3.4.2. Probe with asymmetric corrugations: variation in the azimuthal extension of the corrugations

As a second step, we tried to assess the impact of some geometric parameters on the probe performance. The limited computational resources do not allow us to change dramatically many geometric features, such as the distance between the portions of rings. An analysis of the effect of a variation of the angular extension γ of such corrugations was instead feasible and was carried out by increasing the angular extension from 110° to 160° with a step of 10° (so as to avoid that the extremes of all the corrugations go beyond half of the probe) (Fig. 3.11).

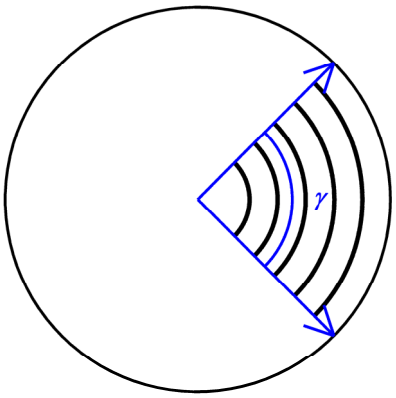

Fig. 3.11 – Schematic of the *xy* projection of a probe with asymmetric corrugations: the angle γ is the angular extension of each corrugation.

Fig. 3.12 reports the field distributions for the H polarization over the 600 nm by 600 nm output plane as a function of the angle for the *amama* configuration, together with their normalized profiles along the *x* and *y* axes (as for the cut probe, each profile is normalized to its own maximum, for a clearer comparison between distributions having different peak values). As visible, in all the cases almost symmetric ultrasmall spots with similar sizes are generated. Compared to the cut (paragraph 3.3) and slit based tips (Nakagawa et al., 2007), the symmetry of the spots is apparently better in all the cases, irrespective of the geometric parameters. However, as the angle increases, the intensity profile shows a more rapid decay.

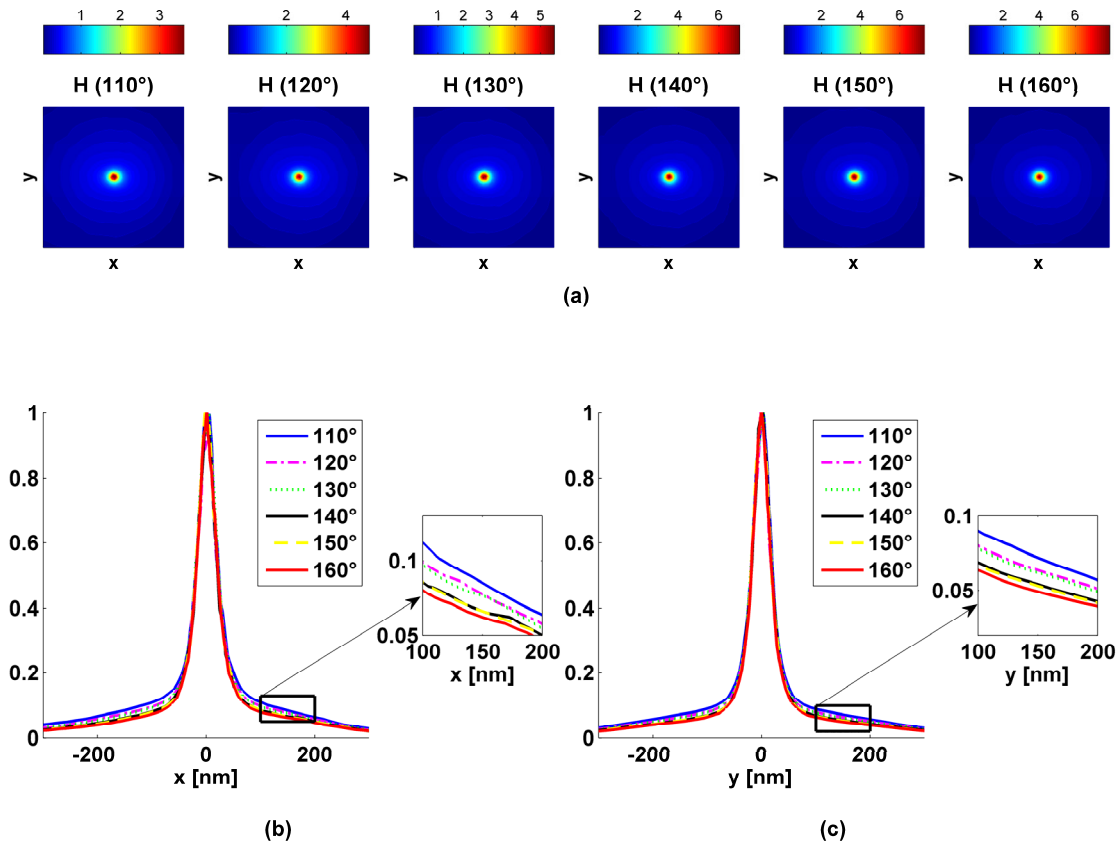

Fig. 3.12 – Normalized near-field intensity distributions under H polarized excitation as a function of the angular extension *γ* of the corrugations (*amama* configuration): (a) plot on a 600 nm by 600 nm square area in a plane located at 10 nm from the tip apex; (b) profile along *x*; (c) profile along *y*. Profiles in (b) and (c) are normalized to their own maximum.

To get better insight into the characteristics of these distributions, a quantitative analysis of the size and peak value of the H hot spots has been carried out (Fig. 3.13).

Simulations reveal no significant variations in the FWHM for the H hot spots, which oscillates between 40 nm to 43 nm without any regular trend (Fig. 3.13(a)).

On the contrary, another figure of merit for the H spot changes remarkably as a function of the azimuthal extension of the corrugations. Fig. 3.13(b) reports the ratio of the H spot peak value with respect to the R hot spot for a standard axisymmetric tip. The ratio increases as the angle increases, which means that stronger intermodal coupling mechanisms occur with a more extended asymmetry, leading to an improvement in the intensity of the H hot spot.

In conclusion, even smaller asymmetries generate field localization and enhancement, which globally improve as the asymmetry involves larger portions of the tip.

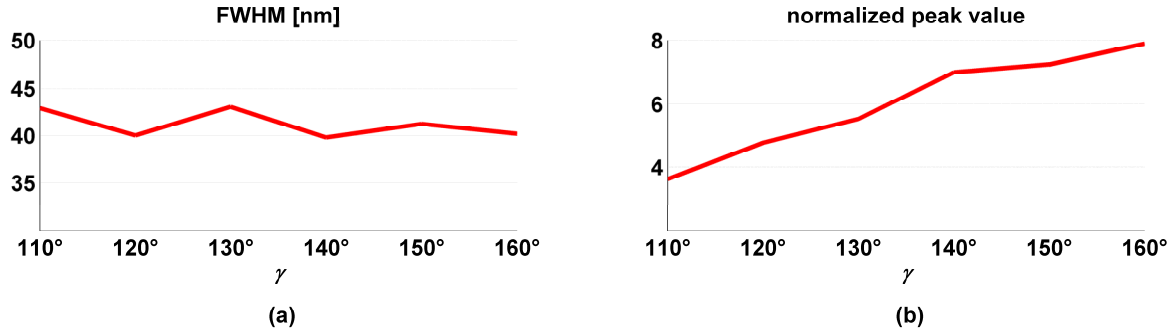

Fig. 3.13 – Characteristics of the near-field intensity distributions in a plane located at 10 nm from the apex of an asymmetric probe under H polarized excitation for variable angular extension γ of the corrugations: (a) FWHM; (b) peak value normalized to the one achieved in an axisymmetric probe under radially polarized excitation.

3.4.3. Probe with asymmetric corrugations: variation in the dielectric material

Finally, we examined the effect of replacing an air indentation with a metal oxide bump. For the case under study, we chose aluminium oxide filling (with index of refraction n=1.54). The reason for the analysis of the effects of metal oxide bumps lies in the fact that, especially for some metals like silver, metal oxide layers are likely to be originated. So far, only metal oxide defects in form of holes perforating the metal coating have been examined (Nakagawa et al., 2006). Simulations of dielectric-metal-dielectric probes under internal radially polarized illumination have shown the possibility to tune the intensity collected at the tip apex by changing the permittivity of a thin dielectric nanocladding surrounding a fully metal-coated probe (Antosiewicz et al., 2009). Such a phenomenon had been experimentally verified for a fully metal-coated probe covered by a dielectric layer whose index of refraction was varied (Abrahamyan and Nerkararyan, 2007; Nerkararyan et al., 2006). Moreover, it has been shown that the coupling between surface modes at the core-conductor interface and the conductor-covering layer interface becomes more efficient when the index of refraction of the core is close to the index of refraction of the covering layer (Janunts and Nerkararyan, 2001; Themistos et al., 2006). The structure we considered is the same as in paragraph 3.4.1 (angular extension of the corrugations equal to 160°), with air replaced by oxide (denoted by the initial *o* in our shorthand notation). Also for this series of simulations, we took into account all the possible permutations of metal and oxide for the five semirings.

Fig. 3.14 shows the field distributions for the *omomo* structure. As visible, the desired field localization for the H polarized mode is achieved, while the V polarized mode is not remarkably affected by the asymmetry.

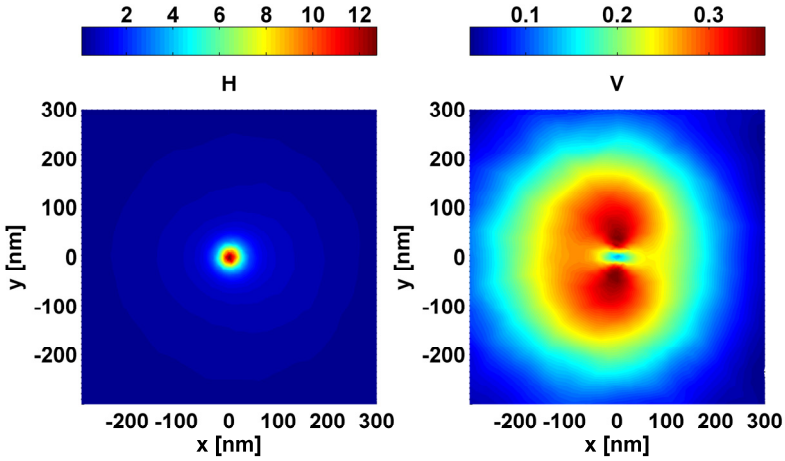

Fig. 3.14 – Normalized near-field intensity distributions over a 600 nm by 600 nm square area in a plane located at 10 nm from the apex of a probe with asymmetric corrugations (*omomo* configuration) under H (*x*) and V (*y*) linearly polarized excitation; as the probe is asymmetric along *x*, field localization is achieved under H linearly polarized excitation; *o* stands for oxide, *m* for metal.

Also for this configuration, we analyzed the characteristics of the H spot originated by the asymmetric corrugation, as the sequence of materials (metal and oxide) changed. First, the FWHM of the H field distributions for all possible permutations were compared (Fig. 3.15(a)). Results show the creation of an ultrasmall hot spot for most of the configurations.

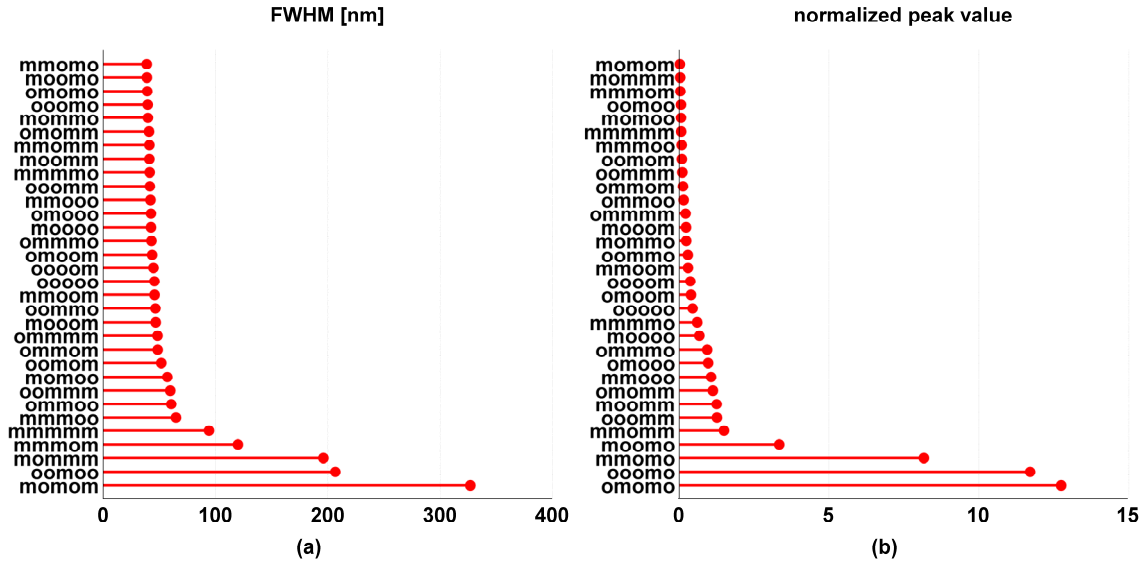

Fig. 3.15 – Characteristics of the near-field intensity distributions in a plane located at 10 nm from the apex of the corrugated probe under H polarized excitation for each of the material permutations in the five semirings (metal oxide - metal based structure): (a) FWHM; (b) peak value normalized to the one achieved in an axisymmetric probe under radially polarized excitation.

The analysis of the peak value of such a spot compared with the one obtained for a fully metal-coated axially symmetric probe under radially polarized excitation (Fig. 3.15(b)) confirms once again that the alternation of dielectric/metal/dielectric in the upper three semirings provides better results, but points out also that the substitution of air with metal oxide gives rise to stronger peak values.

In brief, an overall analysis of the previous graphs confirms the trend shown in the air-metal corrugations, in that some metal-dielectric alternations give better results especially in terms of peak value of the achieved spot. Besides, when air is replaced by metal oxide, a further enhancement in the collected signal occurs, ensuing from a better coupling between the inner and outer SPPs.

3.5. Final remarks

Our finite element based simulations have shown that carefully designed asymmetries introduced in an originally axisymmetric fully metal-coated tip can produce strong field localization under an excitation linearly polarized along a proper polarization direction. The presence of the asymmetry causes the electric fields associated with SPPs on the opposite sides of the tip not to have opposite phases any longer, a phenomenon that leads to destructive interference under linearly polarized injection in an axisymmetric structure. A global analysis of the results obtained for both a cut probe and a tip with asymmetric corrugations has shown that this effect is enhanced when the asymmetry is extended over a broader region. In this way, superfocusing can be achieved with a linearly polarized injection, which is much easier than a radially polarized one, with an enormous simplification in experimental applications.

By cutting the originally fully metal-coated SNOM probe along the x direction, strong field localization is realized for the H polarized mode. The parametric analysis carried out on this configuration and taking into account the height and the angle of the cut showed that steeper angles and lower cuts allow better performances in terms of FWHM and peak value of the H hot spot. Therefore, the use of this configuration combined with a proper choice of the geometric parameters of the structure would provide the possibility of high resolution SNOM by using a linearly polarized input, thus circumventing the cumbersome procedure required for the injection of a radially polarized mode.

The possibility of using asymmetric corrugations in the metal coating of fully metal-coated SNOM tips to induce field localization under linearly polarized excitation was also numerically demonstrated. Our 3D simulations on the effects of five equidistant semicircular corrugations introduced in just one half of the tip, in the form of either bumps or grooves, revealed that the linearly polarized mode oriented along the direction of the asymmetry (x in our simulations) can

undergo a significant spatial shrinkage and increase in intensity for proper choices of material combinations for the corrugations. By studying the effects of all the possible material permutations of air and metal in the five semirings, it was shown that some configurations, especially those involving an air/metal/air alternation in the upper three semirings, can give rise to very high quality ultrasmall hot spots for the H linearly polarized mode. The results were explained as the outcome of the interplay of improved coupling mechanisms between the H mode and the R mode and between the inner SPPs confined at the silica/metal interface and the outer SPPs supported at the metal/air interface.

The structure based on corrugations, even if a bit more challenging from the point of view of fabrication with respect to the cut probe, offers a larger number of possibilities to be tailored. In particular, we explored two possible variants, one based on the change in the dielectric and one based on the variation of a geometric parameter, that is, the azimuthal extension of the corrugations. In the first case, we replaced air by metal oxide. Simulations showed similar trends for the alternation of metal and dielectrics, with better results achieved for an oxide/metal/oxide combination in the upper three semirings. However, the substitution of air by oxide brings about an advantageous enhancement of the intensity of the H hot spot. Then, the angular extension of the corrugations was changed for the air-metal based system. This latter series of simulations generally confirmed the tendency of asymmetries involving more extended portions of a tip to give stronger coupling mechanisms and thus better field localization for the linearly polarized mode.

The proposed structure is still open to other routes for improvement. For example, the effects of really periodic corrugations extended over longer tip sections could be studied, as well as variations in the shape of the corrugation or in the dielectric or even more complicated structures based on alternations of grooves, metal bumps and metal oxide bumps.

Furthermore, a last point worth being highlighted is that our study on asymmetric corrugations, beside proposing a new modified structure to get field localization by injecting a linearly polarized mode, also casts light on the possible effects of unintentional corrugations, which could induce weak coupling mechanisms beneficial for the overall probe behaviour. In fact, so far, defects only in the form of air bubbles or small oxide holes in the metal layer or metal spherical grains close to the tip apex have been taken into account (Martin and Paulus, 2002; Nakagawa et al., 2006), while scars in the metal surface and more extended metal protrusions (resulting, for example, from the combination of closely spaced metal grains) have not been examined. Even if only some specific combinations have been considered in our study, the results of our simulations can give some indications on how unintentional inhomogeneities (like scars and bumps) can affect tip performance.

4. SNOM probes with adirectional asymmetries

A completely new probe concept is introduced in this chapter, based on a novel form of asymmetry, which we name "adirectional". In fact, all the asymmetries considered so far (both the ones proposed in chapter 3 and those suggested by other groups) allow the attainment of field localization only for a linearly polarized mode oriented along one specific spatial direction, the one of the asymmetry (because of this characteristic, we call them "directional"). The reason behind this behaviour is that all the considered structures still exhibit reflection symmetry, that is, they present a plane of symmetry. Hence, although they obviate the need for an awkward radially polarized excitation, they still require some alignment of the direction of the linearly polarized excitation with respect to the asymmetry. If we extend the asymmetry to all spatial directions (adirectional asymmetry), field localization can be achieved for any arbitrary orientation of the input linearly polarized excitation, thereby waiving any requirement on alignment. An asymmetry based on a spiral design is proposed as it intrinsically meets the requirement of lack of any preferential spatial direction. As a proof of concept, first a spiral-shaped corrugation is analysed and then a set of azimuthal corrugations arranged in a spiral-like fashion is proposed as an easier implementation of this innovative probe design. The content of this chapter (including text and figures) is mostly published in Lotito et al. (2011, 2011b, 2012).

4.1. Adirectional vs directional asymmetries

The introduction of an asymmetry in an originally axisymmetric fully metal-coated structure has been proposed and investigated in chapter 3 as a promising solution to get superfocusing under linearly polarized excitation. Two novel asymmetric structures, characterized by easier fabrication and numerous possibilities for optimization compared to other asymmetric configurations proposed in previous works, have been carefully scrutinized.

However, both our novel configurations and those suggested in previous studies are based on the introduction of an asymmetry along one specific direction. Hence, field localization occurs only for the linearly polarized mode that is oriented in the direction of the asymmetry. In other words, given z the direction of the probe axis, if the geometric modification determines an asymmetry along, say, the x direction, then the x linearly polarized mode undergoes significant shrinkage with respect to the axisymmetric structure and also peak value enhancement for a proper choice of the characteristics of the modification; vice versa, the y linearly polarized mode will not be dramatically affected by the

modification, as no asymmetry is present along the *y* direction, and will maintain a weaker, broader and substantially two-lobed distribution. The field localization stems from an interplay of different coupling mechanisms between the WGM and SPPs, the inner and outer SPPs, the linearly polarized mode and the radial one. Similar considerations hold for asymmetries that do not involve the geometry, rather the illumination, as is the case for the offset apertured – metal coated dielectric apertureless structure, where a localized hot spot is obtained by using incident light polarized linearly in the direction perpendicular to the interface between the base of the tip and the offset aperture adjacent to the tip base (Quong and Ellezabi, 2007). All these forms of asymmetries exhibit their own plane of symmetry and are therefore endowed with reflection symmetry: they represent "directional" asymmetries that, of course, cannot guarantee field localization for arbitrarily oriented linearly polarized modes. Even if such modifications bring about a considerable simplification in the injection procedures as a radially polarized excitation is no longer necessary, they still require alignment between the linearly polarized mode and the asymmetry itself. Note that by asymmetry in this thesis we mean a structural modification likely to break the rotational symmetry of the original probe structure; the asymmetric structures we consider are therefore devoid of rotational symmetry, which does not mean that they are devoid of other forms of symmetry, as just observed, for example, for what we defined as "directional" asymmetries. The words "asymmetric" and "asymmetry" are used for simplicity in this sense, as also in other works (e.g. Nakagawa et al., 2007; Yatsui et al., 1997).

To better understand how the misalignment from the preferential spatial direction can affect the performance of a probe with a directional asymmetry, we have investigated the behaviour of a probe based on asymmetric corrugations for variable mutual orientation of the direction of the input linearly polarized excitation with respect to the one of the asymmetry. Such mutual alignment has been defined as the angle α between the direction of the input linear polarization and the angle bisector of the corrugations (Fig. 4.1(a)); the mutual orientation specified by α was changed from -85° to 90° to encompass all the possible mutual positions. Note that α=0° and α=90° correspond to *x* and *y* linearly polarized excitations so far labelled as H and V. Moreover, α=0° represents the position of best alignment of the input linear polarization with respect to the asymmetry in case of the directional asymmetry, with α=90° representing the maximum misalignment.

Fig. 4.1 (b) and (c) report the FWHM and the normalized peak value as a function of α for the *amama* configuration and azimuthal extension of the corrugations equal to 160°. As the misalignment of the input polarization from the preferential direction of the asymmetry increases, both the peak value and the shape of the near-field intensity pattern change. In particular, the peak value decreases and the distribution becomes gradually broader. This is due to the fact that, as α increases, the asymmetry perceived by the input linearly polarized excitation progressively

disappears. In retrospect, the different behaviour can be explained if recalling that a structure asymmetric along *x* appears symmetric for a *y* linearly polarized excitation, which brings about destructive interference of the excited SPPs, similarly to what happens for an axisymmetric structure under linearly polarized excitation. If we consider the average of both the FWHM and the peak value over all the possible mutual positions, from the graphs it can be inferred that maximum deviations of the peak value and of the spot size from the corresponding averages are about 100% and 450%, respectively.

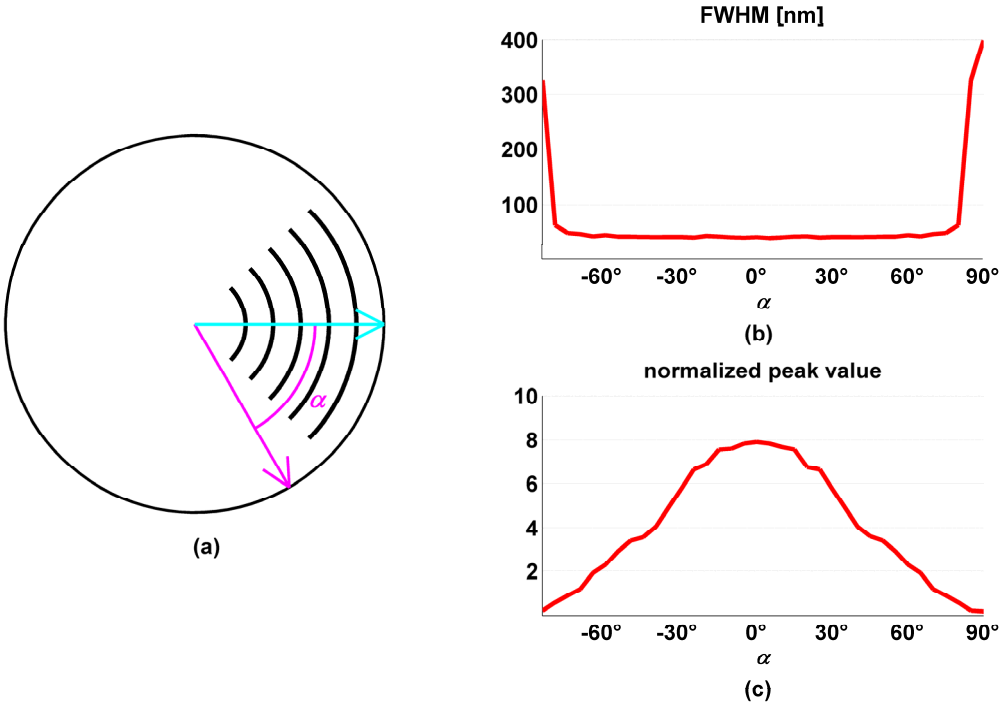

Fig. 4.1 – Behaviour of the probe with asymmetric corrugations for variable orientation of the input linearly polarized excitation with respect to the asymmetry: (a) schematic of the *xy* projection of the probe: the angle *α* is the one between the direction of the input linear polarization (indicated by the magenta line) and the angle bisector of the corrugations (represented with the cyan line); (b) FWHM of the near-field distribution for variable *α* (*amama* configuration); (c) peak value of the near-field distribution normalized to the one of the axisymmetric probe under radially polarized excitation for variable *α* (*amama* configuration).

Similar analyses have been run for various forms of directional asymmetries with different structural parameters. As we are mainly interested in the sensitivity to mode orientation, we report only the maximum deviation of the peak ratio and of the spot size from the average value over all the mutual orientations of the linearly polarized excitation with respect to the asymmetry (Fig. 4.2).

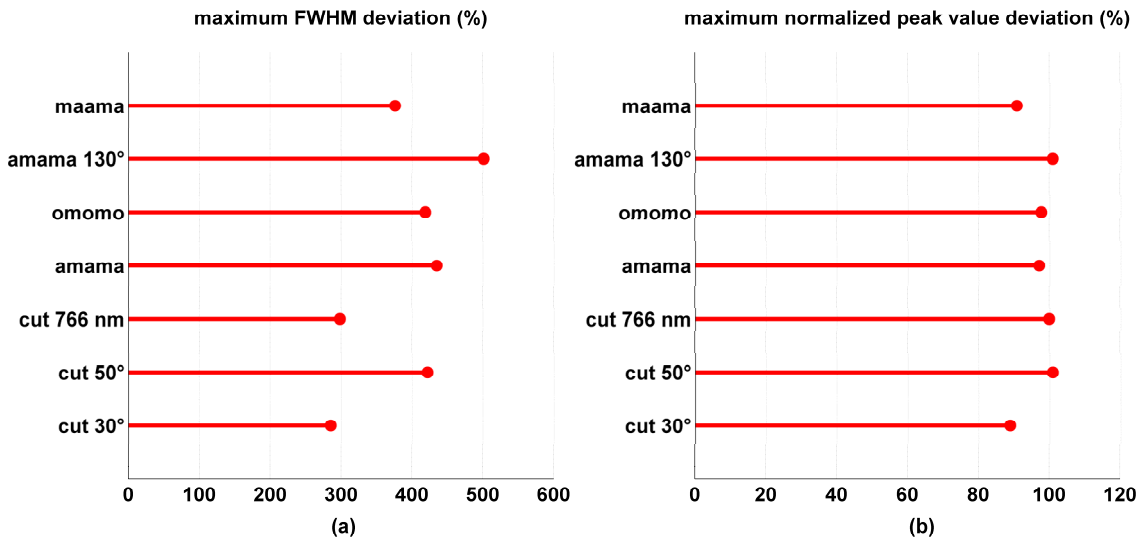

Fig. 4.2 – Characteristics of the near-field intensity distributions for directional asymmetries under linearly polarized excitation for variable orientation α of the asymmetry with respect to the input linear polarization: (a) maximum deviation from the average FWHM; (b) maximum deviation from the average normalized peak value.

Variations of more than 90% in the peak value and, more importantly, stronger than 280% in the spot size are reported. The different sets of material and geometrical parameters considered show that such huge variations do not depend on how much the structures are optimized, but rather on their intrinsic directional nature. Aligning the input polarization in a wrong way implies degradation not only of peak intensity, but also of resolution.

The practical impact of such a result in experimental applications can be appreciated when considering the role played by the orientation of the linearly polarized mode in the images recorded by asymmetric tips based on a tip-on-aperture and on a monopole antenna grown on the rim of an aperture tip (Frey et al., 2002; Taminiau et al., 2007; 2007a). For example, in the studies by Taminiau et al. (2007, 2007a), dramatic variations in the imaging of fluorescent molecules were observed both in resolution and signal intensity by rotating the linearly polarized mode from the direction along which the metal protrusion is present to the orthogonal one, highlighting the strong influence of polarization and the need to excite a suitably polarized mode. However, the control of the direction of the input polarization is not an easy task especially in fibre based tips due to the fact that the actual position of the asymmetry is unknown when the tip is mounted on the microscope and also because of the rotation of the incident light polarization within the probe: in a tip-on-tip analysis of an asymmetric probe, the effective polarization direction close to the asymmetry was determined *a posteriori* by observing the field distribution close to the tip apex and comparing it to simulation

results (Yatsui et al., 1997). The lack of accurate knowledge about the mutual orientation between the polarization direction and the asymmetry would hinder a systematic application of such probes.

Therefore, it would be desirable to attain superfocusing effects for arbitrarily oriented linearly polarized excitation, by using an "adirectional" asymmetry, which means a suitable modification likely to create an asymmetry along all spatial directions.

In this chapter, we propose two different implementations of this pioneering concept. Both structures are based on the introduction of a spiral asymmetry: the spiral intrinsically fits the specification of lack of directionality and offers an interesting case study to scrutinize the feasibility of the concept of orientation-insensitive field localization. First, we analyze the effects of a spiral corrugation on the outer metal surface of a fully metal-coated probe. Then, a more practical implementation based on azimuthal corrugations arranged in a spiral-like fashion will be discussed. A sketch of the two structures is shown in Fig. 4.3.

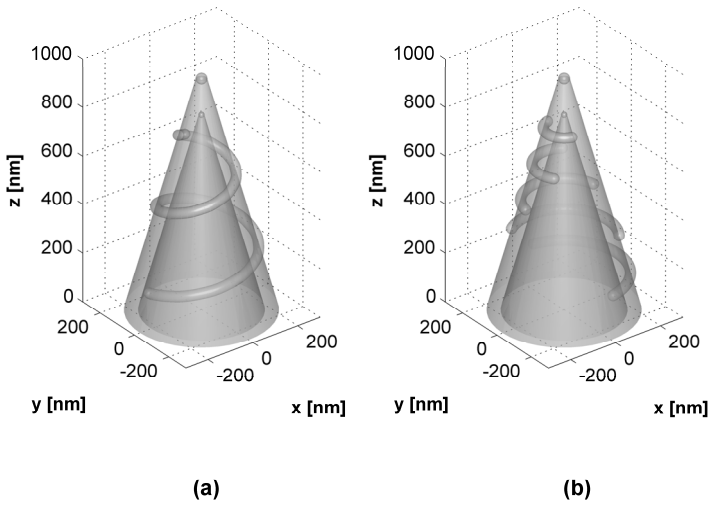

Fig. 4.3 – Sketch of the structures based on an adirectional asymmetry: (a) probe with spiral corrugation; (b) probe with spiral-arranged azimuthal corrugations.

The overall computational model is the one described in chapter 2. Structural details of the two structures are given in the following sections. For each of the two structures, we will show the possibility to get field localization for two orthogonal linearly polarized modes. Then, we will vary the mutual orientation of the linearly polarized modes with respect to the spiral-like asymmetry and compare the results with those achievable with directional asymmetries. We will show that, while the directional asymmetries give rise to orientation-dependent behaviour, the adirectional asymmetry

brings about performance significantly less sensitive to variations in the mutual orientation, which makes the tip even more robust against misalignments.

4.2. Probe with spiral corrugation

The structure we have examined is based on a spiral corrugation on the outer metal coating of the originally axisymmetric structure, in a form likely to cover the entire angular range and to create a fully asymmetric structure along any spatial direction.

The initial axisymmetric structure is the one based on a silica core surrounded by an aluminium coating as described in paragraph 2.4. The spiral corrugation is formed by joining a tapered helix-shaped 3D object (with circular cross-section of radius r) with two hemispherical terminations (having the same radius r). In each point, the centre of the circular cross-section is located along the outer metal surface, so that the spiral winding appears as a semicircular spiral corrugation. The spiral is placed between 150 nm and 750 nm along the z direction and the pitch along z is 300 nm. The spiral corrugation can take on the form of either a groove, i.e. it is filled with air, or a bump, corresponding to metal filling. We have also investigated the effect of metal oxide filling.

In Fig. 4.4 the near-field intensity distributions over a 600 nm by 600 nm square area in a transverse plane located at 10 nm from the probe apex for a spiral metal corrugation with radius r = 25 nm are illustrated. The values are normalized to the peak value of the reference probe under radially polarized excitation in order to better pinpoint the relative field strengths.

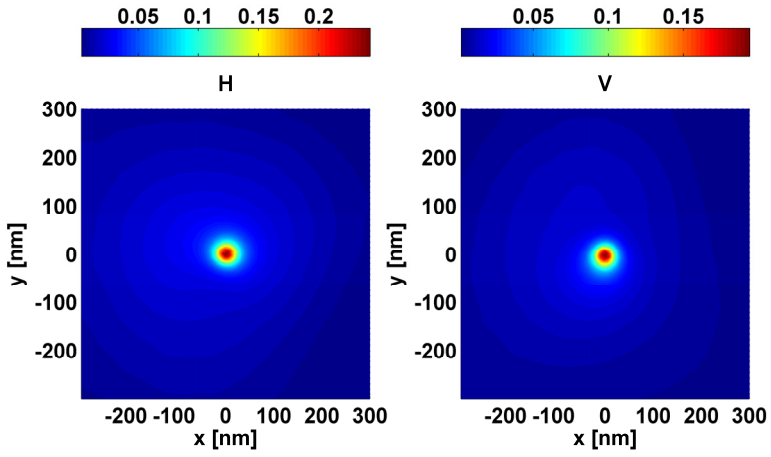

Fig. 4.4 – Normalized near-field intensity distributions over a 600 nm by 600 nm square area in a plane located at 10 nm from the apex of a probe with a spiral metal corrugation of radius r = 25 nm under H (x) and V (y) linearly polarized excitation; as the asymmetry is along all spatial directions, field localization is achieved under both H and V linearly polarized excitation.

As expected, the presence of an adirectional asymmetry results in strong field localization for both the orthogonal linearly polarized modes. The ultrasmall spots are very similar in terms of both FWHM and peak value, even though their peak intensity is still 5 times lower than the one of the radial hot spot of the axisymmetric probe. However, as reported in the next paragraphs, the intensity can be adjusted by varying either the filling material or the radius of the corrugation.

Different physical mechanisms are responsible for field localization: the diverse forms of intercoupling between inner and outer SPPs and between SPPs and WGM induced by the spiral protrusion cause the electric fields associated with SPPs on the opposite sides of the probe not to have opposite phases any more, a phenomenon leading to mutual cancellation at the tip apex for axisymmetric structures. The main advantage with respect to structures based on directional asymmetries lies in the fact that both the linearly polarized modes oriented in orthogonal directions undergo similar processes and experience analogous shrinkage with comparable peak values, because the asymmetry involves all the spatial directions.

It is worth observing that the chirality of the spiral winding (that is whether it wraps the tip in clockwise or counter-clockwise direction) plays no role in this case: similar intensity distributions have been observed by changing this property.

In order to get a deeper insight into the effects of the spiral winding, the FWHM and the peak value normalized to the peak achieved in the reference axisymmetric probe under radially polarized excitation have been calculated for the different mutual orientations α of the direction of the linearly polarized excitation with respect to the asymmetry: according to Fig. 4.5, α=0° corresponds to x linearly polarized excitation, with the two extremes of the spiral winding located along the x axis.

As visible, the most striking feature is that only negligible fluctuations occur in the FWHM. Noticeably, the structure exhibits a spot size almost insensitive to variations in the mutual orientation, offering the potential for an easier implementation of high resolution microscopy. In fact, the FWHM is related to the eventual achievable resolution and, hence, its robustness with respect to misalignments in mode injection allows a marked simplification in experimental applications. Despite this tremendous advantage, the peak value is still slightly dependent on the mutual orientation: nonetheless, the maximum deviation from the average value calculated over all the mutual positions is less than 20%, a value that could still be acceptable if the average value were sufficiently high for detection. Note that, contrary to the case of directional asymmetry where α=0° and α=90° represented the best and worst alignment, for the adirectional asymmetry different orientations are almost equivalent.

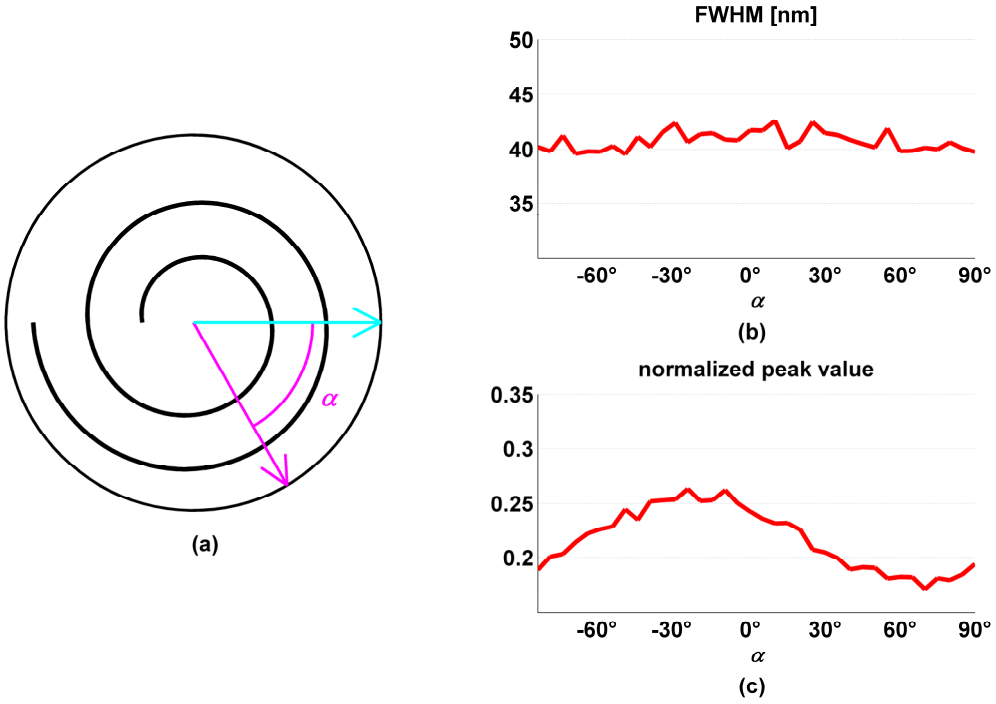

Fig. 4.5 – Behaviour of the probe with spiral corrugation for variable orientation of the input linearly polarized excitation with respect to the asymmetry: (a) schematic of the *xy* projection of the probe: the angle *α* is the one between the direction of the input linear polarization (indicated by the magenta line) and the line along which the two extremes of the spiral are aligned (represented with the cyan line); (b) FWHM of the near-field distribution for the spiral metal corrugation under variable *α*; (c) peak value of the near-field distribution normalized to the one of the axisymmetric probe under radially polarized excitation for the spiral metal corrugation under variable *α*.

4.2.1. Probe with spiral corrugation: variations in material and geometric parameters

Both the FWHM and the peak value can be tuned and optimized by changing the characteristics of the spiral corrugation. As anticipated, an indentation can be used instead of a metal protrusion, that is the metal can be carved in a spiral shape, or, as an alternative, another dielectric such as aluminium oxide (n=1.54) can fill the spiral corrugation. In fact, the coupling between surface modes at two adjacent metal/dielectric interfaces can be modulated by changing the indices of refraction of the dielectric materials (Antosiewicz et al., 2009). Additionally, the radius r of the spiral can be changed to get stronger or weaker asymmetries. This geometric parameter was varied from 15 nm to 30 nm with a step of 5 nm. More specifically, for each structure based on a particular combination of filling material and radius r, we undertook an analysis similar to the one shown earlier for the spiral metal corrugation of radius r = 25 nm, that is, we considered all the possible mutual orientations of the linearly polarized excitation with respect to the spiral winding. Then, we

calculated the average value of the peak ratio and the FWHM for the linearly polarized distributions over all the mutual orientations, and considered these values together with the maximum deviation from the corresponding average as figures of merit for comparison. The results for the three different filling materials as a function of the radius *r* are reported in Fig. 4.6.

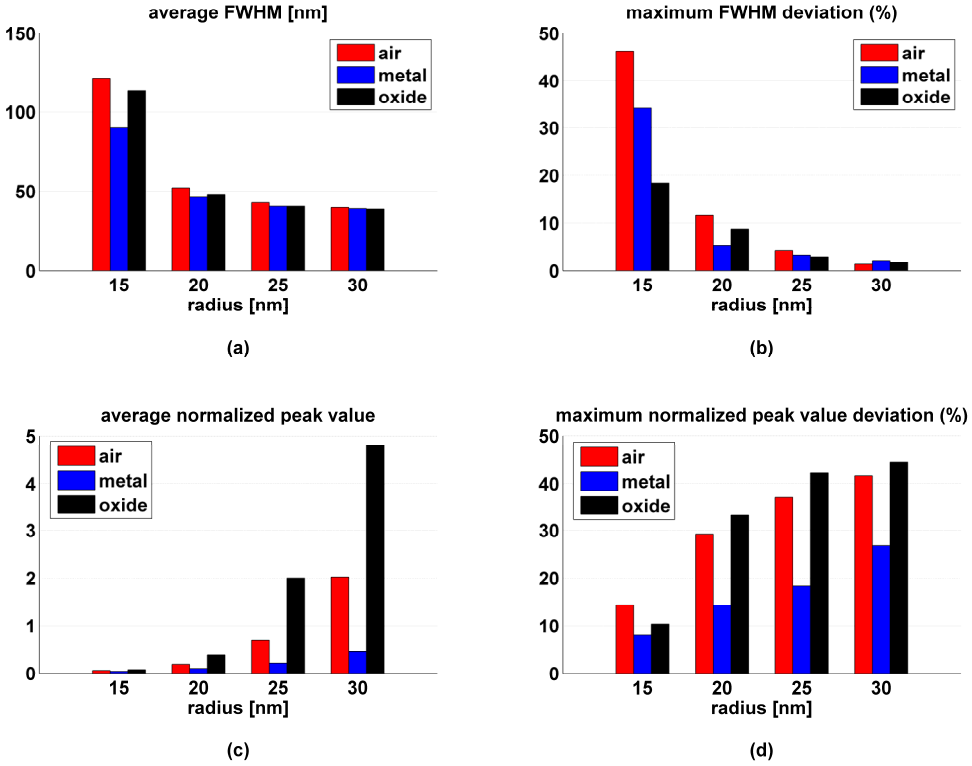

Fig. 4.6 – Characteristics of the near-field intensity distributions for different filling materials and variable radius of the spiral corrugation under linearly polarized excitation: (a) average FWHM; (b) maximum deviation from the average FWHM; (c) average peak value normalized to the one achieved in an axisymmetric probe under radially polarized excitation; (d) maximum deviation from the average normalized peak value.

A global inspection of the graphs reveals that, when the asymmetry is small, the coupling mechanisms are less efficient and the field localization is less effective, giving rise to bigger spot sizes and lower peak intensities. As the asymmetry becomes stronger, the shrinkage in the field distributions gets more remarkable and the FWHM drops to values comparable to the size of the radial spot of the axisymmetric tip (which, as stated in previous chapters, is mostly influenced by the diameter of the metal rounding at the apex). At the same time, the peak value increases as a result of improved coupling mechanisms. The better field localization is the outcome of a stronger asymmetry due to larger *r* values. However, differently from the case of directional asymmetries, these results

are achieved irrespective of the mutual orientation between the linearly polarized mode and the asymmetry introduced in the structure, as confirmed by the data about the maximum deviation. The deviation in FWHM dips as the radius increases until it reaches a point where the spot size can be considered almost constant with a variation in the reciprocal position. Although the peak value shows an opposite trend with a change of the spiral radius, the maximum deviations are still tolerable, especially if combined with a rise in the average value occurring when metal is replaced by air or, even better, by aluminium oxide. The behaviour of the probe as a function of the filling material can be explained as a result of better coupling mechanisms between inner and outer SPPs occurring when air is substituted with metal oxide, because the coupling of surface modes at two adjacent metal-dielectric interfaces becomes more efficient when the indices of refraction of the two dielectrics are closer (Janunts and Nerkararyan, 2001), as also pointed out in chapter 3.

4.3. Probe with spiral-arranged azimuthal corrugations

In the previous paragraph, the spiral corrugation has been considered as a proof of concept to explore the implications of the use of an adirectional asymmetry and the feasibility of orientation-insensitive field localization. A more practical implementation of adirectional asymmetry could be based on simpler modifications arranged in a spiral-like fashion.

In this section, the properties of this novel implementation of adirectional asymmetry, which appears more feasible for fabrication, are illustrated. We show that the more challenging spiral corrugation can be replaced by a simpler series of azimuthal corrugations over arcs of circumference in planes orthogonal to the probe axis shifted one with respect to the other to create a spiral arrangement. The parameters of this new structure can be varied to improve the field localization and enhancement for any orientation of the input linearly polarized excitation. Also for this class of probes, the initial probe structure is the axisymmetric one examined in paragraph 2.4. The azimuthal corrugations are formed by joining truncated toroids with hemispherical terminations as in paragraph 3.2. However, in order to create a spiral arrangement (and hence an adirectional asymmetry distributed over all spatial directions), the corrugations were shifted one with respect to the other as shown in the 2D projection of Fig. 4.7.

The effect of variations in the shift angle β (identical for any two consecutive corrugations) will be examined as well as the impact of variable radius and variable azimuthal extension γ of the single corrugations (which means the arc of circumference over which corrugations are spanned). In Fig. 4.7, the angle α between the direction of the input linearly polarized excitation and the angle bisector of the bottom corrugation is also defined. According to the sketches in Fig. 4.3 and Fig. 4.7, the angle bisector of the bottom corrugation is along the x axis. The z spacing between consecutive

corrugations is 150 nm. Each azimuthal corrugation can be a groove or a bump, i.e. the truncated toroid can be filled either with air or with metal. In paragraph 3.4, the analysis of directional asymmetries based on such azimuthal corrugations (null shift angle β between consecutive corrugations) revealed that the combination resulting in maximum field enhancement consisted in an alternation of grooves and bumps starting from the bottom corrugation (*amama* according to the used notation). On the grounds of our previous study we focused our attention on the same structure.

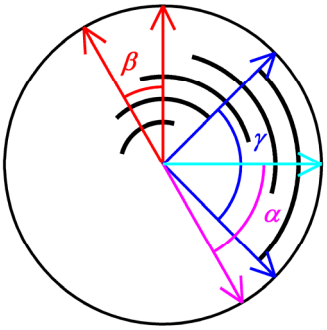

Fig. 4.7 – Schematic of the 2D projection of the probe with spiral-arranged corrugations and relevant parameters; the black arcs represent the corrugations; the angle α is the one between the direction of the input linear polarization (indicated by the magenta line) and the angle bisector of the bottom corrugation (represented with the cyan line); the angle β is the shift angle measured between the angle bisectors of two consecutive corrugations, while the angle γ is the angular extension of each corrugation. The angle bisector of the bottom corrugation is along the x axis.

As pointed out earlier, in order to have an asymmetry distributed along multiple spatial directions, the shift angle β should be different from zero. If β=0°, the structure reduces to the case of directional asymmetry considered in paragraphs 3.4 and 4.1, which means that all the five corrugations create a strong asymmetry along x. Fig. 4.8 reports the square of the norm of the electric field under x and y linearly polarized excitation for a shift angle β of 45° (adirectional asymmetry). The total azimuthal extension γ for each of the five corrugations amounts to 160° and the radius of the truncated toroids is 20 nm. For an easier comparison, the field distributions for the corresponding directional asymmetry (β=0°) already studied in the previous chapter are reported (Fig. 4.8 (a) and (b)). Distributions (calculated over a 600 nm by 600 nm square area centred at the tip apex in a transverse plane located at 10 nm from the probe apex) are normalized to the peak value achieved in an axisymmetric probe under radially polarized excitation, which represents our reference for comparison.

As expected, for β=0°, strong field localization is observed under x linearly polarized excitation, with a peak value about 8 times higher than the one attainable in an axisymmetric probe under

radially polarized excitation (Fig. 4.8(a)), while a broad weak two-lobed distribution results from the orthogonal input linear polarization (Fig. 4.8(b)), as no asymmetry is present along *y*, and no significant change with respect to an axisymmetric probe under linearly polarized excitation is present. Hence, as already said, α=0° (*x* linearly polarized excitation) represents the situation of best alignment, while α=90° (*y* linearly polarized excitation) corresponds to maximum misalignment. On the contrary, for β=45°, superfocusing is achieved for both the orthogonal polarizations (Fig. 4.8 (c) and (d)) as the asymmetry is effective in both directions. Furthermore, as visible, the two distributions show close resemblance in both peak value and FWHM, though the peak value is lower than the one achieved in case of directional asymmetry under *x* polarized excitation for both the input polarizations: orthogonal orientations are almost equivalent.

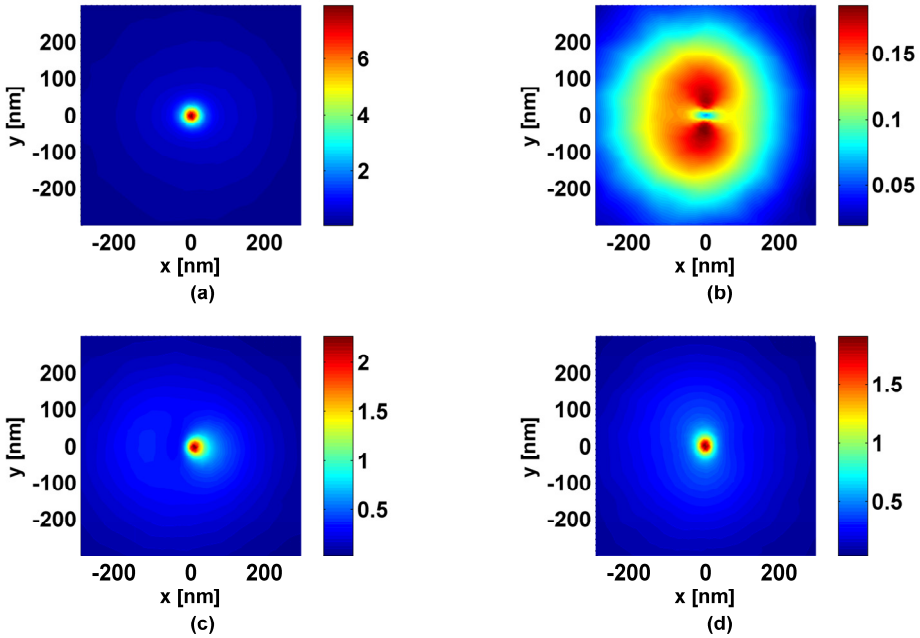

Fig. 4.8 – Comparison between probes with β=0° (directional asymmetry) and β=45° (adirectional asymmetry) (γ=160°; radius 20 nm): normalized near-field distributions in a plane located at 10 nm from the apex of a probe (a) with β=0° under *x* linearly polarized excitation; (b) with β=0° under *y* linearly polarized excitation; (c) with β=45° under *x* linearly polarized excitation; (d) with β=45° under *y* linearly polarized excitation.

In order to further confirm that the alignment of the input linear polarization along one specific direction is no longer necessary with this novel adirectional asymmetry, we compared the behaviour of the probe with directional asymmetry (β=0°; Fig. 4.1 (b) and (c)) with the one based on spiral-arranged corrugations (β=45°; Fig. 4.9 (a) and (b)) under variable orientation of the corrugations

with respect to the input linear polarization. More specifically, the FWHM and the peak value normalized to the one of the axisymmetric probe under radially polarized excitation were examined. As explained earlier, the mutual orientation is defined as the angle α between the direction of the input linear polarization and the angle bisector of the bottom corrugation; the mutual orientation specified by α was changed from -85° to 90° to encompass all the possible mutual positions.

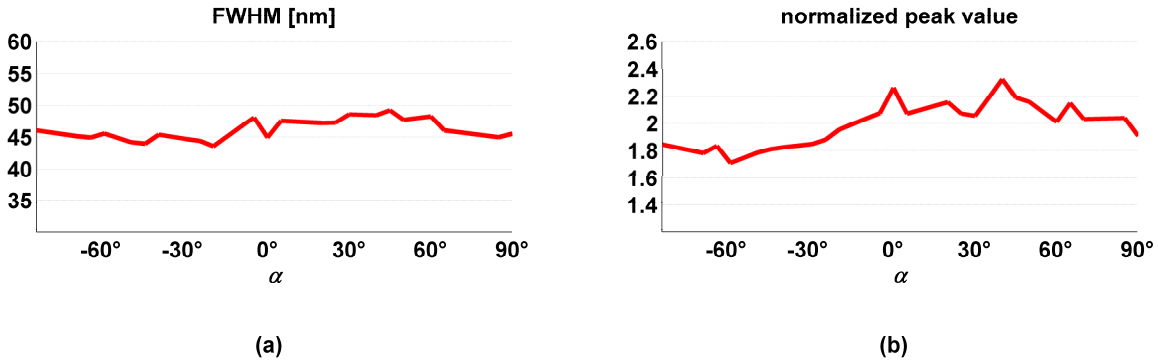

Fig. 4.9 – Behaviour of the probe with spiral-arranged corrugations for variable orientation α of the input linearly polarized excitation with respect to the asymmetry (β=45°; γ=160°; radius 20 nm): (a) FWHM of the near-field distribution for variable α; (b) peak value of the near-field distribution normalized to the one of the axisymmetric probe under radially polarized excitation for variable α.

Deviations of the peak value from the average are below 20% and those of the spot size are less than 10% for the probe with adirectional asymmetry against deviations of about 100% and 450% for the one with directional asymmetry, which demonstrates that the tip with spiral-arranged corrugations can actually afford the achievement of superfocusing under arbitrarily oriented linearly polarized excitation. In particular, the negligible variations in the FWHM indicate that the ultimate achievable resolution is almost insensitive to the input polarization direction. Similar trends were observed by changing the chirality, i.e. the handedness, of the spiral-like arrangement from counter-clockwise to clockwise.

In the next paragraphs, we will investigate the impact of geometric parameters of the corrugations on the superfocusing effect, in particular (i) the shift angle β, (ii) the angular extension γ and (iii) the radius of the corrugation.

4.3.1. Probe with spiral-arranged azimuthal corrugations: variations in the shift angle

In order to study how sensitive such a superfocusing effect is to the shift between consecutive corrugations, we carried out a set of simulations with variable shift angle β. We varied this parameter from 0° to 45°, with a step of 7.5°. The corresponding total shift between the bottom and

top corrugation is $(n-1)\cdot\beta$, where n is the number of the azimuthal corrugations. For each of the simulated structures, we considered the average behaviour over all the possible orientations of the asymmetry with respect to the input linearly polarized mode as specified by α, that is, the average normalized peak value and the average FWHM over all the possible mutual orientations of the corrugations with respect to the input linearly polarized excitation (i.e. over all α between -85° and 90°), together with the maximum variations of these figures of merit from the corresponding averages. Fig. 4.10 illustrates the results obtained for corrugations with angular extension γ of 160° and radius 20 nm.

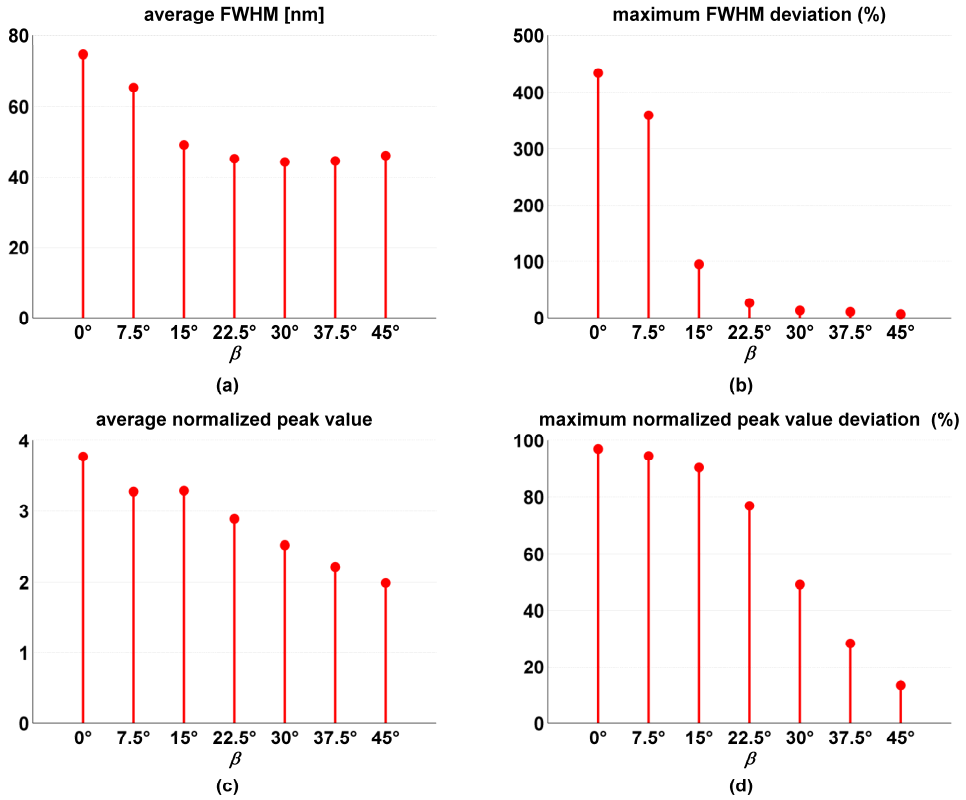

Fig. 4.10 – Characteristics of the near-field intensity distributions for the probes with corrugations arranged in a spiral-like fashion for variable shift angle β (γ=160°; radius 20 nm): (a) average FWHM; (b) maximum deviation from the average FWHM; (c) average peak value normalized to the one achieved in an axisymmetric probe under radially polarized excitation; (d) maximum deviation from the average normalized peak value.

As the shift angle β increases, the average spot size decreases because the asymmetry becomes effective in multiple directions, which allows the achievement of superfocusing under multiple mutual orientations of the input linear polarization with respect to the corrugations (Fig. 4.10(a)).

Correspondingly, the same trend is also shown by the maximum variation in the FWHM (Fig. 4.10(b)). Moreover, with increasing shift angle, the deviation from the average peak value decreases as well (Fig. 4.10(d)), but the average peak value declines slightly (Fig. 4.10(c)). These results can be explained if recalling that, as β rises, the asymmetry turns out to be more equally distributed in all spatial directions. Therefore, the behaviour over all the mutual orientations α becomes more uniform, which accounts for the small deviations from the average peak value and the average FWHM. However, the asymmetry along each spatial direction is weaker than the asymmetry perceived by a x linearly polarized excitation when the asymmetry is fully directional with the angle bisectors of all the corrugations on the x axis (β=0°); hence, the average peak value gets lower.

The same trends with shift angle were observed considering corrugations with the same radius (20 nm) and a different angular extension of the corrugation (γ=90°), as shown in Fig. 4.11. However the achievable peak values are lower than those retrieved with a broader extension, as will be shown also in the analysis of the impact of γ.

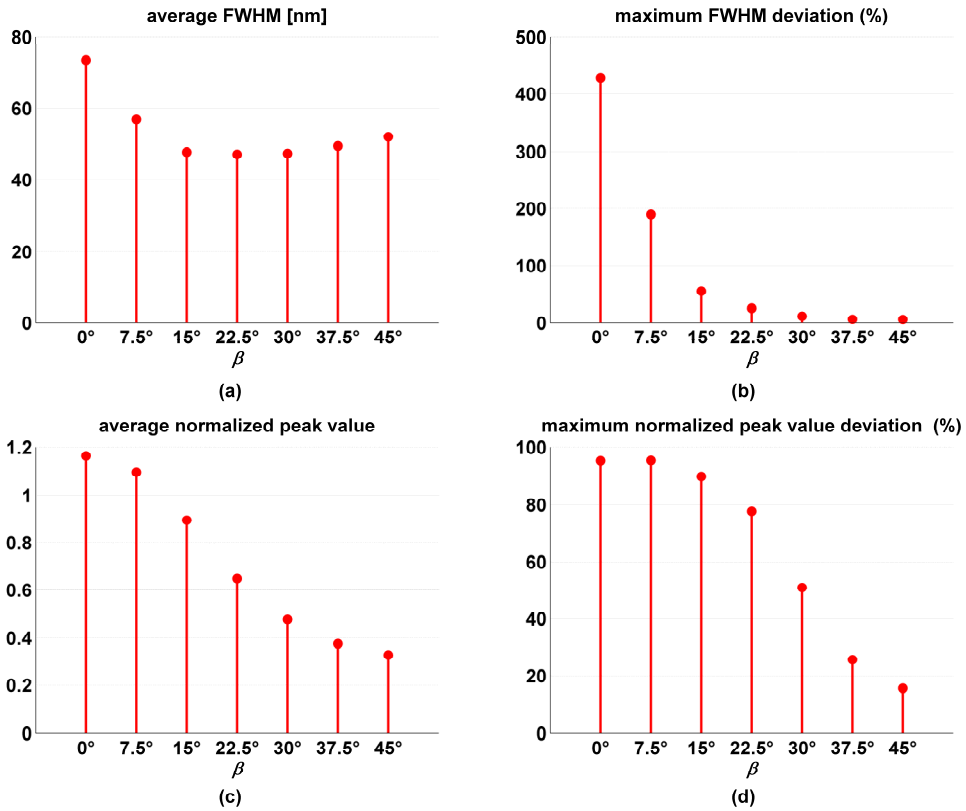

Fig. 4.11 – Characteristics of the near-field intensity distributions for the probes with corrugations arranged in a spiral-like fashion for variable shift angle β (γ=90°; radius 20 nm): (a) average FWHM; (b) maximum deviation from the average FWHM; (c) average peak value normalized to the one achieved in an axisymmetric probe under radially polarized excitation; (d) maximum deviation from the average normalized peak value.

4.3.2. *Probe with spiral-arranged azimuthal corrugations: variations in the angular extension*

Just as in the previous simulations, for the investigation of the effect of another geometric parameter of the corrugation, i.e. its angular extension γ, all the corrugations are supposed to be identical: the radius of each truncated toroid is 20 nm and the shift angle β between consecutive corrugations amounts to 45°. In our calculations we varied the angular extension γ of the corrugations from 30° to 160° with a step of 10°. Also for this set of simulations we considered all the possible mutual orientations α of the input linear polarization with respect to the corrugations and examined the average behaviour and the deviations from the average, as previously explained. Results are reported in Fig. 4.12.

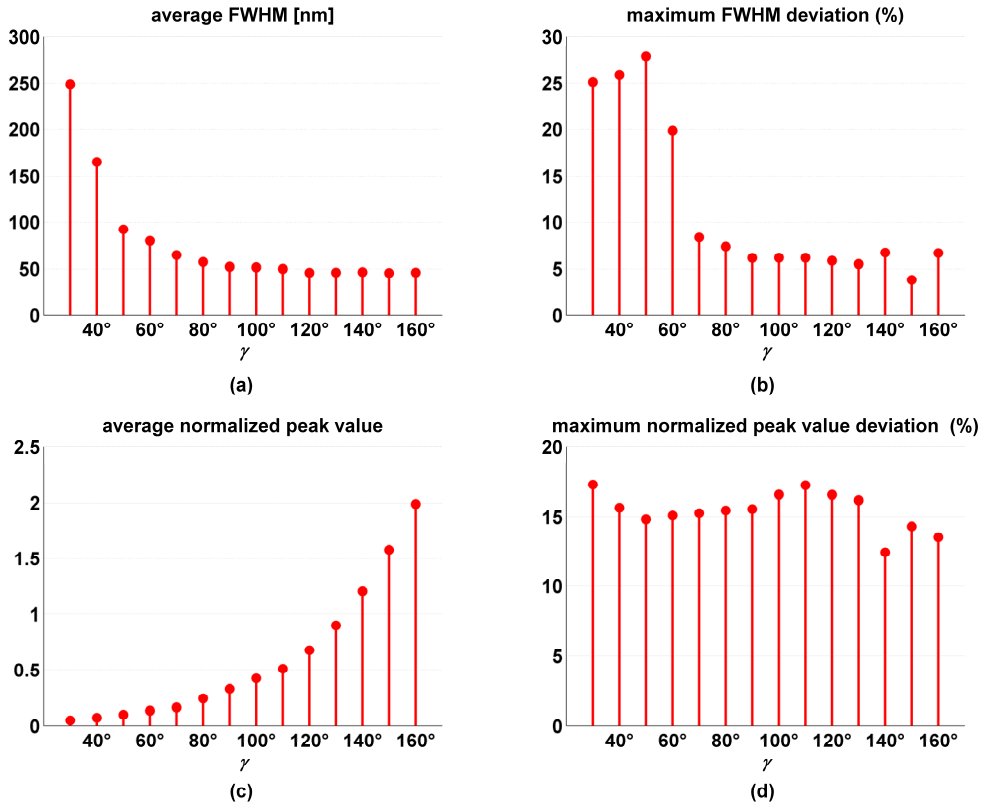

Fig. 4.12 – Characteristics of the near-field intensity distributions for the probes with corrugations arranged in a spiral-like fashion for variable angular extension γ (β=45°; radius 20 nm): (a) average FWHM; (b) maximum deviation from the average FWHM; (c) average peak value normalized to the one achieved in an axisymmetric probe under radially polarized excitation; (d) maximum deviation from the average normalized peak value.

For angular extensions γ above 70°, the field confinement under linearly polarized excitation, as measured with the FWHM, becomes remarkable compared to an axisymmetric probe (Fig. 4.12(a)).

The stronger asymmetry for increasing extension results in higher peak values (Fig. 4.12(c)), but the homogeneity of the probe behaviour in all spatial directions is guaranteed for any value of γ, as demonstrated by the deviations from the average peak value, which are below 20% (Fig. 4.12(d)), and those in the spot size, even under 10% for the cases of stronger confinement (Fig. 4.12(b)). Simulations with a different shift angle (15°) and variable angular extension have shown similar trends in terms of average FWHM and peak value, but higher deviations due to the less homogeneous distribution of the asymmetry for a smaller shift angle commented in Fig. 4.10 and Fig. 4.11.

4.3.3. Probe with spiral-arranged azimuthal corrugations: variations in the radius

Finally, we also assessed the effect of a variation in the radius, which we increased from 15 nm to 30 nm with a step of 5 nm. The shift angle β between corrugations and the angular extension of each single corrugation γ were 45° and 160 nm, respectively. Results are plotted in Fig. 4.13.

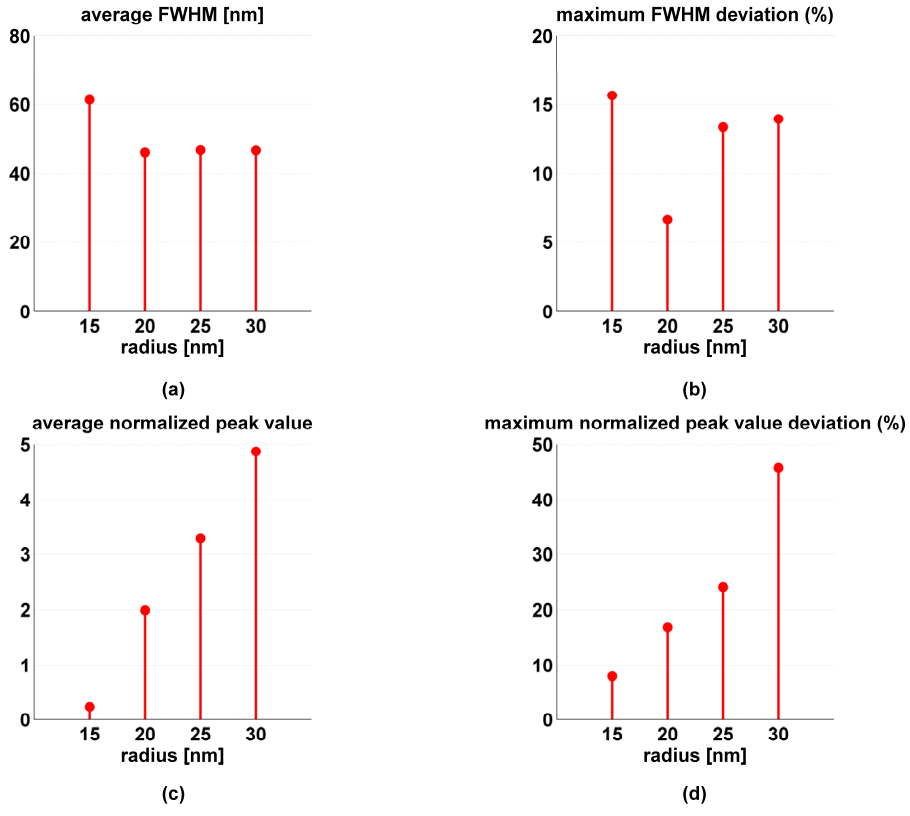

Fig. 4.13 – Characteristics of the near-field intensity distributions for the probes with corrugations arranged in a spiral-like fashion for variable radius of the corrugation (β=45°; γ=160°): (a) average FWHM; (b) maximum deviation from the average FWHM; (c) average peak value normalized to the one achieved in an axisymmetric probe under radially polarized excitation; (d) maximum deviation from the average normalized peak value.

The graphs show that spatial localization of the field is comparable in all the cases (Fig. 4.13 (a) and (b)) with variations in spot size always below 20%; the higher variations in the peak values over all the possible mutual orientations for increasing radius (Fig. 4.13(d)) are compensated by an increase in average peak values (Fig. 4.13(c)). Similar trends were observed also for the probe with a spiral corrugation of variable radius.

4.4. Final remarks

An impressive simplification of the mode injection procedure in fully metal-coated probes can ensue from the introduction of an adirectional asymmetry, that is an asymmetry covering the whole angular range of the tip and devoid of reflection symmetry. The actual structures here proposed as a proof of concept are based on a spiral design, either a single spiral corrugation or azimuthal corrugations arranged in a spiral-like fashion. The lack of a preferential spatial direction allows superfocusing under any arbitrarily oriented linearly polarized excitation, thereby waiving any requirement on alignment typical of asymmetric structures with directional asymmetries. In fact, in this case, the input linear polarization does not need any longer to be aligned along one specific direction, because the asymmetry is present in any spatial direction: light funnelling to an ultrasmall spot is achieved irrespective of the input polarization direction.

The reason for a superfocusing effect under linearly polarized excitation similar to the one observed in an axisymmetric probe under radially polarized excitation is the same for all the asymmetric structures, either directional or adirectional, and lies in the intermingling of mode coupling mechanisms between waveguide modes and SPPs and in the interaction of the SPPs on the outer metal surface with the corrugations. In fact, the presence of the asymmetry avoids destructive interference occurring in the axisymmetric structure under linearly polarized excitation and allows the achievement of field localization typical of the SPPs excited by a radially polarized mode. The main difference between directional and adirectional asymmetries is that, in the latter case, the extension of the asymmetry to all spatial directions allows the attainment of such effect for any linear polarization direction. A more uniform distribution of the asymmetry over all spatial directions corresponds to a more stable behaviour under diverse linear polarization directions, which means lower variations in peak value and spot size as the mutual orientation between the corrugations and the polarization direction changes.

The rate of improvement consequent upon the use of an adirectional asymmetry instead of directional ones has been estimated by comparing the orientation-dependent behaviour of structures based on the two different forms of asymmetries. The maximum deviation in spot size plummets from values between 280% and 500% for directional asymmetries to values of about 45% in the

worst case and even below 2% for proper choices of spiral parameters; likewise, the maximum variation in peak intensity falls from above 90% for directional asymmetries to below 45% for an adirectional asymmetry. Hence, the creation of a hot spot whose size is almost independent of the orientation of the linear polarization and whose peak value changes only within a small range not only allows one to avoid the use of the radially polarized mode, but also permits not to care about the alignment of the linearly polarized mode with respect to the asymmetry. Requirements on alignment are correspondingly significantly relaxed.

Structural parameters of these novel adirectional asymmetries (radius and type of corrugations for the probe based on a single spiral corrugation; shift angle, radius and angular extension of the corrugations for the tip consisting in spiral-arranged azimuthal corrugations) can be adjusted to improve field localization and decrease its sensitivity to the input polarization direction. In agreement with what has been observed for directional asymmetries, better field localization ensues from stronger asymmetries encompassing larger tip sections as is the case, e.g., for azimuthal corrugations with broader angular extension. An enlargement of the computational domain could allow the study of the effects of other parameters, like the period, the number of turns and the shape of the spiral corrugation or the number of corrugations and the period for the spiral-arranged azimuthal corrugations; however, computational limits amply restrict the range of parameters that can be investigated.

As a matter of fact, the use of adirectional asymmetries could bring about a staggering simplification and improvement in experimental applications.

5. Interaction of asymmetric probes with fluorescent molecules

The interaction of our novel asymmetric probes with fluorescent molecules is investigated in this chapter. The motivation for this study is twofold: first of all, single fluorescent molecules offer a powerful technique to characterize the optical properties of novel probes as they provide insight into the single vectorial components of the electric field close to the probe apex. Second, the analysis of this interaction is essential for SNOM applications because of the use of fluorescent molecules in material and life science to investigate the properties of biological molecules and polymers. For both purposes, a thorough theoretical understanding of the achievable near-field fluorescence maps is necessary. Our finite element analysis shows how such near-field probes can be effectively used for high resolution detection of single molecules, in particular those with a longitudinal dipole moment. The content of this chapter (including text and figures) is mostly published in Lotito et al. (2011a).

5.1. Introduction

In the previous chapters, we have observed how axisymmetric fully metal-coated dielectric SNOM probes under internal back excitation can be used for high resolution applications under radially polarized excitation. Moreover, in order to circumvent the inconvenience inherent in the use of a radially polarized excitation and get nanofocusing under linearly polarized excitation, the symmetry of the originally axisymmetric structure can be broken by introducing asymmetric modifications with appropriately tailored characteristics. For this purpose we have designed and modelled different novel probe configurations, which can be grouped into two main subcategories, which we called directional and adirectional depending on whether the asymmetry lies along one specific spatial direction or is distributed along all spatial directions. A proper engineering of the asymmetry can lead to spot sizes comparable to those achieved under radially polarized excitation with even better peak intensity values. Therefore, such asymmetric structures could potentially be promising candidates for high resolution SNOM applications.

However, the accurate characterization of the near-field optical properties of novel probe structures is a challenging task. Among the possible solutions to get a good picture of the near-field emitted at the tip apex, the use of a second near-field tip has been proposed: in the so-called tip-on-tip or probe-to-probe configuration, one tip with known properties is used as a probe to collect the near-field distribution of the novel tip, used under internal illumination, in a constant height mode

(Tortora et al., 2007; Yatsui et al., 2002). As evident, such an arrangement requires a good alignment between the two probe axes, which adds to the complexity of the experimental set-up. A more detailed description of the near-field pattern at the probe apex can be obtained using single fluorescent molecules. In the seminal work by Betzig and Chichester (1993), fluorescent molecules were used to map the electric field distribution of aperture probes: in fact, a fluorescent molecule can be interpreted as an electrical dipole acting as a point detector for the components of the electric field aligned along its absorption dipole direction, because the emitted fluorescence intensity is proportional to the square of the local electric field parallel to its absorption dipole. As a consequence, this characterization technique provides precious glimpse at the vectorial components of the electric field distribution close to the tip apex.

The interaction of single fluorescent molecules with aperture probes has been thoroughly analysed both experimentally and theoretically (Hollars and Dunn, 2000; Moerland et al., 2005; Veerman et al., 1999). The interest in such a topic stems not only from its importance as a characterization technique, but also because single molecule detection is a hot issue in biological as well as in material science (Dunn, 1999; Kulzer and Orrit, 2004). A requisite of paramount importance for single fluorescent molecule detection is the reduction of the excitation volume of the molecule in order to discriminate the signal emitted by a single molecule among the signal arising from surrounding molecules, which acts as an interfering background (Garcia-Parajo et al., 2001). SNOM looks particularly suitable for this purpose due to the strong localization of the field emitted by the probe; moreover, due to the presence of transverse and longitudinal field components close to the probe apex, it has been used for the determination of the 3D orientation of single fluorophores by controlling the polarization of the excitation light (van Hulst et al., 2000). Aperture SNOM probes have been employed for chromosome mapping (van Hulst et al., 1997), in single molecule experiments on dendritic molecules (van Hulst et al., 2000) or for the measurement of the orientation of biological molecules on surfaces and in membranes (Hollars and Dunn, 2000). They have also been helpful in the analysis of crystalline and amorphous phases in polymers (Garcia-Parajo et al., 2001) and for the determination of rotational and translational diffusion constants of single molecules embedded in polymer hosts (Ruiter et al., 1997).

Contrary to the vast literature available for aperture probes, a systematic and comprehensive numerical analysis of the interaction of apertureless probes with single fluorescent molecules is still missing, although high resolution in single fluorescent molecule detection has been demonstrated for measurements performed using apertureless probes under internal radially polarized excitation, due to the better field confinement (Frey et al., 2006). Furthermore, as anticipated, asymmetric SNOM probes excited with linearly polarized light are expected to guarantee field localization with peak intensity comparable or better than axisymmetric fully metal-coated probes under radially polarized

excitation, while enabling a simplification of the injection procedure. Hence, their interaction with single fluorescent molecules is of primary interest as well.

In this chapter, we investigate the interaction between novel asymmetric SNOM probes and a single fluorescent molecule. First, the interaction between an axisymmetric fully metal-coated probe under radially polarized excitation and a single fluorescent molecule will be examined. Next, these results will be compared with those obtained in case of asymmetric probes. It will be shown that the vectorial components of the near-field emitted by an asymmetric probe under proper linearly polarized excitation closely resemble those of an axisymmetric fully metal-coated probe under radially polarized excitation, with the presence of strong longitudinal field components. Hence, on the one hand, single fluorescent molecule detection can be used as a characterization technique to analyse how effective this conversion into a mainly longitudinally polarized emission pattern is for asymmetric probes. On the other hand, asymmetric probes with known near-field distribution can be used for single fluorescent molecule detection as an effective substitute for fully metal-coated axisymmetric probes. In this case, the comparison of the experimental fluorescence measurements with our numerical results may aid in the determination of the 3D orientation of single molecules.

5.2. Single photon emission

The mechanism of fluorescence can be explained using a three-level quantum system approximation (Fig. 5.1(a)) (Garcia-Parajo et al., 2001; Moerner and Fromm, 2003; Novotny and Hecht, 2006), consisting of a singlet ground state S_0 (1), a singlet first excited state S_1 (2) and a triplet state T_1 (3).

A molecule excited by the absorption of a pump photon rapidly relaxes to the lowest electronic excited state via vibrational modes of the molecule (intramolecular vibrational relaxation) and of the host (phonons); from the lowest electronic excited state, fluorescence photons can be emitted; after the emission, further vibrational and phonon relaxation brings the molecule back to the initial ground state (Moerner and Fromm, 2003). Relaxation mechanisms represent energy losses, producing a spectral redshift between absorption and emission bands, known as Stokes shift; although the behaviour of some fluorophores can be described by a simplified two-level system, a more accurate model is given by a three-level system, which takes into account the probability for intersystem crossing in the triplet state manifold, during which the molecule does not absorb or emit photons any longer (Moerner and Fromm, 2003).

The rate of excitation k_{12} of the molecule from the ground state 1 to the first excited state 2 is proportional to the absorption cross section of the molecule σ (approximated at room temperature as $\sigma = 1000\ln(10)\varepsilon / N_A$ [cm^2], with ε being the molar extinction coefficient [L mol^{-1} cm^{-1}] and N_A the Avogadro constant amounting to 6.02214129 × 10^{23} mol^{-1}) and to the incident excitation

intensity I_0 according to $k_{12} = \sigma I_0 / h\nu$ where $h\nu$ is the photon energy (with h being the Planck constant equal to 6.626068 × 10^{-34} m^2 kg s^{-1} and ν the frequency); decay from the excited state can take place radiatively or nonradiatively with decay rates equal to k_r and k_{nr}, respectively (Lakowicz, 2006).

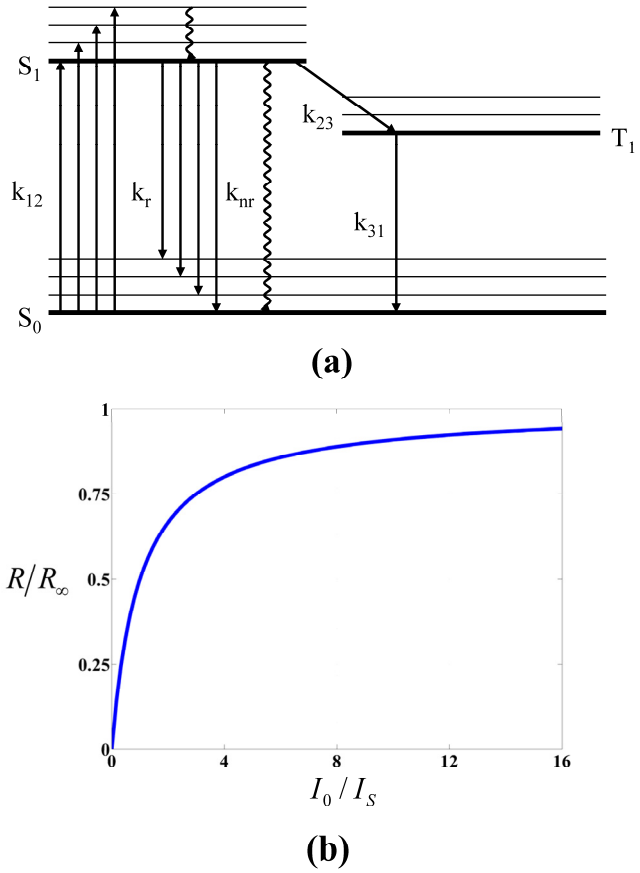

Fig. 5.1 – Photon emission by a fluorescent molecule: (a) typical three-level approximation consisting of a singlet ground state S_0 (1), a singlet first excited state S_1 (2) and a triplet state T_1 (3), with indication of the different transition rates (the lowest energy level of each state is marked with a thick solid line); (b) emission rate R normalized to the emission rate at infinitely strong excitation intensities R_∞ as a function of the excitation intensity I_0 normalized to the saturation intensity I_S (adapted from Moerner and Fromm, 2003 and Novotny and Hecht, 2006).

The total decay rate from the first excited state to the ground state is $k_{21} = k_r + k_{nr} = 1/\tau_F$ with τ_F being the fluorescence lifetime (typically of the order of nanoseconds). Intersystem crossing to the triplet state 3 occurs with a rate k_{23} and relaxation from the triplet state to the ground state occurs at a rate $k_{31} << k_{21}$, with the lifetime of the triplet state k_{31}^{-1} in the range of microseconds to

seconds. The excitation and relaxation mechanisms affecting the population p_i of each state with $i = \{1,2,3\}$ can be formulated in the following set of rate equations (Novotny and Hecht, 2006):

$$\begin{aligned} \dot{p}_1 &= -k_{12} p_1 + (k_r + k_{nr}) p_2 + k_{31} p_3 \\ \dot{p}_2 &= k_{12} p_1 - (k_r + k_{nr} + k_{23}) p_2 \\ \dot{p}_3 &= k_{23} p_2 - k_{31} p_3 \\ 1 &= p_1 + p_2 + p_3 \end{aligned} \qquad \textbf{(5.1)}$$

In steady-state conditions, i.e. for $\dot{p}_i = 0$, the rate R at which the system emits photons exhibits a saturation behaviour described as (Fig. 5.1 (b)) (Novotny and Hecht, 2006):

$$R = p_2 k_r = R_\infty \frac{I_0 / I_S}{1 + I_0 / I_S} \qquad \textbf{(5.2)}$$

where I_0 is the intensity of the exciting light, R_∞ is the emission rate at infinitely strong excitation intensities and I_S is the intensity at which the emission rate equals $R_\infty / 2$.

In order to get a significant fluorescence signal also for moderate excitation intensity one should have high R_∞. As R_∞ is proportional to the so-called fluorescence quantum yield QY defined as (Moerner and Fromm, 2003):

$$QY = \frac{k_r}{k_r + k_{nr}} \qquad \textbf{(5.3)}$$

this means that a high QY is desirable.

5.3. Modelling of probe-molecule interaction

The computational domain and simulation settings for the finite element analysis of the interaction between axisymmetric and asymmetric probes are the same described in paragraph 2.4. In most of the calculations, we considered the cut probe as an example of asymmetric probe due to the simplicity to fabricate this probe using FIB milling, a technique commonly employed for the creation of flat apertures in standard aperture probes. The geometric parameters characterizing this probe are the cut height and the cut angle. The reader is referred to chapter 3 for further elucidations about this probe. Fig. 5.2 shows the axisymmetric and cut probe together with the quantities necessary to describe the dipole moment of the fluorescent molecules.

The interaction with fluorescent molecules with different orientations located at 10 nm from the probe apex has been modelled by recalling that the fluorescence intensity I emitted by a molecule is related to the square of the dot product of the local electric field $\boldsymbol{E}$ and the normalized absorption dipole moment $\boldsymbol{p}$ far from saturation (Betzig and Chichester, 1993):

$$I \propto \left| \boldsymbol{E} \cdot \boldsymbol{p} \right|^2 \tag{5.4}$$

Equation (5.4) highlights the dependence of the fluorescence intensity I on both the absolute value and the direction of the electric field, thereby explaining the ability of a fluorescent molecule to provide a vectorial picture of the local electric field. On the contrary, fluorescent nanobeads contain an ensemble of N randomly oriented and incoherently emitting molecules, giving rise to a fluorescence intensity proportional to (Drezet et al., 2004; 2004a):

$$I \propto \sum_{i=1}^{N} \left| \boldsymbol{E}_i \cdot \boldsymbol{p}_i \right|^2 \approx \frac{N}{3} p^2 \left\langle E^2 \right\rangle_{sphere \quad volume} \tag{5.5}$$

where p is the typical value of the absorption dipole moment. Therefore, fluorescently labelled nanospheres act as isotropic detectors of the average electric field intensity, and, although also used for SNOM probe characterization, they act merely as scalar detectors.

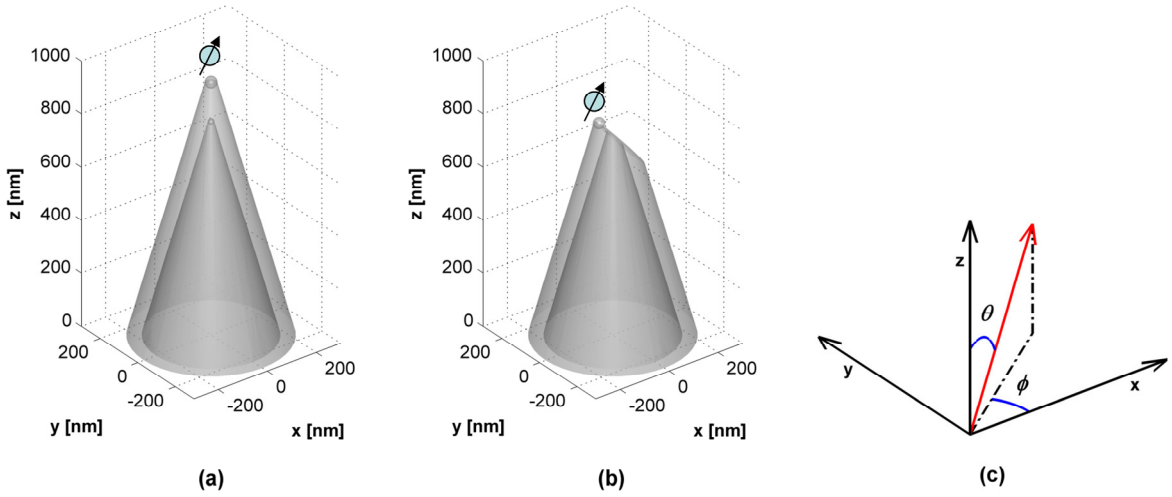

Fig. 5.2 – Sketch of the simulated structures: (a) axisymmetric probe with a stylized representation of a fluorescent molecule close to the apex; (b) asymmetric cut probe with a stylized representation of a fluorescent molecule close to the apex; (c) representation of the orientation of the dipole (red vector) through the polar angle θ and the azimuthal angle ϕ (Betzig and Chichester, 1993; Veerman et al., 1999; Zwillinger, 2012); the origin of the reference system used to define the angles of interest in (c) does not coincide with the one of (a) and (b). According to Fig. 5.2(b), the asymmetry is present along the x axis.

The normalized absorption dipole moment that characterizes the 3D dipole orientation can be formulated as:

$$\boldsymbol{p} = \begin{pmatrix} \sin\theta\cos\phi \\ \sin\theta\sin\phi \\ \cos\theta \end{pmatrix} \tag{5.6}$$

where θ and ϕ represent the polar and azimuthal angle, respectively (Fig. 5.2(c)). In our case the local field $\boldsymbol{E}=(E_x,E_y,E_z)$ coincides with the electric field distribution on the *xy* plane at a distance *z* of 10 nm above the probe apex. For the asymmetric structure, we will consider also the effect of the angle α between the direction of the input linear polarization and the direction along which the asymmetry is present: according to the sketch in Fig. 5.2(b), the asymmetry lies along the *x* axis. In the following paragraphs, the distributions obtained for fluorophores with different orientations for an axisymmetric probe under radially polarized excitation are reported and compared to those obtained for an asymmetric probe under linearly polarized excitation.

5.4. Interaction between an axisymmetric probe and a fluorescent molecule

The axisymmetric probe was excited with a radially polarized excitation, while changing the polar and azimuthal orientation of the fluorescent molecule from 0° to 90° with a step of 30°. The simulated fluorescence intensity distributions calculated according to equation (5.4) on a 400 nm by 400 nm square area centered on the probe apex are shown in Fig. 5.3. The number in the upper left corner of each plot indicates the peak intensity for a molecule with a specific dipole orientation normalized to the peak of the total local electric field intensity $|\boldsymbol{E}|^2$ (square of the norm of the electric field). As apparent, the radially polarized excitation results in a strong longitudinal local field at the tip apex (corresponding to θ=0°), made up of a single hot spot, and weaker orthogonal transverse components (corresponding to θ=90° and ϕ=0° and θ=90° and ϕ=90°, respectively) of almost equal magnitude appearing as two-lobed patterns. Note that we use the adjective longitudinal for the component aligned along the probe axis *z* and transverse for those lying in the *xy* plane. Similarly, we will adopt the same expressions to refer to molecules with a dipole moment either oriented along *z* or lying in the *xy* plane.

The calculated field distributions can help in the interpretation of fluorescence measurements and in the determination of the 3D orientation of a fluorescent molecule. Due to the axial symmetry of both the probe and the input excitation, a variation in the azimuthal angle of the fluorophore does imply almost no change in the peak value and in the overall shape of the intensity distribution, which rotates only its prevalent orientation according to ϕ. On the contrary, a variation of the polar angle θ from 0° to 90° gives rise to a decrease in the peak intensity and a gradual transition from a single spot to a two-lobed distribution, as the dipole absorption moment overlaps dominantly with the weaker transverse components of the local electric field rather than with the stronger longitudinal component. The FWHM varies from about 30 nm for θ between 0° and 60° to a maximum of about 80 nm for a dipole without any longitudinal component (θ=90°).

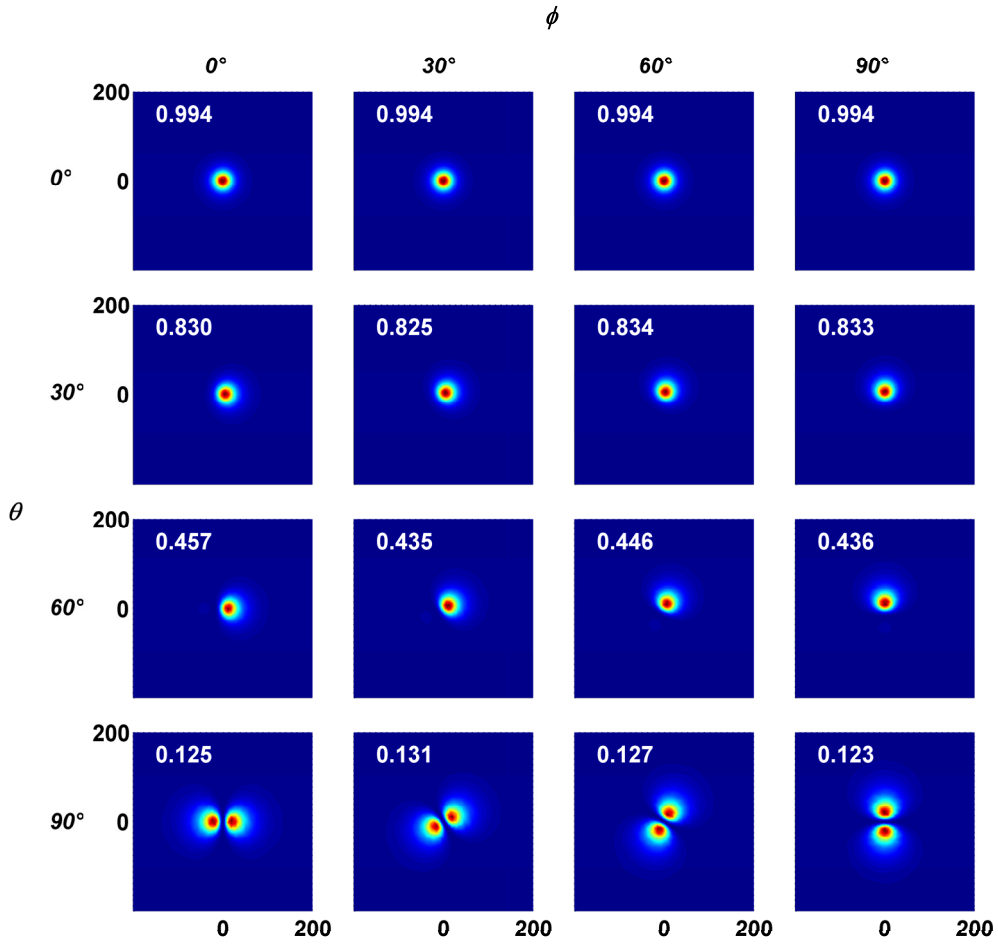

Fig. 5.3 – Simulated fluorescence intensity maps over a 400 nm by 400 nm square area for single molecules with different orientations (as specified by the polar angle θ and the azimuthal angle ϕ) excited by an axisymmetric fully metal-coated probe under radially polarized excitation and located at a distance of 10 nm from the tip apex. All the maps are reported on the same colour scale, with each plot normalized to its peak intensity value.

Some notable features with respect to aperture probes under usual linearly polarized excitation are worth being pointed out. First, the eloquently distinct dominance of a single lobe longitudinal component in the probe near-field distribution marks a striking difference and has important consequences on the imaging of dipoles with a mainly longitudinal dipole moment. These molecules are usually imaged as two lobes with aperture probes, because the longitudinal component of the electric field close to the aperture is strong only on the aperture edge at two diametrically opposite positions aligned along the direction of the input linear polarization. From a practical standpoint, better imaging of molecules with a mainly longitudinal dipole moment (like terrylene molecules in p-terphenyl (Butter and Hecht, 2006) or TRITC-DHPE molecules in DPPC monolayers (Hollars and Dunn, 2000)) could be achieved. Moreover, the determination of the orientation of molecules with

the same polar angle and different azimuthal orientation becomes easier. In fact, such molecules are imaged almost identically in terms of shape and intensity of the fluorescence pattern with fully metal-coated probes under radially polarized excitation, apart from the rotation by ϕ, which allows the determination of the azimuthal component of the fluorophore dipole moment. On the contrary, using aperture probes, strong differences in intensities and shape of the field distributions emerge in molecules with variable azimuthal angle due to the significant differences in orthogonal transverse components close to the aperture, with variations in peak intensities by even two orders of magnitude (Veerman et al., 1999).

5.5. Interaction between an asymmetric probe and a fluorescent molecule

The interaction with single fluorescent molecules has been investigated also for an asymmetric probe based on an oblique cut, creating an asymmetry along *x*. Fig. 5.4 refers to a structure with a cut angle of 30° and a cut height of 766 nm under *x* linearly polarized excitation (i.e. oriented along the direction of the asymmetry; α=0°).

The dominance of the longitudinal component over the transverse components of the electric field is evident also in this case; the two orthogonal transverse components still exhibit a double-lobed structure, even if they are slightly different in magnitude, as the electric field component aligned along the input linear polarization direction prevails against the orthogonal one. Therefore, while for the axisymmetric probe under radially polarized excitation almost no change in the fluorescence intensity mapping occurred with the azimuthal angle ϕ at constant polar angle θ, for the asymmetric probe minor variations are observed upon a change of ϕ due to the slight inequality of the two transverse components. However, such negligible variations do not represent a major pitfall: the close resemblance with the fluorescence distributions obtained for an axisymmetric probe under radially polarized excitation is still remarkable, which makes the asymmetric structure a promising alternative to the axisymmetric one for single fluorescent molecule studies, as it offers the advantages pointed out for the axisymmetric probe, but under an easier linearly polarized excitation.

To better emphasize the similarities of the distributions obtained for the axisymmetric and the asymmetric probes, we examined the projections along the y=0 axis for ϕ=0° and variable θ (Fig. 5.5 (a) and (b)) and along the straight line $x \cdot \tan(\phi)$ for θ=90° and variable ϕ (Fig. 5.5 (c) and (d)).

For both the axisymmetric and the asymmetric probes, the fluorescence map becomes two-lobed as the polar angle θ approaches 90° (Fig. 5.5 (a) and (b)). In the asymmetric probe (Fig. 5.5(b)) a slight asymmetry appears in the two lobes for θ=90° and ϕ=0°, but the overall shape as well as the FWHM are similar to the ones of the axisymmetric structure (Fig. 5.5(a)), with the maximum spot

size varying from about 30 nm for θ between 0° and 60° to about 74 nm for a dipole without any longitudinal component (θ=90°). For variations in the azimuthal orientation of the molecule at constant polar angle θ, we get two-lobed patterns for both structures and all azimuthal angles (Fig. 5.5 (c) and (d)): in case of the asymmetric probe, we observe small asymmetries between the two lobes and peak fluctuations, but the asymmetry between the lobes gradually vanishes as the dipole moment becomes orthogonal to the input linear polarization (Fig. 5.5(d)).

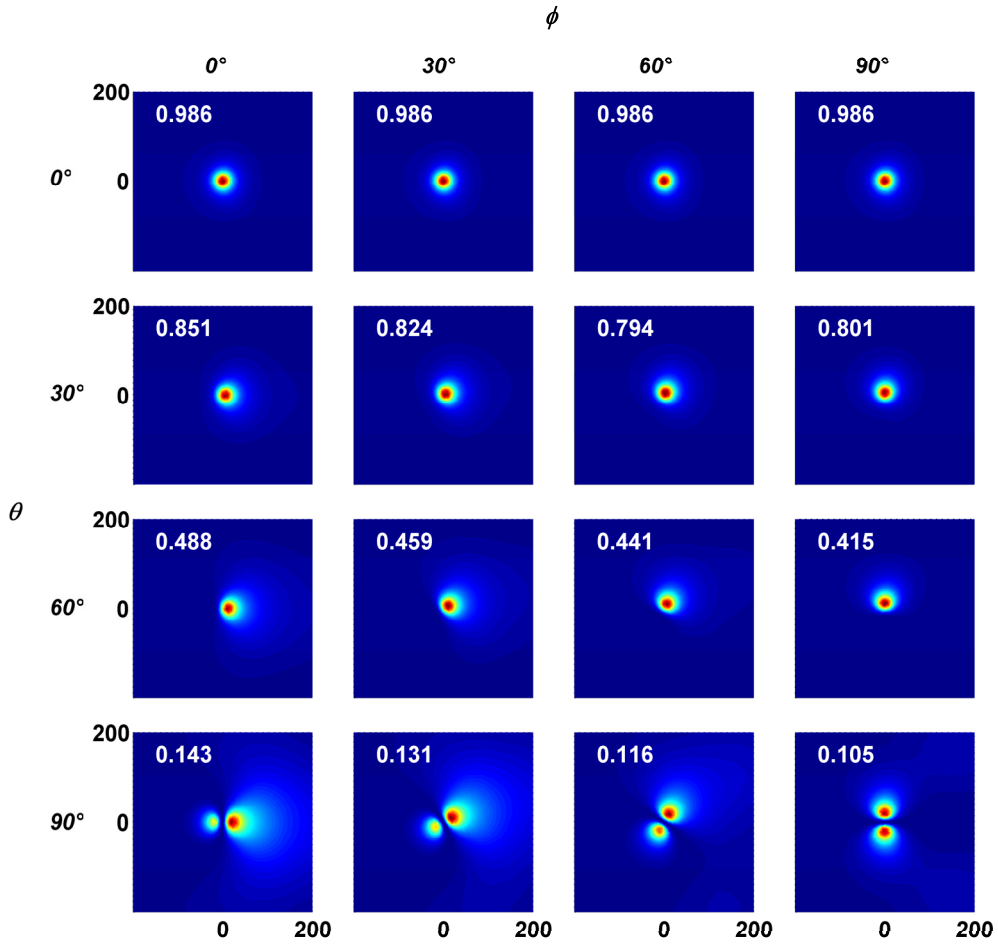

Fig. 5.4 – Simulated fluorescence intensity maps over a 400 nm by 400 nm square area for single molecules with different orientations (as specified by the polar angle θ and the azimuthal angle ϕ) excited by a cut probe under linearly polarized excitation along the direction of the asymmetry (x) and located at a distance of 10 nm from the tip apex. All the maps are reported on the same colour scale, with each plot normalized to its peak intensity value.

To study how effective the conversion into a mainly longitudinally polarized distribution is for asymmetric probes with different geometric parameters (cut height and cut angle), the behaviour of various probe structures has been examined. As figures of merit for a comparison, the following

quantities have been considered (Tab. 5.1): first, the ratio of the peak intensity of the longitudinal and transverse components aligned along x and y to the peak intensity of the total electric field; second, the range of variation of the FWHM for fluorescent molecules with longitudinal and transverse dipole moments. In order to highlight the relative magnitude of the total electric field intensity for the different probe structures, the peak value of the total electric field intensity for each structure normalized to the one of the axisymmetric probe has been reported as well.

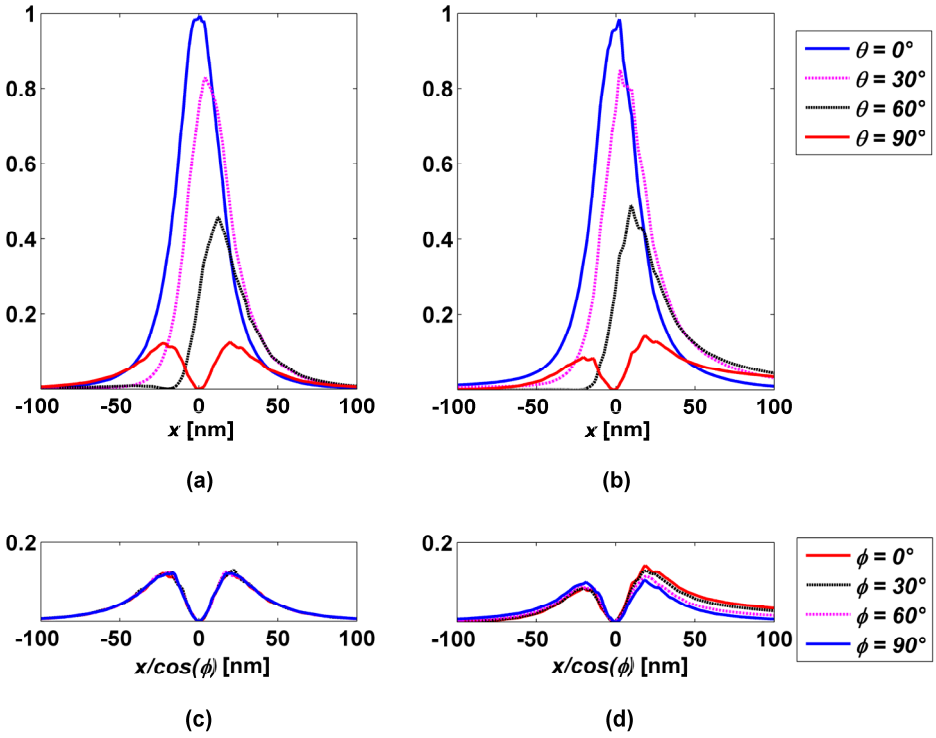

Fig. 5.5 – Line projections of the fluorescence distribution: (a) profile along x for a molecule with azimuthal angle ϕ=0° and variable polar angle obtained with an axisymmetric probe under radially polarized excitation; (b) profile along x for a molecule with azimuthal angle ϕ=0° and variable polar angle obtained with an asymmetric cut probe under x linearly polarized excitation; (c) profile along the straight line $x \cdot \tan(\phi)$ for a molecule with polar angle θ=90° and variable azimuthal angle obtained with an axisymmetric probe under radially polarized excitation; (d) profile along the straight line $x \cdot \tan(\phi)$ for a molecule with polar angle θ=90° and variable azimuthal angle obtained with an asymmetric cut probe under x linearly polarized excitation.

It is noteworthy that, independently of the total electric field intensity, all the asymmetric structures exhibit a highly confined strong longitudinal electric field component and weaker transverse components, like the axisymmetric probe under radially polarized excitation. Hence, probes with optimal total intensities can be chosen. As observed, differently from the axisymmetric

probe, where orthogonal transverse components have almost the same size and peak intensity, the transverse component aligned along the input linear polarization is still slightly higher than the orthogonal component and marginally asymmetric (the two lobes are not identical as observed earlier in Fig. 5.5) which accounts for the variations in the peak value and FWHM for the transverse components reported in Tab. 5.1. Such minor differences would only slightly affect the field distributions for variable ϕ, but are not likely to impair the high resolution mapping of the fluorescent molecules and the determination of their orientation.

Tab. 5.1 - Comparison of asymmetric probes with different geometric characteristics

Probe type	Normalized longitudinal component	Normalized transverse components along *x* and *y*	FWHM (longitudinal) [nm]	FWHM (transverse) [nm]	Normalized total electric field intensity
Axisymmetric	0.994	0.123-0.125	31	82	1
Cut: 766 nm; 30°	0.986	0.105-0.143	30	74-80	1.478
Cut: 816 nm; 30°	0.974	0.095-0.194	31	65-77	0.281
Cut: 816 nm; 40°	0.944	0.101-0.193	32	62-80	0.499
Cut: 741 nm; 30°	0.997	0.097-0.161	30	60-77	2.109
Cut: 816 nm; 50°	0.963	0.119-0.180	31	63-84	2.026

So far, only a linearly polarized excitation along the direction of the asymmetry has been considered. However, the behaviour of such probes based on directional asymmetries is expected to vary as a function of the angle α between the direction of the input linearly polarized excitation and the direction of the asymmetry.

As an example, we considered a molecule with longitudinal dipole moment and studied how the mapping of the molecule varies with a transition from a situation of perfect alignment with respect to the asymmetry (α=0°) to complete misalignment, i.e. linearly polarized excitation orthogonal to the direction of the asymmetry (α=±90°). Fig. 5.6 (a) and (b) report the fluorescence maps for α=0° and α=90° and Fig. 5.6 (c) and (d) show the FWHM and peak value normalized to the one of α=0° obtained for α variable from -85° to 90° with an incremental step of 5°. Plots refer to a cut probe with a cut angle of 30° and a cut height of 766 nm.

As the misalignment of the input polarization from the preferential direction of the asymmetry increases, both the peak value and the shape of the intensity pattern of the fluorescent molecule change. In particular, the peak value decreases and the distribution becomes gradually broader. This is due to the fact that, as α increases, the asymmetry perceived by the input linearly polarized

excitation progressively disappears and the probe near-field distribution undergoes a transition from an essentially longitudinal polarization with higher intensity and strong confinement (α=0°) to a mainly linear polarization with low intensity and broad extension aligned along the direction of the input linear polarization (α=±90°). The latter is characterized by a dominant *y* polarized component, a weaker two-lobed *z* component and an even weaker four-lobed *x* component. In retrospect, the different behaviour can be explained if recalling that a structure asymmetric along *x* appears symmetric for a *y* linearly polarized excitation, which brings about destructive interference of the excited SPPs, similarly to what happens for an axisymmetric structure under linearly polarized excitation.

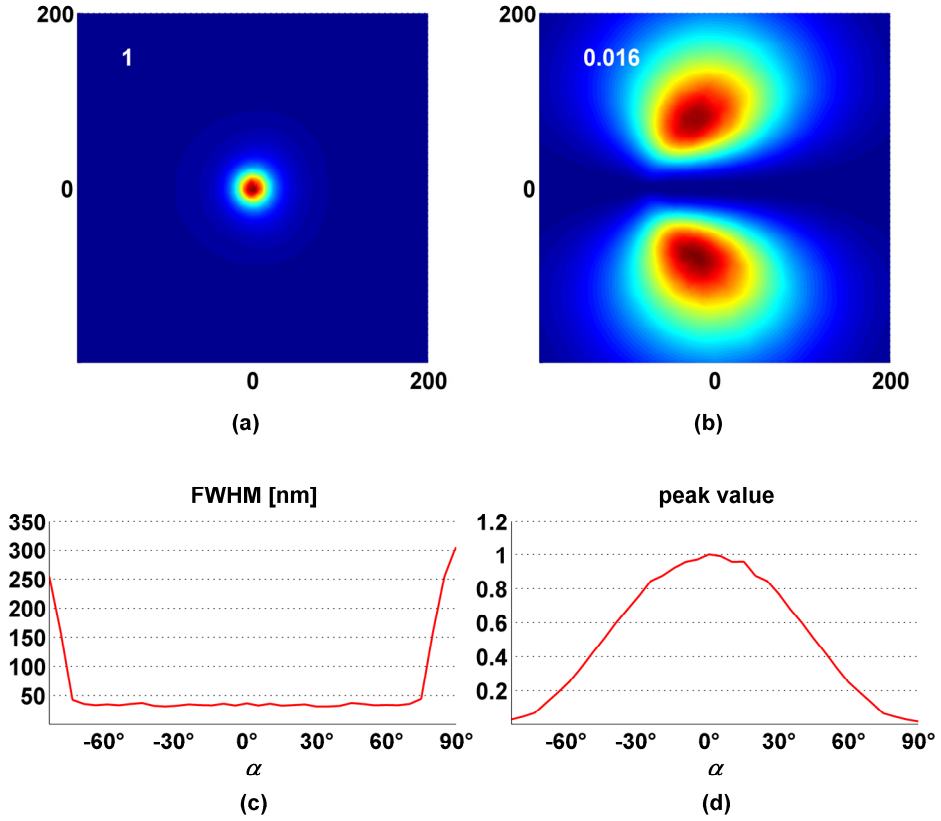

Fig. 5.6 – Mapping of a fluorescent molecule with longitudinal dipole moment with an asymmetric cut probe for variable α: (a) fluorescence map for α=0°; (b) fluorescence map for α=90°; (c) FWHM for variable α; (d) peak values for variable α (peak values normalized to the peak intensity for α=0°). The number in the corner in (a) and (b) reports the peak value normalized to the peak intensity for α=0°.

In conclusion, the simulations confirm the impressive similarity between the axisymmetric probe with radially polarized excitation and the asymmetric probes under linearly polarized excitation

along the direction of the asymmetry, which makes the asymmetric structures eligible to replace the axisymmetric probe for measurements on single fluorescent molecules, as long as the alignment of the input linear polarization with respect to the asymmetry is controllable and the direction of the asymmetry when the probe is mounted on the microscope is known. If such a condition is not met, the introduction of an adirectional asymmetry extended to all the spatial directions (and not oriented along one specific direction as is the case for the previously considered *x*-asymmetric structures) would be advisable.

The advantage inherent in the use of such adirectional asymmetries can be appreciated when considering how the mapping of a fluorescent molecule with longitudinal dipole moment, just as in Fig. 5.6, varies with a change in the angle α using a probe with an adirectional asymmetry like a spiral corrugation (Fig. 5.7).

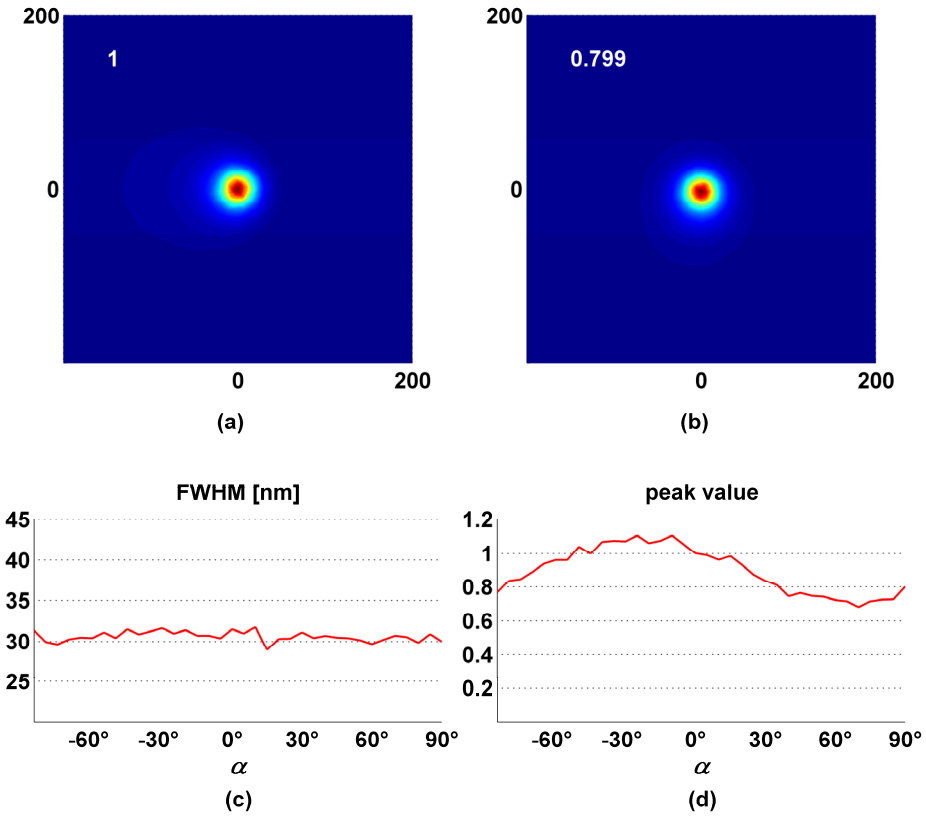

Fig. 5.7 – Mapping of a fluorescent molecule with longitudinal dipole moment with a probe with an adirectional asymmetry based on a spiral corrugation for variable α: (a) fluorescent map for α=0°; (b) fluorescent map for α=90°; (c) FWHM for variable α; (d) peak values for variable α (peak values normalized to the peak intensity for α=0°). The number in the corner in (a) and (b) reports the peak value normalized to the peak intensity for α=0°.

More specifically, plots refer to a probe with a two-turn spiral corrugation in form of an aluminium bump with 25 nm radius (reader is referred to paragraph 4.2 for further details). Note that, in this case, α=0° does not correspond to the position of best alignment (as the asymmetry is no longer directional), but to an arbitrary mutual position corresponding to x linearly polarized excitation and the two extremes of the spiral corrugation located along the x axis (y=0) as depicted in Fig. 4.5(a).

The overall shape and the spot size are almost invariant to α and the fluctuations of peak intensity are no longer as high as two orders of magnitude as for the probe with a directional asymmetry, but amount to only 20%. In fact, in this case, the conversion of the input linearly polarized excitation into a mainly longitudinally polarized near-field distribution with weaker two-lobed transverse components is effective irrespective of α, due to the presence of the asymmetry over any spatial direction. However, even in case of a directional asymmetry (i.e. an asymmetry lying along one specific spatial direction), the mapping of the molecule does not dramatically change in both peak intensity and size for a broad range of misalignment of the input linear polarization from the preferential direction of the asymmetry, as shown in Fig. 5.6 (c) and (d).

5.6. Final remarks

The interaction of fluorescent molecules with fully metal-coated axisymmetric tips and with novel asymmetric tips has been thoroughly scrutinized. Our numerical analysis reveals that the fluorescence maps of molecules with different absorption dipole moments achieved with asymmetric tips under proper linearly polarized excitation are closely akin to those observed with an axisymmetric tip under radially polarized excitation. As single molecules serve as an effective point-like probe for the vectorial components of the near-field distribution close to a SNOM tip, the similarity of the fluorescence distributions suggests a substantial resemblance of such electric field components between the two probe structures. Both of them are characterized by a single-lobed longitudinal field component dominant over two almost identical two-lobed orthogonal transverse components. Hence, variations in the polar orientation of a fluorophore from mainly longitudinal to mainly transverse at constant azimuthal angle are mapped as a transition from a single-lobed to a two-lobed pattern, while changes in the azimuthal angle at constant polar orientation imply a simple rotation of the fluorescence distribution according to the azimuthal angle. This allows a more straightforward interpretation of the 3D orientation of single fluorescent molecules compared to aperture probes, characterized by a two-lobed longitudinal component and by orthogonal transverse components strongly unequal in magnitude and shape, with differences as high as two orders of magnitude.

Our simulations may be used in combination with experimental results to accurately determine the 3D dipole orientation of single fluorescent molecules measured with novel asymmetric probes and for the characterization of novel asymmetric probe structures. Although both axisymmetric fully metal-coated probes and asymmetric probes have been experimentally used in fluorescence experiments, a numerical modelling of the probe-fluorophore interaction was still missing. Our results could be helpful in the interpretation of the experimental data obtained with similar structures (Frey et al., 2002; 2006; Taminiau et al., 2007). Moreover, the model could be extended to encompass measurements on quantum dots, for example by replacing the one-dimensional dipole with a two-dimensional one (Li et al., 2010a).

Noticeably, the numerical demonstration of the attainment of a strong longitudinal field component under linearly polarized excitation by the introduction of an asymmetry in an originally axisymmetric probe opens up interesting perspectives: longitudinal fields are essential not only for fluorescence measurements (especially for the high resolution imaging of fluorescent molecules with a mainly longitudinal dipole moment), but also for other potential applications like near-field second-harmonic generation and Raman spectroscopy (Bouhelier et al., 2003; Hayazawa et al., 2004). Therefore, the possibility to generate them without resorting to a cumbersome radially polarized excitation would foster the development of new exciting horizons.

As pointed out, if the asymmetry lies along one specific spatial direction, alignment of the input linearly polarized excitation with respect to the asymmetry is still necessary. On the contrary, light funnelling to a highly confined mainly longitudinally polarized distribution independent of the orientation of the input linear polarization can be achieved by extending the asymmetry over all the spatial directions.

6. Fabrication of asymmetric probes

In this chapter, the structuring of the asymmetric probes based on an oblique cut and on a spiral groove is described. First, the general steps for the fabrication of a fully metal-coated axisymmetric fiber tip are illustrated. Subsequently, the FIB milling procedure for the introduction of the designed asymmetry is reported.

6.1. Fabrication of fiber-based fully metal-coated probes

As anticipated in paragraph 1.4, the fabrication of a metal-coated probe is fundamentally articulated in two steps, i.e. the creation of the taper and the metallization. The fabrication of high-quality SNOM probes is still an open issue and hinders the attainment of reproducible results. In the following sections, the different techniques used to carry out the two main fabrication steps in fiber probes are discussed.

6.1.1. Taper formation by heating and pulling

This method consists in the simultaneous application of an axial tension on the fiber and of heat in the area where the rupture of the fiber is wished (Lazarev et al., 2003). The most common fiber pulling apparatus is based on commercial micropipette pullers (for instance from Sutter Instruments), which exhibit a two-step pulling cycle, iterated until the fiber pulls apart: first, heat is delivered from the source and concurrently a constant weak pulling force (weak pull) is applied caused by gravitational force on a weight located in the puller; afterwards, once a specified pulling velocity is attained, the pulling force is turned high by a current in the solenoid connected to the pulling arms (strong pull), after which the heating is halted (Valaskovic et al., 1995; Williamson and Miles, 1996). Although the commercial micropipette pullers typically incorporate a resistive heating element, a CO_2 laser at 10.6 μm is often used to heat the glass, which is an efficient absorber at this wavelength (Novotny and Hecht, 2006; Valaskovic et al., 1995). A sketch of the set-up is shown in Fig. 6.1(a). The optical path between the laser and the puller consists of a shutter to control the timing of heating and a lens providing control over the laser spot size (Valaskovic et al., 1995).

Three distinct taper regions can be usually recognized in tips produced with this method (Lazarev et al., 2003) (Fig. 6.1(b)):

1. a first tapered section;
2. a needle-like elongated region with gradually decreasing fiber diameter;

3. the final taper.

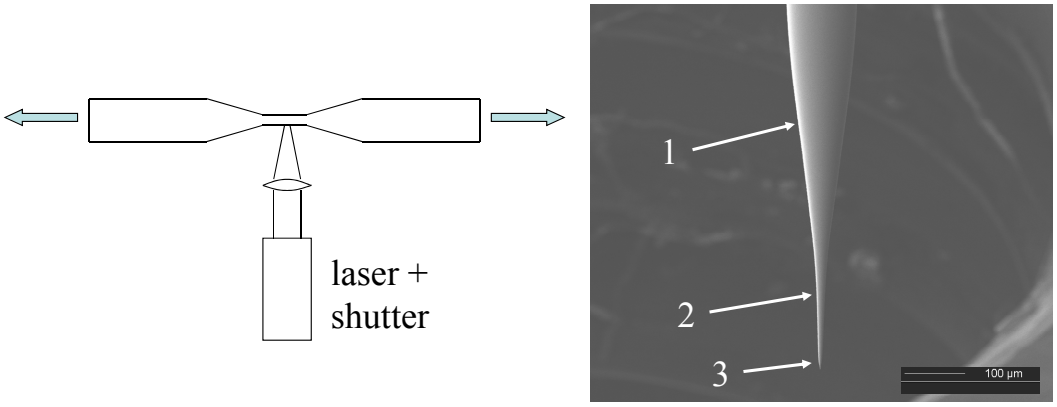

(a) **(b)**

Fig. 6.1 – Heating and pulling: (a) sketch of the set-up; (b) SEM image of a typical taper profile obtained by heating and pulling (metal-coated commercial probe from Lovalite).

Empirical investigations of the heating and pulling method have pointed out the influence of the different process parameters on the final taper profile (Lazarev et al., 2003; Valaskovic et al., 1995), i.e.:

1. laser power: if too low, premature fracture can occur and large apex diameters are observed; if too high, asymmetries are likely to appear, together with a longer needle-like region;
2. laser spot size: it influences the extension of the heated area of the fiber, thereby affecting the steepness of the first taper and the size of the needle-like region; a smaller spot size results in a steeper first taper and in a shorter overall taper length, because the material undergoing plastic deformation is smaller and plastic deformation is faster; a larger spot size results in a longer needle-like taper;
3. weak pull: it affects the steepness of the first taper and the size of the needle-like region, with a weaker pull generally bringing about a slower first taper and a thicker needle-like region;
4. strong pull: it affects the shape and the size of the final taper; typically, its increase gives rise to variations in transition to the final taper from a nipple-like shape to a smoother profile even if inversions in such pulling trend have been observed in case of narrow needle-like regions;
5. pull symmetry: although pulling both ends with equal forces is desirable to get two identical tapers, an asymmetric pulling has turned out to be useful to alter the shapes of the first taper and of the needle-like region;

6. exposure duration: a longer one allows an efficient heat transfer from the portion of the fiber exposed to the laser to the back one, with a consequent more uniform cross section temperature distribution.

The above description provides a qualitative analysis of the typical trends of the taper profile with some process parameters. However, a general quantitative determination of the values of the single parameters cannot be easily derived and would lack general validity. In fact, parameter selection is dependent on the actual implementation and model of the puller (whether home-built, commercial or mixed), on the type of fiber used and on the multi-parameter dependence of the process (empirical studies are usually carried out by varying one single parameter while keeping all the other parameters constant at some chosen value), making puller calibration necessary for a given puller and a selected fiber.

The process of heating and pulling occurs via plastic deformation and softening followed by thinning and breaking of the fiber: melting reduces the viscous forces; fiber rupture occurs when the external tension force exceeds the tensile strength (Lazarev et al., 2003). According to a theoretical investigation of the physical processes occurring during taper formation, the mechanisms leading to the final tip shape can be described as a two-stage process articulated in (Yakobson et al., 1993):

1. pulling and rupture of a fiber heated at some high temperature T_h;
2. cooling and relaxation until viscous flow is negligible.

The initial radius r_i at the end of the first stage is determined by two competing phenomena, i.e. a uniform thinning due to the externally applied pulling pressure p and an intrinsic capillary instability due to the surface tension γ, which tends to split the fiber into separate parts with smaller total surface area (Yakobson et al., 1993). An ultimately atomically sharp tip is theoretically achievable by minimizing the surface tension (for instance, carrying out the pulling process in an ambient other than air) and maximizing the tensile force; however, if a maximum threshold value for the tensile force p_0 is exceeded, brittle fracture of the fiber takes place, leading to the formation of a flat plateau at the tip apex often observed in probes produced by heating and pulling (Novotny and Hecht, 2006; Yakobson et al., 1993). After the formation of the initial tip radius, tip blunting can occur, with an increase in the tip radius which stops as soon as the tip cools down to the glass transition temperature T_g, with a consequent dramatic increase in viscosity; nonetheless, calculation of the final radius r_f using typical material and process parameters reveals a minor role played by post-rupture relaxation in tip formation, with a contribution of a few percent at most (Yakobson et al., 1993).

The overall analysis neglects the determination of taper profiles; however, experimental studies have revealed how small apex diameters less than 50 nm are usually accompanied by very long tapers (of the order of 500 μm) and very small cone angles, which hampers the attainment of good

transmission efficiency (Lambelet et al., 1998; Lazarev et al., 2003). In general, probes produced by heating and pulling are characterized by long tapers and insufficient reproducibility; nevertheless, the method is simple, cost effective and applicable to a wide variety of materials other than optical fibers and produces very smooth tapers favourable for light guiding and for the subsequent metallization of the tip (Lazarev et al., 2003).

6.1.2. Taper formation by etching

There exist three main methods to produce etched tapers:

1. meniscus etching (Turner's method);
2. tube etching;
3. selective etching.

Alongside these three main categories, various other procedures have been developed, which can be used singularly or successively, in different combinations, for optimal taper angle and tip profile (Guo, 2008). In general, chemical etching is attractive because of the potential opportunity of batch fabrication of a large number of identical tips (Novotny and Hecht, 2006). In fact, etching techniques allow the fabrication of shorter tapers (especially selective etching) with large cone angles (Fig. 6.2) and easier control on overall probe performance compared to the heating and pulling method that results in longer non-linear tapers with small taper angles and lower reproducibility (Hoffman et al., 1995; Mononobe, 2005).

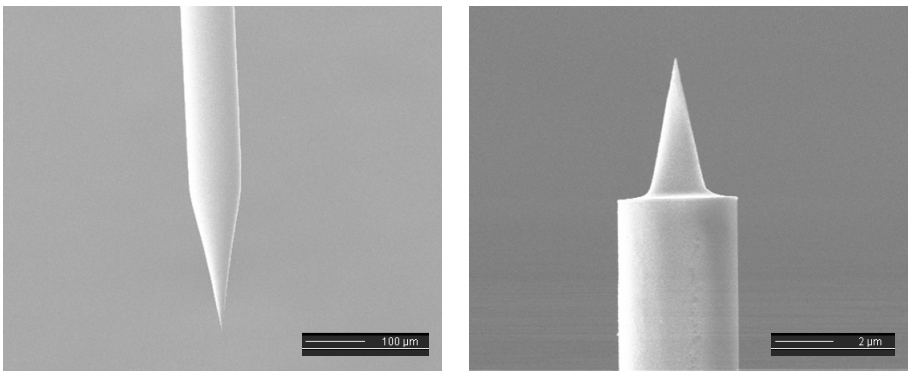

Fig. 6.2 – SEM images of typical taper profiles obtained by etching: (a) metal-coated commercial probe from NT-MDT; (b) metal-coated commercial probe from Jasco. In (b) selective etching allows the attainment of a very short taper (few microns); the initial diameter is first reduced to avoid risk of contact with the sample.

Characteristics of etched probes are more favourable for higher signal throughputs. However, probes produced by etching are often more prone to surface roughness, which is detrimental in the following metallization step, but can be dramatically reduced by using optimized etching procedures.

In the following sections, a brief description of the different methods is reported.

6.1.2.1. Meniscus etching

A fiber, deprived of the plastic coating, is dipped into a hydrofluoric acid (HF) solution, often with the addition of an organic solvent in order to control the height of the meniscus of the HF at the glass fiber and to prevent dangerous vapours from escaping from the etching vessel (Novotny and Hecht, 2006): the formation of the taper occurs at the meniscus between HF and the organic overlayer; the meniscus height is a function of the diameter of the remaining cylindrical fiber; the shrinkage of the fiber diameter during etching implies a reduction of the meniscus height avoiding further etching of the higher parts of the fiber. Tapering of the fiber takes place above the descending meniscus, until the taper cone is formed (Yu et al., 2009). In principle, the process should be self-terminating as it should stop as soon as the fiber diameter approaches zero (Novotny and Hecht, 2006). A sketch of the temporal evolution of the process is reported in Fig. 6.3.

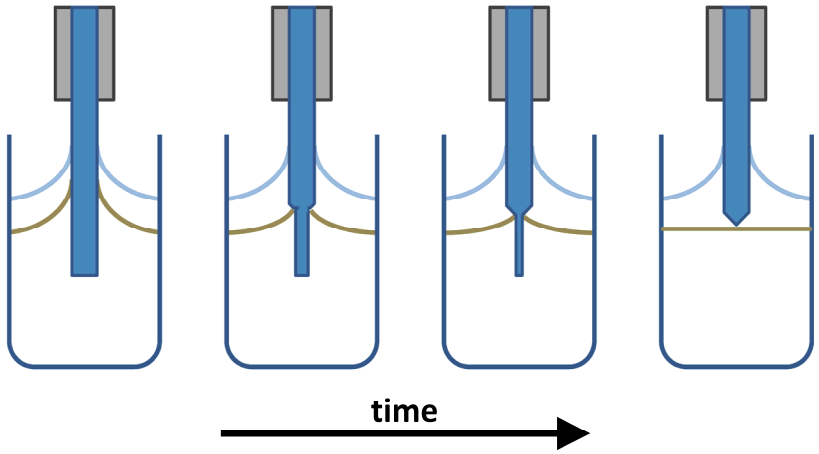

Fig. 6.3 – Temporal evolution of the fiber profile during meniscus etching (adapted from Novotny and Hecht, 2006).

A theoretical prediction of the taper profile (i.e. the etched fiber radius and the meniscus height) has revealed that the profile of the meniscus curve is related to the surface tension of the organic solvent, the gravitational constant and the density difference between the HF etchant and the organic solvent (Yu et al., 2009).

Experimental analyses show that the process is not really self-terminating (because the diffusion of small HF molecules into the organic solvent implies degradation of the tip if it is not immediately removed after formation) and that the surface of the conical taper is rather rough (due to abrupt jumps of the meniscus of HF from one stable position to the other) (Novotny and Hecht, 2006). Nonetheless, shorter tapers (about 200 μm) and larger cone angles compared to the heating and pulling method can be achieved (Lambelet et al., 1998).

In order to change the cone angle, a dynamic etching procedure can be introduced: the fiber is moved vertically while immersed in the etchant, thereby altering the recession speed of the meniscus by moving the fiber up and down at a certain speed that determines the time exposure to the acid of the cross section of the fiber at each height and, hence, the lateral etching at that height; in particular, by moving the fiber upwards, a tip with a long taper is produced; vice versa, moving it downwards, the resulting taper becomes shorter; attention must be paid to turbulences at the interface, which are crucial to tip quality (Hoffman et al., 1995; Lazarev et al., 2003a; Muramatsu et al., 1999). In the static etching process, cone angle can be varied by changing the organic overlayer (Hoffman et al., 1995).

6.1.2.2. Tube etching

Probes produced by meniscus etching are characterized by considerable roughness (due to the sensitivity of the process to environmental conditions, e.g. vibrations, temperature drifts, etc.), which impacts the subsequently applied aluminium coating, with the possible formation of pinholes causing light leakage and undermining the overall probe performance (Stöckle et al., 1999). In order to reduce the surface roughness typical of probes obtained by meniscus etching, a different approach, commonly referred to as tube etching, has been proposed almost simultaneously by two different groups (Lambelet et al., 1998; Stöckle et al., 1999).

Such an approach is based on the chemical etching of the glass fiber through its plastic jacket, as opposed to meniscus etching, where the etching is carried out on the bare fiber, after plastic jacket is stripped off (Lambelet et al., 1998; Stöckle et al., 1999). The glass fiber is dipped with its plastic coating in a HF solution; the HF solution is covered by an organic overlayer (for example *p*-xylene or iso-octane) that protects the fiber against acid vapour, but does not influence tip formation itself (Stöckle et al., 1999). Slight differences in tip formation process are observed, depending on whether the plastic coating is permeable or not to HF (Stöckle et al., 1999) (Fig. 6.4):

- if not permeable, tip formation begins at the lower end of the fiber, without any thinning of the fiber in the upper region; tip shape is preserved while tip shortens inside the tube, once a tip is created; contrary to meniscus etching, no degradation in tip sharpness and smoothness occurs

after tip formation because of the insensitivity of taper angle and surface quality to etching time upon further etching;

- if permeable, the glass fiber is thinned regularly inside the plastic jacket due to the diffusion of HF and a preliminary tip formation is observed at the interface between the HF solution and the organic overlayer; final tip formation occurs above the interface, where lateral diffusion of HF through the jacket is not possible, after complete removal of the thinned part, via the mechanism described for the impermeable polymer coating.

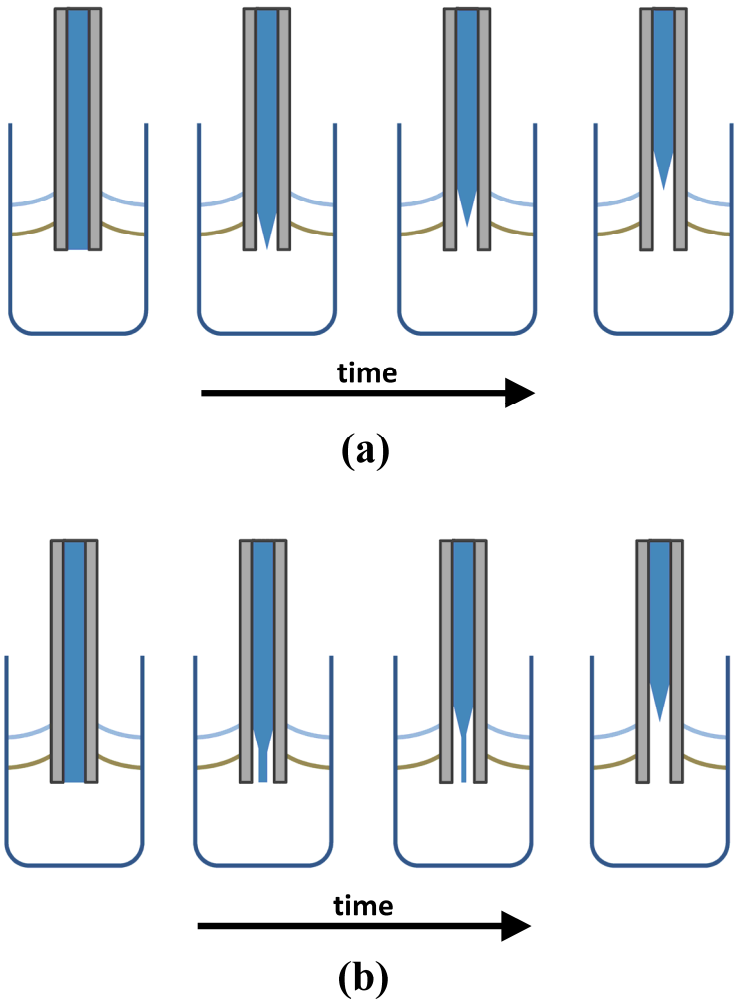

Fig. 6.4 – Temporal evolution of the fiber profile during tube etching: (a) in case of HF impermeable coating; (b) in case of HF permeable coating (adapted from Stöckle et al., 1999).

After etching, the fiber is removed and rinsed and the plastic jacket can be removed either by dissolving it in hot concentrated H_2SO_4 or by mechanical stripping (Lambelet et al., 1998; Stöckle et al., 1999).

From a theoretical point of view, although the etching mechanism is substantially the same as for meniscus etching, tip formation occurs in a different way (Lambelet et al., 1998). First of all, in meniscus etching, the meniscus formed by the acid along the fiber is determined by the acid/organic overlayer/glass interface and its height decreases during the etching process, while in tube etching the meniscus height is determined by the acid/organic overlayer/plastic jacket interface and keeps constant during tip formation (Lambelet et al., 1998). Tip formation can be explained in the light of a microconvection process inside the tube (Stöckle et al., 1999): tip geometry is influenced mainly by the relative magnitude of lateral diffusion and convection and by the dependence of the etching rate on temperature. An increase in temperature leads to an increase in the etching rate, and, hence, to a decrease in the cone angle, but also to less sharp tips due to increased diffusion, because of a more isotropic etching of the tip; therefore, a maximum cone angle is expected for intermediate temperatures; also HF concentration plays a role, because it influences the reaction rate, determining an optimal concentration at a given temperature (Stöckle et al., 1999).

Although the overall probe profile is similar for probes obtained by meniscus and tube etching, the latter method results in smoother surfaces and better yield of usable tips, while being less sensitive to environmental perturbations, like temperature variations and vibrations (Stöckle et al., 1999).

6.1.2.3. Selective etching

Even shorter tapers can be produced by an alternative etching approach called selective etching: this technique exploits the different etching rates of the core and the cladding of the fiber. The procedure has been initially developed for fibers with GeO_2-doped silica core and pure silica cladding (Pangaribuan et al., 1994). The sharpening process of such fibers can be summarized in the chemical reactions of ZO_2 with HF in water solution (where Z can be either Si or Ge) leading to the formation of H_2ZF_6: as the dissolution rate of the core is faster than the one of the cladding, the end of the fiber core would become concave (Pangaribuan et al., 1994). However, the dissolution rate of the core can be decreased by adding NH_4F to HF as a buffer solution: the resultant H_2ZF_6 reacts with NH_3 ionized from NH_4F with the formation of $(NH_4)_2ZF_6$; the difference in the solubility between $(NH_4)_2SiF_6$ and $(NH_4)_2GeF_6$ is responsible for the different etching rates of the core and the cladding (Pangaribuan et al., 1994). Therefore, in selective etching, a buffered solution of HF consisting of a mixture NH_4F:HF:H_2O with volume ratio X:1:1 is used; by adjusting the composition of the etching solution, i.e. by varying the volume ratio X of NH_4F and the doping ratio of GeO_2, different cone angles and tip diameters can be obtained (Mononobe and Ohtsu, 1996; Pangaribuan et al., 1994).

Depending on the value of X, the fiber can be hollowed or sharpened: if R_1 and R_2 are the etching rates of the core and the cladding, respectively (depending on fiber composition/doping ratio), the

fiber will be hollowed if $R_1>R_2$ (X<1.7 for a typical fiber with GeO_2-doped core) and sharpened vice versa (X>1.7); the ratio R_1/R_2 decreases with increasing X and converges to a constant value for X=10-30; fiber shape (i.e. cone angle and apex diameter of the sharpened probe) can be predicted starting from the etching rates (R_1, R_2) and the etching time (Mononobe and Ohtsu, 1996).

Applying this method, probes in which only the core is tapered can be obtained, with an advantageous reduction in the overall taper length h (2-6 μm); the fiber is flat apart from the sharp protrusion in the core (Pangaribuan et al., 1994). However, as the diameter d of the cladding is much bigger (d/h>15), the risk of collision of the cladding edge with the sample is high, but can be avoided using a two-step etching procedure (Fig. 6.5): a first etching step is used to reduce the cladding diameter from d_0 to d_1; in the second step, the cladding diameter becomes d_2 and the fiber is sharpened; the first etching step can be carried out, for example, using the same selective etching procedure with X=1.7 with the diameter decreasing for increasing etching time (Pangaribuan et al., 1994).

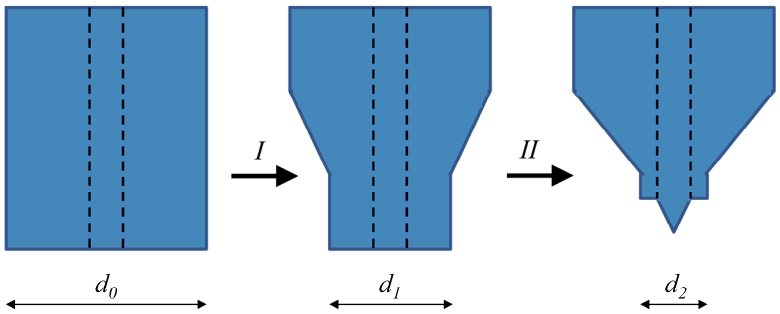

Fig. 6.5 - Selective etching: illustration of two-step etching (adapted from Pangaribuan et al., 1994).

Variants of this technique have been used to fabricate probes with different taper profiles, including multiple tapers (Mononobe et al., 1997a; 1998; Mononobe and Ohtsu, 1998). Although initially developed for GeO_2-doped fibers, selective etching has been adapted to other fibers of different composition (Frey et al., 2002; Mononobe, 2005).

6.1.2.4. Variants of the etching method

Some variants of the etching procedures described in the previous paragraphs have been worked out by several groups. One of them consists in a fiber pre-treatment by meniscus etching to reduce the fiber diameter followed by rinsing and coating of the fiber with polymethylmethacrylate (PMMA) and a subsequent standard tube etching procedure, resulting in better control over tip shape and apex diameter (Yang et al., 2007). Another approach consists in a post-treatment of probes produced by tube etching to further reduce the surface roughness by bevelling the pre-etched fiber against a

grinding plate (Held et al., 2000). Two etched probes can be obtained by a sealed-tube etching procedure, i.e. by sealing with HF impermeable plastic the bottom end (the one dipped in the HF solution) of a fiber with permeable plastic coating: the method is therefore based exclusively on HF lateral diffusion as opposed to conventional tube etching on fibers endowed with HF permeable plastic coating, where HF diffusion is both lateral through the jacket and vertical from the bottom open end of the tube (Shi and Qin, 2005). In the so-called substitute-sheath etching, fibers without plastic jacket are immersed in a wax bath before being dipped into the HF solution, with the wax acting as a substitute sheath in which tip formation occurs; subsequently, wax is removed mechanically, without any need for additional overlayer above the HF to protect the fiber against corrosive vapours as the HF-impermeable wax serves for this purpose; the process results in short tapers, smoother coatings and smaller apex diameters (Chaigneau et al., 2006). A reverse tube etching procedure has been proposed as a way to get larger taper angles: in this case, the fiber with plastic coating is inserted in the HF solution from the bottom instead of being dipped from the top as in conventional tube etching with a chloroform layer acting as protecting layer on the bottom of the solution; the wider cone angles are the outcome of the weakening of the effective longitudinal component of the etching flux (Patanè et al., 2006). A combination of laser or electric arc heating and pulling with static etching has been proposed as well (Huo et al., 2006; Mononobe, 2005).

6.1.3. Probe metallization

The next step for probe fabrication after taper formation is metal deposition; in particular, we will focus our attention on aluminium deposition. A primary requisite for probe metallization is the deposition of smooth and continuous metal films with small grain size because probes ailing from large grains are affected by a series of problems like large background due to pinholes (Valaskovic et al., 1995).

The most widespread technique used for metallization is vacuum deposition by means of thermal evaporation: this method has been used for metallization of probes produced both by heating and pulling or etching and deposition of different metals (Chaigneau et al., 2007; Held et al., 2000; Hollars and Dunn, 1998; Lambelet et al., 1998; Lazarev et al., 2003; Saito et al., 2012; Stöckle et al., 1999a; Valaskovic et al., 1995). The typical evaporation chamber consists of a glass bell jar equipped with a pump to operate in vacuum; different sources can be used, for example a tungsten double helix filament loaded with aluminium for aluminium deposition; fibers are placed in a rotating holder that rotates continuously at a certain frequency during the evaporation process to guarantee deposition of a uniform metal film and are located at a proper distance from the metal source; fibers can be oriented at a certain angle with respect to the evaporation direction in case of fabrication of aperture probes (to induce the formation of apertures by exploiting the shadowing

effect) (Chaigneau et al., 2007; Hollars et al., 1998; Lazarev et al., 2003; Stöckle et al., 1999a; Valaskovic et al., 1995). Smooth thin films of aluminium with small grain size are difficult to evaporate because aluminium tends to form oxide in the presence of both oxygen and water leading to a decrease in film reflectivity and an increase in roughness, with the formation of large oxide grains (Hollars et al., 1998; Valaskovic et al., 1995). The effect of several process parameters on the quality of the evaporated metal films has been investigated by different groups. A first important element to pay attention to is the fiber cleanliness (to reduce pinhole creation during evaporation) that can be optimized by reducing the time lapse between taper formation and metal evaporation (Valaskovic et al., 1995). As far as the aluminium evaporation process itself is concerned, general guidelines for the evaporation of good films are the maintenance of a good quality vacuum with low oxygen content, high rate of deposition and cool substrate (Valaskovic et al., 1995). More specifically, a reduction in vacuum pressure, although increasing the costs, brings about a decrease in surface topography by reducing chemical reactions between aluminium vapour and background oxygen before aluminium reaches the fibers (Hollars et al., 1998). If this condition is satisfied, the major factors leading to oxidation are the reactions between aluminium and oxygen at the substrate surface, which can be minimized by increasing the arrival rate of aluminium atoms compared to that of background gasses. For this purpose, one should operate at low pressure (because the rate of arrival of gas molecules is proportional to vacuum pressure) or increase the rate of deposition of aluminium (Hollars et al., 1998). The use of the mentioned tungsten double-helix filament loaded with aluminium as a source, which has the highest molecular flux to radiant flux ratio compared to other tungsten-based heating sources, meets a two-fold requirement of increasing the deposition rate of aluminium while minimizing radiant heating of the substrate, both important to reduce grain formation (Valaskovic et al., 1995). Thermal evaporation has also been used for the deposition of adhesion layers like titanium and chromium prior to aluminium to increase the thermal resistance of probes by improving the glass-aluminium adhesion (Stöckle et al., 1999a).

As already pointed out, also the temperature of the substrate plays a role in the surface quality of the metal layer: in particular, reducing substrate temperature should imply a reduction in roughness by limiting the diffusion distance of the aluminium atoms on the substrate surface; although cooling the fibers with liquid nitrogen during coating has also been carried out, little improvement has been observed compared to room temperature coating; a better reduction in radiant heating of the fiber tips can be achieved by using electron beam evaporation techniques (Hollars et al., 1998). Differently from thermal evaporation, where metal is heated by the Joule effect, with electron-beam evaporation one bombards the selected metal with a high intensity electron beam emitted from a thermoionic filament in high vacuum; metal is heated until reaching evaporation (Minh et al., 2002). Also this evaporation technique has been used for the deposition of different metals; moreover, as

for thermal evaporation, angled evaporation can be used to create apertures by shadowing, while if the angle of evaporation with respect to probe axis is 90°, the whole fiber is coated with metal (Garcia-Parajo et al., 1995; Lacoste et al., 1998; Veerman et al., 1998; Zhang et al., 2011).

A third method commonly used for metallization is sputtering, a physical vapour deposition method in which the target material (in this case the metal) is bombarded with ions of an inert gas like argon; the atoms are ejected from the target and deposited on the substrate; smooth and uniform metal films can be obtained in this way; as the process is multidirectional, the whole taper is covered (Aiyer et al., 2001; Chaigneau et al., 2006; 2007; 2008; Minh et al., 2002; Pilevar et al., 1998).

6.2. Nanostructuring of asymmetric SNOM probes by focused ion beam milling

For the fabrication of our novel asymmetric probes, fiber-based SNOM tips have been purchased and properly modified using a dual beam FIB/SEM system (FEI Strata DB 235) (Fig. 6.6). In the coming sections, first the principles of FIB milling are discussed together with the characteristics of the used set-up, then the nanostructuring of our asymmetric probes will be described.

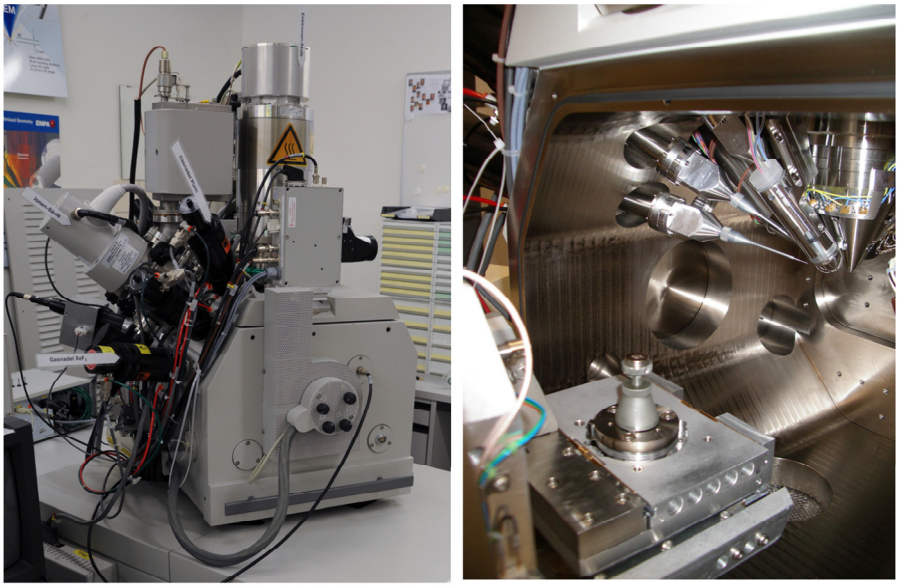

(a) (b)

Fig. 6.6 – Dual beam FIB/SEM system: (a) from outside; (b) chamber.

6.2.1. Overview of the dual beam FIB/SEM system

The system includes an ion beam and an electron beam column tilted one with respect to the other by 52°, allowing the object under study to be investigated with either of them; the ion beam and the

electron beam intersect at a point of the sample, known as coincident point (Fig. 6.7(a)) (FEI, 2005; Lich, 2007).

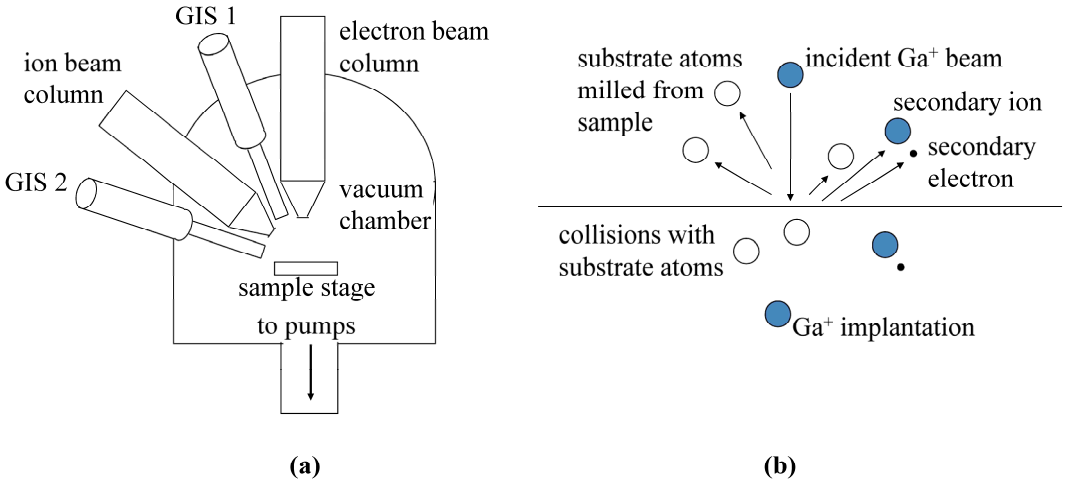

Fig. 6.7 – Principles of FIB milling: (a) sketch of a dual beam FIB/SEM chamber with electron and ion columns tilted by 52° one with respect to the other; GIS 1 and GIS 2 indicate two different gas injection systems; (b) sketch of the interactions of the ion beam with the sample surface (adapted from FEI, 2005 and from Sanchez et al., 2002).

The working principle of a focused ion beam system is akin to the one of a focused electron beam system: in SEM electrons are accelerated and focused onto the sample surface, while in FIB ions are used instead of electrons (Ali et al., 2010; FEI, 2005; Raffa et al., 1992). When the primary ion beam hits the sample surface, secondary ions, neutral atoms and secondary electrons are released from the sample (Fig. 6.7(b)); by scanning the sample with the primary beam (for example gallium ions), an image of the sample is formed by collecting the signal from all charged particles, both ions or secondary electrons; neutral atoms, the main component during the sputtering process, are removed with the pumping system, although some of them can redeposit close to the milling area (FEI, 2005).

The FIB system employed in SNOM probe nanostructuring uses a gallium ion beam. Gallium is metallic and has a low melting temperature, which makes it a convenient solution for a compact gun with limited heating and high brightness (FEI, 2005; Sanchez et al., 2002). In the so-called liquid metal ion source (LMIS) (Fig. 6.8(a)) a gallium reservoir provides liquid gallium by a heating coil; gallium flows to the apex of a tungsten needle; a Taylor cone is formed due to surface tension and to the application of a strong electric field from the extractor; the high electric field at the tiny tip causes ionization and the process of field evaporation produces ion emission (Raffa et al., 1992). The suppressor retards the ion flow to obtain an emission current between 2.2 and 2.4 μA; gallium

ions are accelerated to 30 kV and focused on the sample with a two-lens stacked electrostatic focusing column; the minimum focused ion beam widths are determined by the tip emission currents that can be varied between 1 pA to 20000 pA with variable apertures; blanking plates are present in the column to divert the beam away from the sample when scanning is not desired by the use of a negatively charged plate (Fig. 6.8(b)) (Sanchez et al., 2002).

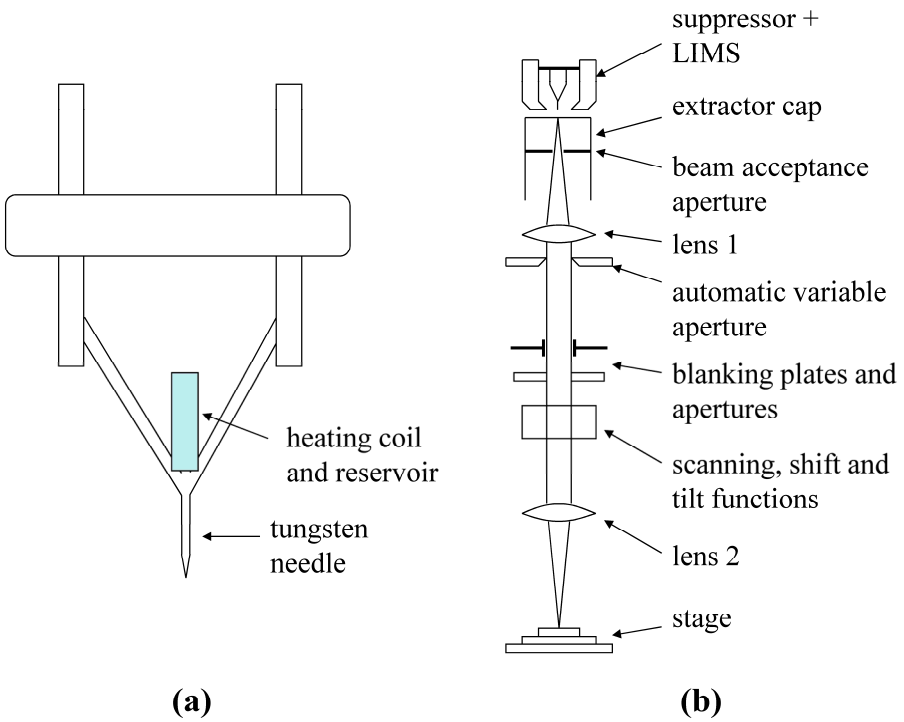

Fig. 6.8 – Sketch of: (a) liquid metal ion source; (b) ion column (adapted from FEI, 2005).

In a computer-controlled machine, milling is carried out via pixel by pixel movement along a pattern discretized in pixels with a certain pixel spacing p_S; the time the beam stays on a target pixel is defined as dwell time t_d (Tseng, 2004). For a beam of FWHM d_f (dependent on the ion beam current), the beam overlap o is defined via the following relationship (Sanchez et al., 2002):

$$p_S = d_f(1-o) \tag{6.1}$$

In order to have a uniform ion flux along the scanning direction, the pixel spacing should be small enough for a proper overlap between adjacent pixels; with a Gaussian approximation for the ion beam profile, a uniform scanning ion flux is obtained if the following condition is met (Tseng, 2004):

$$\frac{p_S}{d_f} \leq 0.637 \tag{6.2}$$

In order to scan a given pattern, either a single-pass or a multi-pass milling strategy can be adopted; with a multi-pass strategy (in which the beam scan over a given scanning pattern is repeated several times), a lower t_d can be used and partial redeposition of the sputtered material, typically occurring during milling, can be reduced (FEI, 2007; Tseng, 2004).

The milling rate is proportional to the ion beam current (FEI, 2005). Moderate and high currents are typically used for milling because in this way a larger amount of material can be removed with precision by adjusting the beam position, dwell time and size; lower beam currents between 1 to 30 pA are used for imaging in order to minimize sample damage by the ion beam because very little material is sputtered (the milling process always takes place during exposure to the beam) and resolution of 7 nm can be achieved (Brunner et al., 2008; FEI, 2005; Sanchez et al., 2002). Lower beam currents corresponding to smaller spot sizes can also be used for precision milling (FEI, 2005). The dual beam FIB/SEM system is suitable for performing micro- and nano-machining with the FIB column, and imaging and analysis with the SEM column (FEI, 2005). The SEM column allows nondestructive, high resolution sample imaging during ion beam milling with a specified resolution of 3 nm at 5 kV.

In the following sections, the fabrication of two different asymmetric structures by FIB milling is described.

6.2.2. Fabrication of asymmetric probes with an oblique cut

FIB milling has been applied in the past to the fabrication of the aperture in aperture SNOM probes, either to improve the quality of apertures created by some other method or to create an aperture in a fully metal-coated probe. Two different approaches have been used for this purpose, i.e. head-on drilling and slicing (Heinzelmann et al., 1999; Muranishi et al., 1997) (Fig. 6.9). In the first approach, the Ga^+ beam is scanned from the top across the tip surface using a previously generated pattern (the ion beam is aligned along the tip axis); typically, ion currents between 12 and 70 pA have been used for ions accelerated at 30 kV with total milling time of 10-20 s; although in this way a better control over shape and size of the aperture can be achieved by choosing an appropriate milling pattern, deep drilling into the tip structure can occur and the ion beam needs to be guided to the center of the tip apex (Heinzelmann et al., 1999; Lacoste et al., 1998; Muranishi et al., 1997). In the second approach, the metal-coated fiber probe is sliced off transversally, i.e. the ion beam is incident at 90° with respect to the probe axis; the size of the aperture can be controlled only indirectly by estimating the correct location for slicing and the size of the milled area; small beam sizes are used to remove thin slices of material with ion currents between 10 and 20 pA (Heinzelmann et al., 1999; Pilevar et al. 1998; Muranishi et al., 1997; Veerman et al., 1998; Zhang et al., 2011).

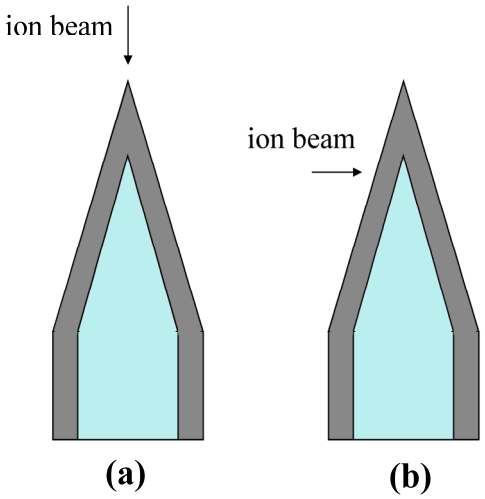

Fig. 6.9 – FIB nanostructuring of a SNOM probe: (a) head-on drilling; (b) transverse slicing.

The slicing approach, properly adapted, is suitable for the fabrication of our probes based on an oblique cut. However, differently from the case of conventional aperture probes, the angle of incidence of the ion beam with respect to the probe axis is no longer 90°, but needs to be chosen according to the desired cut angle. The 5-axis sample stage allows proper positioning of the sample with respect to the incident beam: if *xz* is the plane defined by the ion and electron column (with *z* aligned along the direction of the electron column), the specimen (our commercial fully metal-coated fiber probe) can be rotated from 0° to 360° in the *xy* plane and tilted from -10° to 60° in the *xz* plane. Two different holders (one planar and the other with a slope of 45°) have been used to get any arbitrary cut angle. In all the cases, the fiber probe is mounted in a fiber chuck for better stability. The definition of cut angle corresponds to the one given in chapter 3: hence, a simple aperture probe would correspond to a cut angle of 0°.

The fiber probes used to fabricate and test the probe based on an oblique cut, bought from Lovalite, have been produced by heating and pulling and subsequent deposition of about 70 nm of Al; the fiber is a single mode fiber in the visible range. The apex diameter of the fully metal-coated probe is about 200 nm and the total taper length is about 800 μm; the taper angle at the apex in the final taper is specified to be between 15° and 20°. Smaller apex diameters would result in very long and less reproducible tapers (see paragraph 6.1.1) and hence lower throughput.

For the fabrication, a step-by-step procedure was adopted in which a milling step consisting in scanning the ion beam over a small rectangular area to remove as little material as possible was followed by an imaging step in order to check the results of the previous nanostructuring step. Moreover, with a multi-pass procedure and multiple milling sweeps after inspection the effects of redeposition can be minimized (Pilevar et al., 1998). To get a first knowledge of the aperture size

and metal thickness, first simple aperture probes with diameters between about 70 nm and 200 nm were realized. Then cut probes were produced. Fig. 6.10 shows an example of an aperture probe and of a probe with an oblique cut. Typical ion currents used for probe structuring were between 5 and 11 pA. The chamber was operated at a pressure of 10^{-5}-10^{-6} mbar. Sample stage drift was less than 10 nm per minute and negligible considering that each milling step required just a few seconds. In each milling step, the beam was scanned along a serpentine with a dwell time of 1 μs and an overlap of 50%.

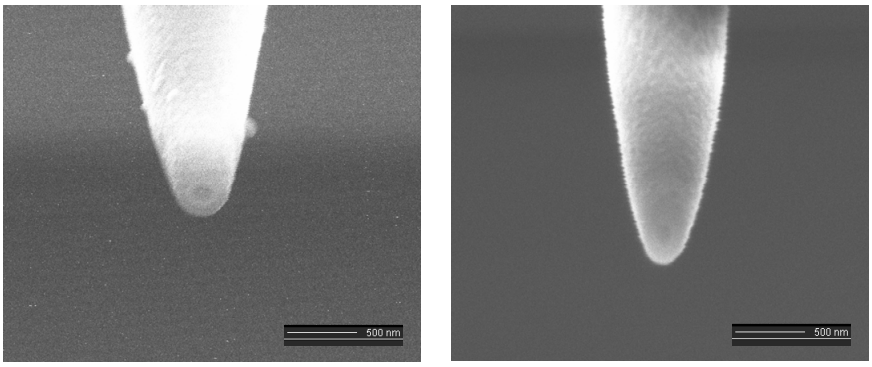

Fig. 6.10 – SEM image of: (a) aperture probe; (b) cut probe. The probes have been structured by FIB milling with a slicing approach.

The nanostructuring of the designed cut probe is easily derived from FIB creation of aperture probes and is extremely simple compared to asymmetric probes based on a monopole antenna. Also such probes have been structured using FIB milling, but the overall process requires several milling steps under different angles: in fact, first a narrow ridge needs to be created in numerous milling steps; next, the probe needs to be rotated to make the ridge thinner and thinner and create the antenna (Taminiau et al., 2007).

6.2.3. Fabrication of asymmetric probes with a spiral corrugation

FIB milling has been applied also to the creation of probes with adirectional asymmetries based on a spiral groove. For this purpose, a head-on drilling approach has been adopted and the pattern generator provided by the control software of the dual beam system has been used. In addition to the typical problem of centering the probe apex inherent in the head-on drilling approach, carving a spiral pattern along the taper imposes also to pay attention to the taper shape, in particular to its angle.

In fact, we should recall that the sputtering yield, i.e. the average number of target atoms removed per incident ion, depends on the angle of incidence of the ion beam with respect to the surface normal of the sample to be milled. For small incidence angles, the sputtering yield for a given incidence energy approximately grows as $(\cos\theta)^{-f_S}$, where the incidence angle θ is defined between the incident ion beam and the surface normal direction and f_S is a function of the energy and of the mass ratio of projectile and target; however, at higher incidence angles, the sputtering yield starts decreasing; a more complete description of angular dependence of the sputtering yield for a given energy of the ion beam over the whole angular range of incidence is given by the following empirical formula (Eckstein, 2005; Vasile et al., 1999; Wei et al., 2008; Yamamura, 1984):

$$Y(\theta) = Y(0) x^{f} e^{-\Sigma(x-1)} \qquad \textbf{(6.3)}$$

where $Y(\theta)$ is the sputtering yield at the incidence angle θ, $Y(0)$ is the sputtering yield at normal incidence ($\theta = 0°$), $x = \frac{1}{\cos(\theta)}$, and f and Σ are adjustable parameters, determined by fitting experimental data with least squares method and depend on the energy of the incident beam and on the projectile/target combination. The sputtering yield increases slowly for small incidence angles, then more rapidly for increasing θ, until reaching a maximum for $\theta_{\max} = \arccos\left(\frac{\Sigma}{f}\right)$; after that point, a steep decrease to zero occurs for $\theta \to 90°$.

For aluminium, $\theta_{\max}$ is close to 80° (Lehrer et al., 2001), which means that, in case of head-on drilling ($\theta = 90° - \xi$ where ξ is the semiangle of the taper), we could be close to the region of maximum sputtering yield, where rapid variations in sputtering yield with θ occur, especially for small ξ. As pointed out in paragraph 6.1, the taper angle and profile of a probe are closely related to the fabrication method. Therefore, in order to have a more complete view of the feasibility of a spiral groove, we have performed nanostructuring on commercial probes produced with different methods resulting in different taper profiles. In particular, we have compared milling results on probes obtained by heating and pulling and by etching.

The code created for the generation of the spiral pattern (which allows definition of the number of turns, the chirality and the overall extension of the spiral) has been first tested on a planar surface and then on the tapers. Fig. 6.11 shows the results (view from the top and from the side) for the spiral grooves on some of the processed probes. The inner radius of the spiral, as seen from the top, has been chosen taking into account the presumable radius of the probe apex as measured from the images, while in all the cases the pitch in the top projection was kept at 100 nm. The dwell time and the ion beam current were about 10 μs and 10 pA, respectively, in all the cases, while the number of

passes was adjusted to account for the different ξ; for all the shown probes the total milling time was of few seconds.

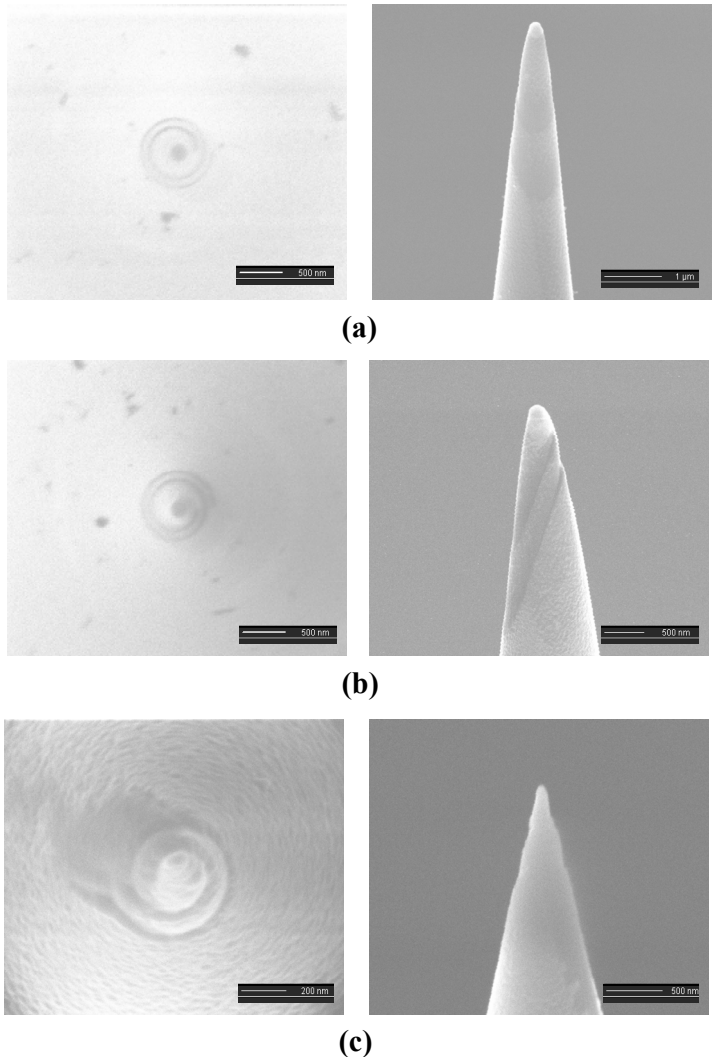

Fig. 6.11 – Top and side view of a spiral groove produced by FIB milling on a fully metal-coated probe: (a) and (b) tapers fabricated by heating and pulling from Lovalite; (c) taper fabricated by selective etching from Jasco.

As we said, the first problem typically encountered in head-on drilling of probes is the identification of the apex. In the first two rows, spirals have been carved on the metal coating of two probes produced by heating and pulling from Lovalite. Such a problem is evident in both the probes, where the spiral groove suffers from imperfect centering due to the difficulty to identify the apex because of its huge size (Fig. 6.11 (a) and (b)). The best results were achieved in the last case (Fig. 6.11(c)): the original probe, bought from Jasco, was created by selective etching on a GeO_2-doped fiber. The smaller apex diameter of the probe (about 90 nm against 200 nm for the previous probes)

allowed easier identification of the apex and, hence, more accurate and reproducible centering; moreover, the higher ξ makes it possible to create a spiral that is less extended along the probe axis compared to the other cases (in fact the pitch along the probe axis will be $p/\tan(\xi)$, where p is the pitch seen from the top projection). The measured width of the corrugations for the probes shown in Fig. 6.11 was between 30 and 40 nm.

The tests carried out on probes with different taper profiles show the feasibility of the creation of a spiral groove on a fully metal-coated SNOM probe. However, attention needs to be paid to the probe profile, which influences the choice of the milling parameters (due to the dependence of the sputtering yield on the incidence angle of the ion beam and, therefore, on the taper semiangle ξ) and the final shape of the groove. Better control over the spiral shape is achievable with probes having a smaller apex and a higher ξ, as is the case for the probe shown in Fig. 6.11(c). Grooves with desired characteristics in terms of pitch and width can be obtained by proper adjustments of the milling parameters.

6.2.4. Hints on fabrication of other asymmetric probes by combination of FIB milling and deposition

In the previous sections, we have shown the feasibility of two of our novel asymmetric structures, both created by FIB milling. However, some of the other asymmetric structures proposed in the previous chapters require both milling and deposition: this is the case, for example, of the probe based on asymmetric corrugations limited to just one half of the tip and of the one based on corrugations arranged in a spiral-like fashion. Good results were obtained for an alternation of grooves and bumps in the investigated five corrugations, which would require metal deposition.

Beside being a tool for maskless milling, FIB can be used also for maskless deposition of metals and insulators, offering a complete tool for both localized subtractive (milling) and additive (deposition) nanostructuring (Reyntjens and Puers, 2001). As shown in Fig. 6.7(a), gas injection systems (GIS) are available, which can be used either for gas-assisted etching, to expedite the milling process by preventing redeposition using reactions with the injected gas (e.g. I_2 or XeF_2), or for injection of precursor gases useful for deposition. In the deposition process, the precursor gases (e.g. organometallic precursors for metals) are sprayed into the work chamber on the surface of the substrate material using a fine needle (nozzle) and adsorb at the surface; the incident ion beam decomposes the adsorbate; the volatile reaction products, desorbing from the surface, are removed by the vacuum system, while the wished reaction products (for example, the metal) are deposited on the surface (Raffa et al., 1992; Reyntjens and Puers, 2001). Platinum (e.g. from trimethyl(methylcyclopentadienyl)platinum), tungsten (e.g. from tungsten hexacarbonyl), copper

(e.g. from hexafluoroacetylacetonato-copper(I)-trimethylvinylsilane Cu(hfac)TMVS), gold (e.g. from dimethyl gold hexafluoroacetylacetonate), aluminum (e.g. from trimethylaluminium TMA or triisobutylaluminium TiBA or trimethylamine alane TMAA or triethylamine alane TEAA) are some of the metals that have been deposited by FIB and the synthesis of new volatile metallo-organic compounds is an active research area; the minimum size for depositions is about 50 nm (Della Ratta et al., 1993; De Marco and Melngailis, 2001; FEI, 2005; Gamo et al. 1984; Gross et al., 1990; Kahng et al., 2009; Kim et al., 2012; Kubena et al., 1988; Shedd et al., 1986; Utke et al., 2008).

Therefore, although, unfortunately, our machine does not allow aluminium deposition, the fabrication of the proposed structures is still possible using FIB nanopatterning: milling and deposition could be carried out either from the top or from the side. The approach can also be extended to probes with metal coatings other than aluminium.

6.3. Final remarks

FIB milling has been successfully applied for the asymmetric shaping of our novel probes starting from fully metal-coated fiber probes. In particular, FIB slicing has been used for the creation of an oblique cut, whereas a head-on drilling approach has been used to carve a spiral groove in the metal coating.

While the slicing approach for the fabrication of cut probes represents a straightforward extension of the well-known process for the production of aperture probes, the head-on drilling on the walls of the taper requires slightly more attention due to the sensitivity of the sputtering yield to the angle of incidence, especially for high incidence angles in case of small taper angle. Therefore, the latter approach is more sensitive to the taper profile that, as we have discussed, depends on the fabrication technique used to create the fiber taper. Tests carried out on commercial probes fabricated by different methods have shown that a spiral groove close to the probe apex can be realized in a more accurate and reproducible way in tapers obtained by selective etching rather than in those fabricated by heating and pulling due to the smaller taper angle and the smaller apex. Despite the fact that the spiral grooves need a bit more care than the oblique cut, the creation of both the asymmetric structures requires a rapid processing of just a few minutes and appears easier than the creation of other asymmetric structures, like the one based on a monopole antenna that requires several milling steps at different angles.

7. Construction of the SNOM set-up

A complete SNOM set-up working in illumination mode has been created including the SNOM head built on top of an inverted microscope, the illumination unit and the detection unit. The arrangement of the set-up has been necessary to accomplish the characterization of our novel probes. Details of the characteristics of the different parts of the system are reported in this chapter.

7.1. Overview of the experimental system

For the characterization of the novel probes, a SNOM set-up working in illumination mode has been arranged. Such a system has been properly assembled to carry out measurements on fluorescent samples, thereby allowing an optical characterization of the probe behaviour as analyzed theoretically in chapter 5. A photograph of the overall set-up of the implemented system is shown in Fig. 7.1.

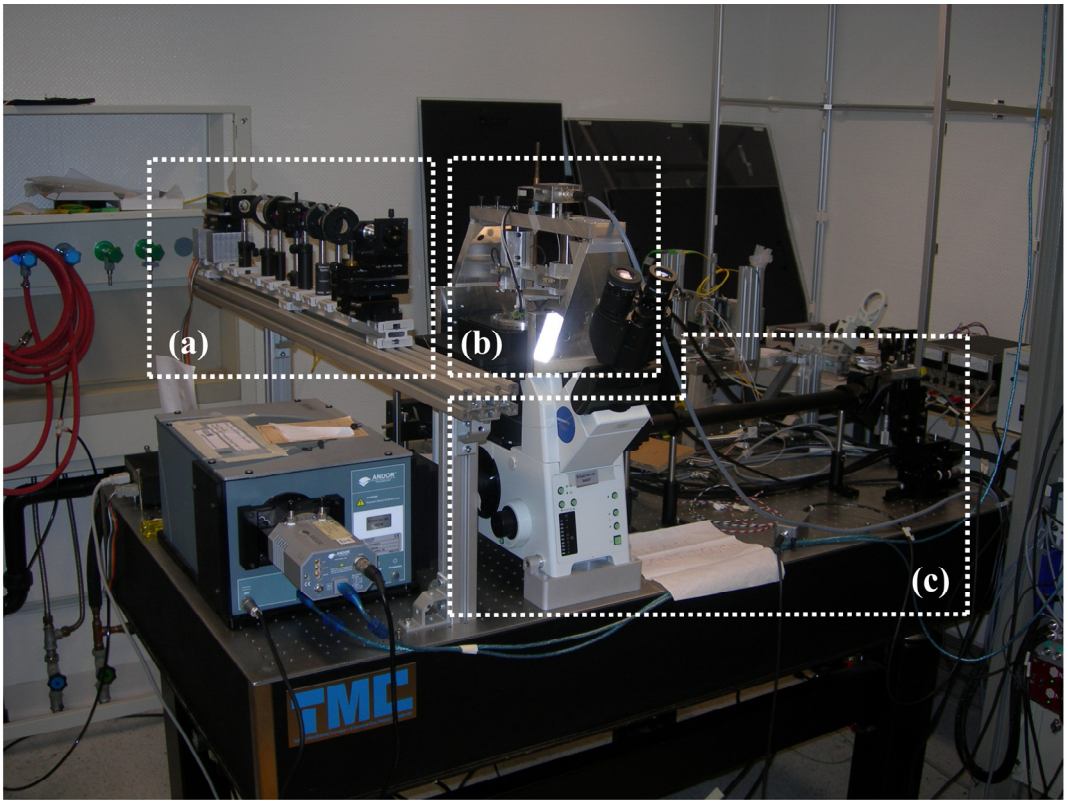

Fig. 7.1 – Photograph of the SNOM set-up: (a) illumination unit; (b) SNOM head and scanning stage; (c) detection unit.

Three fundamental units can be distinguished: the illumination unit, the SNOM head with a scanning stage and sample holder, and the detection unit made up of an inverted optical microscope steering and focusing the signal on the detector. Light from the laser, after proper polarization and power control, is coupled into the SNOM probe mounted on the SNOM head. The SNOM head is mounted atop an inverted microscope. A Nanonis SPM control system is used to provide control electronics and software for the SNOM head and to acquire the detector signals. For vibration damping, the whole set-up is mounted on an optical table with a steel honeycomb core breadboard (TMC 78 Series).

In the following paragraphs, each of the different units is described in more detail.

7.2. The illumination unit

The illumination path consists of (Fig. 7.2):

1. laser;
2. beam expander;
3. optics for power control;
4. optics for polarization control;
5. fiber coupler.

A single mode laser operating at 532 nm (CL532-025-S, CrystaLaser) provides an output beam of 0.36 mm diameter, 2 mrad of divergence and an output power of 25 mW. The output beam, linearly polarized at 45°, is sent through a 6X home-built Galilean beam expander (made up of a Newport plano-concave lens with focal length f_1=-25 mm and a Thorlabs achromatic doublet with focal length f_2=150 mm) for beam expansion and divergence reduction. Then, the power is controlled via a variable attenuator composed of a rotatable half wave plate and a laser line polarizing cube beam-splitter (PBSO-532-100, CVI Melles Griot, in fused silica with low autofluorescence): the amount of transmitted light is adjusted by rotating the half-wave plate. Polarization of the beam is then controlled using rotatable half and quarter wave plates. All the wave plates used in the illumination unit are zero-order precision polymer retarders (NQ-100-532 and NH-100-532, Meadowlark Optics), which have less sensitivity to wavelength change and better angular acceptance compared to quartz wave plates with variations in retardation less than 1% over ±12° incidence angle, so as to reduce the sensitivity to involuntary tilts of the wave plates during rotation. Finally, the beam is coupled into the fiber probe using a single mode fiber coupler (F-916, Newport), which provides submicron resolution via a kinematic tilt stage using fine 100-pitch alignment screws to pivot the objective/fiber holder assembly and three-axis adjustment of the fiber end with respect to

the focused laser beam. Both the fiber coupler and the laser are mounted on a five axis kinematic stage (9081 New Focus). All the illumination unit is built on top of a rail mounted almost at the same height as the SNOM head in order to minimize the fiber length. The characteristics of the objective, in particular its focal length f_{obj}, and the expansion ratio of the beam have been chosen taking into account the relationship between the diameter of the expanded beam D_{beam} and the mode field diameter of the specific fiber at hand d_{fiber}: $f_{obj} = D_{beam} \frac{\pi d_{fiber}}{4\lambda}$.

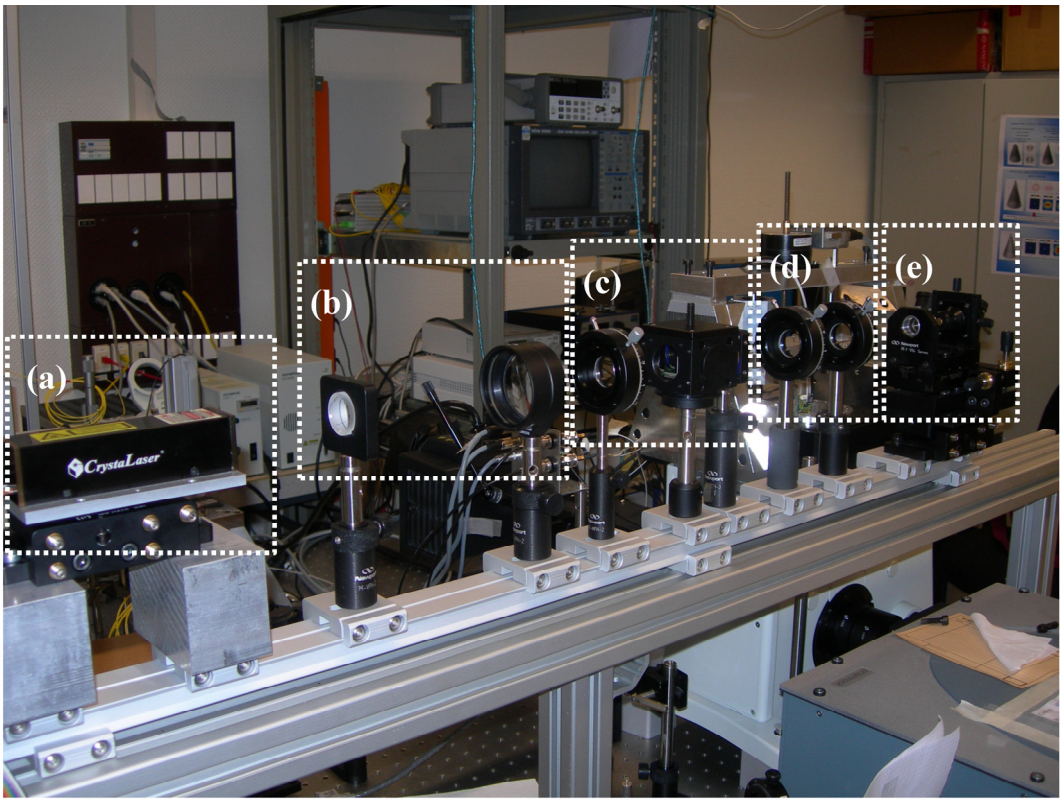

Fig. 7.2 – Illumination unit: (a) laser; (b) beam expander; (c) variable attenuator for power control; (d) optics for polarization control; (e) fiber coupler.

7.3. The SNOM head and the scanning stage

The SNOM head consists of an aluminium frame that can be mounted on the chassis of the inverted microscope, made of two vertical trapezoidal metal plates (which are screwed on the microscope) holding a horizontal arm to which the fiber probe holder is anchored (Fig. 7.3). In our set-up, during the SNOM measurements, only the sample is allowed to move in *x*,*y*,*z* directions, while the fiber probe is kept in a fixed position. However, for coarse positioning, both the probe and the sample can be moved for proper alignment. Therefore, the horizontal arm includes a stepper motor for coarse

approach of the fiber to the sample along *z* and two linear stages, which can be used to regulate the *xy* positioning of the probe with respect to the microscope objective.

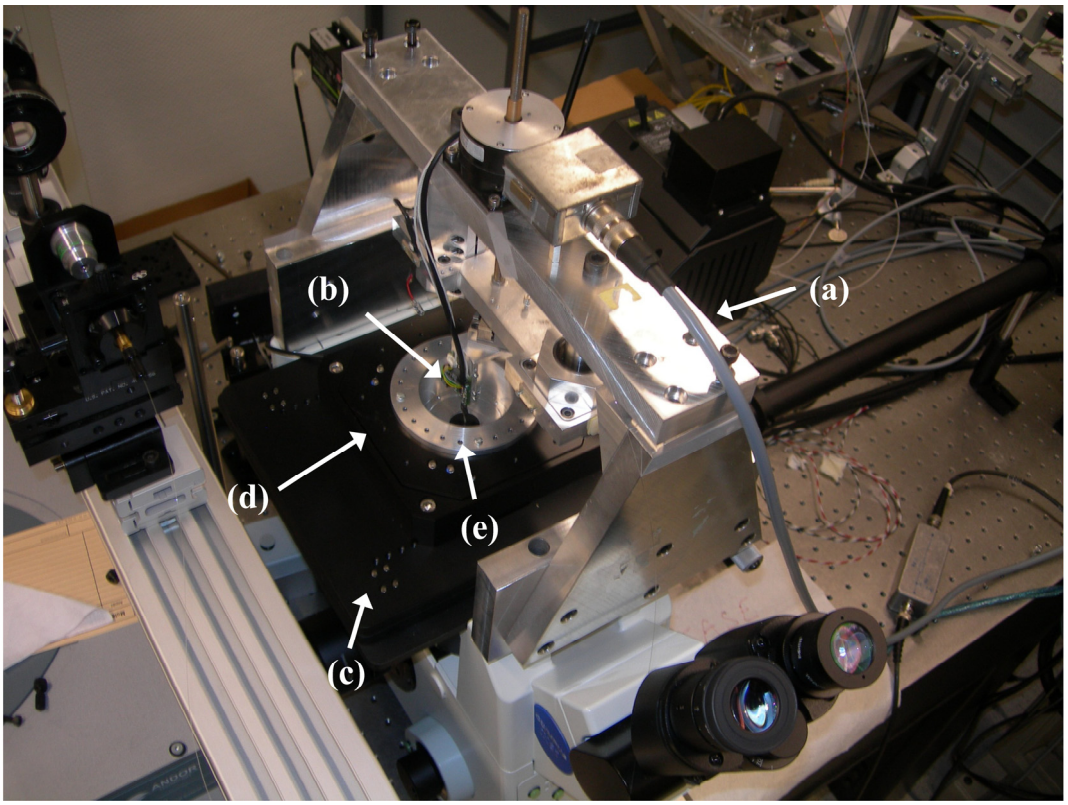

Fig. 7.3 – SNOM head: (a) mechanical support for the probe holder screwed to the inverted microscope and allowing *xyz* coarse positioning of the probe; (b) probe holder with PCB; (c) *xy* scanning stage for coarse positioning of the sample; (d) *xyz* scanning stage for fine scanning of the sample; (e) sample holder.

The L-shaped fiber holder is clamped to the horizontal arm of the aluminium frame through its horizontal part and includes a printed circuit board (PCB), mounted on the vertical part of the L-shaped holder and implementing the circuitry for control of the tuning fork; the tuning fork with a fiber probe previously glued on one of its prongs can be plugged into the bottom of this PCB. Theoretically, with such an arrangement, the fiber probe axis should lie along the *z* axis; however, small misalignments are typically observed; for this purpose, a variant of the aforementioned L-shaped holder has been designed, in which the vertical plate holding the fiber probe is hinged to the horizontal part, allowing rotation of the vertical plate and, hence, better alignment of the probe axis along *z*. Moreover, such a variant allows the fiber probe to be attached to the SNOM head more easily by simply rotating the vertical plate, without dismounting the whole head as in the case of the one-piece holder.

For the coarse and fine motion of the specimen, the sample holder is mounted on a fine scanning stage (P-517.3CL, Physik Instrumente), which, in its turn, is screwed to a coarse scanning stage (M-545.2MO, Physik Instrumente), which can be directly mounted on the inverted microscope. The *xy* coarse manual scanning stage allows coarse positioning of the specimen in the desired region to be addressed before starting the SNOM measurement, using manual micrometers with a total travel range of 25x25 mm and a minimum incremental motion of 1 µm. The *xyz* fine scanning stage, controlled by the Nanonis controller, allows the sample to be scanned over 200x200x20 µm during measurements with a resolution of 1 nm in *xy* and of 0.1 nm along *z*. The sample holder is clamped on the top of the fine scanning stage and is as deep as the fine scanning stage in order to allow focusing the microscope objective onto the sample during optical measurements. The bottom plate of the holder includes a circular hole to allow observation with the microscope objective; two holders with hole diameters of 20 and 35 mm, respectively, have been designed and realized; the latter is preferrable (if the size of the sample permits its use) because it allows the coarse scanning stage to scan over broader areas without risking collisions with the microscope objective.

Photographs of some details of the SNOM head are shown in Fig. 7.4.

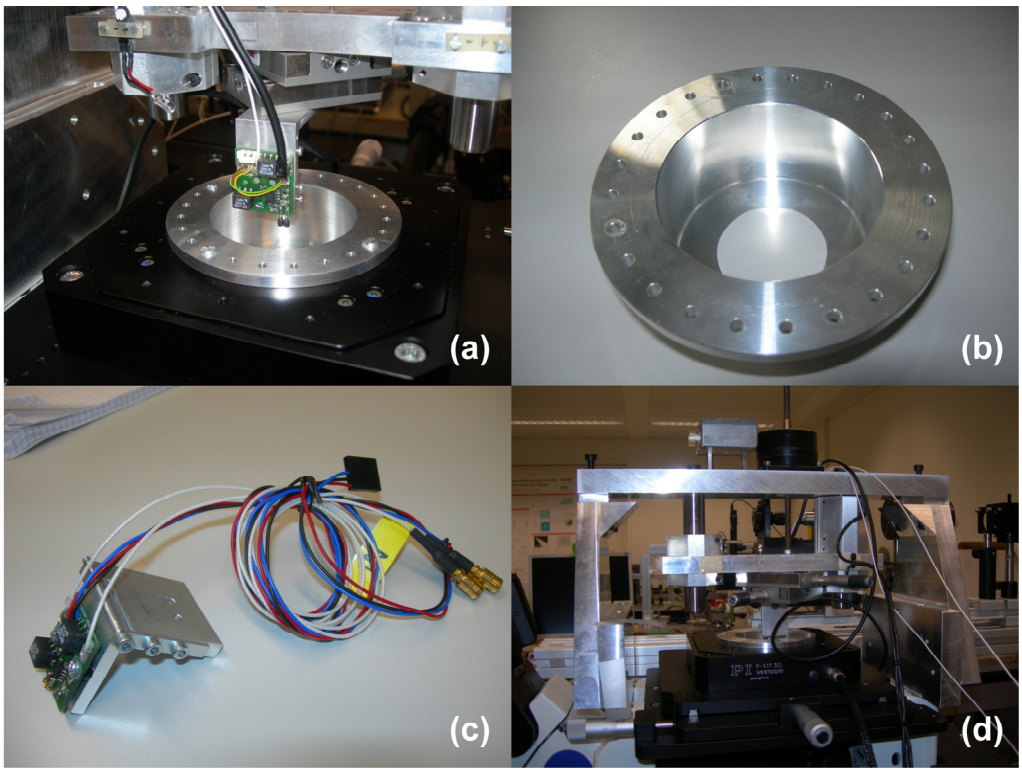

Fig. 7.4 – Details of some components of the SNOM head: (a) L-shaped probe holder with PCB; (b) sample holder; (c) modified L-shaped holder with movable vertical plate; (d) side view of the SNOM head showing the mechanisms for coarse *xyz* positioning of the probe and for coarse positioning and fine scanning of the sample.

7.4. The detection unit

The detection unit is made up of (Fig. 7.5):

1. inverted optical microscope;
2. detection optics;
3. single photon counting avalanche photodiode.

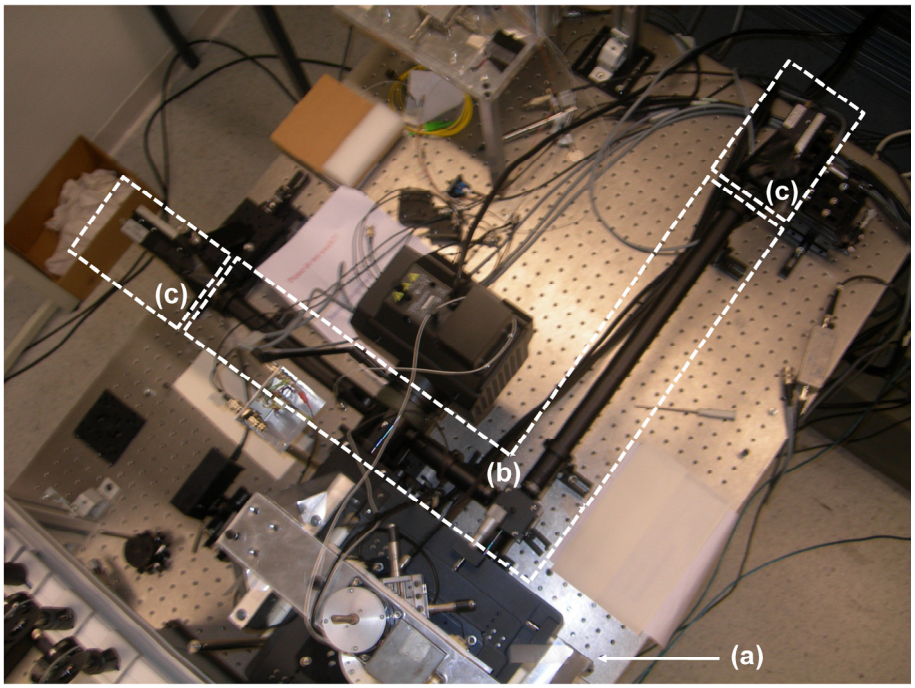

Fig. 7.5 – Detection unit: (a) inverted microscope; (b) light-shielded detection path; (c) single photon counting APDs.

The whole set-up has been built around a motorized inverted microscope frame Olympus IX81 allowing coarse and fine focusing of the objectives over 9 mm with a minimum step size of 10 nm and equipped with a motorized sextuple nosepiece and remote control from the computer. This framework was chosen for its flexible configurable port arrangement including the option of a right-side port with collimated output, which is useful for the insertion of external optical components in the detection path. Three different microscope objectives are available for light collection: a 10x objective with *NA*=0.25 (PLCN10X Plan Achromat C, Olympus), a 40x objective with *NA*=0.95 (UPLSAPO40X2 U Plan S Apo, Olympus), an oil immersion 100x objective with *NA*=1.4 (UPLSAPO100XO U Plan S Apo, Olympus). In the chosen port set-up, 100% of the collected signal can be easily switched betwen the oculars, the left-side port and the right-side port used for SNOM measurements. The inverted microscope, beyond being useful for the detection during SNOM

measurements, provides all the other conventional imaging functionalities to observe the sample before scanning measurements and check the position of the fiber probe during coarse approach with the stepper motor within a stable mechanical structure, which acts also as support for the SNOM head.

The main element of the detection optics for fluorescence measurements is represented by the long-pass filters (LP-03-532RU-25, Semrock, with edge wavelength of 536.4 nm, average transmission of more than 93% between 538.9 and 1200 nm and transition width of 5.3 nm, and BLP01-532R-25, Semrock, with edge wavelength of 542 nm, average transmission of more than 93% between 546.9 and 900 nm and transition width of 13.3 nm, both providing an optical density higher than 6 between 430 and 532 nm) used to suppress the excitation wavelength and collect the fluorescence signal emitted from the sample.

The filtered fluorescence signal needs then to be focused onto a proper detector. A single photon counting avalanche photodiode was used to collect the weak fluorescence signal emitted by the molecules. In particular, two such devices were available: a SPCM-AQRH-16, Excelitas, and a SPCM-AQR-16, Perkin Elmer; both of them allow detection of single photons over the wavelength range between 400 nm and 1060 nm with peak photon detection efficiency higher than 65% at 650 nm using a silicon avalanche photodiode (APD) with a circular active area with a diameter of about 180 μm; the dark count is less than 25 counts/s. When a photon is detected, a transistor-transistor logic (TTL)-level pulse is sent as an output and can be acquired using the pulse counter of the Nanonis controller. The APDs are mounted on an *xyz* translation stage for alignment. The single photon counting modules can be used singularly or simultaneously; in the latter case a broadband polarizing beam-splitter (10FC16PB.3 Newport, with a wavelength range of 420 to 680 nm) can be used to split the incoming filtered signal into two orthogonal polarization channels, which are then focused on each of the two APDs.

All the fluorescence measurements need to be carried out in a dark environment. In order to further suppress any undesired light which could interfere with the weak fluorescence signal, a light shielding provided by a 1 inch lens tube system (SM1), combined with black tissue (rubberized blackout fabric BK5) and adhesive tape (high performance black masking tape T743-2.0) from Thorlabs has been implemented.

7.5. The control electronics

The control electronics is mostly realized within the Nanonis SPM control system (Fig. 7.6). The Nanonis controller has a three-fold function:

1. control of tip approach and tip-sample distance during scanning;

2. control of fine *xy* scanning of the sample;

3. acquisition of the pulses from the detectors for pulse counting.

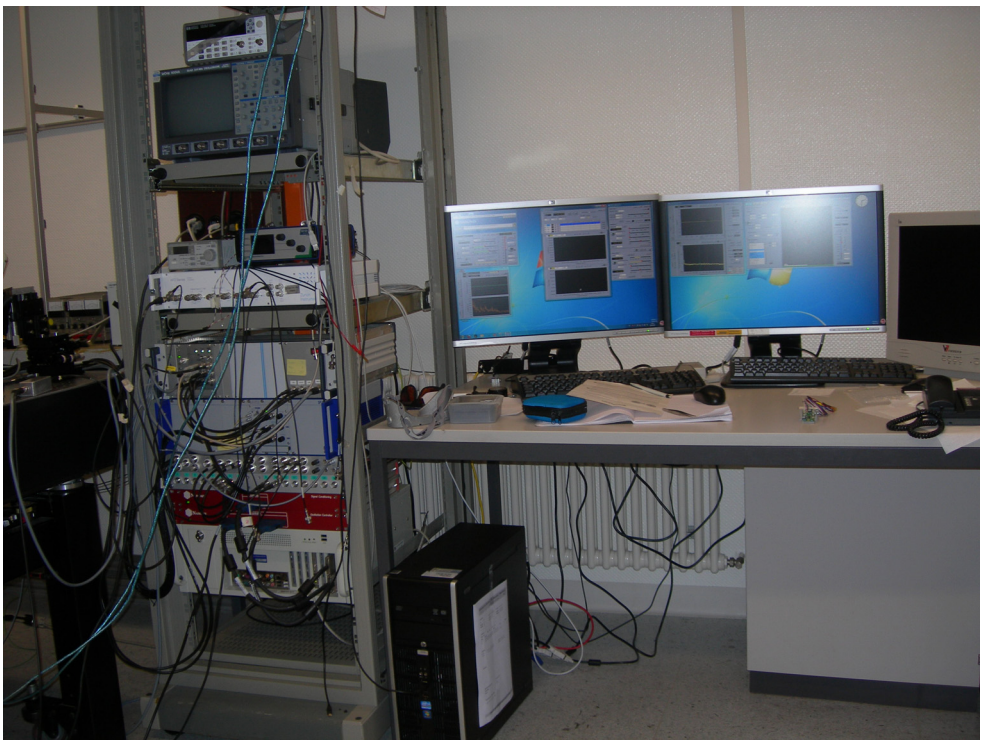

Fig. 7.6 – Control electronics and software.

A tip-sample distance control based on the use of a shear force detection in a tuning fork-based system has been implemented. In particular, the fiber probe is previously glued on one of the prongs of the tuning fork; the tuning fork with the glued fiber probe is oscillated at its resonance frequency resulting in a lateral oscillation of the prongs; as the fiber probe approaches the sample, a variation in the frequency, phase and amplitude of the oscillation is observed; the variation of one or more characteristics of the oscillation is used for probe-sample distance control within a feedback loop to mantain constant distance during scanning.

The tuning fork consists of a micro-machined quartz element with electrodes deposited on its surface with a specific layout (Novotny and Hecht, 2006). The oscillation of the tuning fork can occur either via electrical or mechanical excitation: in the first case, an alternating voltage is applied to the electrodes and results in motion of the prongs against each other in opposite directions in an antisymmetric way; in the second case, the vibration is induced by an external piezoelement located at the base of the tuning fork resulting in the movement of the two prongs in a symmetric fashion (Karrai and Grober, 1995a; Mühlschlegel et al., 2006). The mechanical oscillation of the tuning fork

induces surface charges, which gather at the electrodes and can be detected via an external electronic circuit (Novotny and Hecht, 2006). In case of mechanical excitation, no net useful detectable signal is produced with the tuning fork alone; the fiber probe glued on one of the two prongs breaks the symmetry in the structure and hence in the motion of the two prongs, creating a useful differential electrical signal (Karrai and Grober, 1995a). In our case, electrical excitation has been used.

The equivalent electric circuit of the tuning fork is given by the so-called Butterworth-van Dyke electric circuit consisting of a series LRC circuit with a parallel capacitance C_0, originating from the electrodes and the external cables (Novotny and Hecht, 2006). Therefore, the electrical excitation of the tuning fork is carried out via a center-tapped transformer and a variable capacitor driven by an alternating voltage source; with such a configuration, the stray parallel capacitance C_0 can be cancelled, thereby reducing the equivalent circuit of the electric oscillator to a simple LRC oscillator (Barbic et al., 2007; Grober et al., 2000). Then, the tuning fork oscillates mechanically and the current generated at its electrodes is amplified and converted into a voltage with a trans-impedance pre-amplifier (Karrai and Grober, 1995a) (Fig. 7.7).

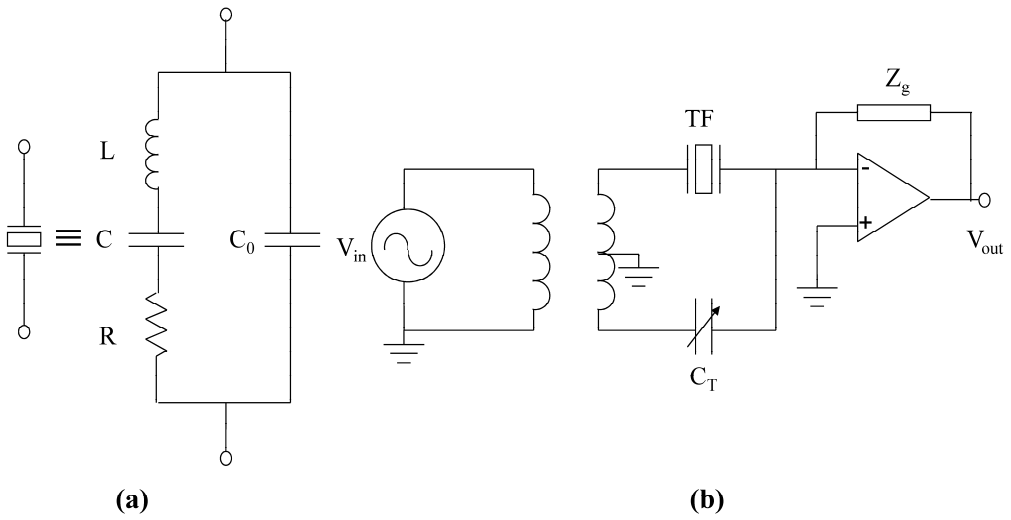

Fig. 7.7 – Sketch of: (a) quartz tuning fork with its equivalent electric circuit; (b) stray capacitance compensation and pre-amplifier (adapted from: Barbic et al., 2007; Grober et al., 2000).

Control of the oscillation is carried out via a phase locked loop (PLL) including a lock-in amplifier, two proportional/integral (PI) controllers and a numerically controlled oscillator, which generates a numerical sine wave and provides the reference signal for the lock-in amplifier. Either of the signals measured within the oscillation control module (e.g. phase, amplitude, frequency shift) can be used as feedback signal in the *z*-control feedback loop; the latter includes a PI controller and generates an output driving the high voltage (HV) amplifier, which regulates the motion of the *z*

scanning stage so as to keep the feedback signal close to the desired set-point. The center-tapped transformer with the circuitry for stray capacitance compensation and the pre-amplifier are implemented externally to the Nanonis controller on the aforementioned PCB.

The sketch of the overall control electronics is reported in Fig. 7.8.

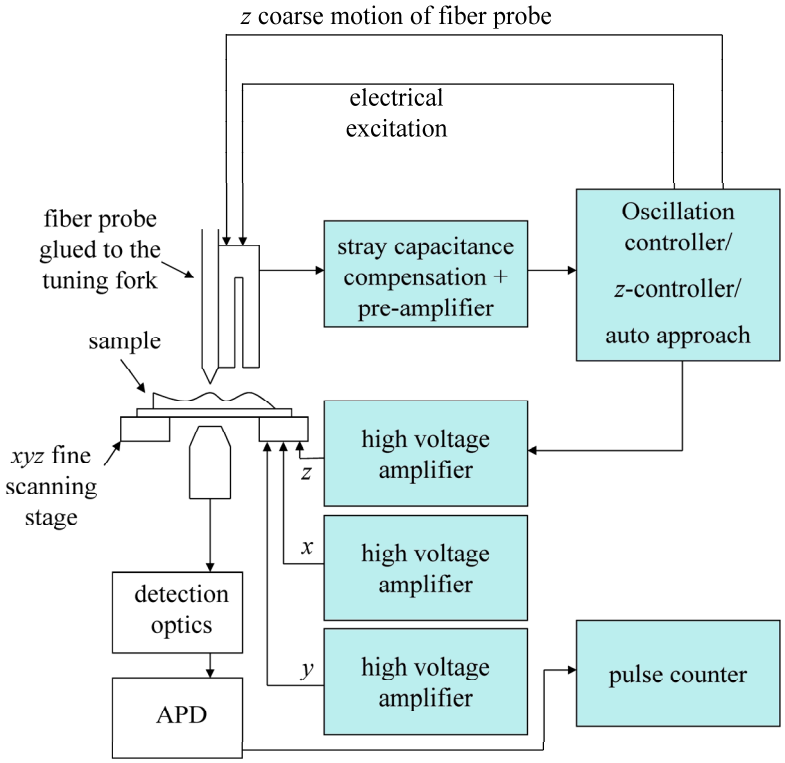

Fig. 7.8 – Sketch of the control electronics: circuitry for stray capacitance compensation and current-to-voltage conversion via the pre-amplifier are realized on the PCB.

The Nanonis controller also drives the stepper motor for coarse *z* movement of the probe. In fact, in the automatic coarse approach procedure, first the fine *z* scanning stage moves the sample towards the probe, while the *z*-control feedback loop is active; if the desired approach point (which means if the desired value for the feedback signal) is not reached over the whole travel range of the fine *z* scanning stage, the latter retracts the sample away from the probe; the probe is then approached towards the sample by one coarse step (smaller than the travel range of the fine *z* scanning stage so as to avoid crashing the probe against the sample) via the stepper motor; the *z*-controller is restarted and the procedure is iterated until the desired approach point is reached; afterwards only the *z*-control feedback loop is active and keeps the probe-sample distance constant. The Nanonis controller also drives the HV amplifiers controlling *xy* fine scanning of the sample over the desired scanning area. The Nanonis software allows definition of the scanning parameters.

The pulse counters from the Nanonis controller allow acquisition of the TTL signals from the APDs up to 40 Mcps (Mcounts/s).

7.6. The mechanical set-up for fiber probe gluing

As anticipated in chapter 1, gluing the fiber to the tuning fork represents a delicate step. In order to facilitate this preliminary step for SNOM measurements, a dedicated mechanical set-up was built up (Fig. 7.9).

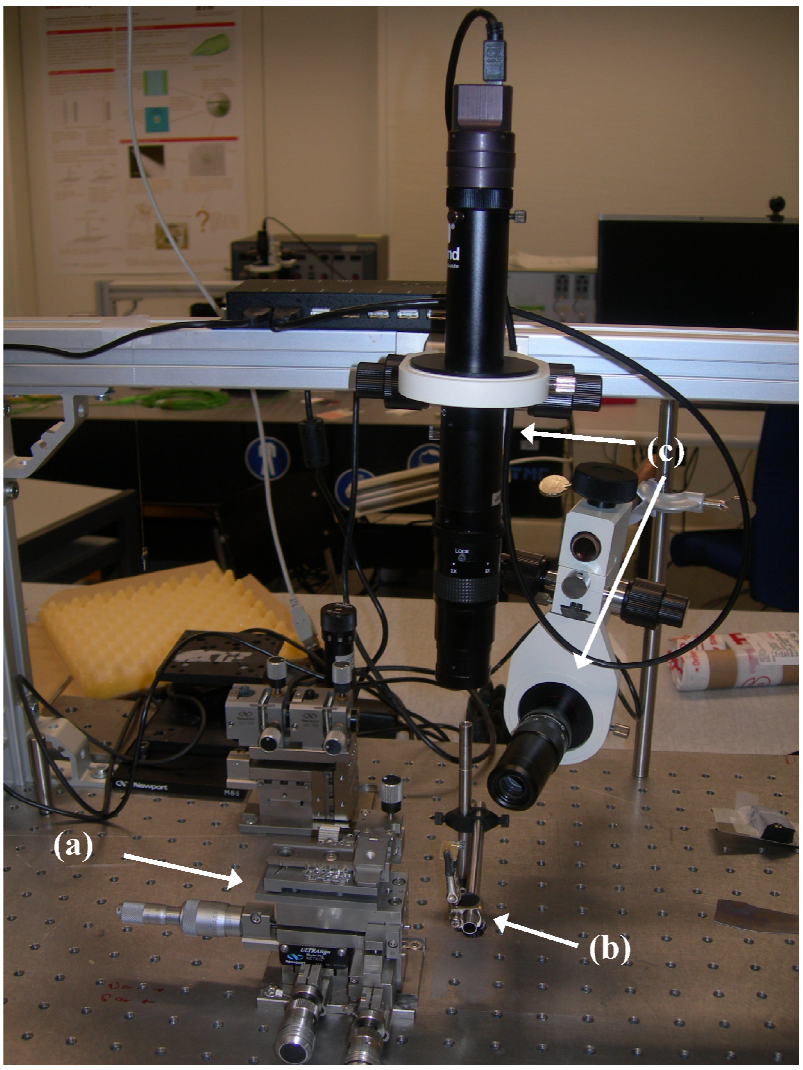

Fig. 7.9 – Gluing set-up: (a) stage for fiber-probe alignment; (b) tuning fork holder; (c) cameras.

It consists of a precision stage for fiber probe positioning and a holder for the tuning fork allowing rough translational and angular adjustment of the tuning fork. The tuning fork (after removal of the protective metal capsule) and the fiber probe are mounted on the two holders. After

rough alignment of the tuning fork with respect to the fiber probe, the fine alignment of the fiber probe is carried out using a six degrees of freedom positioning stage (561 ULTRAlign linear stages in combination with tilt/rotation stages, Newport) using manual micrometers. The glue is applied using a micropositioner. Precise alignment and gluing are monitored with two cameras.

7.7. The measurement sequence

A typical SNOM measurement with the implemented system requires the following steps:

1. The position of the probe, glued to the tuning fork and mounted into the SNOM head and inserted in the fiber coupler, is coarsely adjusted so as to center it with respect to the microscope objective (*xy* coarse adjustment) and to approach it to the sample as much as possible (*z* coarse adjustment with stepper motor); the position of the probe can also be visually checked using the microscope objectives. The *xy* position of the sample is also coarsely adjusted to address the desired area.
2. The resonance curve of the probe/tuning fork system far from the sample is measured using the Nanonis software and controller.
3. Once the fiber probe has been brought close enough to the sample, the automatic approach mechanism provided by Nanonis can be engaged; the probe/tuning fork system is excited at its resonance frequency; at this stage, the feedback loop is activated and can monitor either the amplitude or frequency shift as the probe/sample distance changes; with the automatic approach, the sample is moved upwards along *z* towards the probe using the fine scanning stage; if the desired approach point is not reached over the whole *z* travel range of the fine scanning stage, the sample is retracted downwards to the maximum distance from the probe and the probe is automatically moved downwards by one step with the stepper motor; once the desired approach point is reached, the feedback loop keeps it constant by mantaining the error signal close to zero, thereby guaranteeing constant distance operation.
4. At this point the SNOM scan can start.

7.8. Final remarks

The SNOM set-up working in illumination mode built up in the laboratory has been described in all its units. The whole construction has been intended for the characterization of the SNOM probes, in particular optical characterization via fluorescence measurements.

8. Characterization of a novel asymmetric SNOM probe

The novel probe design based on an oblique cut has been tested. After preliminary topographic measurements, an optical characterization of a probe exhibiting this form of asymmetry has been carried out using fluorescent molecules to map the near-field distribution close to the probe apex. Experimental results have been compared with the theoretical predictions reported in chapter 5.

8.1. Characterization of a novel near-field probe

Characterizing the optical behaviour of a novel SNOM probe is a challenging task. Most of the calibration samples, like gratings or other regular patterns, are characterized by topographic variations that, while suitable to check the operation of the feedback system regulating probe-sample distance, do not allow a straightforward interpretation of the optical behaviour of the probe, which is the most peculiar feature of SNOM as opposed to other scanning probe microscopy techniques.

The reason why samples endowed with topography are not adequate for the optical characterization of a near-field probe resides in the high likelihood of topographic artifacts that typically occur as a result of the coupling between optical and topographic signals due to the strong dependence on distance of the evanescent waves, which affects the detected optical signal especially for a SNOM system operated in constant distance mode (Sandoghdar, 2001). In this case, *z*-modulations (i.e. probe-sample distance modulations) create a contrast corresponding to topography that can be comparable to the true optical contrast (originating from optical or surface-related properties of the sample) or even dominate it; in fact, the detected optical signal $R_{NFO}(x,y)$ can be written as (Hecht et al., 1997; Novotny and Hecht, 2006; Sandoghdar, 2001):

$$R_{NFO}(x,y) = \bar{S}_{NFO}(\bar{z}) + \delta S_{NFO}(x,y,\bar{z}) + \frac{\partial S_{NFO}}{\partial z}\Big|_{\bar{z}} \cdot \delta z \qquad \textbf{(8.1)}$$

where S_{NFO} is the true optical signal, $\bar{z}$ is the average *z*-position of the probe, δz is the variation of the *z* position around $\bar{z}$ due to the feedback. The first two terms are related to background and variations in light intensity corresponding to true optical contrast; the third term represents the coupling between optical and vertical *z* motion. In order to minimize topographic artifacts, the following inequality should be valid (Hecht et al., 1997; Novotny and Hecht, 2006; Sandoghdar, 2001):

$$\delta S_{NFO}(x,y,\bar{z}) >> \frac{\partial S_{NFO}}{\partial z}\Big|_{\bar{z}} \cdot \delta z \qquad \textbf{(8.2)}$$

which is generally not satisfied.

Although constant height mode is less sensitive to such a problem, it presents a more significant risk of collision of the probe against the sample and complicates image interpretation, especially for samples characterized by topographic modulations rather than by variations in optical properties like index of refraction (Sandoghdar, 2001).

Therefore, other solutions for optical characterization need to be devised. One route consists in the use of a second near-field probe to detect the near-field distribution close to the apex of the novel near-field probe under test (Fig. 8.1 (a)). As anticipated in chapter 5, in this set-up named tip-on-tip or probe-to-probe, the field distribution of the novel probe operated in illumination mode is scanned in constant height mode by a known tip operated in collection mode (Tortora et al., 2007; Yatsui et al., 2002). The criticality of such a set-up is immediately apparent as it would require very precise alignment of the axes of the two probes, adding to the complexity of the involved mechanics and imposing an extremely time-consuming procedure. Moreover, as the resulting detected field distribution would be the convolution of the field distribution of the two probes, the instrumental function of a properly selected measuring probe should be taken into account.

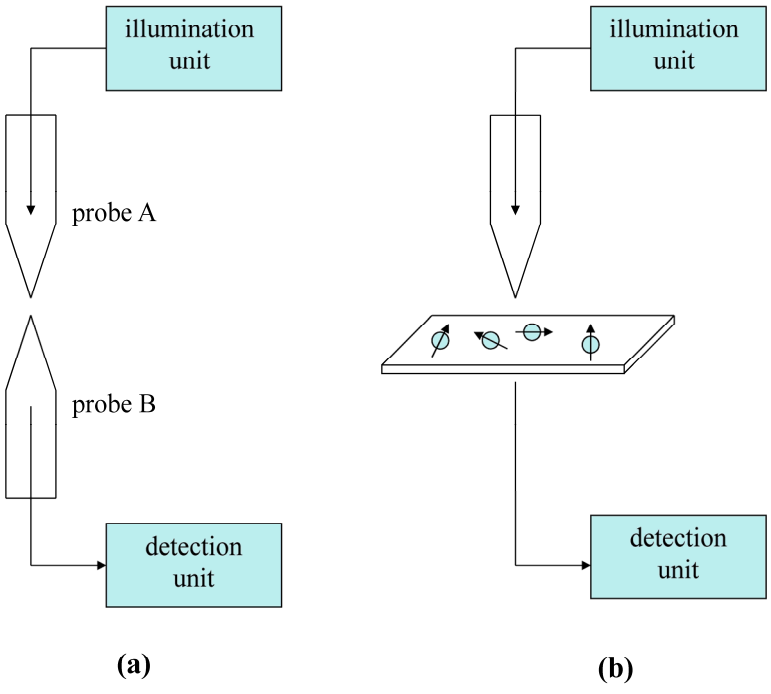

Fig. 8.1 – Sketch of set-ups for optical characterization of SNOM probes: (a) tip-on-tip measurements in which the near-field distribution at the apex of probe A used in illumination mode is analysed using probe B in collection mode; (b) mapping of the near-field distribution with fluorescent molecules acting as point-like detectors of the near-field distribution at the probe apex.

An even better alternative consists in the use of a topography-free sample for SNOM probe characterization. A particularly interesting approach is given by the use of single fluorescent molecules as nearly point detectors to map the near-field distribution of the probe, which, as highligthed in chapter 5, offers the additional advantage of providing a vectorial picture of such an intensity distribution (Fig. 8.1 (b)).

In the following paragraphs, the results of the characterization of a novel probe based on the oblique cut design are reported. The experimental set-up described in chapter 7 has been used for this purpose. The specific structure at hand is based on a commercial Lovalite probe produced by heating and pulling and properly nanostructured with FIB, as described in chapter 6, so as to get a cut angle of 50°. First, a sample with known topographic features has been considered to test the proper operation of the feedback system and the ability of the probe to reproduce the topography of a sample with known features. After this validation, the optical characterization of the novel probe has been carried out using a sample based on single fluorescent molecules.

8.2. Topographic tests

The sample used in our measurements in order to test the ability of the probe to reproduce the topography of a sample with known features is based on metal islands arranged in a regular pattern forming a hexagonal array. Such a sample, known as Fischer pattern after its inventor, is fabricated using a latex sphere shadow mask technique (Ferber et al., 1999; Fischer et al., 2002; Hecht, 1996; Hecht et al., 1998; Winzer et al., 1996): a monolayer of monodispersed latex spheres is deposited on a clean hydrophilic glass slide or on a mica substrate, for example by pouring a droplet of acqueous suspension of latex spheres on the glass with subsequent slow evaporation of water; the monolayer of latex spheres acts as a mask during the subsequent evaporation of metal; afterwards, the latex spheres can be removed with CH_2Cl_2 in an ultrasonic bath or by floating the mask onto a clean surface of water; the remaining pattern consists of nearly triangular metal islands created at the interstices between the spheres (Fig. 8.2).

In our case the sample, bought from Kentax, consists of a 0.15 mm thick glass slide with a latex projection pattern produced by physical vapour deposition of aluminium on a monolayer of latex spheres of diameter *d* equal to 453 nm. The resulting inscribed metal islands can be approximated as equilateral triangles of side length equal to about $d \cdot 2/\sqrt{3} \cdot \left(\sqrt{3} - 3/2\right)$ and height $d\left(\sqrt{3} - 3/2\right)$ (Hecht et al., 1998), corresponding, in our case, to approximately 121 nm and 105 nm, respectively; the nearest neighbour distance between the metal islands is $d/\sqrt{3}$, that is 262 nm.

Scans over areas with different sizes have been performed. Fig. 8.3 shows two scans on a 2x2 μm^2 and on a 4x4 μm^2 *xy* area, respectively: in both cases the expected pattern is clearly

recognizable, as also shown by further analysis of the images. Nearly triangular metal islands are arranged in a hexagonal pattern, apart from a few lattice defects visible in Fig. 8.3 (b).

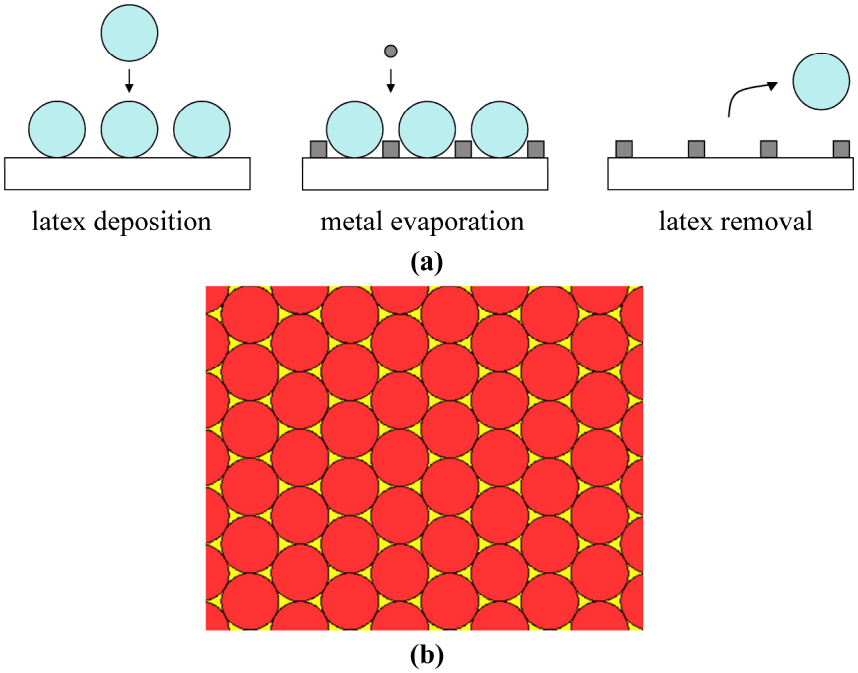

Fig. 8.2 – Sketch of: (a) Fischer pattern fabrication steps consisting of a preliminary deposition of closely packed latex spheres serving as a mask followed by metal evaporation and final removal of the latex spheres by application of an organic solvent (e.g. CH_2Cl_2) in an ultrasonic bath or by floating the mask onto a clean surface of water (adapted from Ferber et al., 1999); (b) resulting pattern: metal islands arranged in a hexagonal array are created at the interstices between the latex spheres.

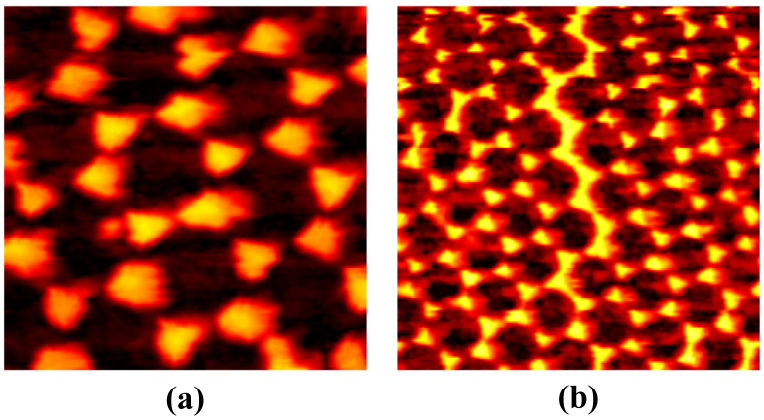

Fig. 8.3 – Topographic scans of a Fischer latex projection pattern performed with the novel asymmetric probe based on an oblique cut: (a) over a 2x2 μm^2 area; (b) over a 4x4 μm^2 area. In both images the hexagonal pattern of the nearly triangular metal islands can be easily identified.

In order to better investigate the ability of the probe to follow the sample topography, line cuts of the Fischer latex projection patterns have been considered. Fig. 8.4 (a) and (b) show the profiles taken along the white lines: even residuals of incomplete latex sphere removal, partial diffusion of the evaporated material underneath the latex spheres and surface defects of the substrate are visible. The cross sections confirm the size and periodicity of the structure determined according to the simple geometric formulas previously calculated.

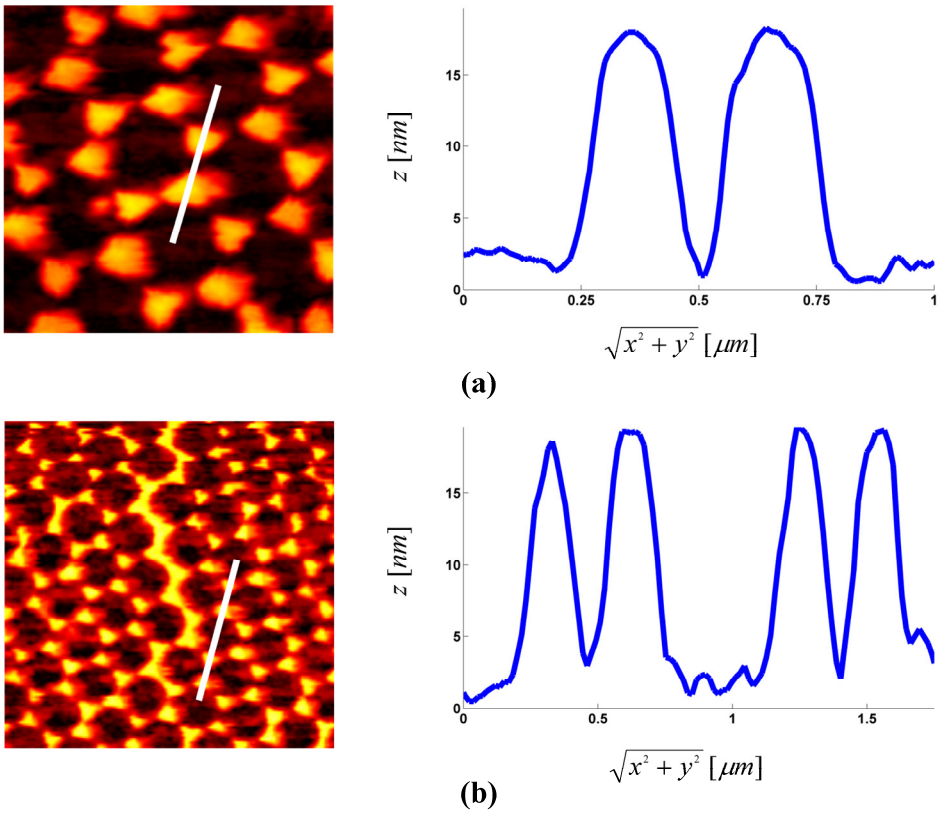

Fig. 8.4 – Topographic profiles of a Fischer latex projection pattern: (a) profile along the white line of the 2x2 µm^2 scan; (b) profile along the white line of the 4x4 µm^2 scan. Cross sections confirm the expected characteristics of the metal island arrangement.

In order to assess the ability to recognize the nearly triangular islands, an object detection and boundary tracing algorithm was applied to detect the triangular shapes, as shown by a detail in Fig. 8.5, which also reports a three-dimensional plot of the topographic scan. An even better insight into the periodicity of the structure not only along a single line but over the entire scanning area (and hence into the ability of the probe-sample distance control mechanism to faithfully follow the surface topography) can be gained by the computation of the two-dimensional Fourier transform of the scanning image. The hexagonal honeycomb structure is apparent in Fig. 8.5 (c).

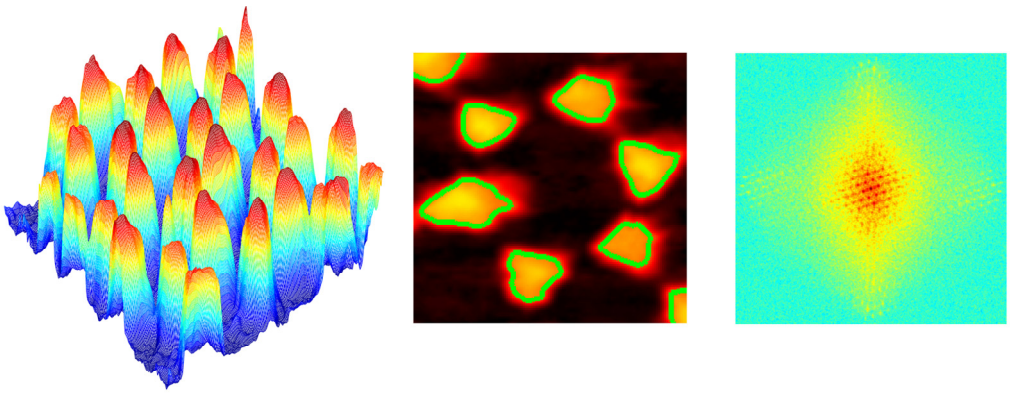

(a) (b) (c)

Fig. 8.5 – Processing of the topographic scans: (a) 3D plot of the scan reported in Fig. 8.3 (a); (b) detail of Fig. 8.3 (a) with application of an object recognition and boundary detection algorithm to identify the nearly triangular islands; (c) 2D Fourier transform of Fig. 8.3 (b) showing the hexagonal pattern. In (a), for a better 3D visualization, the topographic measurement is on a magnified scale compared to the *xy* axes.

8.3. Optical measurements

In order to carry out the optical characterization of the probe, fluorescent molecules have been used. Although a solution of fluorescent molecules could be deposited directly on the cover slip (Ruiter et al., 1997), the sample thus produced would be more sensitive to fluorescence quenching (i.e. a reduction in fluorescence intensity) in the presence of molecular oxygen and due to photo-oxidation of the fluorophore (Moerner and Fromm, 2003). In fact, by energy transfer from the fluorescent molecule (photosensitization) molecular oxygen in the ground triplet state can be excited to the first excited state, known as singlet oxygen, which is a highly reactive molecule (Ishitobi et al., 2009). More specifically, the presence of oxygen has two effects: first, it increases the rate of transitions to the triplet state; second, it quenches the triplet state of the dye molecule via triplet-triplet annihilation with ground state triplet oxygen, with the production of singlet oxygen, which can bring about photochemical oxidation, decreasing the photochemical stability of the dye (Garcia-Parajo et al., 2001). Hence, a reduction in the oxygen exposure would be desirable (Moerner and Fromm, 2003; Protasenko and Gallagher, 2004a).

Different strategies have been worked out to pursue this goal. A first solution consists in operating in vacuum (Moerner and Fromm, 2003; Protasenko and Gallagher, 2004a); as an alternative, the sample may be measured in a controlled atmosphere of an inert gas (e.g. nitrogen or argon atmosphere) for example by a laminar flow of the inert gas (Moerner and Fromm, 2003; Parent et al., 1999); another approach consists in embedding it in a polymer film, like PMMA,

polyvinyl alcohol (PVA) or polystirene (PS) (Betzig and Chichester, 1993; Parent et al., 1999; Protasenko and Gallagher, 2004a). Sometimes, combinations of these strategies are used.

The first approach cannot be implemented in our set-up; the use of a laminar flow of nitrogen is likely to impact adversely on the probe-sample distance control by increasing the noise in the shear force signal, thereby deteriorating the quality of the scans (Stevenson et al., 1999). Therefore, in our case, the last approach has been adopted. In particular, we chose a dialkilcarbocyanine dye, 1,1'-dioctadecyl-3,3,3',3'-tetramethylindocarbocyanine perchlorate (commonly known as $DiIC_{18}(3)$ or DiI), and an Alexa Fluor dye, named Alexa Fluor 532, as fluorescent dyes and PMMA as host polymer film. The molecular structure of the host polymer and of the fluorescent dyes is shown in Fig. 8.6, together with the absorption and emission spectra of the fluorescent molecules. The chosen fluorescent dyes have been already used in experiments performed with near-field probes and offer several advantages like high fluorescence quantum yields and high photostability (Frey et al., 2006; Ruiter et al., 1997; van Hulst et al., 2000). As to the selection of the host polymer, we have to point out how the diffusion constant of oxygen in PMMA is lower than the one in PS; moreover, the rotational mobility of molecules within PMMA is lower than the one in PS; translational and rotational mobility of molecules in PMMA are low due to its large elastic modulus (Garcia-Parajo et al., 2001). The use of the polymer matrix offers the further advantage of increasing the adhesion of the individual molecules (Betzig and Chichester, 1993).

For the preparation of samples based on fluorophores embedded in PMMA, one can follow different methods: for example, the fluorescent molecules can be deposited first on the cover slip and then overcoated by PMMA or the dye solution can be spin-coated on the PMMA layer previously spin-coated on a cover slip or a solution of PMMA already containing the molecules can be spin-coated on the cover slip (Betzig and Chichester, 1993; Novotny et al., 2001; Ruiter et al., 1997). In our case, the last approach was adopted in order to get fluorescent molecules with arbitrary orientation of the absorption dipole moment and a droplet (about 10-20 μl) co-solution of PMMA and fluorophores in toluene was spin-coated on the cover slips, with molar concentration of the fluorophores variable between approximately 10^{-6} and 10^{-9} M. The use of PMMA also reduces quenching effects due to direct metal-fluorophore interactions at short distance, which would prevent the observation of single spots in case of fluorophores with longitudinal dipole moment (Frey et al., 2004).

Fig. 8.7 shows scans over a 500 x 500 nm^2 scanning area of the single fluorescent molecules embedded in PMMA taken with the novel asymmetric probe based on an oblique cut. An interesting feature deserving a more careful analysis is the shape of the different spots. As clearly visible, single- and double-lobed patterns have been observed for the different molecules, as expected for

molecules with arbitrary orientation, with the single-lobed patterns appearing generally brighter than the double-lobed ones and the maximum count rate amounting to 70 kcps.

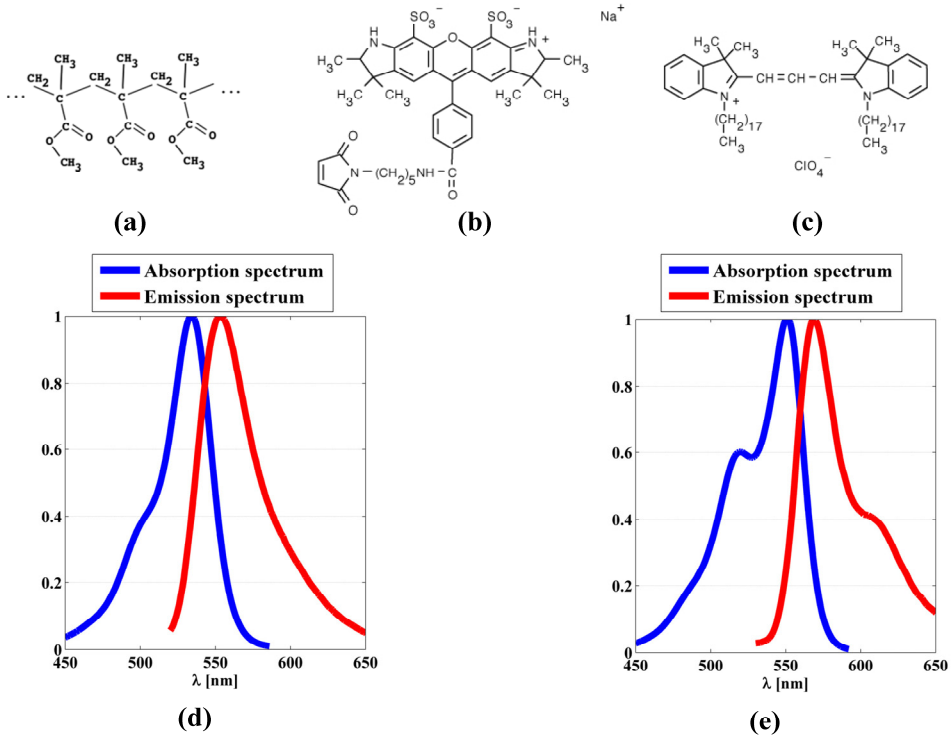

Fig. 8.6 – Fluorescent dyes embedded in PMMA: (a) molecular structure of PMMA $(C_5O_2H_8)_n$; (b) molecular structure of Alexa Fluor 532 $(C_{39}H_{41}N_4NaO_{10}S_2)$; (c) molecular structure of DiI $(C_{59}H_{97}ClN_2O_4)$; (c) absorption and emission spectra of Alexa Fluor 532; (d) absorption and emission spectra of DiI. Samples are prepared by spin coating of a solution of PMMA already containing the molecules on a cover slip.

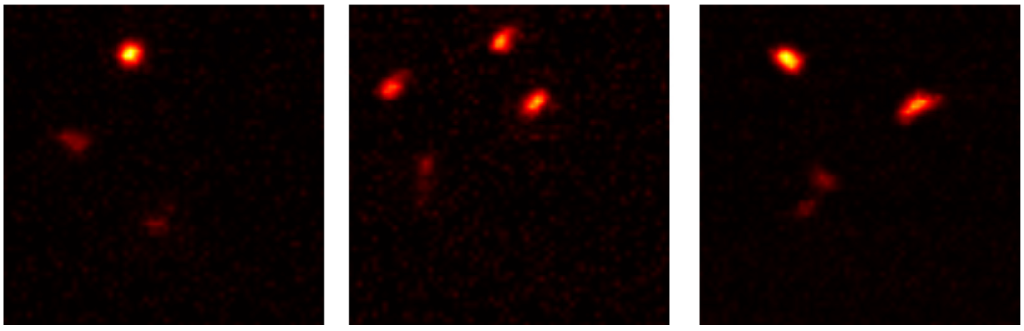

Fig. 8.7 – Scans over a 500 x 500 nm^2 area of single fluorescent molecules embedded in PMMA performed with the novel asymmetric probe based on an oblique cut. Both single- and double-lobed patterns can be recognized due to the random orientation of the dipoles. Maximum count rate amounts to about 70 kcps.

To better investigate the characteristics of the different molecule distributions, which provide precious information about the vectorial properties of the near-field of the probe and on the resolution achievable with the novel asymmetric probe, we considered the cross sections of the fluorescence patterns of the molecules taken along some lines as shown in Fig. 8.8.

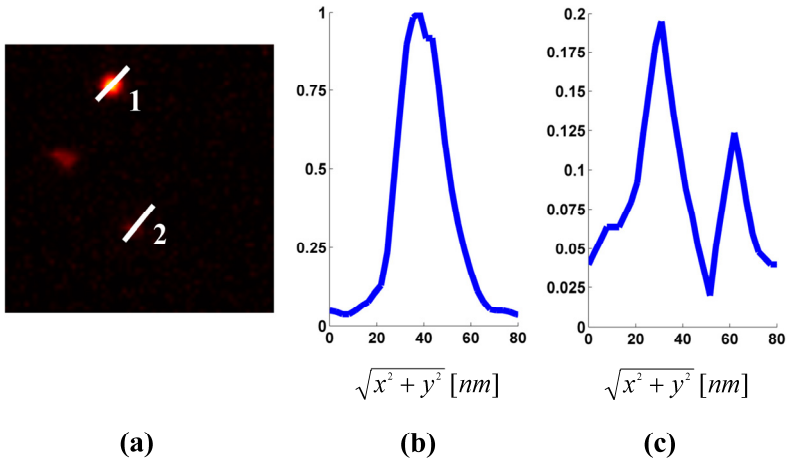

Fig. 8.8 – Profile of the fluorescence signal emitted by different molecules: (a) 2D scan over a 500 x 500 nm^2 area with indication of the lines along which line cuts have been considered; (b) profile of molecule 1; (c) profile of molecule 2. All the profiles are normalized to the maximum count rate measured during the scan so as to emphasize the relative magnitudes. Line cuts reveal features even below 20 nm providing an evidence of the high resolution achievable with the novel asymmetric probe.

Molecule 1 exhibits a clear single hot spot; a transition from a single-lobed to a double-lobed pattern occurs for molecule 2. In particular, according to the theoretical analysis illustrated in chapter 5 and considering that each molecule can be interpreted as a detector of the vectorial distribution of the near-field at the apex of the novel probe, molecule 1 should exhibit an almost longitudinal orientation of the dipole moment (polar angle θ close to 0°), whereas for molecule 2 the dipole moment should be almost transversal (polar angle θ close to 90°). In fact, the near-field distribution at the apex of the asymmetric cut probe was shown to be made up of a dominant single-lobed longitudinal component and two weaker double-lobed transverse orthogonal components. A transition of the dipole moment from θ=0° to θ=90° implies a stronger overlap with the transverse components rather than with the longitudinal one, because each molecule is excited by the component of the electric field parallel to its dipole direction. Beside the variation in intensity and shape of the fluorescence map, also the size (FWHM) of the spot changes, going approximately from 20 nm to 60 nm for molecules with different orientations. Note that for double-lobed patterns the spot size has been calculated over the whole molecule (two lobes) and not for each of the two lobes

that can be even below 20 nm as is visible from the intensity profile of molecule 2 in Fig. 8.8. The results are in good qualitative agreement with the predictions of chapter 5. In fact, the slight differences in spot size compared to computations are due to the fact that the fabricated probe is not identical to the ideal structure considered in the simulations, especially in terms of the effective curvature of the apex, in addition to the variability in the distance from the probe apex of the molecules within the PMMA layer.

To get a better comparison between the measured fluorescence patterns and the theoretical expectations, we varied the final curvature of the probe apex. Better fits between experimental data and computational model were obtained by halving the curvature with respect to the one considered in chapter 5. Fig. 8.9 shows a comparison between an enlarged close-up of the two molecules and the simulated fluorescence patterns, supposing polar angles θ=0° and θ=83° respectively. The azimuthal angle of the double-lobed pattern is determined as the line connecting the peaks of the two lobes and is roughly -130°.

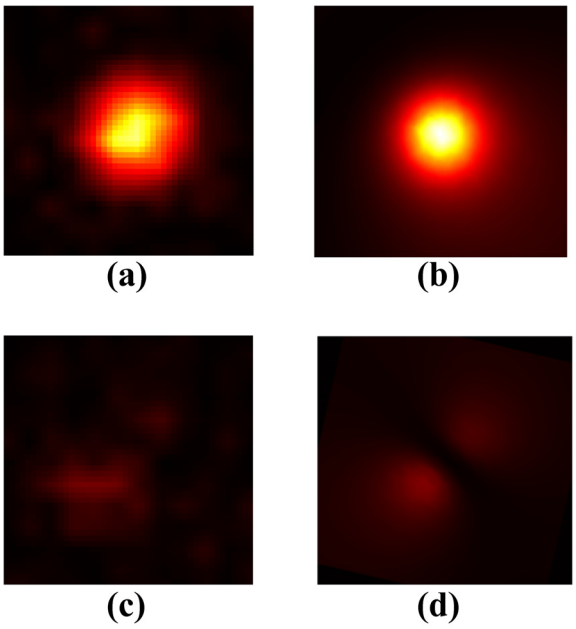

Fig. 8.9 – Comparison between experimental fluorescence patterns of molecules 1 and 2 of Fig. 8.8 and theoretical fluorescence patterns computed for an asymmetric probe based on an oblique cut: (a) close-up of molecule 1; (b) simulated fit for molecule 1 assuming θ=0°; (c) close-up of molecule 2; (d) simulated fit for molecule 2 assuming θ=83°.

Also the line cuts of the measured and theoretical fluorescence intensity distributions have been compared, as reported in Fig. 8.10. For the two molecules we considered the same lines as in Fig. 8.8; in addition, for molecule 1 we considered also the orthogonal one. The good qualitative

agreement between calculations (solid red line) and experiments (blue dots) is apparent, despite minor mismatches in shape, size and intensities. For example, for molecule 1, the experimental spot size varies between 17 to 24 nm, against 19-21 nm for the simulated pattern. However, as pointed out, simulations describe ideal conditions, which are not perfectly reproduced in real measurements. Even though we repeated calculations supposing a smaller curvature, structural deviations between the ideal and the real probe are still present, for example in terms of characteristics of the metal coating and its roughness. Moreover, in addition to other variable factors related to the experimental set-up, like noise, variability in the actual distance from the molecule and non-idealities in the detection system, it should be also considered that during a real scan other effects intervene, including the possibility of dragging molecules with the probe (Ruiter et al., 1997). All these factors are not accounted for during simulations and could be responsible for differences in shape, size and intensity of the patterns. Yet, the qualitative agreement with the theoretical predictions is still good and confirms that the presence of the cut gives rise to a near-field distribution with a prevalent longitudinal component.

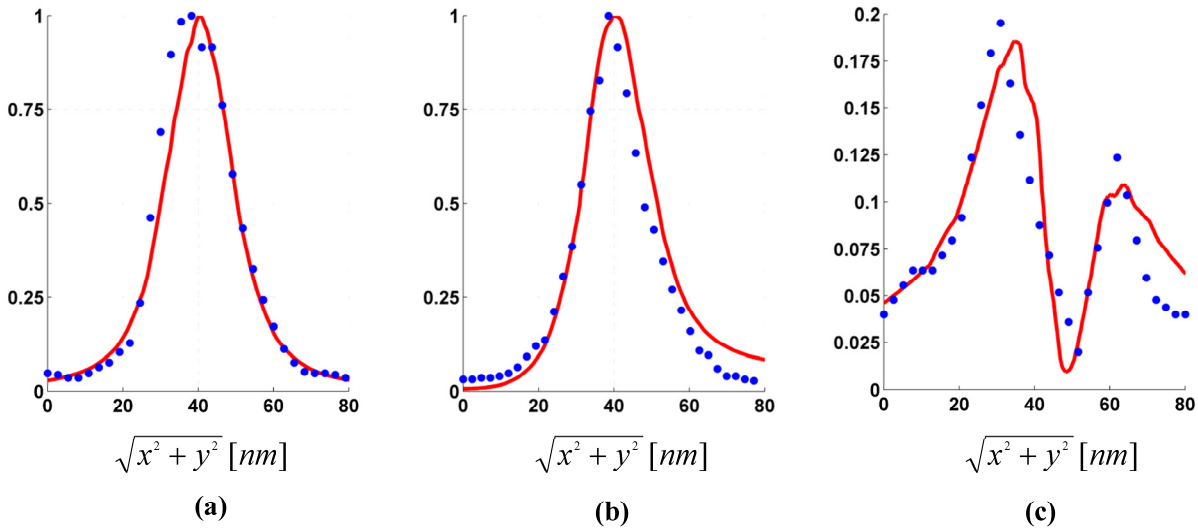

Fig. 8.10 – Comparison between experimental fluorescence profiles for molecules 1 and 2 of Fig. 8.8 and theoretical fluorescence profiles computed for an asymmetric probe based on an oblique cut: (a) profile of molecule 1 taken along the white line shown in Fig. 8.8 (a); (b) profile of molecule 1 taken along a line orthogonal to the white line shown in Fig. 8.8 (a); (c) profile of molecule 2 taken along the white line shown in Fig. 8.8 (a). Solid red lines refer to the simulated profiles, while blue dots represent the measured data. Comparison shows a good fit between theoretical predictions and measurements.

Comparing the fluorescence patterns obtained with our novel asymmetric probe based on an oblique cut with the measurements carried out with an axisymmetric probe under radially polarized

excitation, we notice a strong resemblance between the fluorescence maps (Frey et al., 2006). Single- and double-lobed patterns also with asymmetric shapes according to the orientation of the dipole moments of the fluorophores have been detected with both probe structures with similar spot sizes (about 20 nm). However, in our case, such a strong field localization is obtained under a more straightforward linearly polarized excitation. Numerical calculations and measurements discussed in this paragraph and in chapter 5 have revealed that field confinement is associated with a mainly longitudinal near-field distribution at the probe apex.

Our novel asymmetric probe design based on an oblique cut compares favourably also with other asymmetric designs, like tip-on-aperture and monopole antennas fed by an adjacent aperture resulting in resolution of 20-30 nm (Frey et al., 2002; 2004; Taminiau et al., 2007). As in those cases, better imaging of fluorescent molecules compared to aperture probes is achieved thanks to a highly localized near-field distribution characterized by the dominance of the longitudinal field component, without the need for a more involved radially polarized excitation. However, high resolution is obtained in our structure by an easier fabrication process based on a variant of the FIB slicing approach commonly used for the creation of high quality aperture probes as described in chapter 6, contrary to the more complicated procedures required for the other probes like multiple milling steps at different angles. Moreover the oblique design allows a reduction in the background residual signal coming from the adjacent aperture, which is responsible for faint broader spots (Taminiau et al., 2007).

8.4. Final remarks

A comprehensive characterization of a novel asymmetric structure based on an oblique cut has been carried out by performing both topographic and optical measurements.

First, topographic scans on a Fischer latex projection pattern (sphere diameter of 453 nm) have been done to check the ability of the probe to follow the surface of the hexagonal arrangement of nearly triangular metal islands with known characteristics in terms of size and periodicity. Then, optical measurements have been performed using single fluorescent molecules embedded in a polymer layer. The choice of such a characterization method was dictated by the need to extract purely optical information about the probe behaviour without the risk of artifacts that may potentially arise in optical measurements on samples exhibiting topographic variations, due to the coupling between optical and topographic signals. In addition to being less demanding than other purely optical characterization techniques based, for example, on tip-on-tip measurements, single fluorescent molecules allow getting a vectorial picture of the local electric field at the probe apex, giving an in-depth interpretation of the mechanisms behind field localization.

The fluorescence maps of aribitrarily oriented molecules have revealed the presence of single- and double-lobed patterns with different intensities (maximum count rate of about 70 kcps), confirming the validity of the developed numerical model for probe-molecule interaction. A fitting of the experimental data to the theoretical maps has shown that the brighter and more confined spots are originating from the interaction of the probe with molecules with a mainly longitudinal dipole moment, whereas the faded two-lobed patterns correspond to the excitation of molecules with a mainly transversal dipole moment. This confirms the theoretical prediction of a mainly longitudinal nature of the near-field distribution at the very end of the probe, because molecules are excited by the square of the field component along their dipole moment. Moreover, experimental data evidence that a high resolution of about 20 nm is achievable with our novel asymmetric structures: fluorescence spots feature sizes ranging from below 20 nm (brighter single-lobed spots) to about 60 nm (weaker double-lobed spots still having single sub-peaks below 20 nm).

The novel asymmetric cut probe shows to be competitive not only with axisymmetric probes but also with other asymmetric designs. Similar vectorial distributions and high resolution associated to the dominant highly confined longitudinal field component are obtained, but with linearly polarized excitation instead of radially polarized one. Moreover, compared to other asymmetric probes based on tip-on-aperture and monopole antenna designs excited with a linearly polarized input, our novel probes are obtained by an easier FIB slicing approach, requiring just a few minutes.

In brief, our novel design was both theoretically and experimentally demonstrated to be a promising solution for sub-20 nm field localization. For example, using it for single fluorescent molecule detection (important in both material and life science), molecules can be detected with high resolution and a more straightforward determination of azimuthal and polar orientation compared to aperture probes.

9. Conclusions and outlook

In this thesis, novel SNOM probe configurations have been proposed and investigated both theoretically and experimentally.

In fact, the widespread aperture probe is not adequate to be used routinely for high resolution applications; while an axisymmetric fully metal-coated dielectric probe under internal back excitation could be an interesting alternative for this purpose allowing high resolution without the high background typical of probes excited with external illumination, its optical behaviour is strongly polarization-dependent. More specifically, strong field confinement is affordable only under radially polarized excitation: in this case, due to the rotational symmetry of both the probe structure and the input excitation, the surface plasmons excited on the metal coating have the same polarity on the opposite sides of the probe, thereby interfering constructively at the probe apex and resulting in a highly confined hot spot. On the contrary, surface plasmons excited in case of linearly polarized excitation have opposite polarities on the opposite sides of the probe and, hence, cancel out at the probe apex, giving rise to a weak asymmetric distribution. However, linearly polarized excitation is more straightforward than radially polarized excitation.

In order to get superfocusing effects while benefitting from easier linearly polarized injection procedures, we proposed novel SNOM probe configurations based on the introduction of a structural asymmetry breaking the rotational symmetry of the original axisymmmetric probe. Given z the axis of the probe, we have classified the four different studied configurations into two main subcategories:

1. directional asymmetry: the probe still exhibits reflection symmetry; therefore if xz is the plane of symmetry of the probe, the structure exhibits maximum asymmetry along x and no asymmetry along y.
2. adirectional asymmetry: the probe is based on a spiral design; no reflection symmetry is present and therefore the asymmetry is uniformly distributed in the xy plane.

Two different forms of directional asymmetries have been considered, one based on an oblique cut at the apex with the removal of both the dielectric core and the metal coating, the other consisting in azimuthal corrugations in the metal coating extended to just one half of the probe. The spiral design has been implemented in two different ways, either as a single spiral corrugation or as a set of azimuthal corrugations with the centers shifted by a certain angle one with respect to the other in order to create the spiral arrangement.

Theoretical analysis of the novel probe structures has been carried out by developing a finite element based model, which has been tested first for the study of an axisymmetric probe

representing our benchmark and reference for comparison and then for the novel asymmetric structures.

Numerical calculations have shown that all the proposed structures allow field localization under linearly polarized excitation, enabling a simplification in the excitation procedures compared to the axisymmetric design. The study of the influence of structural variations on probe performance suggests that more extended asymmetries (e.g. probes with steeper oblique cuts or circular corrugations with larger radii and angular extension) generally bring about better performance. However, analyses under variable orientation of the direction of the input linear polarization with respect to the structural asymmetry have revealed that field confinement and enhancement deteriorate in a probe based on a directional asymmetry as the input polarization shifts from the direction of maximum asymmetry to the one of no asymmetry. On the contrary, field localization under arbitrarily oriented linearly polarized excitation is possible using structures based on the pioneering adirectional asymmetry, thus entailing a further simplication in experimental set-ups.

Independently of the specific form and category of the asymmetry, field localization was shown to be associated with the dominance of a highly confined strong longitudinal field component over two weaker orthogonal transverse components, with the vectorial components of the near-field distribution at the apex of an asymmetric probe under linearly polarized excitation closely resembling those obtained in an axisymmetric probe under radially polarized excitation.

FIB milling has been used to introduce an asymmetry in commercial fully metal-coated fiber probes. A slicing approach has allowed the creation of a cut, by orienting the ion beam at an angle between 0° and 90° with respect to the probe axis, so as to obtain the desired cut angle (defined between a plane orthogonal to the probe axis and the plane of the cut itself). The fabrication of the asymmetric structures appeared simple and took only few minutes, differently, for example, from probes based on a monopole antenna requiring several FIB milling steps at different angles.

For the characterization of the probe behaviour, both topographic and optical measurements have been carried out. Fischer latex projection patterns based on nearly triangular metal islands arranged in a hexagonal pattern have been used to test the ability to reproduce the topography of a sample with known size and periodicity using a novel probe based on an oblique cut. Next, optical characterization of the same probe was performed using single fluorescent molecules. Such a method was chosen because it provides exquisitely optical information about the probe behaviour (contrary to samples endowed with topography likely to generate artifacts) and gives a valuable map of the vectorial components of the local field at the apex. Experimental results have shown a good qualitative agreement with a numerical model developed to describe probe-molecule interaction, confirming our predictions on the vectorial components of the field and demonstrating a resolution

below 20 nm. Such results make the oblique cut design competitive not only with the axisymmetric probe as similar field patterns and resolution are obtained under linearly polarized excitation instead of a radially polarized one, but also with other structures working under linearly polarized excitation like the tip-on-aperture and the monopole antenna due to the easier fabrication process. Therefore, our structure could be an ideal candidate to replace such structures in high resolution applications in near-field imaging and lithography. Single molecule detection itself could be an important application, because of the easy imaging and extraction of orientational information essential in both material and life science.

The theoretical and experimental study carried out in this thesis paves the way for interesting future developments. In fact, in addition to the successful fabrication of the asymmetric probe based on an oblique cut and demonstration of high resolution in agreement with the theoretical model, fabrication tests have been carried out to create an adirectional asymmetry with a spiral groove. A head-on drilling approach (i.e. incident ion beam parallel to the probe axis) has been adopted for the creation of a spiral groove in the metal coating. Even though the latter approach turned out to be more sensitive to the taper profiles, with better results obtained for tapers produced by selective etching, ease and rapidity of fabrication were still outstanding compared to structures proposed by other groups. Also the other designed directional and adirectional asymmetries based on azimuthal corrugations and requiring metal bumps could be easily produced by FIB nanostructuring combining deposition and milling: FIB aluminium deposition has been demonstrated, even though it was not possible in our commercial system.

Hence, the feasibility of probes based on both directional and adirectional asymmetries has been experimentally demonstrated.

The groundbreaking adirectional design looks particularly interesting not only because of its robustness to the direction of the input polarization, but also because other innovative applications can be envisaged. An interesting issue deserving further investigation is the behaviour of an adirectional asymmetry under circularly polarized excitation. In fact, while the chirality of the spiral design (i.e. clockwise or counterclockwise) was shown to play no role in case of linearly polarized excitation, the handedness of the input circularly polarized excitation with respect to the handedness of the spiral asymmetry could have effects. Such a chirality-dependent behaviour has been demonstrated in fields different from SNOM, for example for 2D spiral plasmonic lenses with focusing properties changing with the handedness of the polarization (Chen et al., 2010) or in photonic metamaterials made up of 3D gold helices (Gansel et al., 2009) or chiral plasmonic oligomers of individual metallic particles for coupling with chiral biomolecules (Hentschel et al., 2012). The possibility to tune field localization with the handedness of the input polarization could open up new horizons in sensing, imaging and lithography.

Bibliography

Abrahamyan T. and Nerkararyan K., "Surface plasmon resonance on vicinity of gold-coated fiber tip," *Phys. Lett. A* **364**(6), 494–496 (2007).

Adiga V. P., Kolb P. W., Evans G. T., Cubillos-Moraga M. A., Schmadel D. C., Dyott R., Drew H. D., "Development of high-throughput, polarization-maintaining near-field probes," *Appl. Optics* **45**(12), 2597-2600 (2006).

Aiyer H. N., Kawazoe T., Lim J., Echigo Y., Ohtsu M., "Mercury treatment of optical near-field fiber probes for smother tips with reduced light leakage," *Nanotechnology* **12**, 368-371 (2001).

Ali M. Y., Hung W., Yongqi F., "A Review of Focused Ion Beam Sputtering," *Int. J. Precis. Eng. Man.* **11**(1), 157-170 (2010).

Ambrosio A., Allegrini M., Latini G., Cacialli F., "Thermal processes in metal-coated fiber probes for near-field experiments," *Appl. Phys. Lett*. **87**, 033109 1-3 (2005).

Ambrosio A., Fenwick O., Cacialli F., Micheletto R., Kawakami Y., Gucciardi P. G., Kang D. J., Allegrini M., "Shape dependent thermal effects in apertured fiber probes for scanning near-field optical microscopy," *J. Appl. Phys*. **99**, 084303 1-6 (2006).

Antosiewicz T. J. and Szoplik T., "Corrugated metal-coated tapered tip for scanning near-field optical microscope," *Opt. Express* **15**(17), 10920-10928 (2007).

Antosiewicz T. J. and Szoplik T., "Description of near- and far-field light emitted from a metal-coated tapered fiber tip," *Opt. Express* **15**(12), 7845-7852 (2007a).

Antosiewicz T. J., Marciniak M., Szoplik T., "On SNOM resolution improvement." in: C. Sibilia, T. M. Benson, M. Marciniak, Szoplik T. (eds.) *Photonic crystals: physics and technology*, Springer, Milan, chapter 11, 217–238 (2008).

Antosiewicz T. J. and Szoplik T., "Corrugated SNOM probe with enhanced energy throughput," *Opto-electron. Rev.* **16**(4), 451-457 (2008).

Antosiewicz T. J., Wróbel P., Szoplik T., "Nanofocusing of radially polarized light with dielectric-metal-dielectric probe," *Opt. Express* **17**(11), 9191-9196 (2009).

Antosiewicz T. J., Wróbel P., Szoplik T., "Performance of scanning near-field optical microscope probes with single groove and various metal coatings," *Plasmonics* **6**(1),11-18 (2011).

Arslanov N. M., "The optimal form of the scanning near-field optical microscopy probe with subwavelength aperture," *J. Opt. A: Pure Appl. Op*. **8**(3), 338-344 (2006).

Ash E. and Nicholls G., "Super-resolution aperture scanning microscope," *Nature* **237**, 510-512 (1972).

Ashino M. and Ohtsu M., "Fabrication and evaluation of localized plasmon resonance probe for near-field microscopy/spectroscopy," *Appl. Phys. Lett*. **72**(11), 1299-1301 (1998).

Babadjanyan A. J., Margaryan N. L., Nerkararyan K. V., "Superfocusing of surface polaritons in the conical structure," *J. Appl. Phys.* **87**(8), 3785-3788 (2000).

Babayan A. E. and Nerkararyan K. V., "The strong localization of surface plasmon polariton on a metal-coated tip of optical fiber," *Ultramicroscopy* **107**(12), 1136-1140 (2007).

Baida F. I., van Lebeke D., Pagani Y., "Body-of-revolution FDTD simulations of improved tip performance for scanning near-field optical microscopes," *Opt. Commun*. **225**, 241-252 (2003).

Baida F. I. and Belkhir A., “Superfocusing and light confinement by surface plasmon excitation through radially polarized beam,” *Plasmonics* **4**(1), 51-59 (2009).

Bakunov M. I., Bodrov S. B., Hangyo M., “Intermode conversion in a near-field optical fiber probe,” *J. Appl. Phys*. **96**(4), 1775-1780 (2004).

Barbic M., Eliason L., Ranshaw J., “Femto-Newton force sensitivity quartz tuning fork sensor,” Letter to the Editor *Sensors Actuators A-Phys.* **136,** 564–566 (2007).

Barnard T. W. and Lit J. W. Y., “Mode transforming properties of tapered single mode fiber microlenses,” *Appl. Optics* **32**(12), 2090-2094 (1993).

Bethe H. A., “Theory of diffraction by small holes,” *Phys. Rev*. **66**, 163-182 (1944).

Betzig E., Isaacson M., Lewis A., “Collection mode near-field scanning optical microscopy,” *Appl. Phys. Lett*. **51**(25), 2088-2090 (1987).

Betzig J. W. A. and Finn P. L., “Combined shear force and near field scanning optical microscopy,” *Appl. Phys. Lett*. **60**, 2484-2486 (1992).

Betzig E. and Trautman J., “Near field optics: microscopy, spectroscopy and surface modification beyond the diffraction limit,” *Science* **257**, 189-195 (1992).

Betzig E. and Chichester R. J., “Single molecules observed by near-field scanning optical microscopy,” *Science* **262**(5138), 1422-1425 (1993).

Biagioni P., Polli D., Labardi M., Pucci A., Ruggeri G., Cerullo G., Finazzi M., Duò L., “Unexpected polarization behaviour at the aperture of hollow-pyramid near-field probes,” *Appl. Phys. Lett*. **87**, 223112 1-3 (2005).

Biagioni P., Coduri M., Polli D., Virgili T., Labardi M., Cerullo G., Finazzi M., Duò L., “Near-field vs far-field polarization properties of hollow pyramid SNOM tips,” *Phys. Stat. Sol. C 2* **12**, 4078-4082 (2005a).

Biehler B. and La Rosa A. H., “High-frequency bandwidth optical technique to measure thermal elongation time responses of near-field scanning optical microscopy probes,” *Rev. Sci. Instrum*. **73**(11), 3837-3840 (2002).

Bondeson A., Rylander T., Ingelström P., *Computational Electromagnetics* Springer, New York (2005).

Bortchagovsky E., Colas des Francs G., Naber A., Fischer U. C., “On the optimum form of an aperture for a confinement of the optically excited electric near field,” *J. Microsc*. **229**(2), 223-227 (2008).

Bouhelier A., Beversluis M., Hartschuh A., Novotny L., “Near-field second-harmonic generation induced by local field enhancement,” *Phys. Rev. Lett.* **90**(1), 013903 1-4 (2003).

Bouhelier A., Renger J., Beversluis M. R., Novotny L., "Plasmon-coupled tip-enhanced near-field optical microscopy," *J. Microsc.* **210**(3), 220-224 (2003a).

Bouhelier A., Beversluis M. R., Novotny L., “Applications of field-enhanced near-field optical microscopy, *Ultramicroscopy* **100**, 413-419 (2004).

Bouhelier A., Hartschuh A., Novotny L., “Near-field optical microscopy in the nanosciences," in: N. Yao and Z. L.Wang (eds.) *Microscopy for Nanotechnology*, Kluwer Academic, Ch 2, 25-54 (2005).

Bouhelier A., “Field-enhanced scanning near-field optical microscopy,” *Microsc. Res. Techniq*. **69**, 563-579 (2006).

Bouhelier A. and Bachelot R., “Electromagnetic singularities and resonances in near-field optical probes,” in: S. Kalinin and A. Gruverman (eds.) *Scanning probe microscopy – electrical and*

electromechanical phenomena at the nanoscale, Spinger, New York, Vol 1, Chapter I.8, 254-279 (2007).

Bouhelier A. and Novotny L., "Near field optical excitation and detection of surface plasmons," in: M. L. Brongersma and P. G. Kik (eds.) *Surface Plasmon Nanophotonics*, Springer, Dordrecht The Netherlands, Ch 10 139-153 (2007).

Bouwkamp C. J., "On Bethe's theory of diffraction by small holes," *Philips Res. Rep*. **5**, 321-332 (1950).

Bouwkamp C. J., "Diffraction theory,"*Rep. Prog. Phys.* **17**(1), 35-100 (1954).

Bozhevolnyi S. I., Vohnsen B., Bozhevolnaya E. A., "Transfer functions in collection scanning near-field optical microscopy," *Opt. Commun*. **172**, 171-179 (1999).

Brunner S., Tharian P.J., Simmler H., Ghazi Wakili K., "Focused ion beam (FIB) etching to investigate aluminium-coated polymer laminates subjected to heat and moisture loads," *Surf. Coat. Tech.* **202**, 6054–6063 (2008).

Bulgarevich D. S. and Futamata M., "Apertureless tip-enhanced Raman microscopy with confocal epi-illumination/collection optics," *Appl. Spectrosc*. **58**(7), 757-761 (2004).

Butter J. Y. P. and Hecht B., "Aperture scanning near-field optical microscopy and spectroscopy of single terrylene molecules at 1.8 K," *Nanotechnology* **17**, 1547-1550 (2006).

Carminati R. and Greffet J., "Equivalence of constant height and constant intensity images in scanning near field optical microscopy," *Optics Lett*. **21**, 1208-1210 (1996).

Cefalì E., Patanè S., Spadaro S., Gardelli R., Albani M., Allegrini M**.,** "Near Field Probes: from optical fibers to optical nanoantennas," in: Bhushan, H. Fuchs, M. Tomitori (eds.), *Applied Scanning Probe Methods*, Vol. VIII, B, Springer Berlin Heidelberg New York, Chap. 3, 77-135 (2008).

Celebrano M., Biagioni P., Zavelani-Rossi M., Polli D., Labardi M., Allegrini M., Finazzi M., Duò L., Cerullo G., "Hollow-pyramid based scanning near-field optical microscope coupled to femtosecond pulses: a tool for nonlinear optics at the nanoscale," *Rev. Sci. Instrum*. **80**, 033704 1-8 (2009).

Chaigneau M., Ollivier G., Minea T., Louarn G., "Nanoprobes for near-field optical microscopy manufactured by substitute-sheath etching and hollow cathode sputtering," *Rev. Sci. Instrum.* **77**(10), 103702 1-5 (2006).

Chaigneau M., Minea T., Louarn G., "Comparative study of different process-steps for the near-field optical probes manufacturing," *Ultramicroscopy* **107**(10-11), 1042–1047 (2007).

Chaigneau M., Louarn G., Minea T. M., "Nanoaperture formation at metal covered tips by micro-spark optimized for near-field optical probes," *Appl. Phys. Lett.* **92**, 093106 1-3 (2008).

Chen W. and Zhan Q., "Field enhancement analysis of an apertureless near field scanning optical microscope probe with finite element method," *Chin. Opt. Lett.* **5**, 709-711 (2007).

Chen W. and Zhan Q., "Numerical study of an apertureless near field scanning optical microscope probe under radial polarization illumination," *Opt. Express* **15**(7), 4106-4111 (2007a).

Chen W., Abeysinghe D. C, Nelson R. L., Zhan Q., "Experimental confirmation of miniature spiral plasmonic lens as a circular polarization analyzer," *Nano Lett.* **10**, 2075–2079 (2010).

Chevalier N., Nasse M. J., Woehl J. C., Reiss P., Bleuse J., Chandezon F., Huant S., "CdSe single-nanoparticle based active tips for near-field optical microscopy," *Nanotechnology* **16**, 613-618 (2005).

Christensen D. A., "Analysis of near field tip patterns including object interaction using finite-difference time-domain calculations," *Ultramicroscopy* **57**, 189-195 (1995).

Cline J. A., Barshatsy H., Isaacson M., “Scanned-tip reflection-mode near-field scanning optical microscopy,” *Ultramicroscopy* **38**, 299-304 (1991).

Cline J. A. and Isaacson M., “Comparison of different modes of reflection in near-field optical imaging,” *Ultramicroscopy* **57**, 147-152 (1995).

Colas des Francs G., Molenda D., Fischer U. C., Naber A., “Enhanced light confinement in a triangular aperture: experimental evidence and numerical calculations,” *Phys. Rev. B* **72**(16), 165111 1-6 (2005).

Courjon D., Sarayeddine K., Spajer M., “Scanning tunnelling optical microscopy,” *Opt. Commun*. **71**(1-2), 23-28 (1989).

Danzebrink H. U., Dziomba T., Sulzbach T., Ohlsson O., Lehrer C., Frey L., “Nano-slit probes for near-field optical microscopy fabricated by focused ion beams,” *J. Microsc.* **194**(2/3), 335-339 (1999).

Della Ratta A. D., Melngailis J., Thompson C. V., “Focused-ion beam induced deposition of copper,” *J. Vac. Sci. Technol. B* **11**(6), 2195-2199 (1993).

De Marco A. J. and Melngailis J., “Contact resistance of focused ion beam deposited platinum and tungsten films to silicon,” *J. Vac. Sci. Technol. B* **19**(6), 2543-2546 (2001).

Demming F., Jersch J., Klein S., Dickmann K., “Coaxial scanning near-field optical microscope tips: an alternative for conventional tips with high transmission efficiency?,” *J. Microsc*. **201**(3), 383-387 (2001).

Demming L., Festy F., Richards D., “Plasmon resonances on metal tips: understanding tip-enhanced Raman scattering,” *J. Chem. Phys*. **122**, 184716 1-7 (2005).

Descrovi E., Vaccaro L., Aeschimann L., Nakagawa W., Staufer U., Scharf T., Herzig H. P., “On the coupling and transmission of transverse and longitudinal fields into fully metal-coated optical nano-probes,” *Proc. SPIE* **5736**, 96-104 (2005).

Deutsch B., Hillenbrand R., Novotny L., “Visualizing the optical interaction tensor of a gold nanoparticle pair,” *Nano Lett*. **10**, 652-656 (2010).

Dickenson N. E., Erickson E. S., Mooren O. L., Dunn R. C., “Characterization of power induced heating and damage in fiber optic probes for near-field scanning optical microscopy,” *Rev. Sci. Instrum.* **78**, 053712 1-6 (2007).

Ding W., Andrews S. R., Maier S. A., “Internal excitation and superfocusing of surface plasmon polaritons on a silver-coated optical fiber tip,” *Phys. Rev. A* **75**, 063822 1-10 (2007).

Downes A., Salter D., Elfick A., “Finite element simulations of tip-enhanced Raman and fluorescence microscopy,” *J. Phys. Chem. B* **110**, 6692-6698 (2006).

Drezet A., Woehl J. C., Huant S., “Extension of Bethe's diffraction model to conical geometry: application to near-field optics,” *Europhys. Lett.* **54**, 736-740 (2001).

Drezet A., Woehl J. C., Huant S., “Diffraction by a small aperture in conical geometry: application to metal-coated tips used in near-field scanning optical microscopy,” *Phys. Rev. E* **65**, 046611 1-8 (2002).

Drezet A., Nasse M. J., Huant S., Woehl J. C., “In situ characterization of optical tips using single fluorescent nanobeads,” *J. Lumin*. **107**, 176-181 (2004).

Drezet A., Nasse M. J., Huant S., Woehl J. C., “The optical near-field of an aperture tip,” *Europhys. Lett.* **66**, 41-47 (2004a).

Drezet A., Cuche A., Huant S., “Near-field microscopy with single-photon point-like emitter: resolution versus the aperture tip?,” *Opt. Commun*. **284**, 1444-1450 (2011).

Drews D., Ehrfeld W., Lacher M., Mayr K., Noell W., Schmitt S., Abraham M., "Nanostructured probes for scanning near-field optical microscopy," *Nanotechnology* **10**, 61-64 (1999).

Dunn R. C., "Near-field scanning optical microscopy," *Chem. Rev.* **99**, 2891-2927 (1999).

Durkan C. and Shvets I. V., "Reflection-mode scanning near-field optical microscopy: influence of sample-type, tip shape and polarization of light," *J. Appl. Phys*. **83**(3), 1171-1176 (1998).

Eckstein W., "Computer simulation of ion surface collisions with special emphasis to the work by Yamamura," *Nuclear Instruments and Methods in Physics Research B* **232**, 108–116 (2005).

Eghlidi H., Lee K. G., Chen X-W., Götzinger S., Sandoghdar V., "Resolution and enhancement in nanoantenna-based fluorescence microscopy," *Nano Lett*. **9**(12), 4007-4011 (2009).

Erickson E. S. and Dunn R. C., "Sample heating in near-field scanning optical microscopy," *Appl. Phys. Lett.* **87**, 201102 1-3 (2005).

FEI Company, "Focused ion beam technology, capabilities and applications," 030-PB00113 06/05 pp. 20 (2005).

FEI Company, "Application Note Nanofabrication and rapid prototyping with DualBeam™ instruments," 04AP-DB0211 05/07 pp. 12 (2007).

Ferber J., Fischer U. C., Hagedorn N., Fuchs H., "Internal reflection mode scanning near-field optical microscopy with the tetrahedral tip on metallic samples," *Appl. Phys. A: Mater.* **69**(6), 581-589 (1999).

Finot E., Lacroute Y., Bourillot E., Rouessac V., Durand J., "Thermomechanical behaviour of coated tapered optical fibers for scanning force microscopy," *J. Appl. Phys.* **95**(9), 5137-5144 (2004).

Fischer U. C. and Zapletal M., "The concept of coaxial tip as a probe for scanning near field optical microscopy and steps towards a realisation," *Ultramicroscopy* **42**, 393-398 (1992).

Fischer U. C., Heimel J., Maas H.-J., Hartig M., Hoeppener S., Fuchs H., "Latex bead projection nanopatterns, " *Surf. Interface Anal.* **33**(2), 75–80 (2002).

Frey H. G., Keilmann F., Kriele A., Guckenberger R., "Enhancing the resolution of scanning near-field optical microscopy by a metal tip grown on an aperture probe," *Appl. Phys. Lett*. **81**(26), 5030-5032 (2002).

Frey H. G., Witt S., Felderer K., Guckenberger R., "High-resolution imaging of single fluorescent molecules with the optical near-field of a metal tip," *Phys. Rev. Lett.* **93**(20), 200801 1-4 (2004).

Frey H. G., Bolwien C., Brandenburg A., Ros R., Anselmetti D., "Optimized apertureless optical near-field probes with 15 nm optical resolution," *Nanotechnology* **17**(13), 3105-3110 (2006).

Fukura S., Kagi H., Nakai M., Sugiyama M., Fukuda T., "High resolution stress mapping of Al_2O_3/monoclinic ZrO_2 and Al_2O_3/cubic ZrO_2 (Y_2O_3) eutectics using scanning near-field optical microscopy," *J. Crystal Growth* **311**(3), 998–1004 (2009).

Gamo K., Takakura N., Samoto N., Shimizu R., Namba S., "Ion beam assisted deposition of metal organic films using focused ion beams," *Jpn. J. Appl. Phys.* **23**(5), 293-295 (1984).

Gansel J. K., Thiel M., Rill M. S., Decker M., Bade K., Saile V., von Freymann G., Linden S., Wegener M., "Gold helix photonic metamaterial as broadband circular polarizer," *Science* **325**, 1513-1515 (2009).

Garcia-Parajo M., Tate T., Chen Y., "Gold-coated parabolic tapers for scanning near-field optical microscopy: fabrication and optimisation," *Ultramicroscopy* **61**, 155-163 (1995).

García-Parajo M. F., Veerman J.-A., Bouwhuis R., Vallée R., van Hulst N. F., "Optical probing of single fluorescent molecules and proteins," *Chemphyschem.* **2**, 347-360 (2001).

Genolet G., Despont M., Vettiger P., Staufer U., Noell W., de Rooij N. F., Cueni T., Bernal M-P., Marquis-Weible F., "Micromachined photoplastic probe for scanning near-field optical microscopy," *Rev. Sci. Instrum.* **72**(10), 3877-3879 (2001).

Girard C. and Dereux A., "Near field optics theories," *Rep. Prog. Phys*. **59**, 657-699 (1996).

Girard C., "Near fields in nanostructures," *Rep. Prog. Phys*. **68**, 1883-1933 (2005).

Gramotnev D. K., Vogel M. W., Stockman M. I., "Optimized nonadiabatic nanofocusing of plasmons by tapered metal rods," *J. Appl. Phys*. **104**, 034311 1-8 (2008).

Greffet J-J. and Carminati R., "Image formation in near-field optics," *Prog. Surf. Sci*. **56**(3), 133-237 (1997).

Gregor M. J., Blome P. G., Schöfer J., Ulbrich R. G., "Probe surface interaction in near-field optical microscopy: The nonlinear bending force mechanism," *Appl. Phys. Lett.* **68**, 307-309 (1996).

Grober R. D., Acimovic J., Schuck J., Hessman D., Kindlemann P. J., Hespanha J., Morse A. S., Karrai K., Tiemann I., Manus S., "Fundamental limits to force detection using quartz tuning forks," *Rev. Sci. Instrum.* **71**(7), 2776-2780 (2000).

Grosjean T., Ibrahim I. A., Mivelle M., "Multichannel probes for polarization-resolved scanning near-field optical microscopy," *Appl. Optics* **49**(14), 2617-2621 (2010).

Gross M. E., Harriott L. R., Opila R. L., "Focused ion beam stimulated deposition of aluminum from trialkylamine alanes," *J. Appl. Phys.* **68**, 4820-4824 (1990).

Gucciardi P. G., Colocci M., Labardi M., Allegrini M., "Thermal-expansion effects in near-field optical microscopy fiber probes induced by laser light absorption," *Appl. Phys. Lett*. **75**(21), 3408-3410 (1999).

Gucciardi P. G., Patanè S., Ambrosio A., Allegrini M., Downes A. D., Latini G., Fenwick O., Cacialli F., "Observation of tip-to-sample heat transfer in near-field optical microscopy using metal-coated fiber probes," *Appl. Phys. Lett*. **86**, 203109 1-3 (2005).

Guo S. Y., Le Due J. M., Grutter P., "Fabrication of optical fiber probes for scanning near-field optical microscopy," *MSURJ* **3**(1), 32-39 (2008).

Guttroff G., Keto J. M., Shihi G. K., Anselm A., Steetman B. G., "A design of reflection scanning near-field optical microscope and its application to AlGaAs/GaAs heterostructures," *Appl. Phys. Lett.* **68**(25), 3620-3622 (1996).

Hartschuh A., Anderson N., Novotny L., "Near-field Raman spectroscopy using a sharp metal tip," *J. Microsc*. **210**(3), 234-240 (2003).

Hartschuh A., Beversluis M. R., Bouhelier A., Novotny L., "Tip-enhanced optical spectroscopy," *Phil. Trans. R. Soc. Lond. A* **362**, 807-819 (2004).

Hartschuh A., Qian H., Meixner A. J., Anderson N., Novotny L., "Tip-enhanced optical spectroscopy for surface analysis in biosciences," *Surf. Interface Anal*. **38**, 1472-1480 (2006).

Hartschuh A., "Tip-enhanced near-field optical microscopy," *Angew. Chem. Int. Ed*. **47**, 8178-8191 (2008).

Hayazawa N., Saito Y., Kawata S., "Detection and characterization of longitudinal field for tip-enhanced Raman spectroscopy," *Appl. Phys. Lett.* **85**(25), 6239-6241 (2004).

Hecht B., "Forbidden light scanning near-field optical microscopy," University of Basel Phd Thesis (1996).

Hecht B., Bielefeldt H., Inouye Y., Pohl D. W., Novotny L., "Facts and artifacts in near-field optical microscopy," *J. Appl. Phys*. **81**(6), 2492-2498 (1997).

Hecht B., Bielefeld H., Pohl D. W., Novotny L., Heinzelmann H., “Influence of detection conditions on near field optical imaging," *J. Appl. Phys*. **84**, 5873-5882 (1998).

Hecht B., Sick B., Wild U., Deckert V., Zenobi R., Martin O., Pohl D., “Scanning near field optical microscopy with aperture probes: fundamentals and applications,” *J. Chem. Phys*. **112**, 7761-7774 (2000).

Heinzelmann H., Hecht B., Novotny L., Pohl D. W., “Forbidden light scanning near field optical microscopy,” *J. Microsc*. **177**, 115-118 (1995).

Heinzelmann H., Freyland J. M., Eckert R., Huser T., Schürmann G., Noell W., Staufer U., de Rooij N. F., “Towards better scanning near-field optical microscopy probes – progress and new developments,” *J. Microsc*. **194**(2-3), 365-368 (1999).

Held T., Emonin S., Marti O., Hollricher O., “Method to produce high-resolution scanning near-field optical microscope probes by beveling optical surfaces,” *Rev. Sci. Instrum.* **71**, 3118–3122 (2000).

Hentschel M., Schäferling M., Weiss T., Liu N., Giessen H., “Three-dimensional chiral plasmonic oligomers,” *Nano Lett.* **12**, 2542−2547 (2012).

Hillenbrand R., Keilmann F., Hanarp P., Sutherland D. S., Aizpurua J., “Coherent imaging of nanoscale plasmon patterns with a carbon nanotube optical probe,” *Appl. Phys. Lett*. **83**(2), 368-370 (2003).

Hoffmann P., Dutoit B., Salathé R., “Comparison of mechanically drawn and protection layer chemically etched optical fiber tips,” *Ultramicroscopy* **61**, 165-170 (1995).

Hollars C. W. and Dunn R. C., “Evaluation of thermal evaporation conditions used in coating aluminum on near-field fiber-optic probes,” *Rev. Sci. Instrum*. **69**, 1747-1752 (1998).

Hollars W. and Dunn R. C., “Probing single molecule orientations in model lipid membranes with near-field scanning optical microscopy,” *J. Chem. Phys*. **112**(18), 7822-7830 (2000).

Höppener C. and Novotny L., “Antenna-based optical imaging of single Ca2+ transmembrane proteins in liquids,” *Nano Lett*. **8**(2), 642-646 (2008).

Höppener C., Beams R., Novotny L., “Background suppression in near-field optical imaging,” *Nano Lett*. **9**(2), 903-908 (2009).

Huo X., Pan S., Wu S., “Fabrication of optical fiber probe nano-tips by heated micro-pulling combined with static chemical etching,” Proceedings of the 1st IEEE International Conference on Nano/Micro Engineered and Molecular Systems January 18 - 21, Zhuhai, China, 254-257 (2006).

Inouye Y., “Aperturless metallic probes for near-field microscopy,” in S. Kawata (ed.), *Near field optics ad surface plasmon polaritons*, Springer, New York, 29-48 (2001).

Ishitobi H., Kai T., Fujita K., Sekkat Z., Kawata S., “On fluorescence blinking of single molecules in polymers,” *Chem. Phys. Lett.* **468**, 234–238 (2009).

Issa N. A. and Guckenberger R., “Optical nanofocusing on tapered metallic waveguides,” *Plasmonics* **2**, 31-37 (2007).

Janunts N. A. and Nerkararyan K. V., “Modulation of light radiation during input into a waveguide by resonance excitation of surface plasmons,” *Appl. Phys. Lett*. **79**(3), 299–301 (2001).

Janunts N. A., Baghdasaryan K. S., Nerkararyan K. V., Hecht B., “Excitation and superfocusing of surface plasmon polaritons on a silver-coated optical fiber tip,” *Opt. Commun*. **253**(1-3), 118–124 (2005).

Jiang Y., Wang A., Ren B., Tian Z-Q., “Cantilever tip near-field surface-enhanced raman imaging of tris(bipyridine)ruthenium(II) on silver nanoparticles-coated substrates,” *Langmuir* **24**, 12054-12061 (2008).

Jin E. X. and Xu X., “Finite-difference time-domain studies on optical transmission through planar nano-apertures in a metal film,” *Jpn. J. Appl. Phys*. **43**(1), 407-417 (2004).

Jin E. X. and Xu X., “Obtaining super resolution light spot using surface plasmon assisted sharp ridge nanoaperture,” *Appl. Phys. Lett*. **86**, 111106 1-3 (2005).

Jin E. X. and Xu X., “Enhanced optical near field from a bowtie aperture,” *Appl. Phys. Lett*. **88,** 153110 1-3 (2006).

Jin E. X. and Xu X., “Focussed ion beam machined cantilever aperture probes for near-field optical imaging,” *J. Microsc*. **229**(3), 503-511 (2008).

Kahng Y. H., Choi J., Jeong K., Park B. C., Kim D.-H., Lyou J., Lee J.-J., Lee H., Lee T., Ahn S. J., “Fabrication of ball-shaped atomic force microscope tips by ion-beam-induced deposition of platinum on multiwall carbon nanotubes,” *Ultramicroscopy* **110**, 82–88 (2009).

Kalkbrenner T., Ramstein M., Mlynek J., Sandoghdar V., “A single gold particle as a probe for scanning near-field optical microscopy,” *J. Microsc*. **202**(1), 72-76 (2001).

Karrai K. and Grober R. D., “Piezoelectric tip-sample distance control for near field optical microscopes,” *Appl. Phys. Lett*. **66**, 1842-1844 (1995).

Karrai K. and Grober R. D., “Tip-sample distance control for near-field scanning optical microscopes,” *SPIE* **2535**, 69-81 (1995a).

Kato K., Ono A., Inami W., Kawata Y., “Plasmonic nanofocusing using a metal-coated axicon prism,” *Opt. Express* **18**(13), 13580-13585 (2010).

Kazantsev D., Guttroff G., Bayer M., Forchel A., “Sample temperature measurement in a scanning near-field optical microscope,” *Appl. Phys. Lett*. **72**(6), 689-691 (1998).

Keilmann F., “Scattering-type near-field optical microscopy,” *J. Electron Microsc*. **53**(2), 187-192 (2004).

Keilmann F., “Nanoscale conductivity contrast by scattering-type near-field optical microscopy in the visible, infrared and terahertz domain,” *J. Infrared Millim. Te*. **30**(12), 1255-1268 (2009).

Kim B. J., Flamma J. W., ten Have E. S., Garcia-Parajo M. F., van Hulst N. F., Brigger J., “Moulded photoplastic probes for near-field optical applications,” *J. Microsc*. **202**(1), 16-21 (2000).

Kim C.-S., Ahn S.-H., Jang D.-Y., “Review: Developments in micro/nanoscale fabrication by focused ion beams,” *Vacuum* **86**, 1014-1035 (2012).

Krug II J. T., Sànchez E. J., Xie X. S., “Design of near-field optical probes with optimal field enhancement by finite difference time domain electromagnetic simulations,” *J. Chem. Phys.* **116**(24), 10895-10991 (2002).

Kubena R. L, Stratton F. P., Mayer T.M., “Selective area nucleation for metal chemical vapor deposition using focused ion beams,” *J. Vac. Sci. Technol. B* **6**(6), 1865-1868 (1988).

Kulzer F. and Orrit M., “Single-molecule optics**,”** *Ann. Rev. Phys. Chem*. **55**, 585-611 (2004).

Kurihara K., Otomo A., Syouji A., Takahara J., Suzuki K., Yokoyama S., “Superfocusing modes of surface plasmon polaritons in conical geometry based on the quasi-separation of variables approach,” *J. Phys. A: Math. Theor*. **40**(41), 12479–12503 (2007).

Kurihara K., Takahara J., Yamamoto K., Otomo A., “Identifying plasmonic modes in a circular paraboloidal geometry by quasi-separation of variables,” *J. Phys. A: Math. Theor*. **42**, 185401 1-38, (2009).

Lacoste T., Huser T., Prioll R., Heinzelmann H., “Contrast enhancement using polarization-modulation scanning near-field optical microscopy (PM-SNOM),” *Ultramicroscopy* **71**, 333–340 (1998).

Lakowicz J. R., “Instrumentation for fluorescence spectroscopy,” in J. R. Lakowicz (ed.) *Principles of fluorescence spectroscopy*, Springer, chapter 2, 27-62 (2006).

Lambelet P., Savah A., Pfeffer A. I., Phillpona C., Marquis-Weible F., “Chemically etched fiber tips for near-field optical microscopy: a process for smoother tips,” *Appl. Optics* **37**, 7289–7292 (1998).

La Rosa A. H., Yakobson B. I., Hallen H. D., “Origins and effects of thermal processes on near-field optical probes,” *Appl. Phys. Lett*. **67**(18), 2597-2599 (1995).

La Rosa A. H. and Hallen H. D., “Compact method for optical induction of proximal probe heating and elongation,” *Appl. Optics* **41**(10), 2015-2019 (2002).

Latini G., Downes A., Fenwick O., Ambrosio A., Allegrini M., Gucciardi M., Patanè S., Daniel C., Silva C., Daik R., Feast W. J., Cacialli F., “Investigation of heating effects in near-field experiments with luminescent organic semiconductors,” *Synthetic Met*. **147**, 165-169 (2004).

Latini G., Downes A., Fenwick O., Ambrosio A., Allegrini M., Daniel C., Silva C., Gucciardi P. G., Patanè S., Daik R., Feast W. J., Cacialli F., “Optical probing of sample heating in scanning near-field experiments with apertured probes,” *Appl. Phys. Lett*. **86**, 011102 1-3 (2005).

Lazarev A., Fang N., Luo Q., Zhang X., “Formation of fine scanning near-field optical microscopy tips. Part II: By laser-heated pulling and bending,” *Rev. Sci. Instrum.* **74**(8), 3684-3688 (2003).

Lazarev A., Fang N., Luo Q., Zhang X., “Formation of fine near-field scanning optical microscopy tips. Part I. By static and dynamic chemical etching,” *Rev. Sci. Instrum.* **74**(8), 3679-3683 (2003a).

Lee J. S., Han S., Shirdel J., Koo S., Sadiq D., Lienau C., Park N., “ Superfocusing of electric or magnetic fields using conical metal tips: effect of mode symmetry on the plasmon excitation method,” *Opt. Express* **19**(13), 12342-12347 (2011).

Lehrer C., Frey L., Petersen S., Sulzbach Th., Ohlsson O., Dziomba Th., Danzebrink H. U., Rysse H., “Fabrication of silicon aperture probes for scanning near-field optical microscopy by focused ion beam nano machining,” *Microelectron. Eng.* **57–58**, 721–728 (2001).

Lewis A., Isaacson M., Murray A., Harootunian A., “Development of a 500 Å spatial resolution light microscope,” *Ultramicroscopy* **13**, 227-231 (1984).

Li Z-B., Zhou W-Y., Kong X-T., Tian J-G., “Polarization dependence and independence of near-field enhancement through a subwavelength circle hole,” *Opt. Express* **18**(6), 5854-5860 (2010).

Li Q., Chen X.-J., Xu Y., Lan S., Liu H.-Y., Dai Q.-F., Wu L.-J., “Photoluminescence properties of CdSe quantum dots accompanied with rotation of the defocused wide-field fluorescence images,” *J. Phys. Chem. C* **114**, 13427-13432 (2010a).

Li Z-B., Zhou W-Y., Kong X-T., Tian J-G., “Near-field enhancement through a single subwavelength aperture with gaps inside,” *Plasmonics* **6**(1), 149-154 (2011).

Liang K. F. and Grütter P., “Properties of amorphous Al-Yb alloy coating for scanning near-field optical microscopy tips,” *J. Appl. Phys.* **92**(11), 6895-6899 (2002).

Lich B., “Site-specific three-dimensional structural analysis in tissues and cells using automated DualBeam Slice&View,” *Microscopy Today* 26-30 (March 2007).

Liu L. and He S., “Design of metal-cladded near-field fiber probes with a dispersive body-of-revolution finite-difference time-domain method,” *Appl. Opt.* **44**(17), 3429-3437 (2005).

Lotito V., Sennhauser U., Hafner C., “Finite element analysis of asymmetric scanning near field optical microscopy probes,” *J. Comput. Theor. Nanos.* **7**(8), 1596-1609 (2010).

Lotito V., Sennhauser U., Hafner C., “Effects of asymmetric surface corrugations on fully metal-coated scanning near field optical microscopy tips,” *Opt. Express* **18**(8), 8722-8734 (2010a).

Lotito V., Sennhauser U., Hafner C., Bona G.-L., "Fully metal-coated scanning near-field optical microscopy probes with spiral corrugations for superfocusing under arbitrarily oriented linearly polarized excitation," *Plasmonics* **6**, 327-336 (2011).

Lotito V., Sennhauser U., Hafner C., Bona G.-L., "Interaction of an asymmetric scanning near field optical microscopy probe with fluorescent molecules," *PIER* **121**, 281-299 (2011a).

Lotito V., Sennhauser U., Hafner C., "Numerical analysis of novel asymmetric SNOM tips," *PIERS Online* **7**(4), 394-400 (2011b).

Lotito V., Sennhauser U., Hafner C., Bona G.-L., "A novel nanostructured scanning near field optical microscopy probe based on an adirectional asymmetry," *J. Comput. Theor. Nanosci*. **9**, 486-494 (2012).

Maier S. A., Andrews S. R., Martìn-Moreno L., Garcìa-Vidal F. J., "Terahertz surface plasmon-polariton propagation and focusing on periodically corrugated metal wires," *Phys. Rev. Lett*. **97**, 176805 1-4 (2006).

Martin O. J. F. and Paulus M., "Influence of metal roughness on the near-field generated by an aperture/apertureless probe," *J. Microsc*. **205**(2), 147–152 (2002).

Matteo J. A., Fromm D. P., Yuen Y., Schuck P. J., Moerner W. E., Hesselink L., "Spectral analysis of strongly enhanced visible light transmission through single C-shaped nanoapertures," *Appl. Phys. Lett*. **85**(4), 648-650 (2004).

Méndez E. R., Greffet J-J., Carminati R., "On the equivalence between the illumination and collection modes of the scanning near-field optical microscope," *Opt. Commun*. **142**, 7-13 (1997).

Michaelis J., Hettich C., Mlynek J., Sandoghdar V., "Optical microscopy using a single-molecule light source," *Nature* **405**, 325-328 (2000).

Minh P. N., Ono T., Tanaka S., Esashi M., "Near-field optical apertured tip and modified structures for local field enhancement," *Appl. Opt*. **40**(15), 2479-2484 (2001).

Minh P. N., Ono T., Watanabe H., Lee S. S., Haga Y., Esashi M., "Hybrid optical fiber apertured cantilever near-field probe," *Appl. Phys. Lett*. **79**(19), 3020-3022 (2001a).

Minh P. N., Ono T., Tanaka S., Esashi M., "Spatial distribution and polarization dependence of the optical near-field in a silicon microfabricated probe," *J. Microsc.* **202**(1), 28-33 (2001b).

Minh P. N., Takahito O., Masayoshi E., "*Fabrication of Silicon Microprobes for Optical Near-Field Applications*" CRC press, Boca Raton Florida (USA) (2002).

Mitsui T. and Sekiguchi T., "Observation of polarization properties in near-field optical imaging by a polarization-maintaining fiber probe," *J. Electron Microsc*. **53**(2), 209-215 (2004).

Mitsui T., "Development of a polarization-preserving optical fiber-probe for near-field scanning optical microscopy and the influences of bending and squeezing on the polarization properties," *Rev. Sci. Instrum*. **76**(4), 0437031-6 (2005).

Mitsuoka Y., Niwa T., Ichihara S., Kato K., Muramatsu H., Nakajima K., Shikida M., Sato K., "Microfabricated silicon dioxide cantilever with subwavelength aperture," *J. Microsc*. **202**(1), 12-15 (2000).

Mivelle M., Ibrahim I. A., Baida F., Burr G. W., Nedeljkovic D., Charraut D., Rauch J-Y., Salut R., Grosjean T., "Bowtie nano-aperture as interface between near-fields and a single mode fiber," *Opt. Express* **18**(15), 15964-15974 (2010).

Moar P. N., Love J. D., Laudoceur F., Cahill L. W., "Waveguide analysis of heat-drawn and chemically etched probe tips for scanning near-field optical microscopy," *Appl. Opt*. **45**(25), 6442-6456 (2006).

Moerland R. J., van Hulst N. F., Gersen H., Kuipers L., "Probing the negative permittivity perfect lens using near-field optics and single molecule detection," *Opt. Express* **13**(5), 1604-1614 (2005).

Moerner W. E. and Fromm D. P., "Methods of single-molecule fluorescence spectroscopy and microscopy," *Rev. Sci. Instrum*. **74**, 3597-3619 (2003).

Mononobe S. and Ohtsu M., "Fabrication of a pencil-shaped fiber probe for near-field optics by selective chemical etching," *J. Lightwave Technol.* **14**(10), 2231-2235 (1996).

Mononobe S., Naya M., Saiki T., Ohtsu M., "Reproducible fabrication of a fiber probe with a nanometric protrusion for near-field optics," *Appl. Optics* **36**(7), 1496-1500 (1997).

Mononobe S., Maheswari R. U., Ohtsu M., "Fabrication of a pencil-shaped fiber probe with a nanometric protrusion from a metal-film for near-field optical microscopy," *Opt. Express*, **1**(8), 229-233 (1997a).

Mononobe S., Saiki T., Suzuki T., Koshihara S., Ohtsu M., "Fabrication of a triple-tapered probe for near-field optical microscopy in UV region based on selective chemical etching of a multistep index fiber," *Opt. Commun.* **146**, 45-48 (1998).

Mononobe S. and Ohtsu M., "Development of a Fiber Used for Fabricating Application Oriented Near-Field Optical Probes," *IEEE Photonic. Tec. L.* **10**(1), 99-101 (1998).

Mononobe S., "Near-Field Optical Fiber Probes and the Imaging Applications," in M. Ohtsu (Ed.) *Progress in Nano-Electro-Optics III Industrial Applications and Dynamics of the Nano-Optical System*, Springer-Verlag Berlin, Heidelberg, chapter 1, pp. 55 (2005).

Morville J., Liu J., Callegari A., Chergui M., "Q-factor optimization of a tuning fork/fiber sensor for shear-force detection," *Appl. Phys. Lett*. **86**, 064103 1-4 (2005).

Mu C., Mangum B. D., Xie C., Gerton J. M., "Nanoscale fluorescence microscopy using carbon nanotubes," *IEEE J. Sel. Top. Quant*. **14**(1), 206-216 (2008).

Mühlschlegel P., Toquant J., Pohl D. W., Hecht B., "Glue-free tuning fork shear force microscope," *Rev. Sci. Instrum*. **77**, 016105 1-3 (2006).

Muramatsu H., Chiba N., Homma K., Nakajima K., Ataka T., Ohta S., Kusumi A., Fujihira M., "Near-Field Optical Microscopy in Liquids," *Appl. Phys. Lett.* **66**, 3245-3247 (1995).

Muramatsu H., Homma K., Chiba N., Yamamoto N., Egawa A., "Dynamic etching method for fabricating a variety of tip shapes in the optical fibre probe of a scanning near-field optical microscope," *J. Microsc.* **194**(2-3), 383-387 (1999).

Muranishi M., Sato K., Osaka S., Kikukawa A., Shintani T., Ito K., "Control of aperture size of optical probes for scanning near-field optical microscopy using focused ion beam technology," *Jpn. J. Appl. Phys.* **36**(7B), L942-L944 (1997).

Nakagawa W., Vaccaro L., Herzig H. P., "Analysis of mode coupling due to spherical defects in ideal fully metal-coated scanning near-field optical microscopy probes," *J. Opt. Soc. Am. A* **23**(5), 1096–1105 (2006).

Nakagawa W., Vaccaro L., Herzig H. P., Hafner C., "Polarization mode coupling due to metal-layer modifications in apertureless near-field scanning optical microscopy probes," *J. Comput. Theor. Nanosci*. **4**, 692–703 (2007).

Nakamura H., Sato T., Kambe H., Sawada K., Saiki T., "Design and optimization of tapered structure of near-field fibre probe based on finite-difference time-domain simulation," *J. Microsc*. **202**(1), 50-52 (2001).

Neacsu C. C., Berweger S., Raschke M. B., "Tip-enhanced Raman imaging and nanospectroscopy: sensitivity, symmetry and selection rules," *Nanobiotechnol*. **3**, 172-196 (2007).

Neacsu C. C., Berwger S., Olmon R. L., Saraf L. V., Ropers C., Raschke M. B., "Near-field localization in plasmonic superfocusing: a nanoemitter on a tip," *Nano Lett*. **10**, 592-596 (2010).

Nerkararyan K., Abrahamyan T., Janunts E., Khachatryan R., Harutyunyan S., "Excitation and propagation of surface plasmon polaritons on the gold covered conical tip," *Phys. Lett. A* **350**(1-2), 147-149 (2006).

Nerkararyan K. V., Hakhoumian A. A., Babayan A. E., "Terahertz surface plasmon-polariton superfocusing in coaxial cone semiconductor structures," *Plasmonics* **3**, 27-31 (2008).

Noell W., Abraham M., Mayr K., Ruf A., Barenz J., Hollricher O., Marti O., Gühtner P., "Micromachined aperture probe tip for multifunctional scanning probe microscopy," *Appl. Phys. Lett.* **70**(10), 1236-1238 (1997).

Novotny L. and Hafner C., "Light propagation in a cylindrical waveguide with a complex metallic dielectric function," *Phys. Rev. E* **50**, 4094-4106 (1994).

Novotny L., Pohl D. W., Hecht B., "Light confinement in scanning near-field optical microscopy," *Ultramicroscopy* **61,** 1-9 (1995).

Novotny L., Hecht B., Pohl D. W., "Implications of high resolution to near-field optical microscopy," *Ultramicroscopy* **71**, 341-344 (1998).

Novotny L., Beversluis M. R., Youngworth K. S., Brown T. G., "Longitudinal field modes probed by single molecules," *Phys. Rev. Lett.* **86**(23), 5251- 5254 (2001).

Novotny L. and Hecht B., *Principles of Nano-Optics*, Cambridge University Press, New York (2006).

Novotny L. and Stranick S. J., "Near field optical microscopy and spectroscopy with pointed probes," *Ann. Rev. Phys. Chem*. **57**, 303-331 (2006).

Novotny L., "The History of Near-field Optics," in E. Wolf (ed.), *Progress in Optics* **50**, Elsevier, Amsterdam, The Netherlands, chapter 5, 137-184 (2007).

Oesterschulze E., Rudow O., Mihalcea C., Scholz W., Werner S., "Cantilever probes for SNOM applications with single and double aperture tips," *Ultramicroscopy* **71**, 85-92 (1998).

Oesterschulze E., Georgiev G., Müller-Wiegand M., Vollkopf A., Rudow O., "Transmission line probe based on a bowtie antenna," *J. Microsc*. **202**(1), 39-44 (2001).

Ohtsu M., *Progress in Nano-electro-optics III Industrial applications and dynamics of the nano-optical system*, Springer-Verlag Berlin Heidelberg (2005).

Pack A., Hietschold M., Wannemacher R., "Propagation of femtosecond light pulses through near-field optical aperture probes," *Ultramicroscopy* **92**, 251–264 (2002).

Pangaribuan T., Jiang S., Ohtsu M., "High controllable fabrication of fiber probe for photon scanning tunnelling microscope," *Scanning* **16**, 362-367 (1994).

Parent G., Van Labeke D., Barchiesi D., "Fluorescence lifetime of a molecule near a corrugated interface: application to near-field microscopy," *J. Opt. Soc. Am. A* **16**(4), 896-908 (1999).

Patanè S., Cefalì E., Arena A., Gucciardi P. G., Allegrini M., "Wide angle near field optical probes by reverse tube etching," *Ultramicroscopy* **106**, 475-479 (2006).

Patanè S., Cefalì E., Spadaio S., Gardelli R., Albani M., Allegrini M., "Polarization-maintaining near-field optical probes," *J. Microsc*. **229**(2), 377-383 (2008).

Pilevar S., Atia W. A., Davis C. C., "Reflection near-field scanning optical microscopy: an interferometric approach," *Ultramicroscopy* **61**, 233-236 (1995).

Pilevar S., Edinger K., Atia A., Smolyaninov I., Davis C., "Focused ion-beam fabrication of fiber probes with well-defined apertures for use in near-field scanning optical microscopy," *Appl. Phys. Lett.* **72**, 3133–3135 (1998).

Pohl D. W., Denk W., Lanz M., "Optical stethoscopy: Image recording with resolution λ/20," *Appl. Phys. Lett.* **44**, 651-653 (1984).

Pohl D. W., "Optics at the nanometre scale," *Phil. Trans. R. Soc. Lond. A* **362**, 701-717 (2004).

Protasenko V. V., Gallagher A., Nesbitt D. J., "Factors that influence confocal apertureless near-field scanning optical microscopy," *Opt. Commun*. **233**, 45-56 (2004).

Protasenko V. V. and Gallagher A. C., "Apertureless near-field scanning optical microscopy of single molecules," *Nano Lett.* **4**(7), 1329-1332 (2004a).

Quong M. C. and Elezzabi A. Y., "Offset-apertured near-field scanning optical microscope probes," *Opt. Express* **15**(16), 10163-10174 (2007).

Raffa V., Castrataro P., Menciassi A., Dario P., "Focused Ion Beam as a Scanning Probe: Methods and Applications," in B. Bhushan and H. Fuchs (eds.) *Applied Scanning Probe Methods II: Scanning Probe Microscopy Techniques (NanoScience and Technology)* (volume 2), Springer Berlin, Heidelberg Ch 11, 361-412 (1992).

Rao S. S., *The finite element method in engineering* Butterworth-Heinemann, Burlington MA USA, (1999).

Rasmussen A. and Deckert V., "New dimension in nano-imaging: breaking through the diffraction limit with scanning near-field optical microscopy," *Anal. Bioanal. Chem*. **381**, 165-172 (2005).

Reddick R. C., Warmack R. J., Chilcott D. W., Sharp S. L., Ferrell T. L., "Photon scanning tunneling microscopy," *Rev. Sci. Instrum*. **61**, 3669-3677 (1990).

Reyntjens S. and Puers R., "A review of focused ion beam applications in microsystem technology," *J. Micromech. Microeng.* **11,** 287–300 (2001).

Roberts A., "Electromagnetic theory of diffraction by a circular aperture in a thick, perfectly conducting screen," *J. Opt. Soc. Am. A* **4**, 1970-1983 (1987).

Roberts A., "Near zone fields behind circular apertures in thick, perfectly conducting screens," *J. Appl. Phys.* **65**, 2896-2899 (1989).

Ropers C., Neacsu C. C., Elsaesser T., Albrecht M., Raschke M. B., Lienau C., "Grating-coupling of surface plasmons onto metallic tips: a nanoconfined light source," *Nano Lett.* **7**(9), 2784-2788 (2007).

Ropers C., Neacsu C. C., Raschke M. B., Albrecht M., Lienau C., Elsaesser T., "Light confinement at ultrasharp metallic tips*," Jpn. J. Appl. Phys*. **47**(7), 6051-6054 (2008).

Ruiter A. G. T., Veerman J. A., Garcia-Parajo M. F., van Hulst N. F., "Single molecule rotational and translational diffusion observed by near-field scanning optical microscopy," *J. Phys. Chem. A* **101**, 7318-7323 (1997).

Ruppin R., "Effect of non-locality on nanofocusing of surface plasmon field intensity in a conical tip," *Phys. Lett. A* **340**(1-4), 299-302 (2005).

Sadiq D., Shirdel J., Lee J. S., Selishcheva E., Park N., Lienau C., "Adiabatic nanofocusing scattering-type optical nanoscopy of individual gold nanoparticles," *Nano Lett*. **11**, 1609-1613 (2011).

Saiki T., Mononobe S., Ohtsu M., Saito N., Kusano J., "Spatially resolved photoluminescence spectroscopy of lateral pn junctions prepared by Si doped GaAs using a photon scanning tunneling microscope," *Appl. Phys. Lett.* **67**(15), 2191-2193 (1995).

Saiki T., Mononobe S., Ohtsu M., Saito N., Kusano J., “Tailoring a high-transmission fiber probe for photon scanning tunnelling microscope,” *Appl. Phys. Lett*. **68**(19), 2612-2614 (1996).

Saiki T. and Matsuda K., “Near-field optical fiber probe optimized for illumination-collection hybrid mode operation,” *Appl. Phys. Lett*. **74**(19), 2773-2775 (1999).

Saito Y., Ohashi Y., Verma P., “Optimization of s-polarization sensitivity in apertureless near-field optical microscopy,” *Int. J. Optics* **2012**, Article ID 962317, 6 pages doi:10.1155/2012/962317 (2012).

Sakai M., Mononobe S., Akiba S., Matsuda A., Hara W., Yoshimoto M., Saiki T., “High-contrast imaging of nano-channels using reflection near-field scanning optical microscope enhanced by optical interference,” *Opt. Rev.* **13**(4), 266-268 (2006).

Salvi J., Chevassus P., Mouflard A., Davi S., Spajer M., Courjon D., Hjort K., Rosengren L., “Piezoelectric shear force detection: a geometry avoiding critical tip/tuning fork gluing,” *Rev. Sci. Instrum*. **69**(4), 1744-1747 (1998).

Sanchez E. J., Krug II J. T., Xie X. S., “Ion and electron beam assisted growth of nanometric Si_mO_n structures for near-field microscopy,” *Rev. Sci. Instr.* **73**(11), 3901-3907 (2002).

Sandoghdar V. and Mlynek J., “Prospects of apertureless SNOM with active probes,” *J. Opt. A: Pure Appl. Op*. **1**, 523-530 (1999).

Sandoghdar V., “Trends and developments in scanning near field optical microscopy,” Proceedings of the International School of Physics “Enrico Fermi”, pp. 65-119 (2001).

Sandoghdar V., Michaelis J., Hettich C., Schmitt C., Zitzmann J., Kühn S., “Results and thoughts on optical microscopy using a single-molecule probe,” *Single Mol*. **2**(4), 277-281 (2001).

Shedd G. M., Lezec H., Dubner A. D., Melngailis J., “Focused ion beam induced deposition of gold,” *Appl. Phys. Lett.* **49**, 1584-1586 (1986).

Shen L., Chen X., Yang T. J., “Terahertz surface plasmon polaritons on periodically corrugated metal surfaces,” *Opt. Express* **16**(5), 3326–3333 (2008).

Shen L., Chen X., Zhong Y., Agarwal K., “Effect of absorption on terahertz surface plasmon polaritons propagating along periodically corrugated metal wires,” *Phys. Rev. B* **77**(7), 075408 1-7 (2008a).

Shi J. and Qin X. R., “Formation of glass fiber tips for scanning near-field optical microscopy by sealed- and open-tube etching,” *Rev. Sci. Instrum.* **76**, 013702 1-5 (2005).

Shubeita G. T., Sekatskii S. K., Dietler G., Potapova I., Mews A., Basché T., “Scanning near-field optical microscopy using semiconductor nanocrystals as a local fluorescence and fluorescence energy transfer source,” *J. Microsc*. **210**, 274-278 (2003).

Sonnefraud Y., Chevalier N., Motte J.-F., Huant S., Reiss P., Bleuse J., Chandezon F., Burnett M. T., Ding W., Maier S. A., “Near-field optical imaging with a CdSe single nanocrystal-based active tip," *Opt. Express* **14**, 10596-10602 (2006).

Sqalli O., Bernal M-P., Hoffman P., Marquis-Weible F., “Improved tip-performance for scanning near-field optical microscopy by the attachment of a single gold nanoparticle,” *Appl. Phys. Lett*. **76**(15), 2134-2136 (2000).

Stähelin M., Bopp M. A., Tarrach G., Meixner A. J., Zschokke-Gränacher I., “Temperature profile of fiber tips used in scanning near field optical microscopy,” *Appl. Phys. Lett*. **68**(19), 2603-2605 (1996).

Stevenson R., Granström M., Richards D., “Fluorescence scanning near-field optical microscopy of conjugated polymer blends,” *Appl. Phys. Lett.* **75**(11), 1574-1576 (1999).

Stöckle R., Fokas C., Deckert V., Zenobi R., Sick B., Hecht B., Wild U. P., "High-quality near-field optical probes by tube etching," *Appl. Phys. Lett.* **75**, 160–162 (1999).

Stöckle R. M., Schaller N., Deckert V., Fokas C., Zenobi R., "Brighter near-field optical probes by means of improving the optical destruction threshold," *J. Microsc*. **194**(2/3), 378-382 (1999a).

Stockman M. I., "Nanofocusing of optical energy in tapered plasmonic waveguides," *Phys. Rev. Lett.* **93**(13), 137404 1-4 (2004).

Suzuki M. and Saiki T., "Near-field fluorescence correlation spectroscopy using a fiber probe," *Jpn. J. of Appl. Phys*. **48**, 070209 1-3 (2009).

Synge E., "Suggested method for extending microscopic resolution into the ultramicroscopic region," *Phil. Mag. J. Sci.* **6,** 356-362 (1928).

Synge E., "An application of piezo-electricity to microscopy," *Phil. Mag. J. Sci.* **13**(83), 297-300, (1932).

Taminiau T. H., Segerink F. B., Moerland R. J., Kuipers L. (K.), van Hulst N. F., "Near-field driving of a optical monopole antenna,**"** *J. Opt. A: Pure Appl. Opt*. **9**, S315-S321 (2007).

Taminiau T. H., Moerland R. J., Segerink F. B., Kuipers L., van Hulst N. F., "λ/4 resonance of an optical monopole antenna probed by single molecule fluorescence," *Nano Lett.* **7**(1), 28-33 (2007a).

Tanaka K. and Tanaka M., "Optimized computer-aided design of I-shaped subwavelength aperture for high intensity and small spot size," *Opt. Commun*. **233**, 231-244 (2004).

Tanaka K., Katayama K., Tanaka M., "Optical field characteristics of nanofocusing by conical metal-coated dielectric probe," *Opt. Express* **19**(21), 21028-21037 (2011).

Themistos C., Azimur Rahman B. M., Rajarajan M., Rakocevic V., Grattan K. T. V., "Finite element solutions of surface-plasmon modes in metal-clad dielectric waveguides at THz frequency," *IEEE J. Lightwave Technol*. **24**(12), 5111-5118 (2006).

Toledo-Crow R., Yang P. C., Chen Y., Vaez-Iravani M., "Near field differential scanning optical microscope with atomic force regulation," *Appl. Phys. Lett*. **60**, 2957-2959 (1992).

Tortora P., Descrovi E., Aeschimann L., Vaccaro L., Herzig H. P., Dändliker R., "Selective coupling of HE_{11} and TM_{01} modes into microfabricated fully metal-coated quartz probes," *Ultramicroscopy* **107**(2-3), 158-165 (2007).

Tseng A. A., "Recent developments in micromilling using focused ion beam technology," *J. Micromech. Microeng.* **14**, R15–R34 (2004).

Unger M. A., Kossakovski D. A., Kongovi R., Beauchamp J. L., Baldeschwieler J. D., Palanker D. V., "Etched calchogenide fibers for near-field infrared scanning microscopy," *Rev. Sci. Instrum.* **69**(8), 2988-2993 (1998).

Utke I., Hoffmann P., Melngailis J., "Gas-assisted focused electron beam and ion beam processing and fabrication," *J. Vac. Sci. Technol. B* **26**, 1197-1276 (2008).

Vaccaro L., Aeschimann L., Staufer U., Herzig H. P., Dändliker R., "Propagation of the electromagnetic field in fully coated near-field optical probes," *Appl. Phys. Lett.* **83**(3), 584–586 (2003).

Valaskovic G. A., Holton M., Morrison G. H., "Parameter control, characterization, and optimization in the fabrication of optical fiber near-field probes," *Appl. Optics* **34**(7), 1215-1228 (1995).

van Lebeke D. and Barchiesi D., "Scanning-tunneling optical microscopy: a theoretical macroscopic approach," *J. Opt. Soc. Am. A* **9**(5), 732-739 (1992).

van Lebeke D., Baida F., Barchiesi D., Courjon D., "A theoretical model for the inverse scanning-tunneling optical microscope (ISTOM)," *Opt. Commun*. **114**, 470-480 (1995).

van Hulst N. F., Garcia-Parajo M. F., Moers M. H. P., Veerman J.-A., Ruiter A. G. T., "Near-field fluorescence imaging of genetic material: toward the molecular limit," *J. Struct. Biol.* **119**, 222-231 (1997).

van Hulst N. F., Veerman J-A., Garcia-Parajo M. F., Kuipers L., "Analysis of individual (macro)molecules and proteins using near-field optics,**"** *J. Chem. Phys*. **112**(18), 7799-7810 (2000).

Vasile M. J., Xie J., Nassar R., "Depth control of focused ion-beam milling from a numerical model of the sputter process," *J. Vac. Sci. Technol. B* **17**(6), 3085-3090 (1999).

Veerman J. A., Otter A. M., Kuipers L., van Hulst N. F., "High definition aperture probes for near-field optical microscopy fabricated by focused ion beam milling," *Appl. Phys. Lett.* **72**, 115–3117 (1998).

Veerman J. A., Garcia-Parajo M. F., Kuipers L., van Hulst N. F., "Single molecule mapping of the optical field distribution of probes for near-field microscopy," *J. Microsc.* **194**(2-3), 477-482 (1999).

Vogel M. W. and Gramotnev D. K., "Adiabatic nano-focusing of plasmons by metallic tapered rods in the presence of dissipation," *Phys. Lett. A* **363**, 507-511 (2007).

Vogel M. W. and Gramotnev D. K., "Optimization of plasmon nano-focusing in tapered metal rods," *J. Nanophotonics* **2**, 1-17 (2008).

Vogel M. W. and Gramotnev D. K., "Shape effects in tapered metal rods during adiabatic nanofocusing of plasmons," *J. Appl. Phys.* **107**, 044303 1-8 (2010).

Wang X. Q., Wu S-F., Jian G-S., Pan S., "The advantages of a pyramidal probe tip entirely coated with a thin metal film for SNOM," *Phys. Lett. A* **319**(5-6), 514-517 (2003).

Wang Y., Bettermann A. D., van der Weide D. W., "Process for scanning near-field microwave microscope probes with integrated ultratall coaxial tips," *J. Vac. Sci. Technol. B* **25**(3), 813-816 (2007).

Wang Y., Srituranovich W., Sun C., Zhang X., "Plasmonic nearfield scanning probe with high transmission," *Nano Lett*. **8**(9), 3041-3045 (2008).

Wang Y., Wang Y-Y., Zhang X., "Plasmonic nanograting tip design for high power throughput near-field scanning aperture probe," *Opt. Express* **18**(13), 14004-14011 (2010).

Wei Q., Li K.-D., Lian J., Wang L., "Angular dependence of sputtering yield of amorphous and polycrystalline materials," *J. Phys. D: Appl. Phys.* **41**, 172002 1-4 (2008).

Weston K. D. and Buratto S. K., "A reflection near-field scanning optical microscope technique for subwavelength resolution imaging of thin organic films," *J. Phys. Chem. B* **101**(29), 5684-5691 (1997).

Williamson R. L. and Miles M. J., "Melt-drawn scanning near-field optical microscopy probe profiles," *J. Appl. Phys.* **80**(9), 4804-4812 (1996).

Winzer M., Kleiber K., Dix N., Wiesendanger R., "Fabrication of nano-dot and nano-ring-arrays by nanosphere lithography," *Appl. Phys. A. Mater.* **63**, 617-619 (1996).

Wu J. J., Yang T. J., Shen L. F., "Subwavelength microwave guiding by a periodically corrugated metal wire," *J. Electromagn. Waves Appl*. **23**(1), 11-19 (2009).

Yakobson B. I., Moyer P. J., Paesler M. A., "Kinetic limits for sensing tip morphology in near-field scanning optical microscopes," *J. Appl. Phys.* **73**, 7984-7986 (1993).

Yamamura Y., "An empirical formula for angular dependence of sputtering yields," *Radiation Effects* **80**, 57-72 (1984).

Yang J., Zhang J., Li Z., Gong Q., "Fabrication of high-quality SNOM probes by pre-treating the fibres before chemical etching," *J. Microsc.* **228**(1), 40–44 (2007).

Yatsui T., Kourogi M., Ohtsu M., "Highly efficient excitation of optical near-field on an apertured fiber probe with an asymmetric structure," *Appl. Phys. Lett*. **71**(13), 1756-1758 (1997).

Yatsui T., Kourogi M., Ohtsu M., "Increasing throughput of a near-field optical fiber probe over 1000 times by the use of a triple-tapered structure," *Appl. Phys. Lett*. **73**(15), 2090-2092 (1998).

Yatsui T., Itsumi K., Kourogi M., Ohtsu M., "Metallized pyramidal silicon probe with extremely high throughput and resolution capability for optical near-field technology,**"** *Appl. Phys. Lett*. **80**(13), 2257-2259 (2002).

Yu Y., Blake P., Roper D. K., "Tapered optical fibers designed for surface plasmon resonance phase matching," *Langmuir* **25**(1), 59-63 (2009).

Zhang Y., Dhawan A., Vo-Dinh T., "Design and fabrication of fiber-optic nanoprobes for optical sensing," *Nanoscale Res. Lett.* **6**(18), 6 pp. (2011).

Zhu Y., "Scanning near-field magneto-optic microscopy," in: Y. Zhu (ed.) *Modern techniques for characterizing magnetic materials*, Kluiver Academic Publishers, Boston, chapter 12, 455-515 (2005).

Zwillinger D., "*Standard mathematical tables and formulae*," CRC Press, Boca Raton, 32nd Edition (2012).

Acknowledgements

I thank my supervisors, Prof. Dr. Gian-Luca Bona, Prof. Dr. Christian Hafner, Dr. Urs Sennhauser, for giving me the chance to make this experience and for their helpful advice and suggestions.

I gratefully acknowledge the contribution of the following people and institutions: the Swiss National Science Foundation for financial support (project number 200021-115895), Dr. Konstantins Jefimovs and Olivier Scholder (Empa) for assistance in FIB nanostructuring of the probes, Dr. Rolf Brönnimann (Empa) for support in the assemblage of the mechanical parts of the SNOM head, Emanuel Schmid (previously at Empa) for initiating the construction of the electronics for shear force probe-sample distance control, Dr. Rainer F. Mahrt and Dr. Gabriele Rainò (IBM Zurich Research Laboratory) and Dr. Alois Renn (ETH Zurich) for assistance in sample preparation, Silvia Eppenberger and Peter Anderegg (Empa) for administrative support.

Moreover I thank Sergio Sanabria, Sandra Zweifel and Roman Furrer for their friendly and sensitive attitude especially in the most difficult moments.

Finally I would like to express my deepest gratitude to my family, my parents and my sister Adriana, who have inspired in me the strength to cope with the difficulties encountered in my research activity and in everyday life.

Curriculum vitae

Name: Valeria
Surname: Lotito
Nationality: Italian
Place and date of birth: Bari, 30/09/1983

Work experience

- 2008-2012: PhD position ETH Zurich and Empa in Dübendorf, Switzerland; development of novel probes for scanning near-field optical microscopy;
- 2007: Marie Curie Fellowship at Thales Nederland B.V. (multinational corporation developing electronic systems for defence) in Hengelo, the Netherlands; signal processing for multiple target tracking.

Education

- 2004-2006: M.Sc. in Electronic Engineering, Politecnico di Bari, Italy
- 2001-2004: B.Sc. in Electronic Engineering, Politecnico di Bari, Italy
- 1996-2001: Secondary school - Liceo Scientifico "E. Fermi", Bari, Italy

Journal publications

- V. Lotito, C. Hafner, U. Sennhauser, G.-L. Bona "A novel nanostructured scanning near field optical microscopy probe based on an adirectional asymmetry" Journal of Computational and Theoretical Nanoscience 9, 486-494 (2012)
- V. Lotito, U. Sennhauser, C. Hafner, G.-L. Bona "Interaction of an asymmetric scanning near field optical microscopy probe with fluorescent molecules" Progress in Electromagnetics Research 121, 281-299 (2011)
- V. Lotito, U. Sennhauser, C. Hafner, G.-L. Bona "Fully metal-coated scanning near-field optical microscopy probes with spiral corrugations for superfocusing under arbitrarily oriented linearly polarised excitation" Plasmonics 6(2), 327-336 (2011)
- V. Lotito, U. Sennhauser, C. Hafner "Numerical analysis of novel asymmetric SNOM tips" PIERS Online 7(4), 394-400 (2011)
- V. Lotito, U. Sennhauser, C. Hafner "Effects of asymmetric surface corrugations on fully metal-coated scanning near field optical microscopy tips" Optics Express 18(8), 8722-8734 (2010)
- V. Lotito, U. Sennhauser, C. Hafner "Finite element analysis of asymmetric scanning near field optical microscopy probes" Journal of Computational and Theoretical Nanoscience 7(8), 1596-1609 (2010)

Book chapters

- V. Lotito, C. Hafner, U. Sennhauser, G.-L. Bona "Novel SNOM probes based on nanofocusing in asymmetric structures" to be published in K. Y. Kim Ed. "Plasmonics: Principles and Applications", Intech, Rijeka, Croatia, ISBN 978-953-308-91-2

Conference proceedings

- V. Lotito, U. Sennhauser, C. Hafner " Scanning near field optical microscopy probes with adirectional asymmetries" EOS Topical Meetings at Capri, Italy, 26-28 September 2011, ISBN 978-3-00-033710-9
- V. Lotito, U. Sennhauser, C. Hafner "Properties of asymmetric scanning near field optical microscopy probes" EOS Annual Meeting 2010, 26-29 October 2010, Paris, France, ISBN 978-3-00-030509-2

Conferences and workshops

- Oral presentation: V. Lotito, C. Hafner, U. Sennauser, G.-L. Bona "Asymmetric SNOM probes: from design to fabrication" 8th Workshop on Numerical Methods for Optical Nano structures, ETH Zurich, Switzerland, 2-4 July 2012
- Poster: V. Lotito, C. Hafner, U. Sennauser, G.-L. Bona "Asymmetries in scanning near field optical microscopy probes" Nanolight 2012, Benasque, Spain, 11-17 March 2012
- Oral presentation: V. Lotito, U. Sennauser, C. Hafner "Scanning near field optical microscopy probes with adirectional asymmetries" 4th EOS Topical Meeting on Optical Microsystems, Capri, Italy, 26-28 September 2011
- Oral presentation: V. Lotito, U. Sennauser, C. Hafner "Focusing properties of SNOM probes with adirectional asymmetries" 7th Workshop on Numerical Methods for Optical Nano structures, ETH Zurich, Switzerland, 4-6 July 2011
- Oral presentation: V. Lotito "Finite element modelling of SNOM probes with asymmetries" within the series of lectures "Seminar on Electromagnetics and Terahertz Electronics" ETH Zurich, Switzerland, 13 April 2011
- Oral presentation: V. Lotito, U. Sennauser, C. Hafner "Numerical analysis of novel asymmetric SNOM tips" Progress in Electromagnetics Research Symposium, Marrakech, Morocco, 20-23 March 2011
- Oral presentation: V. Lotito, U. Sennauser, C. Hafner "Properties of asymmetric scanning near field optical microscopy probes" EOS Annual Meeting 2010, Paris, France, 26-29 October 2010
- Oral presentation: V. Lotito, U. Sennauser, C. Hafner "Numerical analysis of novel SNOM tip configurations", 6th Workshop on Numerical Methods for Optical Nano structures, ETH Zurich, Switzerland, 5-7 July 2010
- Oral presentation: V. Lotito "Numerical analysis of SNOM tips", within the series of lectures "Seminar on Electromagnetics and Terahertz Electronics" ETH Zurich, Switzerland, 28 April 2010
- Oral presentation: V. Lotito, U. Sennauser, C. Hafner "Finite element analysis of asymmetric SNOM probes" 5th Workshop on Numerical Methods for Optical Nano structures, ETH Zurich, Switzerland, 6-8 July 2009